ISBN 978-82-326-2242-9 (printed version)
ISBN 978-82-326-2243-6 (electronic version)
ISSN 1503-8181

Doctoral theses at NTNU, 2017:85

Torleiv Håland Bryne

Nonlinear Observer Design for Aided Inertial Navigation of Ships

NTNU
Norwegian University of
Science and Technology
Faculty of Information Technology and Electrical
Engineering
Department of Engineering Cybernetics

NTNU
Norwegian University of
Science and Technology

Doctoral theses at NTNU, 2017:85

NTNU

NTNU
Norwegian University of
Science and Technology

Torleiv Håland Bryne

Nonlinear Observer Design for Aided Inertial Navigation of Ships

Thesis for the degree of Philosophiae Doctor

Trondheim, March 2017

Norwegian University of Science and Technology
Faculty of Information Technology and Electrical Engineering
Department of Engineering Cybernetics

NTNU
Norwegian University of
Science and Technology

NTNU
Norwegian University of Science and Technology

Thesis for the degree of Philosophiae Doctor

Faculty of Information Technology and Electrical Engineering
Department of Engineering Cybernetics

ISBN 978-82-326-2242-9 (printed version)
ISBN 978-82-326-2243-6 (electronic version)
ISSN 1503-8181

ITK-report: 2017-5-W

Doctoral theses at NTNU, 2017:85

Printed by Skipnes Kommunikasjon as

Nonlinear Observer Design for Aided Inertial Navigation of Ships

Torleiv Håland Bryne

To dad

and the pillars still being here

Summary

This thesis focuses on strapdown inertial navigation systems for marine vessels, exploiting low-cost micro-electro-mechanical-systems (MEMS) inertial sensors and nonlinear observers for sensor fusion. The motivation behind the research is to investigate the possibility to develop cost-effective inertial navigation systems providing, roll, pitch and heave estimates, similar to typical maritime vertical reference units (VRUs), while providing estimates of the vessel's position, velocity and attitude as well. In addition, such systems should be fault tolerant.

Nonlinear observers serve as alternatives to the well established extended Kalman filter where explicit stability properties are more cumbersome, and in some cases impossible, to achieve. The presented observers are proven to have semiglobal exponentially stability properties, where semiglobality is mainly due to the infeasibility of pure global results when considering attitude estimation of the special orthogonal group of order three. The observers are benchmarked in full-scale experiments using an established navigation suite based on the extended Kalman filter. Similar performance was obtained in state-state conditions.

The observer designs are based on a framework of a nonlinear attitude observer and a translational motion observer, which forms a feedback interconnection. This is extended to incorporate a virtual vertical reference (VVR) measurement for vertical aiding of the inertial navigation system. The reference signal is utilized as an alternative to vertical measurements from position references such as global navigation satellite systems (GNSS). The inclusion of the virtual reference facilitates high-performance heave estimation. The VVR is also beneficial w.r.t. to attitude estimation improving the roll and pitch estimates by exploiting kinematics couplings between the orientational and the translational motion. In addition to including the VVR in the inertial navigation system, the observer structures are further extended to employ time-varying gains. Moreover, the VVR concept is improved utilizing an error model based on sea-state-dependent parameters. Simulations indicate that the industry standard VRU performance specification of five centimeters or five per cent root-mean-square heave error is obtainable with the proposed design. The presented observer structure are also validated using sensor data gathered on an offshore vessel in operation.

Access to the mean motion of the vessel prevents unwanted motion compensation by the control system. Therefore, marine surface craft often apply wave filtering of position and heading measurements in order to reconstruct the mean motion of the vessel, by attenuating the oscillatory motion components, due to waves, embedded in the measurements. In this work, wave filtering based, on estimated and measured signals from the inertial navigation system and inertial sensors, is presented. The presented work is the first to do so, serving as an alternative to traditional observer-based approaches exploiting ship models.

The thesis also consider fault tolerance and sensors redundancy using nonlin-

ear observers. Concepts for fault detection and isolation using position, heading and inertial measurement are presented based on triple-redundant sensor configurations and nonlinear observers. Outcomes related to weighting and averaging of multiple sensor systems are also presented. In contrast to the VRU systems on board offshore vessels, where the measurements often are average on the output, this theses also focuses on weighting directly on the underlying inertial measurements before these are utilized as to estimate the VRU solution. In addition, position, velocity and heading estimates are also obtained with the approach proposed. Hence, the thesis provides a more integrated design compared to the current industrial practice, that is relying on more separated sensors. The fault tolerance properties of the concepts for redundant inertial measurement units (IMUs), are validated using inertial sensors data gather at sea, injected with artificial faults.

In addition, the dissertation presents a study on the difference between loosely and tightly coupled integration in the context of nonlinear observers and on how these can be implemented in discrete time. Using data gather during an unmanned aerial vehicle flight, results related to the performance difference between these two integration techniques, based on measurements from a MEMS IMU and a standalone GNSS receiver, relative to a real time kinematic GNSS positioning solution, are presented.

Finally, the algorithms presented in this thesis have the potential to be implemented and used commercially on ships and on other types of marine surface vessels. The concepts presented have the potential to increase fault tolerance. Multiple MEMS IMUs have to be installed in order to achieve this, however, these combined with the presented methods have the potential to replace existing VRU solutions. Therefore, the cost might be reduced, while the navigation system's performance and its fault-tolerance properties may be increased.

Preface

This thesis is submitted in partial fulfillment of the requirements of the degree of philosophiae doctor (Ph.D.) at the Norwegian University of Science and Technology (NTNU). The work presented in this thesis is the results of the doctoral studies carried out at the Centre for Autonomous Marine Operations and Systems (NTNU AMOS), Department of Engineering Cybernetics, NTNU under supervision of Professors Thor I. Fossen and Tor Arne Johansen. I was employed as one of two Ph.D. candidates by the knowledge building project "Fault-Tolerant Inertial Sensor Fusion for Marine Vessels" with Rolls–Royce Marine as industrial partner. The project was financed by the Research Council of Norway and Rolls–Royce Marine through the Centres of Excellence funding scheme and the MAROFF (Maritime activities and offshore operations) programme, grant numbers, 223254 and 225259 respectively.

Acknowledgments

First I would like to thank Professor Fossen for giving me this opportunity to peruse the Ph.D. degree on a topic of great personal interest. I would also like to thank him for introducing me to Professor Johansen. It has been a great privilege to be a Ph.D. candidate under your supervision. Thank you for a prosperous working environment, where I have received great supervision and guidance from both. I would also like to thank you for being allowed to be autonomous, by giving me the opportunity to shape my own working days and do the research on topics of my own choosing. I feel honored to have had the opportunity to work with two of Norway's most distinguished researchers within the field of control systems.

In conducting practical research, I have been fortunate to have had a great industrial partner in Rolls–Royce Marine, following the research closely, providing us with comments and suggestions, and in so improving the overall research and contributing to making the research industrially relevant. In this regard, I would like to thank doctor Jann Peter Strand, doctor Ivar Flagstad Ihle, doctor Bjørnar Vik, Frode Block, Ronny Tomren, Robert Drønnen, Eivind Vinje, Olga Otmianowska and Tore Gangstad at Rolls–Royce Marine for their time, valuable discussions, technical insight and assistance during this work. In addition to being an academic and technical partner, Rolls–Royce has also contributed by partially financing my Ph.D. For this I am grateful. Also, big thanks go out to the people at Rolls–Royce Marine for facilitating the collaboration with Farstad Shipping and to Farstad for allowing us to install sensors onboard one of their offshore vessels. This has had a major impact on the quality of the research, allowing us to validate and verify the algorithms developed throughout the course of these Ph.D. studies.

In addition to great supervision and industrial collaboration, I also have had the pleasure to work with great colleagues at the Department of Engineering

Cybernetics. Thanks, goes out to Stafano Bertelli, Rune Mellingseter, Terje Haugen, Glenn Angel, John Olav Horrigmo, Åsmund Stavdahl, Lars Semb and former colleague Torkel Hansen for technical assistance in the development of the data acquisition unit, installed on the offshore vessel. I would also like to thank Tove Kristin Blomset Johnsen, Head of administration at the department, for help with administrative tasks, both before and during my Ph.D. research fellowship.

It has been a pleasure to have enlightening discussions with experts on satellite and inertial navigation systems. Therefore, thanks are warranted to Dr. Nadezda Sokolova at the Department of Engineering Cybernetics and SINTEF ICT, and Dr. Aiden Morrison, SINTEF ICT, for valuable discussions on GNSS systems. Thanks also goes out to Kenneth Gade and Kristian Svartveit at the Norwegian Defence Research Establishment (FFI) for discussions on inertial navigation systems. I would also like to thank FFI and Kongsberg Maritime for allowing us access to the navigation software suite, NavLab. In addition, thanks goes out to Håvard Fjær Grip at NASA JPL for valuable discussions related to nonlinear stability theory.

I have also had the privilege of working along many great fellow Ph.D. candidates and Postdoc fellows, which have provided a prosperous working environment, both at AMOS and at the department, including fruitful discussions and insight in a variety of topics related to general control theory, navigation and to marine control systems. There are so many of you. Thank you all for both interesting working days and a nice spare time as well. I will, however, mention one, Robert Harald Rogne, being my closest college, my office mate, employed at the same project. I thank you for a good and rewarding working partnership. Especially, for our joint work, both academic and engineering-wise.

I would also like to thank all my friends for supporting me, for our interesting discussions on non-work-related topics (some work-related topics too) and for all the joy before, throughout, and hopefully after, the time as a Ph.D. candidate.

Finally, I would like to thank my family and extended family for their support, directly and indirectly, throughout this endeavor. Some special thanks are due. My uncle Oddvar has been a source of inspiration, being the first NTH/NTNU engineer in the family. Thank you for that. I would like to thank my aunt Gro for financial support throughout my studies. Big thanks go to my aunt Dina and uncle Runar for supporting and helping my mother. To my grandmother Kari, thank you for being my tailor. Also, Aslak deserves a big thank for being a great brother and roommate. To my mother, thank you for being a parent for two these last seven and half years after dad's passing.

To round off. Even though being a Ph.D. candidate has given me rewarding experiences, it has from time to time been challenging and have required considerable amounts of work. This, however, is perhaps for the better...

> Work saves us from three great evils: boredom, vice and need
>
> *Voltaire, Candide, 1759*

Contents

List of Figures

List of Tables

Abbreviations

6-DOF six degrees of freedom.

AHRS attitude and heading reference system.

ARS angular rate sensor.

AUV autonomous underwater vehicle.

CAEE cumulative absolute estimation error.

dGNSS differential global navigation satellite systems.

DP dynamic positioning.

DR dead reckoning.

ECEF Earth Centered Earth Fixed.

ECI Earth Centered Inertial.

EKF extended Kalman filter.

FDI fault detection and isolation.

FFT fast Fourier transform.

FOG fiber optic gyroscope.

GES global exponential stability.

GNC guidance, navigation and control.

GNSS global navigation satellite systems.

GPS Global Positioning System.

HPR hydroacoustic position reference.

HRG hemispherical resonant gyroscope.

IMU inertial measurement unit.

INS inertial navigation system.

KF Kalman filter.

LF low frequency.

LOS line of slight.

LS least squares.

LTI linear time invariant.

LTV linear time varying.

MEKF multiplicative extended Kalman filter.

MEMS micro-electro-mechanical-systems.

MSE mean square error.

NED North East Down.

NLO nonlinear observer.

PE persistency of excitation.

PosRef position reference.

PSD power spectral destiny.

PVA position, velocity and attitude.

QUEST QUaternion ESTtimation.

RLG ring laser gyroscope.

RMS root mean square.

RTK real time kinematic.

TMO translational motion observer.

UAV unmanned aerial vehicle.

UCC uniformly completely controllable.

UCO uniformly completely observable.

UERE user equivalent range error.

ULES uniform local exponential stability.

USGES uniform semiglobal exponential stability.

VRU vertical reference unit.

VVR virtual vertical reference.

WF wave frequency.

Nomenclature

$\boldsymbol{q}_a^b$ Unit quaternion from frame $\{a\}$ to frame $\{b\}$.

$\boldsymbol{R}_a^b$ Rotation matrix from frame $\{a\}$ to frame $\{b\}$.

$\{i\}$ Inertial coordinate frame.

$\{e\}$ Earth Centered Earth Fixed coordinate frame.

$\{n\}$ North East Down coordinate frame.

$\{t\}$ Tangent coordinate frame.

$\{b\}$ BODY coordinate frame.

ϕ Roll angle.

θ Pitch angle.

ψ Yaw angle.

μ Latitude on the WGS-84 ellipse.

λ Longitude on the WGS-84 ellipse.

h Height over the WGS-84 ellipse.

$\boldsymbol{p}_{bc}^a$ Position vector of frame $\{c\}$ relative frame $\{b\}$ decomposed in frame $\{a\}$.

$\boldsymbol{v}_{bc}^a$ Linear velocity vector of frame $\{c\}$ relative frame $\{b\}$ decomposed in frame $\{a\}$.

$\boldsymbol{f}_{bc}^a$ Specific force of frame $\{c\}$ relative frame $\{b\}$ decomposed in frame $\{a\}$.

$\boldsymbol{\omega}_{bc}^a$ Angular velocity of frame $\{c\}$ relative frame $\{b\}$ decomposed in frame $\{a\}$.

$\boldsymbol{g}_b^a$ Gravity vector decomposed in frame $\{a\}$.

1 Introduction

1.1 Context and Background

Maritime inertial navigation systems (INSs) are the main focus of this dissertation. The usage of the term *navigation* is widely adopted in everyday life with numerous of meanings depending on context. These include the act of moving, and finding one's way in an unknown environment, ascertaining a craft's position or even browsing the pages of the internet. Originally the term meant the art of sailing a ship, in particular steering and maneuvering, and is derived from the Latin words *navis* and *agere*, translated to "ship" and "to drive" (Fossen, 2011). In a contemporary scientific context, navigation usually relates to the ascertainment of position, velocity and attitude (PVA) of some object relative to a reference point. Such usages of the navigation term is applicable for all types of craft and vehicles, such as ships, submarines, aircraft, cars and agricultural machinery. Other definitions of navigation also exist where path planning and maneuvering may be included in the definition. However, when applying the guidance, navigation and control (GNC) framework, as done in this thesis, path planning and maneuvering are included in the guidance and the control system, respectively, (Fossen, 2011, Ch. 9). A generalized overview of the GNC signal flow for marine craft is illustrated in Figure 1.1.

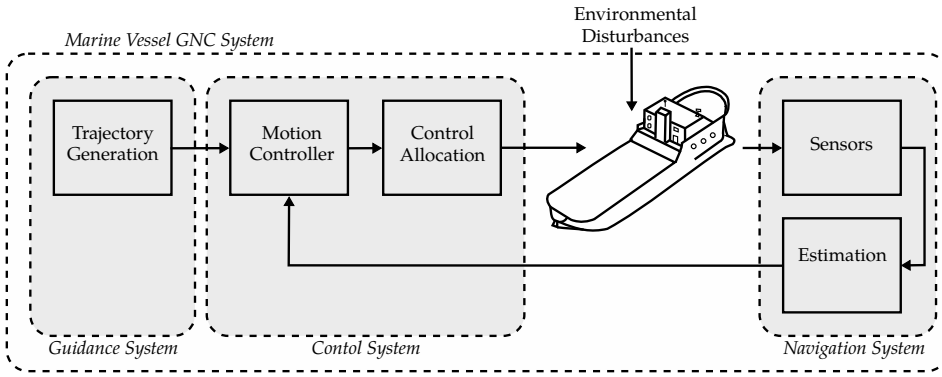

Figure 1.1: Simplified overview of the GNC signal flow. Fossen (2011, Ch. 9–12) can be studied for details.

1.1.1 Marine navigation systems: Past, current and future

Execution of marine of operations, oceanographic research missions and transportation at sea are all examples of situations where access to precise and accurate vessel motion data is vital in order to carry out its operations in a safe and efficient manner. Leverarm compensation of position measurements, attitude corrections

of onboard antennas, heave corrections of oceanographic data and heave compensation of cranes and drilling equipment are specific examples of tasks requiring high-quality motion data. Also automatic and autonomous docking systems require high precision and high accuracy PVA estimates. Motion data is also used by onboard decision support systems. Access to accurate, precise and reliable PVA information is necessary in all these examples. Often the PVA signals are obtained by the navigation system, Figure 1.1, before used by the other systems onboard to guide and control the vessel. Now-a-days navigation systems filters measured signals and reconstructs unknown states or signals from noisy measurements using some filtering and estimation software.

Before the advent of motion sensors, computers and electronic navigational aids, navigation at sea was carried out with sextant and, at the time, accurate clocks to manually obtain the position on Earth through measurements and calculations. By crudely estimating the ship's speed and heading, one could calculate a new position based on a previously known one, a process referred to as dead reckoning (DR). The origin of DR as an expression is not known, but one possibility is that it stems from ded reckoning, short for deduced reckoning, (Misra and Enge, 2011, Ch. 1). As time developed one of the major breakthroughs in navigation technology and an essential innovation in paving the way for automatic control of ships where the invention of the gyrocompass, first installed by Anschutz in 1907, and the ballistic compass by Elmer A. Sperry three years later. Such a device was one of the key parts of the first autopilot known as *Metal Mike*. The gyrocompass, based on gimbal inertial sensor technology and physical self-alignment, has later established itself as the de facto standard of heading determination on ships and free floaters. The first complete INS for PVA estimation was developed by the Charles Stark Draper Laboratory (MIT Instrumentation Laboratory at the time) in the 1950s.

Modern INSs provide the user with PVA information with high resolution independent of the vehicle platform using strapdown sensors. Strapdown INS is a type of INSs based on accelerometer and angular rate measurements from sensors mounted directly to the craft's hull or fuselage, while the rotational and translational PVA motion of the craft, relative to the Earth, is obtained through software by mechanization of the kinematic strapdown equations in a DR fashion. Commercially available global navigational aids based on global navigation satellite systems (GNSS) technology, in particular the Global Positioning System (GPS), have paved the way for wide spread INS utilization based on low-cost inertial sensors, which are in need of frequent position corrections. The reason for this can be understood from the complementary nature of GNSS and inertial measurements indicated in Table 1.1. High-grade sensors are still frequently used in GNSS denied environments and in applications where GNSS outage should not impede the PVA determination properties of the navigation system.

Future maritime navigation systems may turn out to be quite similar to the

Table 1.1: GNSS/INS: Complementary features. Positive and negative features/characteristics are indicated with green and red, respectively.

GNSS	INS
Bounded errors	Unbounded errors
Good long-term accuracy	Poor long-term accuracy
Poor short-term accuracy	Good short-term accuracy
Relies on external information sources (sat. pos. & velo.)	Self-contained
Medium dependent: Susceptible to obstruction, jamming and spoofing	Non-jammable and spoofable
Attitude not estimated[a]	Attitude estimated

[a] Heading can be estimated with a dual-receiver solution.

state-of-the-art systems of today. The cost and size, however, will go down and reliability must increase to enable more remote sensing using autonomous underwater vehicles (AUVs) and unmanned aerial vehicles (UAVs), applying georeferencing. Similar developments will enable commercialization and widespread use of autonomous ships and aircraft in e.g. oceanic and coastal mapping and monitoring and transportation of goods and people.

1.1.2 Inertial navigation – Sensor technology

Inertial sensors measure angular rates and specific forces, using rate gyros (or angular rate sensors (ARSs)) and accelerometers, respectively. High-end inertial sensing products can be based on mechanical gimbal-based systems or on sensor technology based on fiber optic gyroscopes (FOGs), hemispherical resonant gyroscopes (HRGs) and ring laser gyroscopes (RLGs), (Armenise et al., 2010). Sensors based on micro-electro-mechanical-systems (MEMS) technology have considerable lower cost, but also lower performance w.r.t. larger sensor biases, both static and dynamic. The static bias is often referred to as offset representing turn-on or run-to-run bias. The dynamic bias is the in-run variation of the bias also known as bias stability. In addition to sensor bias there are there are other sensor errors such as scale factor and scale factor nonlinearity, (Titterton and Weston (2004, Ch. 4-8), Grewal et al. (2013, Ch. 3.3–3.4)). Rate gyros also have g-sensitivity induced errors. Sensor assemblies having tri-axial and orthogonal mounts of both rate gyros/ARSs and accelerometers are referred to as inertial measurement units (IMUs), illustrated in Figure 1.2. These sensors may also be misaligned internally in the triad. A resulting comprehensive measurement model (Groves, 2013, Ch. 4.4) of

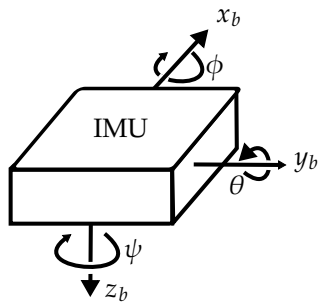

Figure 1.2: Illustration of an IMU measuring six-degree-of-freedom motion.

an IMU, measuring specific force, $\boldsymbol{f}_{ib}^{b}$, and angular rate, $\boldsymbol{\omega}_{ib}^{b}$, may look like

$$\boldsymbol{f}_{\text{IMU}}^{b} = (\boldsymbol{I}_3 - \boldsymbol{M}_{\text{acc}})\, \boldsymbol{f}_{ib}^{b} + \boldsymbol{b}_{\text{acc}}^{b} + \boldsymbol{w}_{\text{acc}}^{b} \tag{1.1}$$

$$\boldsymbol{\omega}_{\text{IMU}}^{b} = \left(\boldsymbol{I}_3 - \boldsymbol{M}_{\text{gyro}}\right) \boldsymbol{\omega}_{ib}^{b} + \boldsymbol{b}_{\text{gyro}}^{b} + \boldsymbol{G}(\boldsymbol{f}_{ib}^{b}) + \boldsymbol{w}_{\text{gyro}}^{b} \tag{1.2}$$

where the bias $\boldsymbol{b}_{\star}^{b}$ have two components;

$$\boldsymbol{b}_{\star}^{b} = \boldsymbol{b}_{\star\,\text{offset}}^{b} + \boldsymbol{b}_{\star\,\text{dynamic}}^{b}, \tag{1.3}$$

and

$$\boldsymbol{M}_{\star} = \begin{pmatrix} s_{\star,x} & \mu_{\star,xy} & \mu_{\star,xz} \\ \mu_{\star,yx} & s_{\star,y} & \mu_{\star,yz} \\ \mu_{\star,zx} & \mu_{\star,zy} & s_{\star,y} \end{pmatrix}, \tag{1.4}$$

with $\boldsymbol{s}_{\star} = \left(s_{\star,x}; s_{\star,y}; s_{\star,z}\right)$ containing the respective triad's scale factors, while

$$\boldsymbol{m}_{\star} = \left(\mu_{\star,xy}; \mu_{\star,xz}; \mu_{\star,yx}; \mu_{\star,yz}; \mu_{\star,zx}; \mu_{\star,zy}\right)$$

represents the six misalignment angles. $\boldsymbol{G}(\boldsymbol{f}_{ib}^{b})$ is the g-induced error on the rate gyros, and $\boldsymbol{w}_{\star}^{b}$ represents remaining errors, typically modeled as white noise in estimators. Furthermore, $\{b\}$ and $\{i\}$, represent the BODY and inertial coordinate frames, respectively, in compliance with the definitions in Chapter 2. For many rate gyro technologies, such as MEMS, a more accurate term would be ARS since often none of the sensor's parts are rotating. However, in this thesis the term *gyro* or *rate gyro* is used independently of sensor technology due to the established practice in the literature, (Titterton and Weston, 2004; Farrell, 2008; Groves, 2013).

1.1.3 Inertial navigation – INS aiding and corrections

As stated above, inertial sensor measurements are corrupted with errors such as bias and noise. Therefore pure DR, integration of angular rate and specific force measurements, once and twice, respectively, through a kinematic model, will result in the INS's estimation error to grow without bounds. Hence, INSs are dependent of corrections or aiding from some reference measurements to maintain

accurate PVA estimation over time. In early gimbals-based solutions for attitude determination, the attitude correction was done mechanically, based on accelerometer measurements and constant realigning of the gyro-stabilized platform, such that the platform's orientation in space remained constant (zero angular velocity relative inertial space) regardless of the motion of the vehicle it was attached to (Britting, 1971). When using strapdown inertial sensors, the realignment is implicitly carried out in software by mechanization of the strapdown equation, when fusing the aiding measurements with the inertial sensor outputs. The traditional sensor fusion algorithms of choice are variants of the nonlinear extension of the Kalman filter (KF), the extended Kalman filter (EKF), which has been covered in the literature for five decades, such as in Gelb et al. (1974); Maybeck (1979); Titterton and Weston (2004); Farrell (2008); Grewal et al. (2013); Groves (2013), often using an error-state implementation based on complementary filtering (Appendix D). If the attitude is represented using a unit quaternion, a multiplicative extended Kalman filter (MEKF), such as Markley (2003), can be used to estimate the attitude indirectly by filtering on the multiplicative unit quaternion error.

EKF-based sensor fusion algorithms for INSs are well established with high performance. Nonetheless, one could argue that the lack of, or at least the difficulty of obtaining and verifying, global stability properties of the EKF's error dynamics, due to linearization about the INSs's given trajectory, is a disadvantage. Nonlinear observer theory offers a way around these potential limitations and is applied throughout this thesis.

1.1.4 Nonlinear observers estimation of position, velocity and attitude

In the last two to three decades numerous nonlinear observers (NLOs) have been developed in the context of attitude estimation. The basis for these observers has been that either some direct attitude measurement is available or that the attitude can be estimated by comparing vector measurements with known reference vectors. The first principle was utilized in Salcudean (1991); Vik and Fossen (2001); Thienel and Sanner (2003), while results such as Hamel and Mahony (2006); Mahony et al. (2008, 2009); Hua (2010); Martin and Salaün (2010); Roberts and Tayebi (2011); Grip et al. (2012a); Batista et al. (2012c,b,a); Hua et al. (2014); Zlotnik and Forbes (2016); Hua et al. (2016) used the latter principle. All of these works, except Hua (2010), Roberts and Tayebi (2011), Batista et al. (2012a) and Hua et al. (2016) provide estimates of the gyro bias. In addition, the observer of Batista et al. (2012a) is actually not a NLO, where the attitude was estimated with a linear observer, while avoiding use of linearization as with EKFs. Estimates on $SO(3)$ were obtained by orthogonalization of the outputs from the linear observer.

Loosely coupled GNSS/INS integration strategies using NLOs have also developed with position and velocity references to estimate six-degrees-of-freedom (6-DOF) motion. In Vik and Fossen (2001), the PVA were estimated based on iner-

tial, attitude and GNSS measurements. Hua (2010), Roberts and Tayebi (2011) and Hua et al. (2016) are examples of what is often referred to as *velocity-aided attitude observers* in the literature, where GNSS velocity, together with Earth magnetic field and inertial measurements were fused to estimate linear velocity in addition to the attitude. Further results on estimating PVA, using nonlinear theory, based on inertial, magnetometer and GNSS position (and velocity) measurements were provided by Grip et al. (2013, 2015). These results estimated PVA using a feedback-interconnected design, based on the unit quaternion and the rotation matrix as attitude representation, respectively. The results were obtained by extending the results of Grip et al. (2012a) in order to incorporate estimation of position and linear velocity based on the framework of Grip et al. (2012b). In Grip et al. (2013), a semiglobal result was obtained, similar to Grip et al. (2012a). The semiglobal result, instead of global, was obtained due to the topological constraint on $SO(3)$, (Bhat and Bernstein, 2000). Grip et al. (2015) circumvented this by allowing the estimated rotation matrix to evolve freely on $\mathbb{R}^{3\times3}$ instead of being constraint to $SO(3)$ as in Grip et al. (2013). Similar to Batista et al. (2012a), rotation matrices on $SO(3)$ were obtained by orthogonalization of the estimates evolving on $\mathbb{R}^{3\times3}$. Other contemporary results on integration strategies of position reference (PosRef) systems and inertial sensor based on ranging, applying linear and nonlinear theory, also exists. Some examples can be found in Batista (2015); Johansen and Fossen (2016); Johansen et al. (2016); Bayat et al. (2016); Johansen et al. (2017). Since both the rate gyro and accelerometer triads are used to estimate the attitude and the respective biases, tri-axial gyro and accelerometer biases are unfortunately not uniformly observable (Groves, 2013, Ch. 11.9) regardless of choice of estimator. Therefore the accelerometer biases are often assumed to be compensated for during calibration when using GNSS/INS integration based on NLOs. There are some exceptions such as Grip et al. (2012a, 2016) where the accelerometer biases are estimated online based on a persistency-of-excitation (PE) condition. Similar statements related to observability and PE are given in Batista et al. (2009).

1.2 Scope, Objective and Contributions

The thesis covers selected topics within the field of navigation systems for marine surface vessels. The objective of the research is to investigate and develop algorithms in order to enable increased usage of low-cost inertial sensing technology onboard ships, and in particular on dynamically positioned (DP) ships, based on loosely coupled GNSS/INS integration. The scope of the work is closely linked to the vision of the research project Fault-Tolerant Inertial Sensor Fusion for Marine Vessels[1]. The vision was: *Gaining high-quality and redundant position and motion estimates by fusion of position reference, inertial sensors, and vessel modeling to improve*

[1]A knowledge-building projection funded by the Research Council of Norway and Rolls–Royce Marine through the MAROFF programme.

fault-tolerance, safety and performance of ships' path monitoring, control and advisory systems. The work that has resulted in this dissertation has been focused towards the performance aspects of the project.

The largest classification society in the world DNV GL (2011) defines a vessel equipped with a DP system according to:

Definition 1.1 (Dynamically positioned vessel)**.** *A vessel which automatically maintains its position and heading (fixed location or predetermined track) exclusively by means of thruster force.*[2]

State-of-the-art DP systems often relies on MEMS IMU indirectly through so called vertical reference units (VRUs) (Ingram et al., 1996), being a black box providing roll, pitch and sometimes heaves estimates. The roll and pitch signals are e.g. used for leverarm compensation of position reference on DP vessel. They can also be used in ballast system when controlling the trim and heel angles of a vessel. The heave signal, together with roll and pitch, can be used for motion compensation of onboard cranes and in decisions support systems.

Current classification notations 2 and 3 for DP vessels, such as DNV GL (2011), related to the sensor system design onboard require two or three VRUs. The internal IMU measurements in these units are often totally separated from the position measurements which is potentially neither optimal for performance nor fault-tolerance of both the attitude and position estimation in the DP system. The main focus of this work is aimed towards how both single and redundant sensor configurations can be exploited more efficiently based on the same type of inertial sensors often used inside VRUs using NLO-based sensor fusion. By doing so global or semiglobal stability properties is obtained with overall high estimation performance. In addition, both synergies and potentials pit falls related to the fault-tolerance aspects have also been studied. This is done by using the unambiguous kinematic relations and couplings between the respective sensors available on a DP vessel.

1.2.1 Main contributions

The thesis have developed nonlinear observers for INS solutions based on low-cost strapdown MEMS IMUs. The main contributions are summarized as:

- Extending the works of recent years developments of 6-DOF estimators based on NLOs by developing tailor-made algorithms for marine surface vessels (Bryne et al., 2014, 2015b, 2016, n.d.). By doing so, a VRU solution is achieved together with estimates of the ship's position and velocity (Bryne et al., 2014, 2015b, 2016).

[2] Thruster force may include propulsion and steering (rudder) forces for backup purposes only.

- Heave estimates are obtained without vertical aiding from PosRef systems, such as vertical GNSS and hydroacoustic position reference (HPR) system measurements. Neither of these provide accurate vertical measurements. Instead a new concept branded the *Virtual Vertical Reference (VVR)* principle is developed (Bryne et al., 2014, 2015b, 2016, n.d.). The VVR-based heave estimation is performed with and without exploiting an error model, employing sea-state-dependent parameters.
- The developed observers have guaranteed robustness due to the proven uniform semiglobal exponential stability (USGES) properties cf. Appendix A.1, (Bryne et al., 2014, n.d.).
- Wave-filtering algorithms for shipborne INSs are developed (Bryne et al., 2015a). Wave-filtering is performed in order to attenuate the wave-induced motions of ships' PVAs estimates before providing these to the control system such that positioning of the vessel is done based on the mean trajectory of the vessel.
- Redundant sensor configurations are exploited to improve performance, robustness and fault-tolerance of NLO-based INSs for marine vessel (Bryne et al. (2015a), Rogne et al. (n.d.a)).
- Nonlinear observer implementation aspects are presented, in particular related to error modeling, discretization and Riccati-based gain assignment (Bryne et al., 2017a).

The proposed algorithms are validated and compared to maritime industry standard VRUs. The attitude estimates are verified using NavLab (Gade, 2004), a navigation software suite developed by the Norwegian Defence Research Establishment (FFI) and Kongsberg Maritime. In addition, a comparison study related to the estimation performance, obtained with loosely and tightly coupled GNSS/INS integration using NLOs, is carried out.

1.2.2 Inertial sensor deployment on an offshore ship

In order to experimentally validate the developed NLO-based sensor fusion algorithms during the course of this work, a data acquisition system was developed, shown in Figure 1.3, containing multiple ADIS16485 IMUs by Analog Devices and one STIM300 IMU by Sensonor, and installed on an ship operating in the Norwegian Sea. Data from the inertial sensors was collected in the Fall of 2015 together with measurements from onboard sensors. The ship in question is an offshore vessel with a Rolls–Royce Marine Icon DP system. The vessel type is shown in Figure 1.4. A track of the vessel is seen in Figure 1.5, showing where the data were collected off the coast of Norway. More details on the data collection is presented in Appendix E.

Figure 1.3: The data acquisition system used for IMU data collection.

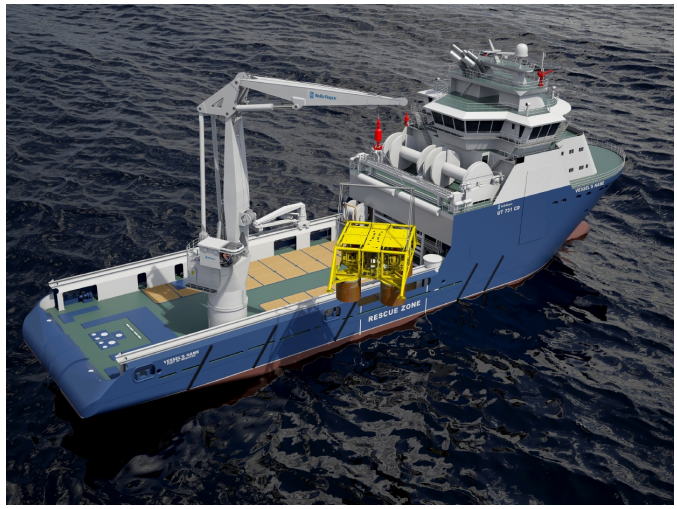

Figure 1.4: Illustration of the offshore vessel. Courtesy Rolls–Royce Marine.

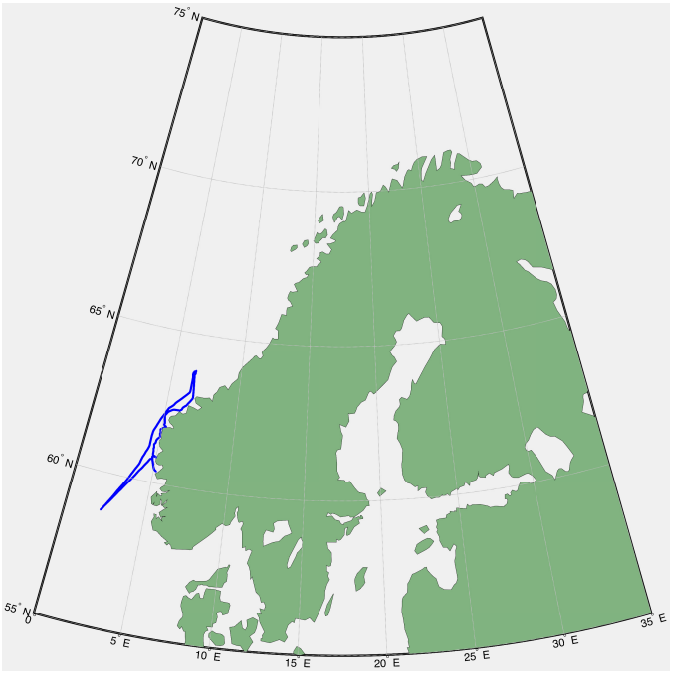

Figure 1.5: Track of the vessel off the coast of Norway.

1.2.3 Publications and organization of thesis

This thesis is based on the following publications in internationally recognized journals and conferences:

Journal publication and magazine articles:

- Bryne, T. H., Fossen, T. I., and Johansen, T. A. (2015a). Design of inertial navigation systems for marine craft with adaptive wave filtering aided by triple-redundant sensor packages. *International Journal of Adaptive Control and Signal Processing*, pp. 1–23. doi: 10.1002/acs.2645

- Bryne, T. H., Hansen, J. M., Rogne, R. H., Sokolova, N., Fossen, T. I., and Johansen, T. A. (2017a). Nonlinear observers for integrated INS/GNSS navigation – Implementation aspects. *IEEE Control Systems Magazine*. To Appear

- Bryne, T. H., Rogne, R. H., Fossen, T. I., and Johansen, T. A. (n.d.). A virtual vertical reference concept for integrated inertial navigation at the sea surface. *Control Engineering Practice*. Submitted for publication

- Rogne, R. H., Bryne, T. H., Fossen, T. I., and Johansen, T. A. (n.d.a). Redundant MEMS-based inertial navigation using nonlinear observers. *ASME Journal of*

Dynamic Systems, Measurement and Control. Submitted for publication

- Rogne, R. H., Bryne, T. H., Fossen, T. I., and Johansen, T. A. (n.d.b). Strapdown inertial navigation on ships using MEMS sensors and nonlinear observers. *IEEE Transactions On Control System Technology*. Submitted for publication

Conference publications:

- Bryne, T. H., Fossen, T. I., and Johansen, T. A. (2014). Nonlinear observer with time-varying gains for inertial navigation aided by satellite reference systems in dynamic positioning. In *Proc. of the IEEE Mediterranean Conference on Control and Automation*, pp. 1353–1360, Palermo, Italy. doi: 10.1109/MED.2014.6961564

- Bryne, T. H., Fossen, T. I., and Johansen, T. A. (2015b). A virtual vertical reference concept for GNSS/INS applications at the sea surface. In *Proc. of the 10th IFAC Conference on Manoeuvring and Control of Marine Craft (MCMC)*, pp. 127–133, Copenhagen, Denmark. Received the best regular paper award at IFAC MCMC'15. doi: j.ifacol.2015.10.269

- Bryne, T. H., Rogne, R. H., Fossen, T. I., and Johansen, T. A. (2016). Attitude and heave estimation for ships using MEMS-based inertial measurements. In *Proc. of the 10th IFAC Conference on Control Applications in Marine Systems (CAMS)*, pp. 568–575, Trondheim. doi: 10.1016/j.ifacol.2016.10.496

Publications not included in the thesis:

I have also contributed to

- Rogne, R. H., Bryne, T. H., Fossen, T. I., and Johansen, T. A. (2016a). MEMS-based inertial navigation on dynamically positioned ships: Dead reckoning. In *Proc. of the 10th IFAC Conference on Control Applications in Marine Systems (CAMS)*, pp. 139—146, Trondheim. doi: 10.1016/j.ifacol.2016.10.334

- Rogne, R. H., Bryne, T. H., Johansen, T. A., and Fossen, T. I. (2016b). Fault detection in lever-arm-compensated position reference systems based on nonlinear attitude observers and inertial measurements in dynamic positioning. In *Proc. of the American Contr. Conf.*, pp. 985–992, Boston, Ma. doi: 10.1109/ACC.2016.7525043

- Bryne, T. H., Rogne, R. H., Fossen, T. I., and Johansen, T. A. (2017b). Inertial sensors for risk-based redundancy in dynamic positioning. In *Proc. of the ASME 2017 36th International Conference on Ocean, Offshore and Arctic Engineering, OMAE2017*, Trondheim, Norway. To Appear

However, these publications are not included in the thesis.

The content of the considered publications is organized as follows:

Chapter 2: Kinematics and Sensor Models

A general modeling chapter presenting the underlying coordinate frames together with kinematic and sensor models applied in the observer design of this work.

Chapter 3: GNSS/INS Integration Using Nonlinear Observers – Implementation Aspects

This chapter include a general presentation of INSs based on NLOs and the feedback-interconnected framework applied throughout this thesis. GNSS/INS integration strategies, discretization and implementation aspects are considered and is based upon

- Bryne, T. H., Hansen, J. M., Rogne, R. H., Sokolova, N., Fossen, T. I., and Johansen, T. A. (2017a). Nonlinear observers for integrated INS/GNSS navigation – Implementation aspects. *IEEE Control Systems Magazine*. To Appear.

Chapter 4: The Virtual Vertical Reference Principle – Vertical Aiding of INSs for Marine Surface Vessels

This is the main chapter of this thesis covering design, discretization, evaluation and validation of NLOs tailored for marine surface vessel providing 6-DOF vessel motion estimates. The chapter is based on the work presented in

- Bryne, T. H., Fossen, T. I., and Johansen, T. A. (2014). Nonlinear observer with time-varying gains for inertial navigation aided by satellite reference systems in dynamic positioning. In *Proc. of the IEEE Mediterranean Conference on Control and Automation*, pp. 1353–1360, Palermo, Italy. doi: 10.1109/MED.2014.6961564
- Bryne, T. H., Fossen, T. I., and Johansen, T. A. (2015b). A virtual vertical reference concept for GNSS/INS applications at the sea surface. In *Proc. of the 10th IFAC Conference on Manoeuvring and Control of Marine Craft (MCMC)*, pp. 127–133, Copenhagen, Denmark. Received the best regular paper award at IFAC MCMC'15. doi: j.ifacol.2015.10.269
- Bryne, T. H., Rogne, R. H., Fossen, T. I., and Johansen, T. A. (n.d.). A virtual vertical reference concept for integrated inertial navigation at the sea surface. *Control Engineering Practice*. Submitted for publication.

Chapter 5: INS on Ships

This chapter covers more practical aspects of MEMS-based INS using NLOs on ships and is based on

- Rogne, R. H., Bryne, T. H., Fossen, T. I., and Johansen, T. A. (n.d.b). Strapdown inertial navigation on ships using MEMS sensors and nonlinear observers. *IEEE Transactions On Control System Technology*. Submitted for publication.

- Bryne, T. H., Rogne, R. H., Fossen, T. I., and Johansen, T. A. (2016). Attitude and heave estimation for ships using MEMS-based inertial measurements. In *Proc. of the 10th IFAC Conference on Control Applications in Marine Systems (CAMS)*, pp. 568–575, Trondheim. doi: 10.1016/j.ifacol.2016.10.496

- Bryne, T. H., Fossen, T. I., and Johansen, T. A. (2015a). Design of inertial navigation systems for marine craft with adaptive wave filtering aided by triple-redundant sensor packages. *International Journal of Adaptive Control and Signal Processing*, pp. 1–23. doi: 10.1002/acs.2645.

The two former articles cover filtering, validation and tuning aspects of different NLO configurations. The latter article covers the aspects of wave-filtering for INS.

Chapter 6: Sensor Redundancy and Fault Tolerance

This chapter presents the work on redundant sensor configurations and fault tolerance in aided INS in the context of DP. The chapter is based on

- Bryne, T. H., Fossen, T. I., and Johansen, T. A. (2015a). Design of inertial navigation systems for marine craft with adaptive wave filtering aided by triple-redundant sensor packages. *International Journal of Adaptive Control and Signal Processing*, pp. 1–23. doi: 10.1002/acs.2645

- Rogne, R. H., Bryne, T. H., Fossen, T. I., and Johansen, T. A. (n.d.a). Redundant MEMS-based inertial navigation using nonlinear observers. *ASME Journal of Dynamic Systems, Measurement and Control*. Submitted for publication.

Chapter 7: Concluding Remarks

This chapter summarizes the results of the thesis.

Appendices

- Appendix A presents the applied stability properties and the proofs of the theoretical results of the thesis.

- Appendix B outlines mathematical notions and definitions applied throughput the thesis.

- Appendix C presents some background material related to modeling of GNSS errors together with simulation and validation case studies.

- Appendix D presents some background material on the concept of complementary filtering.

- Appendix E presents an overview of the collection of sensor data, used for full-scale validation and verification of the algorithms developed, carried out on an offshore vessel.
- Appendix F presents algorithms for discrete-time implementation of the nonlinear attitude observer and for averaging of unit quaternions.

2 Kinematics and Sensor Models

Navigation systems, and in particular INS, fuses information, from sensors or other information sources, containing parts of the motion of a vessel, general craft or robot. The type of sensor determines which reference or coordinate frames the motion information is related to. This chapter presents the coordinate frames applied in the thesis, the accompanying kinematic strapdown equations applied to fuse strapdown inertial measurements with respective references, and the sensor models used.

The mathematical notations and definitions serving as the foundation of this chapter, and the remainder of the thesis, is presented Appendix B.

2.1 Coordinate Frames

This thesis employs five coordinate frames; The Earth Centered Inertial (ECI) frame, the Earth Centered Earth Fixed (ECEF) frame, the North East Down (NED) frame, a tangent frame equivalent of an Earth fixed NED frame, and the BODY coordinate frame, denoted $\{i\}$, $\{e\}$, $\{n\}$, $\{t\}$ and $\{b\}$, respectively relating to each other as seen in Figure 2.1. ECI is an assumed inertial frame following the Earth, where the x-axis points towards vernal equinox, the z-axis is pointing along the Earth's rotational axis and the y-axis completes the right hand frame. ECEF is defined with x-axis points towards the zero meridian, the z-axis points along the Earth's rotational axis, while the y-axis completes the right hand frame. The Earth's rotation rate $\omega_{ie} = 7.292115 \cdot 10^{-5}$ rad/s is assumed to be constant and given by the WGS-84 datum. It is further decomposed in the ECEF and tangent frame as

$$\boldsymbol{\omega}_{ie}^{e} = \begin{pmatrix} 0 \\ 0 \\ 1 \end{pmatrix} \omega_{ie}, \quad \boldsymbol{\omega}_{ie}^{t} = \begin{pmatrix} \cos(\mu) \\ 0 \\ -\sin(\mu) \end{pmatrix} \omega_{ie}, \tag{2.1}$$

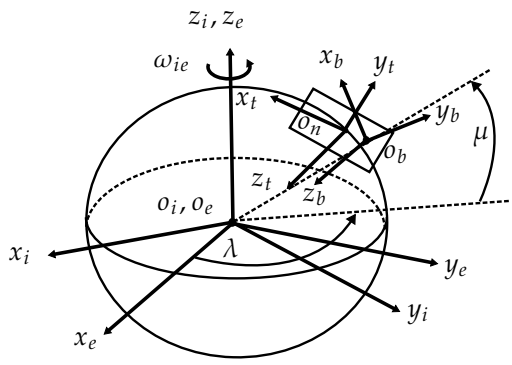

Figure 2.1: Definitions of the BODY, tangent, ECEF and ECI reference frames.

where μ is the latitude on the Earth and $\boldsymbol{\omega}^{\star}_{\star\star}$ represents angular velocity. The longitude is denoted λ. The tangent frame is an Earth fixed frame and has it's origin on the surface on WGS-84 at some latitude and longitude, where the x-axis points towards north, the y-axis points towards east, and the z-axis points downwards. The BODY frame is fixed to the vessel. The origin of $\{b\}$ is located at the nominal center of gravity of the vessel. The x-axis is directed from aft to fore, the y-axis is directed to starboard and the z-axis points downwards.

2.2 Kinematic Models – Strapdown Equations

The subsequent rigid body kinematic models, used as a basis for the aided INSs in this thesis, follows from works such as Britting (1971); Farrell (2008), where $\boldsymbol{p}^{\star}_{\star b}$, $\boldsymbol{v}^{\star}_{\star b}$, $\boldsymbol{f}^{\star}_{ib} \in \mathbb{R}^3$ are position, linear velocity and specific force, respectively where $\star$ represents the chosen navigation coordinate frame. The attitude is represented both with the rotation matrix $\boldsymbol{R}^{\star}_{b}$ or the unit quaternion $\boldsymbol{q}^{\star}_{b}$. $\boldsymbol{\omega}^{\star}_{i\star}$ represent angular velocity of a given frame $\star$ relative to the inertial frame, decomposed in the given coordinate system, represented by $\star$. See, Appendix B for details. Other representations of attitude than the mentioned rotation matrix and unit quaternion also exist. A survey on attitude representations is found in Shuster (1983).

2.2.1 Inertial frame representation

Newtons laws of motion apply in the inertial frame. An approximate inertial frame is the ECI frame. The ECI frame representation of the strapdown takes the form of

$$\dot{\boldsymbol{p}}^{i}_{ib} = \boldsymbol{v}^{i}_{ib}, \tag{2.2}$$

$$\dot{\boldsymbol{v}}^{i}_{ib} = \boldsymbol{R}^{i}_{b}\boldsymbol{f}^{b}_{ib} + \boldsymbol{g}^{i}_{b}(\boldsymbol{p}^{i}_{ib}), \tag{2.3}$$

$$\dot{\boldsymbol{R}}^{i}_{b} = \boldsymbol{R}^{i}_{b}\boldsymbol{S}\left(\boldsymbol{\omega}^{b}_{ib}\right). \tag{2.4}$$

The alternative representation of (2.4), using the unit quaternion takes the form of

$$\dot{\boldsymbol{q}}^{i}_{b} = \frac{1}{2}\boldsymbol{q}^{i}_{b} \otimes \begin{pmatrix} 0 \\ \boldsymbol{\omega}^{b}_{ib} \end{pmatrix}. \tag{2.5}$$

When the NED frame is assumed inertial, the strapdown equations related to the translational motion take a similar form to that of (2.2)–(2.3) with

$$\dot{\boldsymbol{p}}^{n}_{nb} = \boldsymbol{v}^{n}_{nb}, \tag{2.6}$$

$$\dot{\boldsymbol{v}}^{n}_{nb} = \boldsymbol{R}^{n}_{b}\boldsymbol{f}^{b}_{ib} + \boldsymbol{g}^{n}_{b}, \tag{2.7}$$

while for the attitude, using the unit quaternion representation, $\boldsymbol{q}^{n}_{b}$, between the $\{b\}$ and the $\{n\}$ frame evolves according to

$$\dot{\boldsymbol{q}}^{n}_{b} = \frac{1}{2}\boldsymbol{q}^{n}_{b} \otimes \begin{pmatrix} 0 \\ \boldsymbol{\omega}^{b}_{ib} \end{pmatrix}, \tag{2.8}$$

where $\boldsymbol{f}_{in}^{b}$ and $\boldsymbol{\omega}_{in}^{b}$ are assumed to be negligible.

2.2.2 Earth Centered Earth Fixed frame representation

The ECEF frame representation is given as

$$\dot{\boldsymbol{p}}_{eb}^{e} = \boldsymbol{v}_{eb}^{e}, \tag{2.9}$$

$$\dot{\boldsymbol{v}}_{eb}^{e} = -2\boldsymbol{S}\left(\boldsymbol{\omega}_{ie}^{e}\right)\boldsymbol{v}_{eb}^{e} + \boldsymbol{R}_{b}^{e}\boldsymbol{f}_{ib}^{b} + \boldsymbol{g}_{b}^{e}(\boldsymbol{p}_{eb}^{e}), \tag{2.10}$$

$$\dot{\boldsymbol{R}}_{b}^{e} = \boldsymbol{R}_{b}^{e}\boldsymbol{S}\left(\boldsymbol{\omega}_{ib}^{b}\right) - \boldsymbol{S}\left(\boldsymbol{\omega}_{ie}^{e}\right)\boldsymbol{R}_{b}^{e}. \tag{2.11}$$

The vector $\boldsymbol{g}_{b}^{e}(\boldsymbol{p}_{eb}^{e})$ denotes the plumb bob gravity vector, which is a function of the vehicle's position decomposed in the ECEF frame and is obtained with a gravity model. The alternative representation of (2.11), using the unit quaternion takes the form of

$$\dot{\boldsymbol{q}}_{b}^{e} = \frac{1}{2}\boldsymbol{q}_{b}^{e} \otimes \begin{pmatrix} 0 \\ \boldsymbol{\omega}_{ib}^{b} \end{pmatrix} - \frac{1}{2}\begin{pmatrix} 0 \\ \boldsymbol{\omega}_{ie}^{e} \end{pmatrix} \otimes \boldsymbol{q}_{b}^{e}. \tag{2.12}$$

2.2.3 Tangent frame representation

The tangent frame representation of the strapdown equations takes the form of

$$\dot{\boldsymbol{p}}_{tb}^{t} = \boldsymbol{v}_{tb}^{t}, \tag{2.13}$$

$$\dot{\boldsymbol{v}}_{tb}^{t} = -2\boldsymbol{S}\left(\boldsymbol{\omega}_{ie}^{t}\right)\boldsymbol{v}_{tb}^{t} + \boldsymbol{R}_{b}^{t}\boldsymbol{f}_{ib}^{b} + \boldsymbol{g}_{b}^{t}(\boldsymbol{p}_{tb}^{t}), \tag{2.14}$$

$$\dot{\boldsymbol{R}}_{b}^{t} = \boldsymbol{R}_{b}^{t}\boldsymbol{S}\left(\boldsymbol{\omega}_{ib}^{b}\right) - \boldsymbol{S}\left(\boldsymbol{\omega}_{it}^{t}\right)\boldsymbol{R}_{b}^{t}, \tag{2.15}$$

where

$$\boldsymbol{\omega}_{it}^{t} = \boldsymbol{\omega}_{ie}^{t} + \boldsymbol{\omega}_{et}^{t} \tag{2.16}$$

is the angular velocity of the tangent frame relative the inertial frame. However, $\boldsymbol{\omega}_{et}^{t} = \boldsymbol{0}_{3\times 1}$ since the tangent frame is Earth fixed. Thus,

$$\boldsymbol{\omega}_{it}^{t} = \boldsymbol{\omega}_{ie}^{t} = \boldsymbol{R}_{e}^{t}(\mu, \lambda)\boldsymbol{\omega}_{ie}^{e}, \tag{2.17}$$

where μ, λ is constant, which result is given in (2.1). The alternative representation of (2.15), using the unit quaternion, takes the form of

$$\dot{\boldsymbol{q}}_{b}^{t} = \frac{1}{2}\boldsymbol{q}_{b}^{t} \otimes \begin{pmatrix} 0 \\ \boldsymbol{\omega}_{ib}^{b} \end{pmatrix} - \frac{1}{2}\begin{pmatrix} 0 \\ \boldsymbol{\omega}_{it}^{t} \end{pmatrix} \otimes \boldsymbol{q}_{b}^{t}. \tag{2.18}$$

2.3 Sensor Models

2.3.1 Inertial sensor models

In this work a simpler IMU model than presented in (1.1)–(1.2), is utilized in conjunction with the feedback-interconnected NLO design (Chapter 3). Throughout

most of this thesis the IMU model,

$$\boldsymbol{f}^b_{\text{IMU}} = \boldsymbol{f}^b_{ib} + \boldsymbol{\varepsilon}^b_f, \tag{2.19}$$

$$\boldsymbol{\omega}^b_{\text{IMU}} = \boldsymbol{\omega}^b_{ib} + \boldsymbol{b}^b_{\text{gyro}} + \boldsymbol{\varepsilon}^b_\omega, \tag{2.20}$$

$$\dot{\boldsymbol{b}}^b_{\text{gyro}} = \boldsymbol{0}_{3\times 1}, \tag{2.21}$$

is assumed to be sufficiency accurate, where $\boldsymbol{f}^b_{ib} = \boldsymbol{R}^b_\star \left(\boldsymbol{a}^\star_{ib} - \boldsymbol{g}^\star_b(\boldsymbol{p}^\star_{\star b}) \right)$, with $\boldsymbol{a}^\star_{ib}$ being the acceleration decomposed in the navigation frame of choice ($\{n\}$, $\{t\}$, $\{e\}$ in this thesis), measured by the IMU. $\boldsymbol{b}^b_{\text{gyro}}$ denotes the rate gyro/ARS bias. Accelerometer errors, such as run-to-run bias, are mostly assumed to be compensated for using offline and online calibration methods such as Grip et al. (2012a, Sec. VI). In addition, $\boldsymbol{\varepsilon}^b_\star$ represents the residual noise and error components of (1.1)–(1.2). In addition, the tri-axial measurements of (2.19) and (2.20) can be described componentwise as

$$\boldsymbol{f}^b_{\text{IMU}} = \left(f^b_{\text{IMU},x}, f^b_{\text{IMU},y}, f^b_{\text{IMU},z} \right)^\intercal, \tag{2.22}$$

$$\boldsymbol{\omega}^b_{\text{IMU}} = \left(\omega^b_{\text{IMU},x}, \omega^b_{\text{IMU},y}, \omega^b_{\text{IMU},z} \right)^\intercal, \tag{2.23}$$

where the subscripts x, y and z, denote the forward, starboard and downwards axes, respectively, in the BODY frame.

2.3.2 Other sensors models

In addition to the IMU sensor model, PosRef system, compass and magnetometer measurement models are often chosen, if not otherwise specified, as

$$\boldsymbol{p}^\star_{\text{PosRef}} = \boldsymbol{p}^\star_{\star b} + \boldsymbol{\varepsilon}^\star_{\text{PosRef}}, \tag{2.24}$$

$$\psi_{\text{c}} = \psi + \varepsilon_{\text{c}}, \tag{2.25}$$

$$\boldsymbol{m}^b_{\text{mag}} = \boldsymbol{m}^b_{eb} + \boldsymbol{\varepsilon}^b_{\text{mag}}, \tag{2.26}$$

where $\boldsymbol{\varepsilon}^\star_\star$ and ε_ψ represent the respective sensor noise and errors.

3 GNSS/INS Integration Using Nonlinear Observers – Implementation Aspects

The chapter is mainly based on Bryne et al. (2017a) and considers the NLOs of Grip et al. (2013) and Johansen and Fossen (2015); Johansen et al. (2017) estimating PVA using loosely and tightly coupled GNSS/INS integration, respectively. The main focus of the chapter is on how the NLOs can be realized with time-varying gains and how the observers can be implemented explicitly in discrete-time. Conceptual differences of the two integration strategies are presented and an illustration of the respective performance difference obtained using data collected in a UAV flight.

The NLOs of Grip et al. (2013) and Johansen and Fossen (2015); Johansen et al. (2017) are based on complementary filtering on $SO(3)$, inspired by the work of Mahony et al. (2008), in combination with a linear approach to design a translational motion observer (TMO), which in turn is used to estimate the position, linear velocity and specific force. The origin of the two observers' error dynamics have USGES and uniform local exponential stability (ULES) properties, respectively, proven in the original works. An introduction to complementary filtering can be found in Appendix D.

In applied usage, NLOs are immature, in particular related to implementation aspects and handling imperfect measurements with different errors, resolution and sample rates. In addition to presenting implementation related aspects of NLOs, further re-design is addressed in this chapter to answer the research questions presented above. The basis for this work include linear methods for exact discretization of the translational motion part of the observer, error model augmentation, and usage of the methods in Fossen (2011, Ch. 11.3.4), Hua et al. (2014) for discretization, tuning and multi-rate implementation of the attitude observer. Based on this, the main contributions of the chapter are:

- A linear time-varying (LTV) representation of the observer error dynamics is exploited to formulate a time-varying Riccati equation to select time-varying gains in the update of velocity and position estimates (as well as some auxiliary variable estimates).
- Strategies originally developed for the Kalman filter are exploited in handling sequential single-measurement updates to accommodate multi-rate and asynchronous measurements in estimation of PVA.
- Inclusion of GNSS error models in order to take into account the dynamic noise characteristic of GNSS observables.
- Experimental validation of the presented methods using data collected during a UAV test flight mission.

First an overview of the nonlinear observer structures for loose and tightly coupled GNSS/INS is presented before going into detail by presenting the attitude observer. The presentation follows with the two TMOs, estimating the position, linear velocity and specific forces. The TMO required for the loosely coupled integration scheme is presented first, then the tightly coupled GNSS/INS integration scheme is presented, both with the respective GNSS noise and error models. The experimental validation of the presented methods concludes the chapter.

3.1 Overview of GNSS/INS Integration using Nonlinear Observers

The two most common GNSS/INS integration techniques are known in the navigation literature as loosely coupled and tightly coupled integration, and are described below.

With loosely coupled integration the receiver's measurements of position, and sometimes velocity, are fused with the inertial measurements. When applying this integration strategy, the GNSS position and velocity measurements are given as $\boldsymbol{p}^e_{\text{GNSS}} = \boldsymbol{p}^e_{eb} + \boldsymbol{\delta}_p$ and $\boldsymbol{v}^e_{\text{GNSS}} = \boldsymbol{v}^e_{eb} + \boldsymbol{\delta}_v$ where $\boldsymbol{\delta}_\star$ represents the errors and noise. These are calculated by the receiver, in the ECEF frame, either with a least squares (LS) estimator or by using an EKF (Groves, 2013, Ch. 9.4).

With a tightly coupled integration strategy, the raw GNSS observables, pseudorange and Doppler range-rate, are utilized as aiding measurements by relating these to the inertial measurements using (2.9)–(2.12). Here the pseudorange and range-rate measurements are denoted $\boldsymbol{y}_i$ and $\boldsymbol{\nu}_i$, respectively, representing measurements from the i^{th} satellite out of m satellites in view. These measurements are determined based on the knowledge of satellite position and velocity, denoted $\boldsymbol{p}^e_{eb_i}$ and $\boldsymbol{v}^e_{eb_i}$, calculated with the help of broadcasted satellite ephemeris.

An advantage of the loosely coupled approach is the ease of implementation as the receiver takes care of all considerations about satellite constellation and integrity of the raw GNSS observables. On the other hand this also entails that only complete solutions can be used, whereas for tightly coupled integration a few raw GNSS observables, that would be insufficient for a standalone solution, could be utilized to aid the INS. A disadvantage of tightly coupled integration is that not all receivers grants access to the raw GNSS observables, Groves (2013). Moreover, the implementation and tuning of GNSS/INS integration is more straight forward with loosely coupled integration than with tightly coupled integration due to pseudorange measurements with different elevation angles may have considerably different noise characteristics. On the other hand, integrity monitoring is easier with tightly coupled integration in the range domain compared to its counterpart in the position domain since erroneous pseudorange measurements may be excluded while maintaining GNSS aiding. If a GNSS fault in loosely coupled integration is detected, GNSS aiding is lost until the fault has been remedied.

A schematic overview of the difference between the two integration strategies, applying the same NLO for attitude determination, is shown in Figure 3.1. Two key features are obtained using the NLO in feedback interconnection with the TMO as depicted in Figure 3.1; The first feature is that the attitude is estimated without linearization, in opposite to KF-based techniques, making the attitude observer robust to initialization errors allowing for large initial attitude errors. The second, is that the attitude observer is utilizing the estimated specific force in the navigation frame provided by the TMO as reference vector when calculating attitude corrections. The latter feature is particularly useful when the navigation system is accelerated.

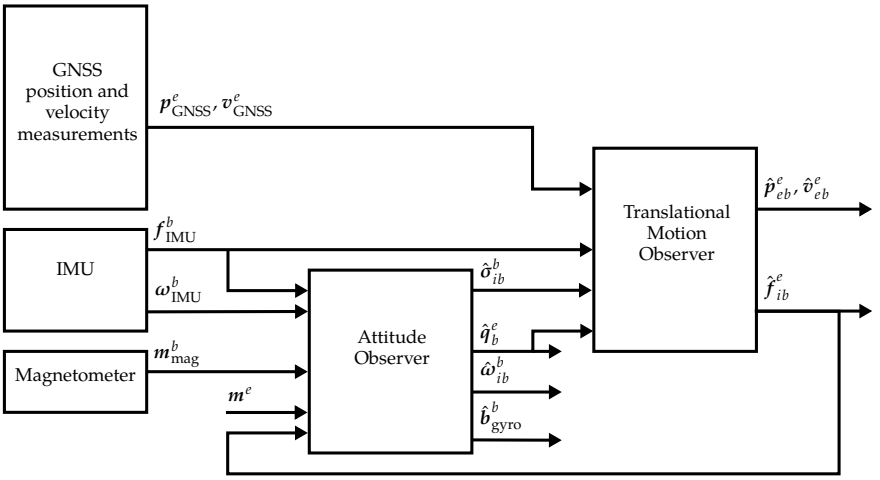

(a) Loosely coupled GNSS/INS integration. With this integration scheme, position (and velocity) measurements are provided by the GNSS receiver and integrated with the IMU measurements.

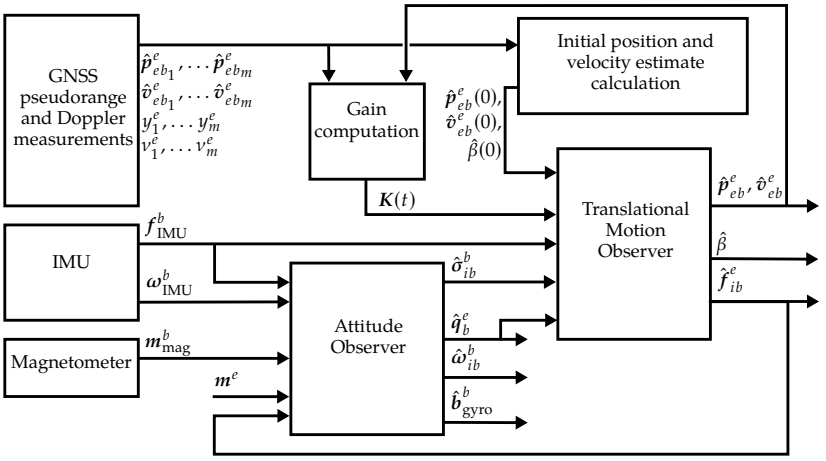

(b) Tightly coupled GNSS/INS integration. With this integration scheme, the position and velocity solution is obtained using GNSS pseudorange and Doppler range-rate measurements in combination with the IMU measurements. An algebraic pseudorange solver is used to initialize the translational motion observer

Figure 3.1: Overview of the two feedback-interconnected observer structures used for integration of GNSSs and INSs.

3.2 Attitude Observer

The proposed loosely and tightly coupled GNSS/INS integration schemes, are both dependent on the nonlinear attitude observer. The latter is presented in detail in this section, where discretization prior to implementation, also is discussed.

The attitude observer used is based on Mahony et al. (2008) and Grip et al. (2012a, 2013), employing complementary filtering,

$$\dot{\hat{\boldsymbol{q}}}_b^e = \frac{1}{2}\hat{\boldsymbol{q}}_b^e \otimes \left(\bar{\boldsymbol{\omega}}_{\text{IMU}}^b - \bar{\hat{\boldsymbol{b}}}_{\text{gyro}}^b + \bar{\hat{\boldsymbol{\sigma}}}_{ib}^b\right) - \frac{1}{2}\bar{\boldsymbol{\omega}}_{ie}^e \otimes \hat{\boldsymbol{q}}_b^e, \tag{3.1}$$

$$\dot{\hat{\boldsymbol{b}}}_{\text{gyro}}^b = \text{Proj}\left(-k_I \hat{\boldsymbol{\sigma}}_{ib}^b, \|\hat{\boldsymbol{b}}_{\text{gyro}}^b\|_2 \leq M_{\hat{b}_{\text{gyro}}}\right), \tag{3.2}$$

$$\hat{\boldsymbol{\sigma}}_{ib}^b = k_1 \boldsymbol{f}_{\text{IMU}}^b \times \boldsymbol{R}^\intercal(\hat{\boldsymbol{q}}_b^e)\text{sat}_{M_f}(\hat{\boldsymbol{f}}_{ib}^e) + k_2 \boldsymbol{m}_{\text{mag}}^b \times \boldsymbol{R}^\intercal(\hat{\boldsymbol{q}}_b^e)\boldsymbol{m}_{eb}^e, \tag{3.3}$$

using the notation of (B.11) related to the quaternion product, where k_1, k_2, k_I are gains. k_I is the gain of the gyro/angular rate bias estimator, providing the NLO with integral action, whereas Proj($\star, \star$) is a projection operator ensuring that the gyro/angular rate bias estimates are bounded, $\|\hat{\boldsymbol{b}}_{\text{gyro}}^b\|_2 \leq M_{\hat{b}_{\text{gyro}}}$ using the algorithm of (Krstić et al., 1995, App. E). See Grip et al. (2012a, 2013) for details. The injection term $\hat{\boldsymbol{\sigma}}_{ib}^b$ is utilized to correct the attitude and compensate for the gyro bias in (3.1), by estimating the latter in (3.2), with the goal of obtaining an estimate of $\boldsymbol{\omega}_{ib}^b$ with $\hat{\boldsymbol{\omega}}_{ib}^b = \boldsymbol{\omega}_{\text{IMU}}^b - \hat{\boldsymbol{b}}_{\text{gyro}}^b$. The injection term $\hat{\boldsymbol{\sigma}}_{ib}^b$ is based on comparing the measured vectors in the BODY frame, here specific force and magnetic field from the accelerometer and the magnetometer, respectively, with the corresponding reference vector in the ECEF frame, rotated to the BODY frame using $\boldsymbol{R}(\hat{\boldsymbol{q}}_b^e)$. If there are discrepancies between the two, the nonlinear injection term $\hat{\boldsymbol{\sigma}}_{ib}^b$ acts as an angular velocity in (3.1) to compensate for this error. The reference vectors in question are $\boldsymbol{m}_{eb}^e$, being the Earth's magnetic field and assumed to be known, and the estimated specific force $\hat{\boldsymbol{f}}_{ib}^e$. Moreover, $\text{sat}_{M_f}(\cdot)$ is a saturation operator, such that specific force estimate remains bounded, $\|\hat{\boldsymbol{f}}_{ib}^e\|_2 \leq M_f$. As in Grip et al. (2013), $\hat{\boldsymbol{f}}_{ib}^e$ is obtained from the TMO, presented later on, which offers an accurate estimate $\hat{\boldsymbol{f}}_{ib}^e$ also when the vehicle is accelerated. This is beneficial, compared to assuming that $\boldsymbol{f}_{ib}^e \approx -\boldsymbol{g}_b^e(\hat{\boldsymbol{p}}_{eb}^e)$, where the gravity component $\boldsymbol{g}_b^e$ is obtained with a gravity model based on the estimated position $\hat{\boldsymbol{p}}_{eb}^e$, an assumption that holds only when the vehicle in question is not exposed to acceleration for prolonged periods of time. More vector measurement/reference pairs may be added to (3.3) depending on the application. A minimum of two non-parallel vectors are required in order to guarantee convergence regardless of the vehicle trajectories. The injection term $\hat{\boldsymbol{\sigma}}_{ib}^b$ is calculated in a way that resembles how the linearized attitude error enters the measurement matrix when using the quaternion-based MEKF, Markley (2003), algorithm to estimate the attitude.

3.2.1 Alternative implementation of the injection term and continuous-time gain selection

There exist other alternatives than (3.3) to construct the vector measurement/reference pairs. Normalized versions of $\boldsymbol{m}_{\text{mag}}^b$, $\boldsymbol{m}_{eb}^e$, $\boldsymbol{f}_{\text{IMU}}^b$ and $\text{sat}_{M_f}(\hat{\boldsymbol{f}}_{ib}^e)$ can be implemented

using

$$\underline{f}^b = \frac{f^b_{\text{IMU}}}{\|f^b_{\text{IMU}}\|_2}, \qquad \underline{m}^b = \frac{m^b_{\text{mag}}}{\|m^b_{\text{mag}}\|_2},$$
$$\underline{f}^e = \frac{\text{sat}_{M_f}(\hat{f}^e_{ib})}{\|\text{sat}_{M_f}(\hat{f}^e_{ib})\|_2}, \quad \underline{m}^e = \frac{m^e_{eb}}{\|m^e_{eb}\|_2}.$$

By doing so, the gains k_1 and k_2 can be viewed as cutoff frequencies of a complementary filter as described in Mahony et al. (2008); Hua et al. (2014) with the same unit as the angular velocity, ω^b_{IMU}, in (3.3) since the vector pairs become dimensionless. This means that for motion with frequencies above k_1 (rad/s), the rate gyro is the primary sensor used for estimating the attitude in the directions excited by the first reference vector, while for lower frequencies, correction associated with the first reference vector dominates. Similarly k_2 essentially determines the cutoff frequency for use of low-frequency information from the second reference vector. Furthermore, the construction of vector pairs may be additionally extended, inspired by the TRIAD algorithm (Black, 1964), by crossing the k-th vector pair with the previous vector pair, making the vectors in each frame perpendicular to each other. Hence, the new vectors $\underline{v_1}^b$, $\underline{v_1}^e$, $\underline{v_2}^b$ and $\underline{v_2}^e$ take the form of,

$$\underline{v_1}^b = \underline{f}^b, \quad \underline{v_2}^b = \underline{f}^b \times \underline{m}^b,$$
$$\underline{v_1}^e = \underline{f}^e, \quad \underline{v_2}^e = \underline{f}^e \times \underline{m}^e,$$

resulting in $\hat{\sigma}^b_{ib}$ becoming,

$$\hat{\sigma}^b_{ib} = k_1 \underline{v_1}^b \times R^\intercal(\hat{q}^e_b)\underline{v_1}^e + k_2 \underline{v_2}^b \times R^\intercal(\hat{q}^e_b)\underline{v_2}^e, \tag{3.4}$$

with the possibility to increase the attitude estimation performance compared to using (3.3). Alternatively to (3.4), a linearization of the complementary attitude filter is provided in Hua et al. (2014, Eq. (37)), and may be used to develop an optimal gain selection algorithm given the noise covariances.

3.2.2 Discretization of the attitude observer

The rate gyro measurements are integrated at a high rate $f = 1/T_s$, updating the attitude estimates whenever a new angular rate measurement is available, as in Hua et al. (2014). If T_s is small enough to assume that $\hat{\omega}^b_{ib}(t)$ remains constant between samples, the exact discretization of the kinematic equation (3.1), is obtained using

$$\hat{q}^e_b[k] = \mathbf{e}^{\left(\frac{T_s}{2}\Omega(\hat{\omega}^b_{ib}[k])\right)}\mathbf{e}^{\left(-\frac{T_s}{2}\bar{\Omega}(\omega^e_{ie})\right)}\hat{q}^e_b[k-1], \tag{3.5}$$

where

$$\hat{\boldsymbol{\omega}}_{ib}^{b}[k] = \boldsymbol{\omega}_{\text{IMU}}^{b}[k] - \hat{\boldsymbol{b}}_{\text{gyro}}^{b}[k-1] + \hat{\boldsymbol{\sigma}}_{ib}^{b}[k], \tag{3.6}$$

$$\boldsymbol{\Omega}(\omega) = \begin{pmatrix} 0 & -\boldsymbol{\omega}^{\intercal} \\ \boldsymbol{\omega} & -\boldsymbol{S}(\boldsymbol{\omega}) \end{pmatrix}, \quad \bar{\boldsymbol{\Omega}}(\boldsymbol{\omega}) = \begin{pmatrix} 0 & -\boldsymbol{\omega}^{\intercal} \\ \boldsymbol{\omega} & \boldsymbol{S}(\boldsymbol{\omega}) \end{pmatrix}, \tag{3.7}$$

$$\mathbf{e}^{\left(\frac{T_s}{2}\boldsymbol{\Omega}(\boldsymbol{\omega})\right)} = \cos\left(\frac{T_s}{2}\|\boldsymbol{\omega}\|_2\right) I_4 + \frac{T_s}{2}\text{sinc}\left(\frac{T_s}{2}\|\boldsymbol{\omega}\|_2\right)\boldsymbol{\Omega}(\boldsymbol{\omega}), \tag{3.8}$$

and

$$\mathbf{e}^{\left(-\frac{T_s}{2}\bar{\boldsymbol{\Omega}}(\boldsymbol{\omega})\right)} = \left(\cos\left(\frac{T_s}{2}\|\boldsymbol{\omega}\|_2\right) I_4 + \frac{T_s}{2}\text{sinc}\left(\frac{T_s}{2}\|\boldsymbol{\omega}\|_2\right)\bar{\boldsymbol{\Omega}}(\boldsymbol{\omega})\right)^{-1}. \tag{3.9}$$

According to Hua et al. (2014), the expressions $\cos(\cdot)$ and $\text{sinc}(\cdot)$ can, in practice, be approximated for by their first- or second-order approximation or by using a lookup table to increase the computational efficiency of (3.5). After (3.5) is calculated, re-normalization of $\hat{\boldsymbol{q}}_b^e$ is carried out,

$$\hat{\boldsymbol{q}}_b^e[k] = \frac{\hat{\boldsymbol{q}}_b^e[k]}{\|\hat{\boldsymbol{q}}_b^e[k]\|_2}, \tag{3.10}$$

to account for numerical round-off errors. The gyro bias estimates can be updated using exact integration of (3.2) with

$$\hat{\boldsymbol{b}}_{\text{gyro}}^{b}[k] = \hat{\boldsymbol{b}}_{\text{gyro}}^{b}[k-1] - T_s\, k_I[k]\, \hat{\boldsymbol{\sigma}}_{ib}^{b}[k], \tag{3.11}$$

where a projection algorithm, such as that of Grip et al. (2012a), is straightforward to add. In this implementation, one or both terms in $\hat{\boldsymbol{\sigma}}_{ib}^{b}[k]$ is not included if there is no valid vector measurement available at time index k. To ensure that the cutoff frequency, chosen for each measurement vector, maps from continuous to discrete time, $\hat{\boldsymbol{\sigma}}_{ib}^{b}[k]$ is implemented as

$$\hat{\boldsymbol{\sigma}}_{ib}^{b}[k] = \hat{\boldsymbol{\sigma}}_{ib,1}^{b}[k] + \hat{\boldsymbol{\sigma}}_{ib,2}^{b}[k], \tag{3.12}$$

such that if $i = 1 \in \mathcal{I}_k$, where $\mathcal{I}_k$ is a set containing the indices of available measurements (Appendix C.4), then $\hat{\boldsymbol{\sigma}}_{ib,1}^{b}[k]$ is implemented as

$$\hat{\boldsymbol{\sigma}}_{ib,1}^{b}[k] = \frac{\delta t_{\text{acc}}}{T_s} k_1[k]\, \underline{\boldsymbol{v}_1}^{b}[k] \times \boldsymbol{R}^{\intercal}(\hat{\boldsymbol{q}}_b^e[k-1])\underline{\boldsymbol{v}_1}^{e}[k], \tag{3.13}$$

else $\hat{\boldsymbol{\sigma}}_{ib,1}^{b}[k] = \mathbf{0}_{3\times 1}$. If $i = 2 \in \mathcal{I}_k$, then

$$\hat{\boldsymbol{\sigma}}_{ib,2}^{b}[k] = \frac{\delta t_{\text{mag}}}{T_s} k_2[k]\, \underline{\boldsymbol{v}_2}^{b}[k] \times \boldsymbol{R}^{\intercal}(\hat{\boldsymbol{q}}_b^e[k-1])\underline{\boldsymbol{v}_2}^{e}[k], \tag{3.14}$$

else $\hat{\boldsymbol{\sigma}}_{ib,2}^{b}[k] = \mathbf{0}_{3\times 1}$. δt_{acc} and δt_{mag} denote the time intervals since the previous valid accelerometer and magnetometer measurements were available, respectively.

This ensures that gains and bandwidth of the respective vector measurements are independent of sampling frequency and only decided by the continuous-time cutoff frequencies k_1 and k_2. Typically, the specific force measurement is available at the same rate as the rate gyro readings such that $\delta t_{\text{acc}} = T_s$. In this case

$$\hat{\boldsymbol{\sigma}}^b_{ib,1}[k] = k_1[k]\, \underline{\boldsymbol{v}_1}^b[k] \times \boldsymbol{R}^\top(\hat{\boldsymbol{q}}^e_b[k-1])\underline{\boldsymbol{v}_1}^e[k],$$

if $i = 1 \in \mathcal{I}_k$. This implementation strategy assumes that a valid specific force measurement is available when a new magnetometer measurement is available due to the cross product of normalized vectors embedded in the implementation of $\hat{\boldsymbol{\sigma}}^b_{ib,2}[k]$. An outline of the implementation of the nonlinear attitude observer is presented in Algorithm 4, Appendix F. Moreover, the described implementation strategy, for nonlinear and potentially low-rate injection terms is in compliance with the corrector-predictor scheme presented in Fossen (2011, Ch. 11.3.4) and allows for k_1, k_2 and k_I to be time-varying.

Situations where the assumption of constant angular velocities between IMU samples, for a given sampling time T_s, is not deemed to be sufficiently accurate may arise. This can happen if the IMU is exposed to high-frequency vibrations, and may be addressed with a more elaborate attitude mechanization (Groves, 2013, Ch. 5.1.1) to avoid coning (Groves, 2013, Ch. 5.5.4), resulting in drift in the attitude estimates. The more elaborate mechanization, however, comes with the cost of being more computational intensive. In addition, using an incremental angle (also known as Δ-angle) configuration, related to the IMU's angular rate output, is beneficial. Then, the average angular rates of the IMU between samples $k-1$ and k are provided based on the maximum internal IMU sampling frequency. Concerning the accelerometer configuration, outputting incremental velocity (also known as Δ-velocity), is beneficial in order to avoid sculling (Groves, 2013, Ch. 5.5.4). This can also benefit the attitude estimation since the specific forces are embedded in the injection term (3.12), which again acts as an angular velocity in (3.6), used in the attitude update.

Having presented the attitude observer, the following two sections present in detail the respective TMOs used for loosely and tightly coupled GNSS/INS integration.

3.3 Translation Motion Observer for Loosely Coupled Integration

The TMO presented first is used together with the attitude observer to perform the loosely coupled GNSS/INS integration. In addition to the algorithm itself, conditions for stability, and gain selection are presented. Discretization and implementation considerations are also covered.

For loosely coupled GNSS/INS integration, the TMO is obtained from Grip et al. (2013),

$$\dot{\hat{\boldsymbol{p}}}^e_{eb} = \hat{\boldsymbol{v}}^e_{eb} + \vartheta \boldsymbol{K}^0_{pp}(\boldsymbol{p}^e_{GNSS} - \hat{\boldsymbol{p}}^e_{eb}) + \boldsymbol{K}^0_{vp}(\boldsymbol{v}^e_{GNSS} - \hat{\boldsymbol{v}}^e_{eb}), \tag{3.15}$$

$$\begin{aligned}\dot{\hat{\boldsymbol{v}}}^e_{eb} = &-2\boldsymbol{S}(\boldsymbol{\omega}^e_{ie})\hat{\boldsymbol{v}}^e_{eb} + \hat{\boldsymbol{f}}^e_{ib} + \boldsymbol{g}^e_b(\hat{\boldsymbol{p}}^e_{eb}) \\ &+ \vartheta^2 \boldsymbol{K}^0_{pv}(\boldsymbol{p}^e_{GNSS} - \hat{\boldsymbol{p}}^e_{eb}) + \vartheta \boldsymbol{K}^0_{vv}(\boldsymbol{v}^e_{GNSS} - \hat{\boldsymbol{v}}^e_{eb}),\end{aligned} \tag{3.16}$$

$$\dot{\hat{\boldsymbol{\xi}}}^b_{ib} = -\boldsymbol{R}(\hat{\boldsymbol{q}}^e_b)\boldsymbol{S}(\hat{\boldsymbol{\sigma}}^b_{ib})\boldsymbol{f}^b_{\text{IMU}} + \vartheta^3 \boldsymbol{K}^0_{p\xi}(\boldsymbol{p}^e_{GNSS} - \hat{\boldsymbol{p}}^e_{eb}) + \vartheta^2 \boldsymbol{K}^0_{v\xi}(\boldsymbol{v}^e_{GNSS} - \hat{\boldsymbol{v}}^e_{eb}), \tag{3.17}$$

$$\hat{\boldsymbol{f}}^e_{ib} = \boldsymbol{R}(\hat{\boldsymbol{q}}^e_b)\boldsymbol{f}^b_{\text{IMU}} + \boldsymbol{\xi}^e_{ib}. \tag{3.18}$$

The rotation matrix $\boldsymbol{R}(\hat{\boldsymbol{q}}^e_b)$ is obtained using (B.3). See Appendix B.2.2 for details. The state $\boldsymbol{\xi}^e_{ib}$ is an auxiliary parameter/state, necessary to assist the estimation of the specific force, $\boldsymbol{f}^e_{ib}$, motivated by the analysis in Grip et al. (2012a) applied in Grip et al. (2013, 2015). This state couples the rotational and translational motions, facilitating precise attitude estimation also when the vehicle is accelerated. The feedback of $\hat{\boldsymbol{f}}^e_{ib}$ from the TMO to the attitude observer requires stability analysis leading to some restrictions on the observer gains, that are discussed next.

3.3.1 Stability conditions

The TMO for loosely coupled integration can now be written as a continuous LTV system,

$$\dot{\hat{\boldsymbol{x}}}^* = \boldsymbol{A}^*\hat{\boldsymbol{x}}^* + \boldsymbol{B}^*(t, \hat{\boldsymbol{q}}^e_b)\boldsymbol{u}^* + \boldsymbol{D}^*(t, \hat{\boldsymbol{x}}^*) + \boldsymbol{K}^*(\boldsymbol{y} - \boldsymbol{C}^*\hat{\boldsymbol{x}}^*), \tag{3.19}$$

with the state, input and output, defined respectively as

$$\begin{aligned}\hat{\boldsymbol{x}}^* &:= (\hat{\boldsymbol{p}}^e_{eb}; \hat{\boldsymbol{v}}^e_{eb}; \hat{\boldsymbol{\xi}}^e_{ib}), \\ \boldsymbol{u}^* &:= (\boldsymbol{f}^b_{\text{IMU}}; -\boldsymbol{S}(\hat{\boldsymbol{\sigma}}^b_{ib})\boldsymbol{f}^b_{\text{IMU}}), \\ \boldsymbol{y} &:= (\boldsymbol{p}^e_{GNSS}; \boldsymbol{v}^e_{GNSS}),\end{aligned}$$

and with the matrices,

$$\boldsymbol{A}^* = \begin{pmatrix} \boldsymbol{0}_{3\times3} & \boldsymbol{I}_3 & \boldsymbol{0}_{3\times3} \\ \boldsymbol{0}_{3\times3} & \boldsymbol{0}_{3\times3} & \boldsymbol{I}_3 \\ \boldsymbol{0}_{3\times3} & \boldsymbol{0}_{3\times3} & \boldsymbol{0}_{3\times3} \end{pmatrix}, \qquad \boldsymbol{B}^*(t, \hat{\boldsymbol{q}}^e_b) = \begin{pmatrix} \boldsymbol{0}_{3\times3} & \boldsymbol{0}_{3\times3} \\ \boldsymbol{R}(\hat{\boldsymbol{q}}^e_b) & \boldsymbol{0}_{3\times3} \\ \boldsymbol{0}_{3\times3} & \boldsymbol{R}(\hat{\boldsymbol{q}}^e_b) \end{pmatrix},$$

$$\boldsymbol{C}^* = \begin{pmatrix} \boldsymbol{I}_3 & \boldsymbol{0}_{3\times3} & \boldsymbol{0}_{3\times3} \\ \boldsymbol{0}_{3\times3} & \boldsymbol{I}_3 & \boldsymbol{0}_{3\times3} \end{pmatrix}, \qquad \boldsymbol{D}^*(t, \hat{\boldsymbol{x}}^*) = \begin{pmatrix} \boldsymbol{0}_{3\times1} \\ \boldsymbol{g}^e_b(\hat{\boldsymbol{p}}^e_{eb}) - 2(\boldsymbol{\omega}^e_{ie})\hat{\boldsymbol{v}}^e_{eb} \\ \boldsymbol{0}_{3\times1} \end{pmatrix},$$

$$\boldsymbol{K}^* = \begin{pmatrix} \boldsymbol{K}_{pp} & \boldsymbol{K}_{vp} \\ \boldsymbol{K}_{pv} & \boldsymbol{K}_{vv} \\ \boldsymbol{K}_{p\xi} & \boldsymbol{K}_{v\xi} \end{pmatrix} = \begin{pmatrix} \vartheta \boldsymbol{K}^0_{pp} & \boldsymbol{K}^0_{vp} \\ \vartheta^2 \boldsymbol{K}^0_{pv} & \vartheta \boldsymbol{K}^0_{vv} \\ \vartheta^3 \boldsymbol{K}^0_{p\xi} & \vartheta^2 \boldsymbol{K}^0_{v\xi} \end{pmatrix},$$

such that the system $(\boldsymbol{A}^*, \boldsymbol{B}^*, \boldsymbol{C}^*)$ is both controllable and observable. For the latter to hold, however, effects due to $\boldsymbol{D}(t, \hat{\boldsymbol{x}})$ must be assumed to be negligible. The term $-2\boldsymbol{S}(\boldsymbol{\omega}^e_{ie})\hat{\boldsymbol{v}}^e_{eb}$ is not an issue; if $-2\boldsymbol{S}(\boldsymbol{\omega}^e_{ie})$ instead was included in the $\boldsymbol{A}^*$-matrix, this would not alter the rank of the observability matrix

$$\boldsymbol{O} = \left(\boldsymbol{C}^*; \boldsymbol{C}^*\boldsymbol{A}^*; \ldots; \boldsymbol{C}^*\boldsymbol{A}^{*9-1}\right), \tag{3.20}$$

due to the structure of $\boldsymbol{A}^*$, since $\boldsymbol{\omega}^e_{ie}$ is considered to be constant. Furthermore, changes in the gravity $\boldsymbol{g}^e_b(\hat{\boldsymbol{p}}^e_{eb})$ are negligible as a results of its small variations w.r.t. to position, since the gravity is assumed to be Lipschitz.

For the nominal case when there are no sensor errors or noise, the origin of the feedback interconnection of the attitude and translational motion observer is USGES and established in Grip et al. (2013) under the following conditions:

- Two attitude measurement vectors available, being non-parallel. This is satisfied if there exists a constant $c_{\text{obs}} > 0$ such that $\|\boldsymbol{f}^b_{\text{IMU}} \times \boldsymbol{m}^b_{\text{mag}}\|_2 \geq c_{\text{obs}}$ or $\|\underline{v_1}^b \times \underline{v_2}^b\|_2 \geq c_{\text{obs}}$, for all $t \geq t_0$.
- Attitude observer gains k_1, k_2, and k_I satisfy $k_1, k_2 \geq k_P$, for some $k_P > 0$, and $k_I > 0$.
- The gravity vector $\boldsymbol{g}^e_b(\boldsymbol{p}^e_{eb})$ is a Lipschitz continuous function of the position, $\boldsymbol{p}^e_{eb}$. This is supported by physical intuition.
- The constant gains in the matrix

$$\boldsymbol{K}^0 = \begin{pmatrix} \boldsymbol{K}^0_{pp} & \boldsymbol{K}^0_{vp} \\ \boldsymbol{K}^0_{pv} & \boldsymbol{K}^0_{vv} \\ \boldsymbol{K}^0_{p\xi} & \boldsymbol{K}^0_{v\xi} \end{pmatrix},$$

  of the TMO can be chosen arbitrarily provided that the linear error dynamics matrix $\boldsymbol{A}^* - \boldsymbol{K}^0\boldsymbol{C}^*$ is Hurwitz, and $\vartheta \geq \vartheta^*$, where $\vartheta^* \geq 1$ is sufficiently large, Grip et al. (2013). The intuitions behind a large ϑ is that it implies that the estimate of $\hat{\boldsymbol{f}}^e_{ib}$ is dominated by position measurements, such that the attitude estimation errors do not lead to a large error in $\hat{\boldsymbol{f}}^e_{ib}$, which could otherwise destabilize the attitude observer.

With these requirements fulfilled, the attitude estimate is guaranteed to not diverge since the scalar part, $\tilde{s}$, of the quaternion error,

$$\tilde{\boldsymbol{q}} = \boldsymbol{q}^e_b \otimes \hat{\boldsymbol{q}}^{e*}_b = (\tilde{s}; \tilde{\boldsymbol{r}}), \tag{3.21}$$

is bounded away from zero with a margin $\tilde{s} > \bar{\epsilon}$, for some constant $\bar{\epsilon} \in (0, \frac{1}{2})$, such that (A.3), of Appendix A.1, holds for the given initial conditions due to sufficiently high gains (k_P and ϑ sufficiency high), thus fulfilling Definition A.2,

concerning uniform semiglobal exponential stability. Furthermore, this yields that origin of the overall error dynamics, of the NLO's and the TMO's estimation errors, is USGES. This even holds if the reference vectors $\underline{\boldsymbol{f}}^e$ or $\underline{\boldsymbol{f}}^e \times \underline{\boldsymbol{m}}^e$ temporarily come close to zero in the transient phase. For details, see Theorem 1 of Grip et al. (2013). For more on unit quaternions and the quaternion conjugate $\boldsymbol{q}_b^{e*}$, see Appendix B.2.2.

The practical implication of the USGES property is the robustness to large initialization errors in both position and attitude since no linearization is needed in the nonlinear attitude estimator. In addition, temporary violation of the condition related to the availability of two non-parallel vector measurements, and the corresponding reference vectors, can be tolerated since the attitude estimate can be updated using only the angular rate measurements, or one of the vectors measurements, for shorter periods of time.

3.3.2 Continuous-time gain selection

The gain conditions of Grip et al. (2013), reviewed above, are of limited practical use since they are general and sufficient (not always necessary) conditions where a non-conservative bound ϑ^* may be difficult to find. Moreover, ϑ^* also depends on the attitude observer gains k_1, k_2, k_I. In a practical approach to tuning, the gains in the matrix $\boldsymbol{K}_0$ of the TMO may be tuned using a minimum-variance estimation criterion by taking into account the influences of measurement noises. This is done by choosing $\vartheta = 1$ and

$$\boldsymbol{Q}^* = \text{blockdiag}(\boldsymbol{S}_f, \boldsymbol{S}_{\hat{\sigma} f}), \qquad \boldsymbol{R} = \text{blockdiag}(\boldsymbol{S}_p, \boldsymbol{S}_v),$$

as input and output noise covariance matrices, respectively. Regarding $\boldsymbol{R}$, the matrices $\boldsymbol{S}_p$ and $\boldsymbol{S}_v$ represents the covariance matrices of the position and velocity measurement noise components $\boldsymbol{\varepsilon}_p^e$ and $\boldsymbol{\varepsilon}_v^e$, respectively. In practice the GNSS position and velocity measurements are time-varying and correlated as the user position estimates are used to determine the user-to-satellite line-of-sight (LOS) vector in the velocity computation procedure. An alternative can then be to include cross terms $\boldsymbol{S}_{pv}$ and $\boldsymbol{S}_{vp}$ such that

$$\boldsymbol{R} = \begin{pmatrix} \boldsymbol{S}_p & \boldsymbol{S}_{pv} \\ \boldsymbol{S}_{vp} & \boldsymbol{S}_v \end{pmatrix}, \quad \boldsymbol{S}_{pv} = \boldsymbol{S}_{vp}.$$

The covariance matrices $\boldsymbol{S}_f$ and $\boldsymbol{S}_{\hat{\sigma} f}$ are obtained from the accelerometer's measurement noise by $\boldsymbol{S}_f = E[\boldsymbol{\varepsilon}_f \boldsymbol{\varepsilon}_f^\intercal]$ and $\boldsymbol{S}_{\hat{\sigma} f} = E[\boldsymbol{S}(\hat{\boldsymbol{\sigma}}_{ib}^b)\boldsymbol{\varepsilon}_f \boldsymbol{\varepsilon}_f^\intercal \boldsymbol{S}^\intercal(\hat{\boldsymbol{\sigma}}_{ib}^b)]$. The latter term goes to a steady-state value when the attitude estimates has converged.

A gain matrix that gives an approximately minimum variance estimate is given by the Riccati equation solution $\boldsymbol{P}^* = (\boldsymbol{P}^*)^\intercal > 0$ motivated by the fact that the TMO's error dynamics are identical to the time-scaled error dynamics of the

Kalman and Bucy (1961) filter

$$\boldsymbol{K}^0 = \boldsymbol{P}^*(\boldsymbol{C}^*)^\intercal \boldsymbol{R}^{-1}, \tag{3.22}$$

$$\frac{1}{\vartheta}\dot{\boldsymbol{P}}^* = \boldsymbol{A}^*\boldsymbol{P}^* + \boldsymbol{P}^*(\boldsymbol{A}^*)^\intercal + \boldsymbol{B}^*\boldsymbol{Q}^*(\boldsymbol{B}^*)^\intercal - \boldsymbol{P}^*(\boldsymbol{C}^*)^\intercal \boldsymbol{R}^{-1}\boldsymbol{C}^*\boldsymbol{P}^*. \tag{3.23}$$

One reason for (3.19)–(3.23) only being an approximately minimum variance estimator is that $\hat{\boldsymbol{q}}_b^e$ and $\hat{\boldsymbol{\sigma}}_{ib}^b$ are correlated with $\boldsymbol{f}_{\text{IMU}}^b$. Therefore the accelerometer's noise $\boldsymbol{\varepsilon}_f^b$ and the accompanying covariance $\boldsymbol{S}_f$ are correlated with $\boldsymbol{B}^*$. The result of Johansen and Fossen (2015, Lemma 6) shows that it is possible to choose ϑ independently from $\boldsymbol{P}^*$, using the time-varying Riccati equation (3.23) such that the USGES stability properties posed in Grip et al. (2013) still hold when calculating the gains with (3.22)–(3.23). However, choosing $\vartheta > 1$ is suboptimal with respect to the minimum variance optimization problem the Kalman-Bucy filter solves. In addition, the covariance matrix $\boldsymbol{S}_{\hat{\sigma}f}$, associated with $\boldsymbol{\xi}_{ib}^e$, is not necessarily straight forward to determine since $\boldsymbol{S}(\hat{\boldsymbol{\sigma}}_{ib}^b)$ is correlated with $\boldsymbol{\varepsilon}_f^b$. These terms are also further correlated with $\boldsymbol{R}(\hat{\boldsymbol{q}}_b^e)$. As an alternative, ad hoc tuning of $\boldsymbol{S}_{\hat{\sigma}f}$ can be considered. By always choosing $\boldsymbol{S}_{\hat{\sigma}f}$ larger than zero, the gains associated with the state $\boldsymbol{\xi}_{ib}^e$ never become zero, guaranteeing stability.

A simulation case study, presented in Appendix C.2, illustrates the benefit using time-varying gains in both the attitude observer and TMO in order to obtained fast convergence the feedback-interconnected NLO

3.3.3 Position space GNSS error models

The position and velocity measurements provided by the GNSS receiver's least squares estimator or EKF are subjected to time-varying errors inflicted by three main effects; Satellite errors, signal propagation errors and receiver errors, (Grewal et al., 2013, Ch. 7).

The GNSS position and velocity errors can be characterized by their spectral contents. Using spectral factorization and a state-space realization of the resulting filtered white noise processes for loosely coupled integration leads to an m-th order linear error model on the form

$$\dot{\boldsymbol{z}} = \boldsymbol{F}\boldsymbol{z} + \boldsymbol{G}\boldsymbol{n}, \qquad \boldsymbol{\delta} = \boldsymbol{H}\boldsymbol{z} + \boldsymbol{\varepsilon}_{pv}^e, \tag{3.24}$$

where $\boldsymbol{\delta} = (\boldsymbol{\delta}_p; \boldsymbol{\delta}_v) \in \mathbb{R}^6$ represents the position and velocity errors, and $\boldsymbol{\varepsilon}_{pv}^e \in \mathbb{R}^6$ and $\boldsymbol{n} \in \mathbb{R}^6$ are vectors with unity white noise where $\boldsymbol{n} \sim (0, 1)$ and $\boldsymbol{\varepsilon}_{pv}^e \sim (0, \sigma_{pv}^2)$. Hence, the receiver outputs position and velocity estimates $\boldsymbol{p}_{\text{GNSS}}^e = \boldsymbol{p}_{eb}^e + \boldsymbol{\delta}_p$ and $\boldsymbol{v}_{\text{GNSS}}^e = \boldsymbol{v}_{eb}^e + \boldsymbol{\delta}_v$, respectively. The model (3.24), related to the GNSS position measurements can be chosen to be a first-order Gauss-Markov process (Rankin, 1994; Mohleji and Wang, 2010). By defining $\boldsymbol{z} := (\boldsymbol{z}_p; \boldsymbol{z}_v)$, the dynamic GNSS position error is represented by the system

$$\dot{\boldsymbol{z}}_p = \boldsymbol{F}_p\boldsymbol{z}_p + \boldsymbol{G}_p\boldsymbol{n}_p, \quad \boldsymbol{\delta}_p = \boldsymbol{H}_p\boldsymbol{z}_p + \boldsymbol{\varepsilon}_p^e, \tag{3.25}$$

with $\boldsymbol{F}_p = -\boldsymbol{T}_p^{-1}$, where $\boldsymbol{T}_p$ is the correlation time constant. The elements of $\boldsymbol{G}_p$ are chosen equal to the appropriate standard deviations of the driving noise.

It is evident that even though the GNSS velocity measurements can be very precise (root mean square (RMS) error of down to 0.1 m/s), these also contain some dynamic errors, depending on satellite geometry and the dynamic error corrupting the raw GNSS observables. Moreover, for the dynamic error of the GNSS velocity measurement can be represented by

$$\dot{\boldsymbol{z}}_v = \boldsymbol{F}_v \boldsymbol{z}_v + \boldsymbol{G}_v \boldsymbol{n}_v, \quad \boldsymbol{\delta}_v = \boldsymbol{H}_v \boldsymbol{z}_v + \boldsymbol{\varepsilon}_v^e. \tag{3.26}$$

By also choosing $\boldsymbol{F}_v = -\boldsymbol{T}_v^{-1}$, where $\boldsymbol{T}_v$ is the assumed correlation time and the elements of $\boldsymbol{G}_v$ corresponds to the standard deviations of the driving noise (3.26), the steady-state covariance of the Gauss-Markov processes $\boldsymbol{z}_p$ and $\boldsymbol{z}_v$ become

$$\boldsymbol{P}_{z_p}(\infty) = -\frac{1}{2}\boldsymbol{F}_p^{-1}\boldsymbol{G}_p\boldsymbol{G}_p^\intercal, \quad \boldsymbol{P}_{z_v}(\infty) = -\frac{1}{2}\boldsymbol{F}_v^{-1}\boldsymbol{G}_v\boldsymbol{G}_v^\intercal, \tag{3.27}$$

respectively for sufficiently long measurement periods since $\boldsymbol{F}_p = \boldsymbol{F}_p^\intercal$, $\boldsymbol{F}_v = \boldsymbol{F}_v^\intercal$. For higher-order models $\boldsymbol{P}_{z_\star}(\infty)$ is obtained by solving

$$\boldsymbol{F}_\star \boldsymbol{P}_{z_\star} + \boldsymbol{P}_{z_\star}\boldsymbol{F}_\star^\intercal + \boldsymbol{G}_\star\boldsymbol{G}_\star^\intercal = \boldsymbol{0}_{l\times l}, \tag{3.28}$$

where $\star$ is a placeholder for p or v and l being the dimension of $\boldsymbol{F}_\star$.

3.3.4 Augmented TMO for loosely coupled integration including GNSS error models

To account for colored GNSS measurement noise, the TMO is augmented with an estimator of the noise dynamics

$$\dot{\hat{\boldsymbol{z}}} = \boldsymbol{F}\hat{\boldsymbol{z}} + \boldsymbol{K}_{pz}(\boldsymbol{p}_{GNSS}^e - \hat{\boldsymbol{p}}_{eb}^e - \hat{\boldsymbol{\delta}}_p) + \boldsymbol{K}_{vz}(\boldsymbol{v}_{GNSS}^e - \hat{\boldsymbol{v}}_{eb}^e - \hat{\boldsymbol{\delta}}_v), \tag{3.29}$$

such that the augmented state vector becomes $\boldsymbol{x} = (\boldsymbol{x}^*; \boldsymbol{z})$ which is leads to

$$\dot{\boldsymbol{x}} = \boldsymbol{A}\boldsymbol{x} + \boldsymbol{B}_1(t, \boldsymbol{q}_b^e)\boldsymbol{u}^* + \boldsymbol{B}_2\boldsymbol{n} + \boldsymbol{D}(t, \boldsymbol{x}), \tag{3.30}$$

and the corresponding TMO

$$\dot{\hat{\boldsymbol{x}}} = \boldsymbol{A}\hat{\boldsymbol{x}} + \boldsymbol{B}_1(t, \hat{\boldsymbol{q}}_b^e)\boldsymbol{u}^* + \boldsymbol{D}(t, \hat{\boldsymbol{x}}) + \boldsymbol{K}(\boldsymbol{y} - \boldsymbol{C}\hat{\boldsymbol{x}}), \tag{3.31}$$

where the augmented system is defined by

$$\begin{aligned}
\boldsymbol{A} &= \begin{pmatrix} \boldsymbol{A}^* & \boldsymbol{0}_{9\times l} \\ \boldsymbol{0}_{l\times 9} & \boldsymbol{F} \end{pmatrix}, \qquad \boldsymbol{C} = \begin{pmatrix} \boldsymbol{C}^*, & \boldsymbol{H} \end{pmatrix}, \\
\boldsymbol{B}_1(t, \hat{\boldsymbol{q}}_b^e) &= \begin{pmatrix} \boldsymbol{B}^*(t, \hat{\boldsymbol{q}}_b^e) \\ \boldsymbol{0}_{l\times 6} \end{pmatrix}, \qquad \boldsymbol{B}_2 = \begin{pmatrix} \boldsymbol{0}_{9\times m} \\ \boldsymbol{G} \end{pmatrix}, \\
\boldsymbol{B} &= \begin{pmatrix} \boldsymbol{B}_1 & \boldsymbol{B}_2 \end{pmatrix}, \quad \boldsymbol{D}(t, \hat{\boldsymbol{x}}) = \begin{pmatrix} \boldsymbol{D}^*(t, \hat{\boldsymbol{x}}) \\ \boldsymbol{0}_{l\times 1} \end{pmatrix}, \\
\boldsymbol{K} &= \begin{pmatrix} \boldsymbol{K}^* \\ \boldsymbol{K}_z \end{pmatrix},
\end{aligned}$$

and where $\boldsymbol{B}$ is used to calculate $\boldsymbol{K} = \vartheta \boldsymbol{L}_\vartheta^{-1} \boldsymbol{K}^0 \boldsymbol{E}_\vartheta$ from the augmented equivalent of (3.22)–(3.23), that is

$$\boldsymbol{K}^0 = \boldsymbol{P}\boldsymbol{C}^\intercal \boldsymbol{R}^{-1}, \tag{3.32}$$

$$\frac{1}{\vartheta}\dot{\boldsymbol{P}} = \boldsymbol{A}\boldsymbol{P} + \boldsymbol{P}\boldsymbol{A}^\intercal + \boldsymbol{B}\boldsymbol{Q}\boldsymbol{B}^\intercal - \boldsymbol{P}\boldsymbol{C}^\intercal \boldsymbol{R}^{-1}\boldsymbol{C}\boldsymbol{P}, \tag{3.33}$$

with

$$\boldsymbol{L}_\vartheta = \text{blockdiag}\left(\boldsymbol{I}_3, \frac{1}{\vartheta}\boldsymbol{I}_3, \frac{1}{\vartheta^2}\boldsymbol{I}_3, \boldsymbol{I}_{l_p}, \frac{1}{\vartheta}\boldsymbol{I}_{l_v}\right), \tag{3.34}$$

$$\boldsymbol{E}_\vartheta = \boldsymbol{C}\boldsymbol{L}_\vartheta \boldsymbol{C}^\dagger. \tag{3.35}$$

Moreover, $l = l_p + l_v$ is the degrees of freedom of the Gauss-Markov process, where l_p and l_v are the respective dimensions of the GNSS position and velocity error models. In addition, $\boldsymbol{G}$ is a $l \times m$ matrix, where $l = m$ for first-order Gauss-Markov models. If only the position measurement is corrupted by colored noise, $l := 3$ resulting in $\boldsymbol{L}_\vartheta = \text{blockdiag}\left(\boldsymbol{I}_3, 1/\vartheta \cdot \boldsymbol{I}_3, 1/\vartheta^2 \cdot \boldsymbol{I}_3, \boldsymbol{I}_l\right)$. However, if this is also applicable for the velocity measurement, $l := 6$ with the spectral factorization chosen above. The pair $(\boldsymbol{A}, \boldsymbol{C})$ can be shown to always be observable for any $\boldsymbol{T}_p, \boldsymbol{T}_v > 0$ when the chosen spectral factorization results in a first-order Gauss-Markov process since

$$\text{rank}(\boldsymbol{O}) = 9 + l, \tag{3.36}$$

where

$$\boldsymbol{O} = \left(\boldsymbol{C}; \boldsymbol{C}\boldsymbol{A}; \ldots; \boldsymbol{C}\boldsymbol{A}^{9+l-1}\right), \tag{3.37}$$

hence satisfying Kalman's rank condition of observability of linear time-invariant systems, Kalman and Bucy (1961). With this state-space augmentation, and by defining $\boldsymbol{Q} = \text{blockdiag}\left(\boldsymbol{Q}^*, \boldsymbol{I}_l\right)$, the TMO is realized using (3.31), where the gain can be obtained using (3.32)–(3.33).

3.3.5 Simulation case study: Effects of colored GNSS noise

GNSS position and velocity measurements contain colored noise components, (Grewal et al., 2013, Ch. 7). To illustrate the effect of the colored noise on the GNSS/INS integration performance, induced by (3.24), a GNSS receiver is simulated, at high latitude, where the measurement is given in the NED frame, $\boldsymbol{p}^n_{\text{GNSS}} = \boldsymbol{p}^n_{nb} + \boldsymbol{z}_p + \boldsymbol{\varepsilon}^n_p$ and $\boldsymbol{v}^n_{\text{GNSS}} = \boldsymbol{v}^n_{nb} + \boldsymbol{z}_v + \boldsymbol{\varepsilon}^n_v$ and the model parameters are chosen as $\boldsymbol{F} = \text{blockdiag}(\boldsymbol{F}_p, \boldsymbol{F}_v)$ and $\boldsymbol{G} = \text{blockdiag}(\boldsymbol{G}_p, \boldsymbol{G}_v)$ with

$$\begin{aligned}
&\boldsymbol{F}_p = -1/T_p \cdot \boldsymbol{I}_3, \boldsymbol{F}_v = -1/T_v \cdot \boldsymbol{I}_3, \\
&\boldsymbol{G}_p = \text{diag}(1.2, 0.7, 2), \\
&\boldsymbol{G}_v = \text{diag}(1, 1, 2).
\end{aligned}$$

The time constant related to the position error was chosen to be $T_p = 1100$ s as in Rankin (1994), (Beard and McLain, 2012, Ch 7.5), while the time constant related to the velocity error was chosen as $T_v = 2$ s. The latter was chosen based on the assumption that the GNSS velocity measurements, obtained from the receiver, primarily are based on the Doppler range-rate measurements. The time constant related to these can be much smaller than for the noise embedded in the C/A code-based pseudoranges. This is due to the GNSS carrier phase and code observables being affected differently by various error sources. Furthermore, with this choice of $\boldsymbol{G}$, it is taken into account that the horizontal measurements are more accurate than the vertical counterparts and that the eastern measurements are more precise than the northern at higher latitudes using GPS. The chosen noise and bias parameters related to the simulated inertial sensors are equal to those presented in the simulation example in Appendix C.2.

The motion simulated is of a small UAV flying in a circular motion with a speed 25 m/s and with a constant altitude of 150 meters over ground. The UAV is flying with a constant yaw rate with a roll angle and pitch angles of $\phi = -3$ and $\theta = 2$ degrees, respectively. The North-East motion in shown in Figure 3.2.

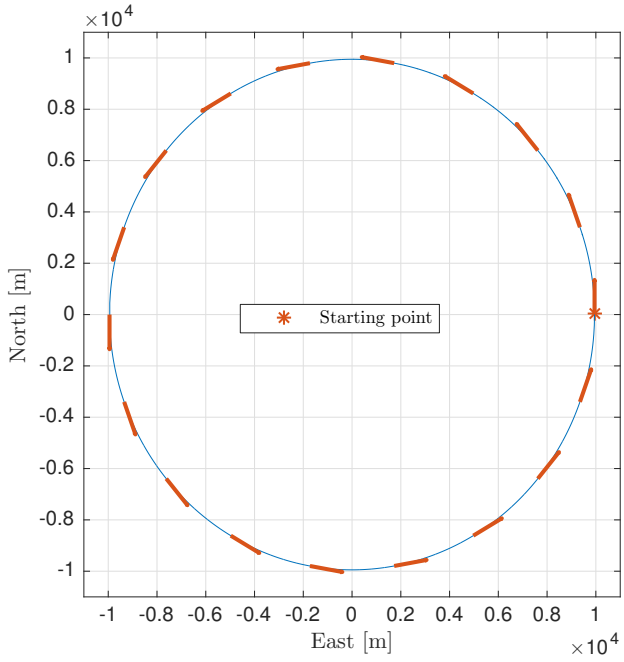

Figure 3.2: Overview of the simulated horizontal UAV motion. The motion simulated is a circle with radius of 10 000 meters, where the initial heading of the UAV was zero. The chosen simulated UAV speed was 25 m/s. The blue circle indicates the UAV path, while the red arrows depicts the heading of the UAV at fixed intervals.

Case 1: Only GNSS position measurement available

This first case is simulated with only position measurements available.

Figures 3.3–3.4 show the position estimation error and performance of the GNSS colored noise estimation. It is obvious that even though rank $(\mathcal{O}) = 12$, such that the pair $(\boldsymbol{A}, \boldsymbol{C})$ is observable, the GNSS transient error is not captured by the model augmentation. Due to the stochastic properties, in this case, the system

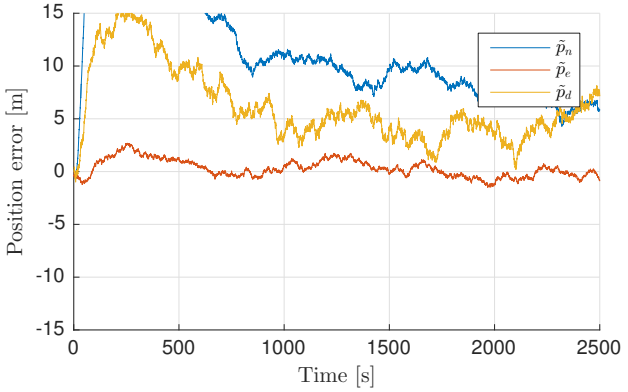

Figure 3.3: Case 1, position estimation error. North, east and down axes are denoted n, e and d, respectively. The position estimation error obtained in simulation when applying GNSS position measurements containing colored noise.

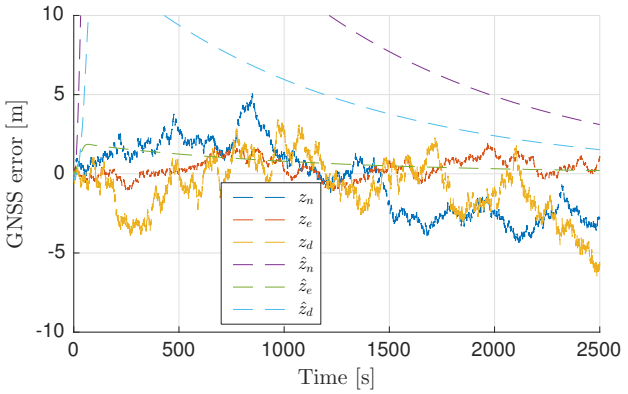

Figure 3.4: Case 1, GNSS error state estimates. North, east and down axes are denoted n, e and d, respectively. The true GNSS error states (colored noise) are shown in blue, red and yellow, respectively. The corresponding respective estimates are presented in purple, green and light blue. It can be seen that the TMO fails in estimating the colored GNSS correctly.

$(\boldsymbol{A}, \boldsymbol{C})$ is only weakly observable as indicated by the estimation error covariance $\boldsymbol{P}$.

Figure 3.5, based on the stationary estimation error covariance $\boldsymbol{P}(\infty)$, shows the error ellipsis, with 95% confidence interval, illustrating that the states associated with the colored GNSS noise are highly correlated with the position error. Hence, it can be expected that the position covariance is close to that of (3.27), the Gauss-Markov process describing the colored noise.

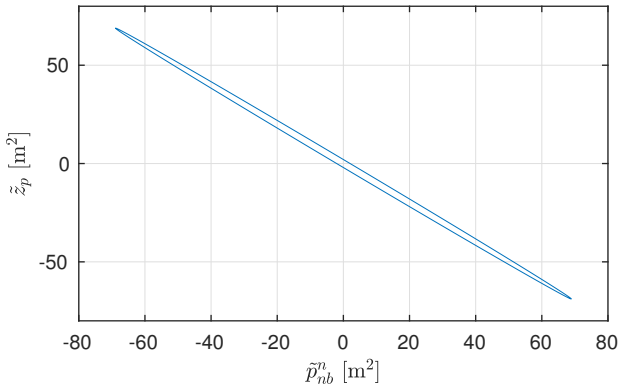

Figure 3.5: Case 1, error ellipsis of the north position estimation error and the corresponding colored noise estimate of the position measurement. The error ellipsis presented shows that the position estimation error and the colored GNSS noise estimation error are significantly correlated. This indicates that the TMO struggles to separate the colored noise from the true position. Similar ellipsis are also obtainable for the East and Down axes.

Case 2: GNSS position measurements together and a velocity measurement with white noise

In this case, unrealistic GNSS velocity measurements are added, containing the true velocity and only corrupted with white noise for illustrative purposes.

Figures 3.6–3.7 show the position estimation error and performance of the GNSS colored noise estimation error when the velocity measurements, only corrupted with white noise, are added as an aiding measurements in the TMO. The deterministic observability properties are still the same with rank 12, however the performance has increased significantly. Hence, now the TMO is able to track the colored GNSS position error to a large extent. This is reflected in Figure 3.6 where the position estimation error is reduced compared to the performance shown in Figure 3.3.

Case 3: GNSS position and velocity measurements containing colored noise

In this last case, a more realistic GNSS velocity measurement is used, having some dynamic error such that $\boldsymbol{v}^n_{\text{GNSS}} = \boldsymbol{v}^n_{nb} + \boldsymbol{z}_v + \boldsymbol{\varepsilon}^n_v$, as described earlier, where $\boldsymbol{z}_v$

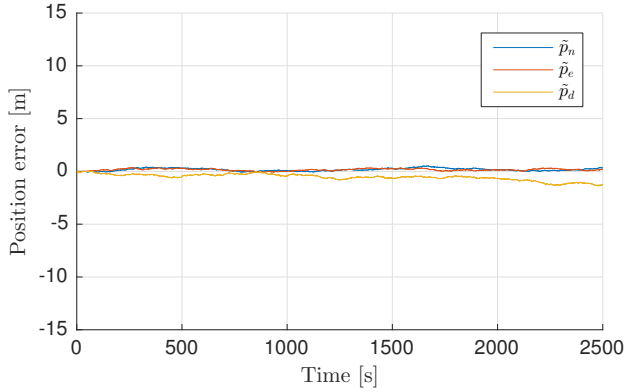

Figure 3.6: Case 2, position estimation error. North, east and down axes are denoted n, e and d, respectively. The position estimation error obtained in simulation when applying GNSS position measurements containing colored noise together with GNSS velocity measurements containing white noise. The estimation accuracy is better with velocity measurements corrupted by white noise compared to solely applying position measurements.

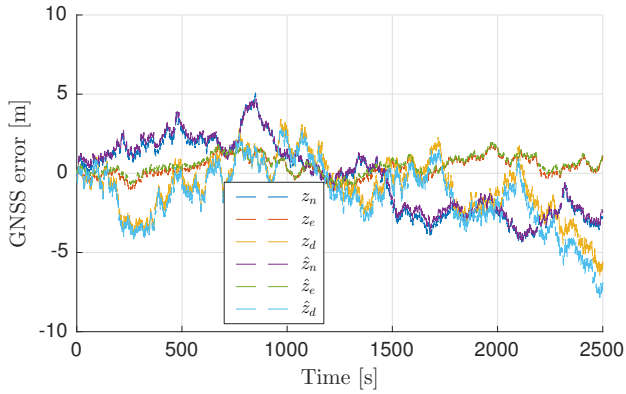

Figure 3.7: Case 2, GNSS error state estimates. North, east and down axes are denoted n, e and d, respectively. The true GNSS error states (colored noise), associated with position, are shown in blue, red and yellow, respectively. The corresponding respective estimates are presented in purple, green and light blue. It can be seen that the TMO estimates the colored GNSS error more accurate after the velocity measurements were introduced.

is generated as a Gauss-Markov process with time constant $T_v = 2$. Related to case 2 only minor differences are seen considering Figures 3.8–3.9 compared to Figures 3.6–3.7. The augmented observer structure of (3.31) is able to utilize the velocity measurements with colored noise, hence improving the position accuracy compared to Case 1 and Figures 3.3–3.4. Even though the absolute position error

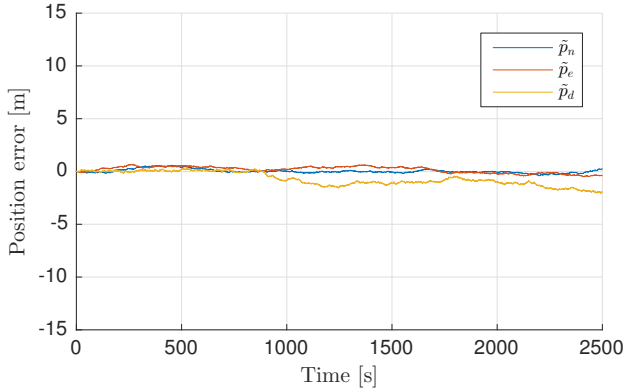

Figure 3.8: Case 3, position estimation error. North, east and down axes are denoted n, e and d, respectively. The position estimation error obtained in simulation when applying GNSS position and velocity measurements containing colored noise. The estimation accuracy is better with velocity measurements compared to solely applying position measurements, however, still worse than applying a velocity measurement only corrupted by white noise.

is reduced compared to Case 1, the covariance of the estimation error still indicates the same problem; the TMO may still struggle to distinguish the colored noise of the position measurements from the true position as seen in Figure 3.10 showing the error ellipsis of $\boldsymbol{P}(\infty)$, where the cross correlation between the $\tilde{\boldsymbol{p}}^n_{nb}$ and $\tilde{\boldsymbol{z}}_p$ still is significant, however reduced compared to case 1 where only the position measurements were used.

Discussion

The reason why the augmented observer, (3.31), applying loosely coupled GNSS/INS integration struggles to separate the true position from the slowly-varying colored GNSS noise is the relatively high noise in the IMUs accelerometers. Since the rotated accelerometer noise is integrated twice in the TMO, the TMO gains are synthesized, using (3.32)–(3.33), such that the uncertainty in the position estimate is minimized and by that stabilizing the observer. Hence, the gains, in practice, become so large that the position estimate in the observer tracks the slowly-varying colored GNSS noise. To illustrate this, a Bode diagram related to the northern position estimation error and the GNSS errors from Case 1 is shown in Figure 3.11. The transfer functions shown are the transfer function from the IMU noise $\boldsymbol{\varepsilon}^n_f$,

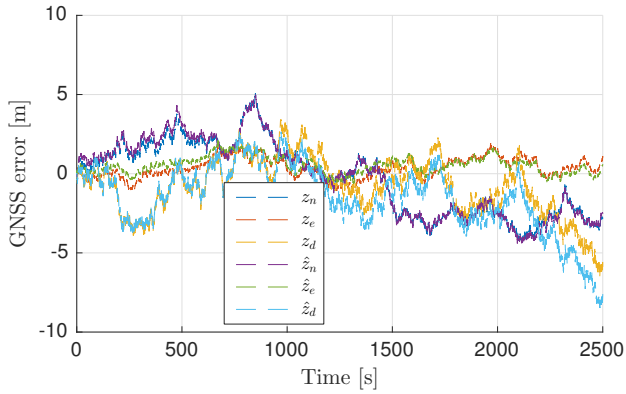

Figure 3.9: Case 3, GNSS error state estimates. North, east and down axes are denoted n, e and d, respectively. The true GNSS error states (colored noise), associated with position, are shown in blue, red and yellow, respectively. The corresponding respective estimates are presented in purple, green and light blue. It can be seen that the TMO estimates the colored GNSS error more accurate with velocity measurements than without, however, not as accurate as when the velocity measurements only were corrupted with white noise.

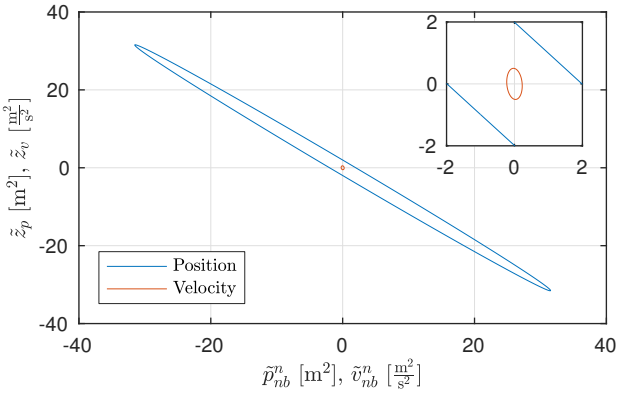

Figure 3.10: Case 3, error ellipsis of the north position and velocity estimation error and the corresponding colored noise estimate of the position and velocity measurement. The error ellipsis associated with position is shown in blue, while error ellipsis associated the velocity is shown red. The error position ellipsis shows that the position estimation error and the colored global navigation satellite system noise estimation error still are significantly correlated, however, the correlation is significantly reduced by introducing the velocity measurement. Regarding the velocity estimation error and the velocity colored noise, the correlation is significantly smaller the compared to the position equivalent.

rotated to the NED frame, to the position estimation error, $\tilde{\boldsymbol{p}}^n_{nb} = \boldsymbol{p}^n_{nb} - \hat{\boldsymbol{p}}^n_{nb}$, the transfer function from the GNSS measurement error $\boldsymbol{\delta}_p = \boldsymbol{H}_p \boldsymbol{z}_p + \boldsymbol{\varepsilon}^n_p$ to the position estimation error, and the transfer function from the input of the GNSS colored noise model, $\boldsymbol{n}_p$, to the output of the model, $\boldsymbol{z}_p$. These are denoted

$$\frac{\tilde{\boldsymbol{p}}^n_{nb}}{\boldsymbol{\varepsilon}^b_f} = \boldsymbol{h}_{\text{INS}}(s), \tag{3.38}$$

$$\frac{\tilde{\boldsymbol{p}}^n_{nb}}{\boldsymbol{\delta}_p} = \boldsymbol{h}_{\text{PosErr}}(s), \tag{3.39}$$

and

$$\frac{\boldsymbol{z}_p}{\boldsymbol{n}_p} = \boldsymbol{h}_{\text{CN}}(s), \tag{3.40}$$

respectively, where

$$\boldsymbol{h}_{\text{INS}}(s) = \bar{\boldsymbol{C}} \left(s\boldsymbol{I}_3 - (\boldsymbol{A}^* - \boldsymbol{K}^*\boldsymbol{C}^*)\right)^{-1} \boldsymbol{B}^*, \tag{3.41}$$

$$\boldsymbol{h}_{\text{PosErr}}(s) = \bar{\boldsymbol{C}} \left(s\boldsymbol{I}_3 - (\boldsymbol{A}^* - \boldsymbol{K}^*\boldsymbol{C}^*)\right)^{-1} \boldsymbol{K}^*\boldsymbol{C}^*, \tag{3.42}$$

$$\boldsymbol{h}_{\text{CN}}(s) = \boldsymbol{I}_3 \left(s\boldsymbol{I}_3 - (\boldsymbol{F}_p)\right)^{-1} \boldsymbol{G}_p, \tag{3.43}$$

with $\bar{\boldsymbol{C}} = (\boldsymbol{I}_3, \boldsymbol{0}_{3\times3}, \boldsymbol{0}_{3\times3})$. It is evident from Figure 3.11 that the INS has higher bandwidth than the GNSS colored noise. This is due to the gains synthesis obtained from (3.32)–(3.33) is emphasizing the correction of the position estimate significantly more than the update of corresponding GNSS error state. As a result, the estimated position tracks the colored noise contained in the GNSS position measurements regardless of the model augmentation.

The results from Case 3 indicate that velocity measurements are beneficial to improve the position estimation accuracy, using loosely coupled GNSS/INS integration. However, the parameters representing the colored noise characteristics are time-varying and difficult to know in general. These are highly receiver dependent, and dependent on the user's location on Earth with respect to satellite geometry, elevation of the satellites, the ionosphere, and whether the Doppler observables are utilized in the GNSS receiver's estimator. In particular, knowledge on how the velocity measurements are calculated is difficult to know using off-the shelf equipment. Typically, the current position estimate is used in the velocity estimation process to determine user-to-satellite LOS vectors or to estimate the receiver's velocity without the Doppler measurement, yielding that the position information is being accounted for twice in the GNSS/INS observer. Knowing the cross correlation between the position and velocity measurements are of utmost importance in such situations. If not known, using only the position measurements may be advised.

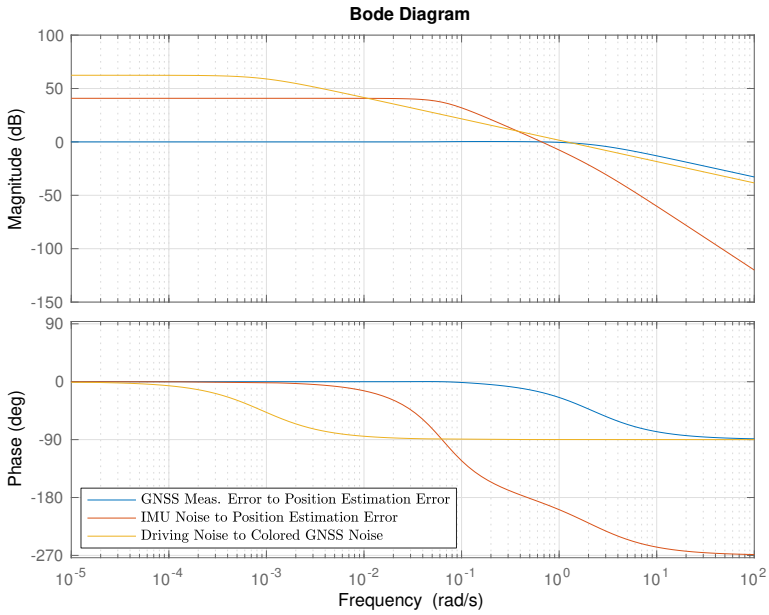

Figure 3.11: Bode plot. Three bode plots are shown; the transfer function from the GNSS measurements error to the position estimation error is shown in blue, the transfer function from the IMU noise to the position estimation error is shown in red and the transfer function from the driving noise of the GNSS error model to the colored GNSS position noise model output is shown in yellow. From the three frequency responses, the conclusion is that the bandwidth of the navigation system is higher than the slowly-varying colored noise component embedded in the GNSS position measurements.

3.3.6 Discretization of the translational motion observer

The main principle for the discrete-time implementation is to approximate the continuous time behavior despite the finite data rate. It implies that the estimates are only corrected when the output measurements contained in the injection terms are valid, and otherwise integrate the measured inputs, using the model, at their highest available update rate. Measurement updates can be processed sequentially by a KF, assuming the measurements are uncorrelated such that the $\boldsymbol{R}$ matrix is diagonal, with benefits for processing structure and complexity Farrell (2008); Groves (2013). Due to the close relationship between (3.32)–(3.33) and the KF, a similar strategy can be applied also for NLOs. The TMO (3.31) is straightforward to discretize due to its linearity and the simple $\boldsymbol{A}$-matrix, allowing for exact discretization of the unforced dynamics. In particular, the one-step ahead predicted

state, $\boldsymbol{x}^-$ can be computed by

$$\begin{aligned}\boldsymbol{x}^-[k+1] = \mathbf{e}^{\boldsymbol{A}T_s}\boldsymbol{x}^+[k] &+ \int_{kT_s}^{(k+1)T_s} \mathbf{e}^{\boldsymbol{A}\left((k+1)T_s-\tau\right)}\boldsymbol{B}_1(\tau)\boldsymbol{u}^*(\tau)\,\mathrm{d}\tau \\ &+ \int_{kT_s}^{(k+1)T_s} \mathbf{e}^{\boldsymbol{A}\left((k+1)T_s-\tau\right)}\boldsymbol{D}(\tau)\mathrm{d}\tau,\end{aligned} \tag{3.44}$$

from the estimate $\boldsymbol{x}^+[k]$, where

$$\boldsymbol{A}_d = \mathbf{e}^{\boldsymbol{A}T_s} = \begin{pmatrix} \boldsymbol{I}_3 & T_s\boldsymbol{I}_3 & \frac{T_s^2}{2}\boldsymbol{I}_3 & \mathbf{0}_{3\times l} \\ \mathbf{0}_{3\times 3} & \boldsymbol{I}_3 & T_s\boldsymbol{I}_3 & \mathbf{0}_{3\times l} \\ \mathbf{0}_{3\times 3} & \mathbf{0}_{3\times 3} & \boldsymbol{I}_3 & \mathbf{0}_{3\times l} \\ \mathbf{0}_{l\times 3} & \mathbf{0}_{l\times 3} & \mathbf{0}_{l\times 3} & \boldsymbol{e}^{\boldsymbol{F}T_s} \end{pmatrix}, \tag{3.45}$$

based on the model parameters of (3.31). Assuming the specific force input, the rotation matrix and the gravity vector are constant between the sampling intervals, $\boldsymbol{f}^b_{\mathrm{IMU}}(t) = \boldsymbol{f}^b_{\mathrm{IMU}}[k]$, $\boldsymbol{R}(t) = \boldsymbol{R}(\boldsymbol{q}^e_b[k])$ and $\boldsymbol{g}^e_b(\boldsymbol{p}^e_{eb}(t)) = \boldsymbol{g}^e_b(\hat{\boldsymbol{p}}^e_{eb}[k])$, for $t \in [kT_s, (k+1)T_s)$, it follows from (3.44)

$$\boldsymbol{B}_{d,1}[k] := \begin{pmatrix} \frac{T_s^2}{2}\boldsymbol{R}(\hat{\boldsymbol{q}}^e_b[k]) & \frac{T_s^3}{6}\boldsymbol{R}(\hat{\boldsymbol{q}}^e_b[k]) \\ T_s\boldsymbol{R}(\hat{\boldsymbol{q}}^e_b[k]) & \frac{T_s^2}{2}\boldsymbol{R}(\hat{\boldsymbol{q}}^e_b[k]) \\ \mathbf{0}_{3\times 3} & T_s\boldsymbol{R}(\hat{\boldsymbol{q}}^e_b[k]) \\ \mathbf{0}_{l\times 3} & \mathbf{0}_{l\times 3} \end{pmatrix}, \quad \boldsymbol{B}_{d,2}[k] := \begin{pmatrix} \mathbf{0}_{9\times l} \\ \boldsymbol{F}^{-1}\left(\mathbf{e}^{\boldsymbol{F}T_s} - \boldsymbol{I}_l\right)\boldsymbol{G} \end{pmatrix},$$

$$\boldsymbol{B}_d[k] = \begin{pmatrix} \boldsymbol{B}_{d,1}[k] & \boldsymbol{B}_{d,2}[k] \end{pmatrix}, \quad \boldsymbol{D}_d[k] := \begin{pmatrix} \frac{T_s^2}{2}\left(\boldsymbol{g}^e_b(\hat{\boldsymbol{p}}^e_{eb}[k]) - 2\boldsymbol{S}(\boldsymbol{\omega}^e_{ie})\boldsymbol{v}^e_{eb}[k]\right) \\ T_s\left(\boldsymbol{g}^e_b(\hat{\boldsymbol{p}}^e_{eb}[k]) - 2\boldsymbol{S}(\boldsymbol{\omega}^e_{ie})\boldsymbol{v}^e_{eb}[k]\right) \\ \mathbf{0}_{3\times 3} \\ \mathbf{0}_{l\times 3} \end{pmatrix}.$$

Then, the state estimate can be recursively propagated by iterating through the time update

$$\boldsymbol{x}^-[k+1] = \boldsymbol{A}_d[k]\boldsymbol{x}^+[k] + \boldsymbol{B}_{d,1}[k]\boldsymbol{u}^*[k] + \boldsymbol{D}_d[k], \tag{3.46}$$

$$\boldsymbol{P}^-[k+1] = \boldsymbol{A}_d[k]\boldsymbol{P}^+[k]\boldsymbol{A}_d^\intercal[k] + \boldsymbol{B}_d[k]\boldsymbol{Q}_d[k]\boldsymbol{B}_d^\intercal[k], \tag{3.47}$$

as many times as necessary. $\boldsymbol{Q}_d$ can be approximated as $\boldsymbol{Q}_d = \boldsymbol{Q}\cdot T_s$. Alternatively, the term $\boldsymbol{B}_d[k]\boldsymbol{Q}_d[k]\boldsymbol{B}_d^\intercal[k]$ can be replaced with $\bar{\boldsymbol{Q}}_d$ calculated by using van Loan's method (van Loan (1978), Brown and Hwang (2012, p. 126)).

If all measurements in the vector $\boldsymbol{y}[k]$ were available at time index k, a gain matrix $\boldsymbol{K}_d[k]$ can be calculated in the same way as the discrete-time KF, (Farrell, 2008; Groves, 2013)

$$\boldsymbol{K}_d[k] = \boldsymbol{P}^-[k]\boldsymbol{C}^\intercal[k]\left(\boldsymbol{C}[k]\boldsymbol{P}^-[k]\boldsymbol{C}^\intercal[k] + \boldsymbol{R}[k]\right)^{-1}, \tag{3.48}$$

and the updated estimate could be obtained as

$$\hat{\boldsymbol{x}}^+[k] = \boldsymbol{x}^-[k] + \boldsymbol{K}_d[k]\left(\boldsymbol{y}[k] - \boldsymbol{C}[k]\boldsymbol{x}^-[k]\right), \tag{3.49}$$

$$\boldsymbol{P}^+[k] = (\boldsymbol{I}_{9+l} - \boldsymbol{K}_d[k]\boldsymbol{C}[k])\boldsymbol{P}^-[k]. \tag{3.50}$$

If measurements with indices in the set $\mathcal{I}_k$ are available at time index k, they can be proceed sequentially as follows, Farrell (2008); Groves (2013). First, use the propagated estimate and covariance,

$$\hat{\boldsymbol{x}}^+[k] \leftarrow \boldsymbol{x}^-[k],$$
$$\boldsymbol{P}^+[k] \leftarrow \boldsymbol{P}^-[k],$$

as the starting point for the update loop. Then, for each $i \in \mathcal{I}_k$, where $\mathcal{I}_k$ is set of aiding measurements available at time $t = kT_s$ in time, loop through the updates

$$\boldsymbol{K}_{d,i}[k] \leftarrow \boldsymbol{P}^+[k]\boldsymbol{C}_i^\intercal[k]/(\boldsymbol{C}_i[k]\boldsymbol{P}[k]\boldsymbol{C}_i[k]^\intercal + \boldsymbol{R}_{ii}[k]),$$
$$\hat{\boldsymbol{x}}^+[k] \leftarrow \hat{\boldsymbol{x}}^+[k] + \boldsymbol{K}_{d,i}[k]\left(\boldsymbol{y}_i[k] - \boldsymbol{C}_i[k]\hat{\boldsymbol{x}}^+[k]\right),$$
$$\boldsymbol{P}^+[k] \leftarrow (\boldsymbol{I}_{9+m} - \boldsymbol{K}_{d,i}[k]\boldsymbol{C}_i[k])\boldsymbol{P}^+[k],$$

where $\boldsymbol{C}_i$ is the i^{th} row of the matrix $\boldsymbol{C}$, and $\boldsymbol{R}_{ii}$ is the i^{th} diagonal element of the matrix $\boldsymbol{R}$. As a result, such implementation yields a corrector-predictor effect where the measurement update is bypassed for all $i \notin \mathcal{I}_k$ corresponding to $\boldsymbol{K}_{d,i}[k] = 0$. A practical consequence is that the elements of the covariance $\boldsymbol{P}[k]$ associated with $i \notin \mathcal{I}_k$, at a given point in time k, increase due to the positive definite process noise covariance matrix $\boldsymbol{Q}_d[k]$ in the time update. Furthermore, for low-frequency measurement updates, the resulting effect is that these are emphasized more at each measurement correction, when available, than high rate measurements. In comparison, the corrector-predictor algorithm of Fossen (2011, Ch. 11.3.4), for fixed-gain observers, is realized with an explicit time-scale separation where the gain associated with the low-rate measurement i is multiplied with the rate ratio, of the observer relative the aiding sensor, similar to that done in the presentation of the attitude observer discretization.

If the assumptions of a constant rotation matrix and constant specific forces between the IMU samples are not deemed to be sufficiently accurate, for a given sampling time, T_s, a more elaborate specific force transformation from $\{b\}$ to $\{e\}$ can be carried out (Groves, 2013, Ch. 5.1.2), in addition to the improved attitude mechanization mentioned in Section 3.2.2. Also here, the IMU output configuration can be considered. By using an incremental velocity configuration, the average specific force, which the IMU is exposed to between sample $k-1$ and k, is provided based on the maximum internal IMU sampling frequency. This reduces the probability of acceleration errors, and thereby velocity errors, due to e.g. sculling (Groves, 2013, Ch. 5.5.4) when the IMU is exposed to vibrations.

3.3.7 Time delay

If the measurements, typically GNSS and/or magnetometer, Hansen et al. (2015), used in the NLO experiences a significant time delay, the resetting of the INS state may be a delayed state estimate at the time with index $k - j$ corresponding to the time of validity of the measurement delayed with j samples relative to current time. In this case the INS also contains a "fast-forward" function to rapidly compute the current state estimate based on intermediate IMU measurements. Efficient implementation methods are given in Khosravian et al. (2014, 2015) for such problems.

3.4 Tightly Coupled Translational Motion Observer

This section introduces the TMO for tightly coupled GNSS/INS integration in detail. The main difference between the loosely and tightly coupled integration is that the aiding sensor information from GNSS changes from the position domain to range domain.

An observer for tightly coupled GNSS/INS integration was presented by Johansen and Fossen (2015); Johansen et al. (2017) where an altered version of the TMO for the loosely coupled observer, (3.15)–(3.18), was introduced. In Johansen and Fossen (2015); Johansen et al. (2017), the TMO was integrated with the same attitude observer as presented earlier and in applied to estimate position, velocity and acceleration in the ECEF frame.

Tightly coupled integration utilize the raw GNSS observables, range and range-rate (Doppler) measurements, to alter the TMO injection terms from the position domain to the range domain. The range measurements y_i can either be pseudoranges, obtained with C/A or other code-phase techniques, or with carrier-phase based ranges, where the subscript i indicate measurements from the i^{th} satellite. The range-rate measurement is the Doppler frequency v_i here measured in meters per second.

The range and range-rate measurements are subject to disturbances and errors represented by, for instance, the clock range error β between the atomic satellite clocks and the less accurate receiver clock. Even a small error in timing can have a large impact as it is multiplied with the speed of light. It is therefore vital that β is estimated in the observer. More on error sources and GNSS/GPS is found in Grewal et al. (2013, Ch. 7). Other disturbances on the satellite measurements include ionospheric and tropospheric disturbances which delay the signals due to obstructions in the signal path. Such disturbances can be opposed by a dual frequency receiver where an ionospheric-free linear combination can be formed using two measurements based on different frequencies. One examples is a combination using measurements derived using the GPS L1 and L2 frequency bands. The drawbacks of this approach is the higher cost of receiver and antenna and

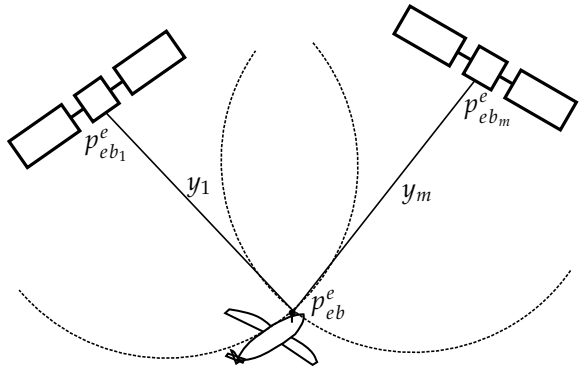

Figure 3.12: Concept illustration of the ranging done in GNSS-based navigation. The receiver position is denoted $\boldsymbol{p}^e_{eb}$, while the satellite positions are denoted $\boldsymbol{p}^e_{eb_i}$, where $i \in [1, \ldots, m]$. The position of the GNSS receiver may be located anywhere along the circles with radius y_i and origin $\boldsymbol{p}^e_{eb_i}$. Because of this, the (pseudo)range y_i relate to the position of the receiver nonlinearly. The figure is a simplification. With pseudorange $y_i = \varrho_i + \beta$, where $\varrho_i = \|\boldsymbol{p}^e_{eb} - \boldsymbol{p}^e_{eb_i}\|_2$ is the geometric distance between the receiver and the i^{th} satellite and β being the receiver's clock error multiplied with the speed of light, the nonlinearities become hyperbolic for $\beta > 0$, not circular as indicated.

the amplification of the noise in the linear combination due to amplification of multipath and receiver noise. Another approach is to utilize a dual receiver configuration where the satellite measurements are differenced with measurements at a known location close by, thereby cancelling the delays. In Hansen et al. (2016) observers using single- and double-differenced measurements are proposed using an observer structure similar to the one presented here.

Assuming measurements from at least four satellites ($m \geq 4$) are available, the TMO takes the form of

$$\dot{\hat{\boldsymbol{p}}}^e_{eb} = \hat{\boldsymbol{v}}^e_{eb} + \sum_{i=1}^{m} \left(\boldsymbol{K}_i^{pp} e_{y,i} + \boldsymbol{K}_i^{pv} e_{v,i} \right), \tag{3.51}$$

$$\dot{\hat{\boldsymbol{v}}}^e_{eb} = -2\boldsymbol{S}(\boldsymbol{\omega}^e_{ie})\hat{\boldsymbol{v}}^e_{eb} + \hat{\boldsymbol{f}}^e_{ib} + \boldsymbol{g}^e_b(\hat{\boldsymbol{p}}^e_{eb}) + \sum_{i=1}^{m} \left(\boldsymbol{K}_i^{vp} \boldsymbol{e}_{y,i} + \boldsymbol{K}_i^{vv} \boldsymbol{e}_{v,i} \right), \tag{3.52}$$

$$\dot{\hat{\boldsymbol{\xi}}}^e_{ib} = -\boldsymbol{R}(\hat{\boldsymbol{q}}^e_b)\boldsymbol{S}(\hat{\boldsymbol{o}}^b_{ib})\boldsymbol{f}^b_{\text{IMU}} + \sum_{i=1}^{m} \left(\boldsymbol{K}_i^{\xi p} e_{y,i} + \boldsymbol{K}_i^{\xi v} e_{v,i} \right), \tag{3.53}$$

$$\hat{\boldsymbol{f}}^e_{ib} = \boldsymbol{R}(\hat{\boldsymbol{q}}^e_b)\boldsymbol{f}^b_{\text{IMU}} + \boldsymbol{\xi}^e_{ib}, \tag{3.54}$$

$$\dot{\hat{\beta}} = \sum_{i=1}^{m} \left(K_i^{\beta p} e_{y,i} + K_i^{\beta v} e_{v,i} \right). \tag{3.55}$$

The observer structure of (3.51)–(3.55) is similar to the loosely coupled equivalent

(3.15)–(3.18), however it has different injection terms and it includes estimation of the clock error parameter β accounting for synchronization errors between the satellites' and receiver clocks. The clock bias error is the reason why at least four, and not three, satellites are required to calculate the three position coordinates from the pseudoranges. The error is expressed as a time-varying range: $\beta := c\Delta_c$, where c is the speed of light and Δ_c is the clock error. However, due to the injection signals $e_{y,i}$ $e_{v,i}$ some colored noise is going to be embedded in β over time. As indicated by (3.55), β is assumed constant in the deterministic observer design; $\dot{\beta} = 0$. Incorporating this with a minimum variance optimization criterion, similar to (3.32)–(3.33), this model might be considered as a Wiener process, $\dot{\beta} = n_c$, in the tuning process, where n_c is considered to be Gaussian white noise with variance σ_c^2 representing the drift rate of the receiver's clock. Hence, the time-varying dynamics of β is captured by the TMO through the injection terms obtained using the raw GNSS observables.

The injection terms of the observer, based on pseudorange and range-rate measurements, are driven by the errors $e_{y_i} := y_i - \hat{y}_i$ and $e_{v,i} := \nu_i - \hat{\nu}_i$, with the estimated measurements

$$\hat{y}_i = \hat{\varrho}_i + \hat{\beta}, \tag{3.56}$$

$$\hat{\nu}_i = \left(\frac{\hat{\boldsymbol{p}}^e_{eb} - \boldsymbol{p}^e_{eb_i}}{\hat{\varrho}_i} \right)^{\mathsf{T}} \left(\hat{\boldsymbol{v}}^e_{eb} - \boldsymbol{v}^e_{eb_i} \right), \tag{3.57}$$

where the position and velocity of the i^{th} satellite are denoted $\boldsymbol{p}^e_{eb_i}$ and $\boldsymbol{v}^e_{eb_i}$. The estimated geometric distance between satellite and receiver is given as $\hat{\varrho}_i = \|\hat{\boldsymbol{p}}^e_{eb} - \boldsymbol{p}^e_{eb_i}\|_2$. The estimation errors are defined as $\tilde{\boldsymbol{p}}^e_{eb} := \boldsymbol{p}^e_{eb} - \hat{\boldsymbol{p}}^e_{eb}$, $\tilde{\boldsymbol{v}}^e_{eb} := \boldsymbol{v}^e_{eb} - \hat{\boldsymbol{v}}^e_{eb}$, and $\tilde{\beta} := \beta - \hat{\beta}$. When estimating the satellite measurements and geometric distance, the position and velocity of the satellites are assumed known. This assumption is satisfied by using the updated broadcasted ephemeris data to determine the positions and the velocities of the satellites in view.

Similar to (3.31) the observer (3.51)–(3.55) can be written

$$\dot{\hat{\boldsymbol{x}}} = \boldsymbol{A}\hat{\boldsymbol{x}} + \boldsymbol{B}(t, \hat{\boldsymbol{q}}^e_b)\boldsymbol{u} + \boldsymbol{D}(t, \hat{\boldsymbol{x}}) + \boldsymbol{K}(\boldsymbol{y} - \boldsymbol{h}(\hat{\boldsymbol{x}})), \tag{3.58}$$

however with a nonlinear observation vector $\boldsymbol{h}(\hat{\boldsymbol{x}})$, and the matrices and vector,

$$\boldsymbol{A} = \text{blockdiag}(\boldsymbol{A}^*, 0), \quad \boldsymbol{B}(t, \hat{\boldsymbol{q}}^e_b) = \begin{pmatrix} \boldsymbol{B}^*(t, \hat{\boldsymbol{q}}^e_b) \\ \boldsymbol{0}_{1\times 3} \end{pmatrix}, \quad \boldsymbol{D}(t, \hat{\boldsymbol{x}}) = \begin{pmatrix} \boldsymbol{0}_{3\times 1} \\ \boldsymbol{g}^e_b(\hat{\boldsymbol{p}}^e_{eb}) - 2\boldsymbol{S}(\boldsymbol{\omega}^e_{ie})\hat{\boldsymbol{v}}^e_{eb} \\ \boldsymbol{0}_{3\times 1} \\ 0 \end{pmatrix},$$

and where the linearized matrix,

$$\boldsymbol{C}(t, \hat{\boldsymbol{x}}) = \left. \frac{\delta \boldsymbol{h}}{\delta \boldsymbol{x}} \right|_{\boldsymbol{x}=\hat{\boldsymbol{x}}}, \tag{3.59}$$

takes the form of

$$\boldsymbol{C}(t,\hat{\boldsymbol{x}}) = \begin{pmatrix} \frac{\left(\hat{\boldsymbol{p}}^e_{eb} - \boldsymbol{p}^e_{eb_1}\right)^\intercal}{\hat{\varrho}_1} & \boldsymbol{0}_{1\times 3} & \boldsymbol{0}_{1\times 3} & 1 \\ \vdots & \vdots & \vdots & \vdots \\ \frac{\left(\hat{\boldsymbol{p}}^e_{eb} - \boldsymbol{p}^e_{eb_m}\right)^\intercal}{\hat{\varrho}_m} & \boldsymbol{0}_{1\times 3} & \boldsymbol{0}_{1\times 3} & 1 \\ \frac{\left(\hat{\boldsymbol{v}}^e_{eb} - \boldsymbol{v}^e_{eb_1}\right)^\intercal}{\hat{\varrho}_1} & \frac{\left(\hat{\boldsymbol{p}}^e_{eb} - \boldsymbol{p}^e_1\right)^\intercal}{\hat{\varrho}_1} & \boldsymbol{0}_{1\times 3} & 0 \\ \vdots & \vdots & \vdots & \vdots \\ \frac{\left(\hat{\boldsymbol{v}}^e_{eb} - \boldsymbol{v}^e_{eb_m}\right)^\intercal}{\hat{\varrho}_m} & \frac{\left(\hat{\boldsymbol{p}}^e_{eb} - \boldsymbol{p}^e_{eb_m}\right)^\intercal}{\hat{\varrho}_m} & \boldsymbol{0}_{1\times 3} & 0 \end{pmatrix}, \tag{3.60}$$

when using GNSS pseudorange and range-rate measurements. The time-varying $\boldsymbol{C}$-matrix consists of estimated line-of-slight (LOS) vectors describing the direction from rover to each satellite. As the distance between rover and satellites is large compare to the relative velocity, the LOS vectors are slowly time-varying. As illustrated in Figure 3.12 the pseudoranges relate to the position $\boldsymbol{p}^e_{eb}$ nonlinearly. Hence, the linerization (3.59) is necessary to obtain $\boldsymbol{C}(t,\hat{\boldsymbol{x}})$. If the $\boldsymbol{C}$-matrix is applied to the augmented version of (3.23) with $\boldsymbol{A}$ and $\boldsymbol{B}$ to obtain $\boldsymbol{P}(t)$, the compound observer gain for (3.51)–(3.55) can be calculated as

$$\boldsymbol{K} = \vartheta \boldsymbol{L}_\vartheta^{-1} \boldsymbol{K}^0 \boldsymbol{E}_\vartheta, \tag{3.61}$$

with

$$\boldsymbol{K}^0 = \boldsymbol{P}\boldsymbol{C}^\intercal \boldsymbol{R}^{-1}, \tag{3.62}$$

where $\boldsymbol{P} = \boldsymbol{P}^\intercal > 0$ is the solution of (3.33) and

$$\boldsymbol{L}_\vartheta = \text{blockdiag}\left(\boldsymbol{I}_3, \frac{1}{\vartheta}\boldsymbol{I}_3, \frac{1}{\vartheta^2}\boldsymbol{I}_3, \frac{1}{\vartheta^4}\right), \tag{3.63}$$

$$\boldsymbol{E}_\vartheta = \boldsymbol{C}\boldsymbol{L}_\vartheta \boldsymbol{C}^\dagger, \tag{3.64}$$

where (3.64) is valid according to Johansen and Fossen (2015, Lemma 4). The conditions for (3.51)–(3.64) are satisfied when four or more pseudoranges are available (except in degenerate configurations), thereby ensuring observability of the system (Johansen and Fossen, 2015). Also here, the variations in $\boldsymbol{g}^e_b(\hat{\boldsymbol{p}}^e_{eb})$, induced by position changes, are assumed to not affect the observability. In contrast to the loosely coupled GNSS/INS integration, the origin of the error dynamics of the feedback interconnection of (3.51)–(3.55) with the attitude observer, is only ULES, with respect to position and velocity initialization errors, since the $\boldsymbol{C}$-matrix is based on linearization of the pseudorange and Doppler measurement equations about the estimated position and velocity. Accurate initialization procedures are easily applied (Johansen and Fossen, 2015) so this is not a significant problem in practice.

To accommodate colored noise, when applying tightly coupled integration, the $\boldsymbol{R}$-matrix can be increased in an ad hoc manner. An example using such strategy, is designing a tuning rule based on the elevation angle of each satellite in view (Groves, 2013, Ch. 9.4.2.4). By doing this, it is possible to weight pseudoranges from low elevation satellites less than measurements from high elevation satellites (with high elevation satellites, the GNSS signal travels through less atmosphere compared to the signals from the low elevation satellites and therefore has less errors).

3.4.1 Augmented TMO for tightly coupled integration including clock error model

Above, the clock error was modeled in range space as $\beta = c \cdot \Delta_c$ with Δ_c being the clock error. This can be extended further by considering that Δ_c is dependent on the clock frequency error, such that β is no longer considered as a constant, but expressed with a state-space model with a constant clock frequency error f_{clock} such that $\ddot{\beta} = 0$, (Farrell (2008, Ch. 8.4.3.2), Groves (2013, Ch 9.4.2.3)):

$$\begin{pmatrix} \dot{\beta} \\ \dot{f}_{\text{clock}} \end{pmatrix} = \begin{pmatrix} 0 & 1 \\ 0 & 0 \end{pmatrix} \begin{pmatrix} \beta \\ f_{\text{clock}} \end{pmatrix} + \begin{bmatrix} 0 \\ n_f \end{bmatrix}, \tag{3.65}$$

where n_f is the driving process noise assumed to be white. By introducing the additional clock error state, (3.55) in the TMO is replaced by

$$\dot{\hat{\beta}} = \hat{f}_{\text{clock}} + \sum_{i=1}^{m} \left(K_i^{\beta p} e_{y,i} + K_i^{\beta v} e_{v,i} \right), \tag{3.66}$$

$$\dot{\hat{f}}_{\text{clock}} = \sum_{i=1}^{m} \left(K_i^{fp} e_{y,i} + K_i^{fv} e_{v,i} \right). \tag{3.67}$$

By doing this, (3.58) is augmented accordingly. With this augmentation, the $\boldsymbol{C}(t, \hat{\boldsymbol{x}})$-matrix of (3.60), in (3.23), is replaced with $\boldsymbol{C}_{\text{aug}}$, given as

$$\boldsymbol{C}_{\text{aug}}(t, \hat{\boldsymbol{x}}) = \begin{pmatrix} \boldsymbol{C}(t, \hat{\boldsymbol{x}}) & \boldsymbol{C}_{\text{f}} \end{pmatrix}, \tag{3.68}$$

where $\boldsymbol{C}_{\text{f}} = (\boldsymbol{0}_{m\times 1}; \boldsymbol{1}_{m\times 1})$. The standard deviation of the white noise n_f ought to be chosen small (less than 0.02 m/s as proposed in Farrell (2008, Ch. 8.4.3.2)). However, by modeling of the clock bias as (3.65), compared to $\dot{\beta} = 0$ as done in Johansen and Fossen (2015), only minor effects (centimeter level) on the estimation of β were observed. Therefore major effects on the position and velocity estimates cannot be expected with this augmentation. Also with this clock error model, it is necessary to take into account that noncompensated common residuals of the time-varying errors due to signal delays, in the ionosphere and troposphere or stemming from multipath, may be embedded in β and f_{clock} since these are the only nuisance parameters related to the GNSS in this TMO.

3.5 Experimental Validation

3.5.1 Validation platform

The experimental validation was carried out using a Penguin B fixed-wing UAV as shown in Figure 3.13. Its technical specifications are presented in Table 3.1. Figure 3.14 presents the flight path of a UAV test flight, conducted from Eggemoen,

Figure 3.13: Penguin B UAV in flight. Photo: Jakob M. Hansen.

Table 3.1: Penguin B UAV Technical Specifications.

Engine type:	Gasoline
Wingspan:	3.3 m
Length:	2.27 m
MTOW:	21.5 kg
Endurance:	5+ hours
Cruise speed:	28 m/s
Max level speed:	36 m/s

Norway.

In the setup used for validation the UAV is equipped with an ADIS16488 IMU measuring specific force, rotation rate and magnetic field of the vehicle, configured for 410 Hz output. Additionally a u-Blox LEA-6T GNSS receiver supplies computed position as well as pseudoranges at 5 Hz. The sensors are synchronized using a microcontroller in order to accurately timestamp the measurements. Engine induced vibrations are significant and can typically be seen as a signal of magnitude close to 1 m/s^2 at 70 Hz on the accelerometer measurements.

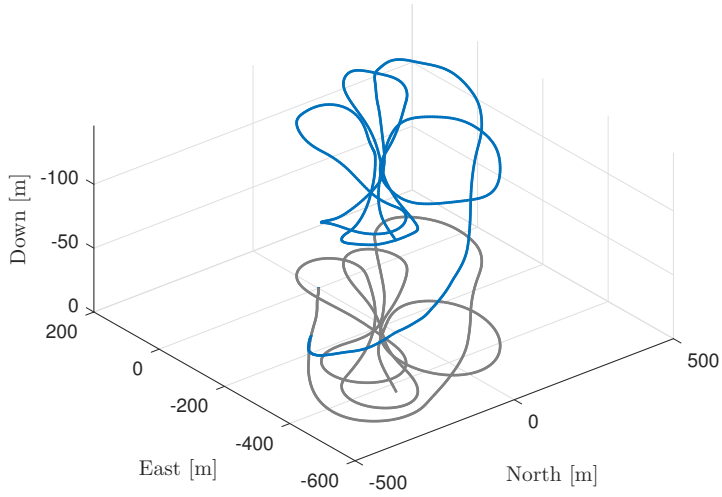

Figure 3.14: Flight path. The flight path using a Penguin B UAV is shown. Takeoff of the UAV is used as the origin. The flight path is shown in blue, while the ground track is shown in gray.

3.5.2 Experimental results

This section presents a comparison of the performance of the discussed observer structures using experimental data collected during the UAV mission presented in Section 3.5.1. The dataset used here has a length of approximately 22 minutes with a flight part consisting of multiple circles and figures-of-eight over an area of one square kilometer.

During the flight, a stationary GNSS receiver of the same type was placed at a known location to serve as base station for a real time kinematic (RTK) positioning solution. The RTK position was computed by the open source software package RTKLIB (2013), where the position is obtained using carrier-phase positioning, with a fixed or float integer ambiguity solution, indicating decimeter accuracy, Groves (2013). The RTK position is used as reference when comparing the performance of the loosely and the tightly coupled observer structures. The base station also logged the transmitted satellite ephemeris data, used to calculate the satellites' positions and velocities. RTK is a type of differential GNSS (dGNSS). For details, Grewal et al. (2013, Ch. 8) can be advised.

The loosely and tightly coupled observer structures are compared. Since no velocity measurements were available, the state-space augmentation, introduced above, in order to estimate colored GNSS noise, with loosely integration, was discarded due to the results presented in Section 3.3.5. To guarantee a fair comparison, the standalone GNSS position solution used in the loosely coupled integration is based on the tightly coupled observer using solely the pseudoranges as observ-

Table 3.2: Navigation performance comparison.

	RMS error (x,y,z) [m]			Std (x,y,z) [m]		
Tightly coupled	3.412	3.341	1.106	1.067	0.561	1.005
No IMU	4.541	3.732	2.184	2.951	1.756	2.065
Loosely coupled	4.442	3.818	2.264	2.836	1.868	2.177

ables. Hence, no IMU is used to generate this aiding position solution. Therefore, the tuning will also reflect this where (3.32) and (3.33) were modify accordingly such that

$$\boldsymbol{K}^0 = \boldsymbol{P}\boldsymbol{C}^\intercal \boldsymbol{R}_\star^{-1}, \tag{3.69}$$

$$\frac{1}{\vartheta}\dot{\boldsymbol{P}} = \boldsymbol{A}\boldsymbol{P} + \boldsymbol{P}\boldsymbol{A}^\intercal + \boldsymbol{Q}_\star - \boldsymbol{P}\boldsymbol{C}^\intercal \boldsymbol{R}_\star^{-1}\boldsymbol{C}\boldsymbol{P}, \tag{3.70}$$

was chosen to realize the gain $\boldsymbol{K}^0$ for all three observers with the tuning parameters $\boldsymbol{Q}_\star$ and $\boldsymbol{R}_\star$ matrices. For the loose integration, the matrices were chosen

$$\begin{aligned}\boldsymbol{Q}_l &= \text{blockdiag}(\boldsymbol{0}_{3\times3}, 10^{-10}\cdot\boldsymbol{I}_3, 2.5\cdot10^{-3}\cdot\boldsymbol{I}_3),\\ \boldsymbol{R}_l &= \text{blockdiag}(2.5\cdot\boldsymbol{I}_3).\end{aligned}$$

For the tightly coupled integration, the tuning matrices were chosen

$$\begin{aligned}\boldsymbol{Q}_t &= \text{blockdiag}(\boldsymbol{Q}_l, 1),\\ \boldsymbol{R}_t &= \text{blockdiag}(1\cdot\boldsymbol{I}_m).\end{aligned}$$

The observers used the same constant attitude estimator gains: $k_I = 0.004$, $k_1 = 0.25$, and $k_2 = 0.75$.

The comparison of the observers are seen in Figure 3.15, depicting the position estimation error. Figure 3.16 shows the estimated attitude, while Figure 3.17 displays the estimated gyro bias. The position estimation was evaluated in terms of RMS error and standard deviation (Std) relative to the RTK solution and summarized in Table 3.2.

As presented above, tuning of the $\boldsymbol{Q}_\star$ matrix associated with the velocity state is based on statistics describing the accelerometer's noise characteristics. These can either be based on the data collected or from a data sheet. For a standalone GNSS solution (IMU not used), tuning of the $\boldsymbol{Q}_\star$ matrix reduces to an ad hoc procedure based on the assumed host-vehicle dynamics. Groves (2013, Ch. 9.4) recommends $1^2\,\text{m/s}^2$, $10^2\,\text{m/s}^2$ and $100^2\,\text{m/s}^2$ for pedestrian, automotive and military aircraft, respectively associated with the velocity state. As seen in Figure 3.15, the tightly coupled GNSS/INS integration strategy provides the position estimates with smallest variation and also the smallest deviation from the

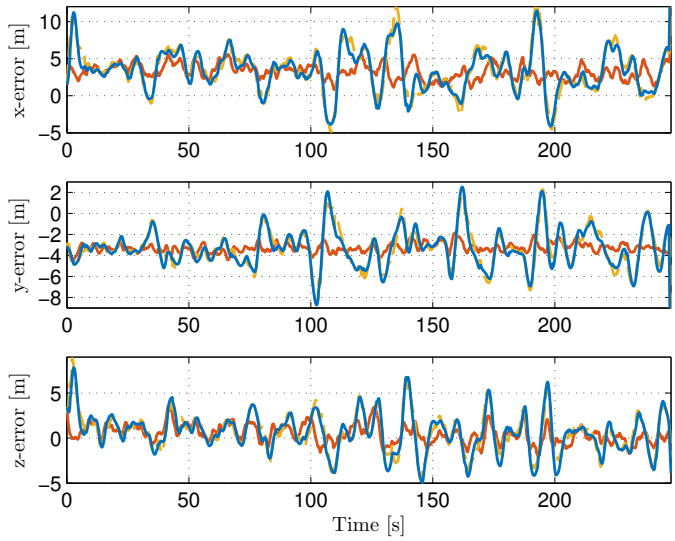

Figure 3.15: Position estimation error. The results are presented in the ECEF frame relative the RTK positioning solution. The result obtained using loosely coupled integration is shown in blue, the result obtained using tightly coupled integration is shown in red, while the standalone GNSS solution is presented in yellow. These results indicate that tightly coupled integration of inertial and GNSS measurements yield more accurate position estimation compared to loosely coupled integration and standalone GNSS when applying a satellite-based navigation system based on the standard GNSS positioning service.

RTK positioning solution. This statement is backed up by Table 3.2. The difference between the standalone GNSS solution and the loosely coupled integration seems less evident from Figure 3.15 and Table 3.2. This is however expected, taking into account the simulation results in Section 3.3.5 related to the loosely coupled GNSS/INS integration and the estimation of colored GNSS noise presented earlier. The benefit of loosely coupled integration, relative not using an IMU at all, is however evident in Figure 3.18. The loosely coupled solution provides a smoother estimate than the standalone GNSS solution and is hence more suitable to be used in conjunction with autopilots that operate at high sampling rates. The INS also provides fault tolerance when GNSS fails or is degraded. Moreover, one large benefit of loosely coupled GNSS/INS, relative to a standalone GNSS solution, is that the attitude estimates also are obtained with high accuracy.

As mentioned, the most accurate and precise position estimates relative to the RTK solution are obtained with the tightly coupled integration strategy. Since the pseudoranges are directly fused with the inertial measurements, instead of calculating the GNSS position before using this as aiding in loosely coupled integration, more of the colored noise, embedded in the GNSS pseudoranges, is captured by

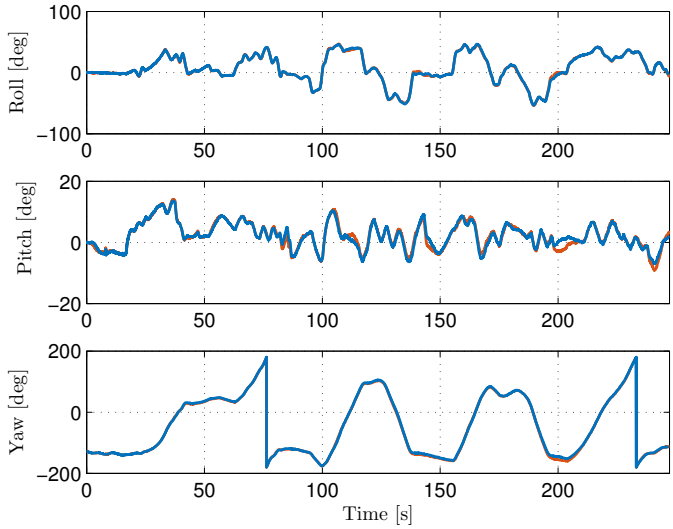

Figure 3.16: Attitude estimates. The results are presented using Euler angles as attitude representation. The estimate obtained using loosely coupled integration is shown in blue, while the estimate obtained using tightly coupled integration is shown in red. The standalone GNSS navigation solution did not provide attitude estimates.

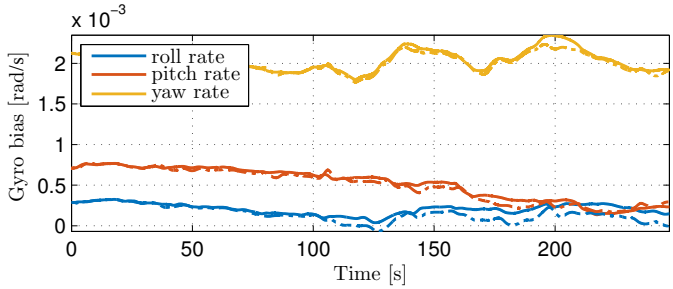

Figure 3.17: Gyro bias estimates. The result obtained using loosely coupled integration is shown with dotted lines, while the result obtained using tightly coupled integration is shown with solid lines.

the receiver's clock bias estimate. This is possible since the specific force measurements and attitude estimates are available between GNSS samples. Hence, every new position and clock error calculation, made by the observer, is based on the current predicted position between GNSS samples using inertial data rather than using a 0.2 to 1 second old estimate obtained at the previous GNSS update. This point however, is mainly relevant for low-cost GNSS receivers, as higher grade receivers can output raw data at frequencies of 20 Hz or more. A contributing factor

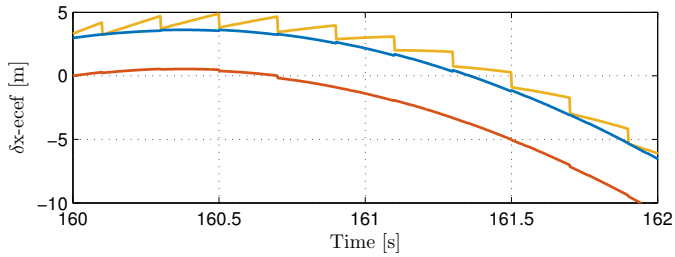

Figure 3.18: Normalized position error. The results are related to the RTK positioning solution between 160 and 162 seconds of flight. The error relative the RTK solution applying the loosely coupled integration is shown in blue and the error relative the RTK solution applying the tightly coupled integration is shown in red, while the error relative RTK using pure GNSS positioning is shown in yellow. The error relative RTK is smallest applying tightly coupled integration. The error using loosely coupled integration and pure GNSS is of similar magnitude, however, the integrated solution is smoother than pure GNSS since inertial data is available between GNSS samples.

to the performance differences of the two integration schemes may also be due to the 5 Hz GNSS update. By sampling the GNSS that fast, more of the pseudorange measurements can become correlated in time compared to using 1 Hz position calculation. If differential GNSS is utilized, more accurate position estimates can be obtained for both integration schemes.

The attitude estimates obtained with both loosely and tightly coupled integration are mostly similar except from a few significant differences. These differences are most likely due to the attitude estimate $\hat{\boldsymbol{q}}_b^e$ has two components, the unit quaternion from BODY to NED, $\boldsymbol{q}_b^n$, and the unit quaternion from NED to ECEF, $\boldsymbol{q}_n^e$, and how the GNSS information enters the TMOs. The latter quaternion $\boldsymbol{q}_n^e$ is in principle a horizontal position estimate containing information of the craft's latitude and longitude. Therefore, the attitude estimates from the two integration strategies may differ as a result of the difference in how the position information enters the TMO due to the feedback interconnection with the attitude observer and the TMO through the auxiliary state $\boldsymbol{\xi}_{ib}^e$. This again will also affect the gyro bias estimation, seen in Figure 3.17, and therefore explaining that the estimates obtained using tightly coupled GNSS/INS integration resulted in more steady estimates compared to applying loosely coupled integration.

3.6 Conclusions

Accurate and precise position, velocity and attitude estimates are needed in numerous areas such as the automotive, robotics, marine and aircraft applications. The need for computationally efficient and robust algorithms achieving this is

growing due to a wide-spread interest in unmanned platforms, such as UAVs, with potential limited computational power available. This need can be met by applying nonlinear feedback-interconnected observers for integrated GNSS/INS navigation with known stability properties.

The experimentally verified simulation results, using data collected during an unmanned aerial vehicle flight, show that the estimation of translational motion benefits from a minimum-variance-like implementation applying the Riccati equation. Using such an implementation strategy, compared to a fixed-gain strategy, accelerates the observers convergence. This is also reflected in the attitude estimates due to the feedback-interconnection relating the two observers.

The attitude estimates are obtained with an exponentially stable and computationally efficient observer based on complementary filtering and vector measurements. In contrast to the Kalman filter, this is not a stochastic method, but based on the desired observer bandwidth and nonlinear stability theory.

The results presented here indicate that tightly coupled GNSS/INS integration outperforms loosely coupled integration when considering position accuracy. By fusing the pseudorange measurements directly with the inertial data, more of the colored noise embedded in the pseudoranges is captured by the receiver's clock error estimate, compared to that achieved with the augmented loosely coupled integration scheme posed. Compensation of the colored GNSS noise proved to be difficult even though the TMO including the GNSS error state was observable when using loosely coupled integration. A case study indicated that this was because of the TMO's bandwidth resulting in the GNSS error to influence the position estimate if not a highly precise and accurate velocity measurement is available. Such design, more so than the tightly coupled design, is also highly dependent of tuning of the GNSS error parameters.

The attitude estimates obtained with both loosely and tightly coupled integration are mostly similar. Differences are possibly due to the different amount of colored noise being fed from the respective TMO to the attitude observer.

Accuracy of the loosely and tightly coupled integration schemes can be increased by applying pseudorange corrections using differential GNSS, carrier-phase smoothed pseudoranges or dual-frequency solutions canceling the ionospheric delay. The improvements in accuracy with the latter strategy is, however, at the expense of increased noise.

4 *The Virtual Vertical Reference Principle – Vertical Aiding of INSs for Marine Surface Vessels*

This chapter is mainly based on Bryne et al. (2014, 2015b, n.d.), presenting the main results of the thesis, covering INSs, aided using the VVR principle. The VVR concept also serves as key component and foundation of most of the results presented in the following chapters of the thesis.

Here two feedback–interconnected NLOs providing 6-DOF PVA motion estimates, tailored for marine surface craft, are presented. The two observers, Bryne et al. (2014, 2015b) and Bryne et al. (n.d.), are inspired by NLOs for loosely coupled GNSS/INS integration, providing 6-DOF PVA motion estimates, such as Grip et al. (2013, 2015) and custom heave estimators, bridging the two concepts. Both observers are extensions of (Grip et al., 2013), based on the initial work of Grip et al. (2012b), merged with the work done by Mahony et al. (2008) and Grip et al. (2012a). The second observer (Bryne et al., n.d.) is an extension of the former (Bryne et al., 2014, 2015b) accompanied with improved heave estimation performance. Furthermore, the origin of the error dynamics of both observers were proven USGES. In addition, both NLOs are evaluated through simulations and validated experimentally using data gathered at sea. For more details on the observer validation and data collection, see Appendix E.

4.1 Motivation

From Chapter 1 we know that marine vessels are equipped with motion sensing capabilities in order to provide the crew and onboard systems with PVA data. Examples include PVA estimates being utilized by the DP system when controlling the vessel's motion, the crew monitoring the PVA data, PVA estimates used for motion compensation of oceanographic research data such as bathymetric mapping, leverarm compensation of PosRef measurements, motion compensation of the pose of onboard antennas and active heave compensation of cranes.

Roll, pitch and heave data of marine vessels are often provided by VRUs. Such solutions have established themselves as black boxes where the outputted signals are considered as measurements by users in the maritime industry. Moreover, academia have in large extent not focused on similar solutions. However, there are some published results on verification and comparison of industrial products such as Ingram et al. (1996) and Vik and Marçal (2003).

Related to a VRU solution, the attitude information of a ship can be obtained using different type of estimators or observers using IMU measurements, based on

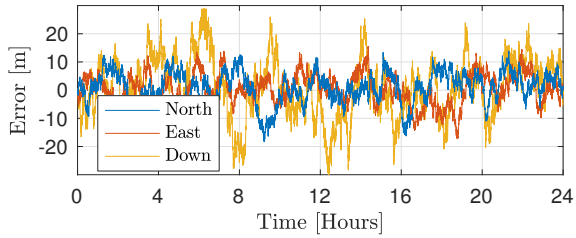

(a) Standard GNSS

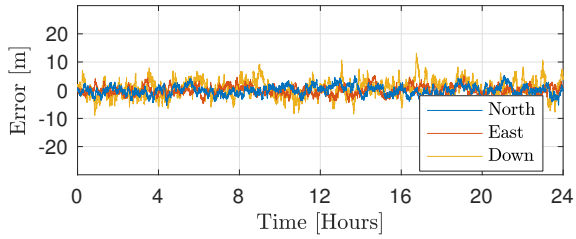

(b) Differential corrected GNSS

Figure 4.1: Example of typical GNSS errors. The vertical measurements are typically 1.5-2 times less precise than the horizontal components.

both linear and nonlinear theory. Roll and pitch estimates can be obtained using numerous results in the litterateur, such as Markley (2003); Hamel and Mahony (2006); Mahony et al. (2008); Martin and Salaün (2010); Küchler et al. (2011b); Grip et al. (2012a); Batista et al. (2012c,b,a); Hua et al. (2014); Zlotnik and Forbes (2016). None of these results are specific for marine vessels.

Heave estimation is more complicated and also specific for marine surface vessels which have resulted in less attention by the open research community. One reason for this might be due to the low precision of the vertical measurement component of PosRef systems such as GNSS, indicated in Figure 4.1. Therefore, sole usage of conventional GNSS aiding (or HPR for vessels in the vicinity of a site with deployed transponders) to estimate the heave motion is not optimal due to the low precision of the vertical position measurement compared to the horizontal counterparts. This is due to the geometry of the baselines of such systems. To circumvent this issue, custom heave estimators have been developed independent of external position aids. One example is Godhavn (1998), where an IMU was utilized together with a bandpass filter motivated by that the average heave position of a marine surface craft is zero. This technique was modified by Richter et al. (2014) to compensate for amplitude and phase errors by using additional adaptive filters. Another heave estimation strategy, based on the assumption that the heave motion could be described by a sum of cosines, while applying an accelerometer, was presented in Küchler et al. (2011a) and also applied in Auestad et al. (2013). With this strategy, however, the heave estimation performance will be reduced if

large roll and pitch motions are experienced. An alternative to custom heave estimators, with potentially higher accuracy, is RTK GNSS, as presented in Godhavn (2000). However, the coverage of RTK is limited at sea and the real-time availability is not necessarily guaranteed.

The works of Grip et al. (2013, 2015), in addition to provide estimates of roll, pitch and heave, also provide heading, linear velocity and position estimates using loosely coupled GNSS/INS integration. These results, however, require an aiding measurement of the vertical position component, which is, as indicated above, not optimal. Therefore a combination of the two concepts of custom heave estimators and NLOs, providing a complete INS solution estimating 6-DOF PVA, is beneficial. This was achieved by introducing the *virtual vertical reference (VVR)* principle.

4.2 The Vertical Vertical Reference Concept

The VVR concept (or principle) was introduced in Bryne et al. (2014, 2015b), and later extended in Bryne et al. (n.d.), as vertical aiding measurement to a full 6-DOF strapdown INS without any vertical GNSS measurements. The concept is based the average heave displacement of a marine surface craft is zero relative to the mean sea surface as illustrated in Figure 4.2. From this the VVR concept is defined as

$$y_{\text{VVR}} := \lim_{T\to\infty} \frac{1}{T} \int_0^T d_{\text{heave}}(t)\, \mathrm{d}t = 0, \tag{4.1}$$

where d_{heave} is the heave displacement of the vessel in relation to the mean sea surface. A similar definition is used in Godhavn (1998).

For marine surface vessels, the kinematics of (2.6)–(2.7), can further be extended with the auxiliary variable $p^t_{nb,I}$. The augmentation, first applied in Bryne et al. (2014), is motivated by (4.1). One may write

$$\lim_{T\to\infty} \frac{1}{T} \int_0^T p^n_{nb,z}(t)\mathrm{d}t = 0, \tag{4.2}$$

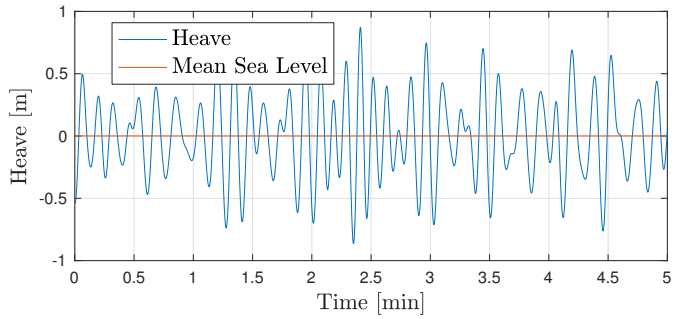

Figure 4.2: Example of the heave motion and the mean sea level.

when $\{n\}$ is used as navigation frame. Furthermore, based on (4.2), the strapdown equations of (2.6)–(2.7) are augmented with $p^n_{nb,I}$ by defining:

$$\dot{p}^n_{nb,I} := p^n_{nb,z}, \tag{4.3}$$

in order to integrate the vertical (down) position associated with the heave motion. Then a natural choice would be to exploit (4.1) and define a VVR measurement (Bryne et al., 2014, 2015b) by choosing

$$y^n_{VVR} = p^n_{nb,I} = 0, \quad \forall t \geq 0. \tag{4.4}$$

To the author's knowledge, at the time of writing, the works presented here is the first to propose the VVR aiding concept. Due to kinematic couplings, improvements of the attitude estimation performance is also excepted when utilizing the VVR instead of vertical measurements from traditional PosRef system, such as GNSS and HPR, as vertical INS aiding. Figure 4.3 illustrates the difference in how the vertical aiding from PosRefs and from the VVR is incorporated into the INS's vertical channel. Nominal vertical aiding using PosRefs is shown in Figure 4.3a, while its equivalent, using the VVR concept, is illustrated in Figure 4.3b.

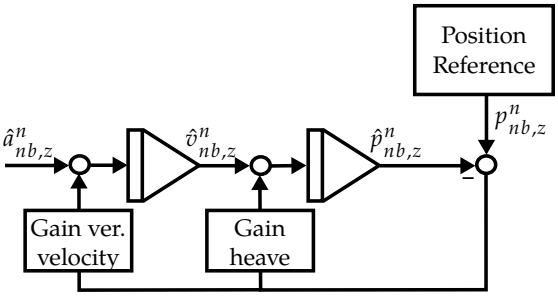

(a) Vertical aiding with nominal position references

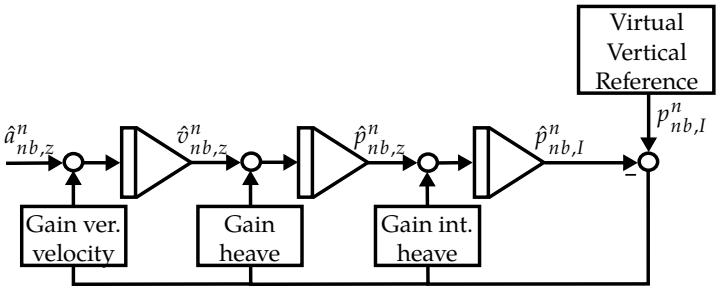

(b) Vertical aiding with the VVR concept

Figure 4.3: VVR illustration: Block diagram of the nominal aiding from a position reference system versus the VVR aiding concept. The z-subscript refers to the vertical z-axis of the translational motion.

It should be mentioned that the VVR zero-reading should not be considered as a perfect measurement even though it is free of noise. This is due to the fact that the integrated heave position is only zero on average. Hence, the VVR is not applicable as an equality constraint in constrained estimation frameworks, such as Simon (2009, Ch.7.5.), which is a common way to utilizing virtual measurements. An alternative to the VVR would be to use a zero heave measurement (Groves, 2013, Ch. 15.4).

By applying (4.2)–(4.4), the $\{n\}$-frame will not have constant altitude above the seabed due to, among other, tides, changes in draft due to load conditions and changes in sea state. In many application such effects must be compensated for. Examples include diving operations, subsea installations and bathymetric mapping. In such situations, inducing a combination of GNSS and HPR might be beneficial in order to compensate for vessel motions with especially slow dynamics (time constants in the range tens of minutes to hours).

4.3 Nonlinear Observer for INSs Aided by VVR

This work expands the work of Grip et al. (2013) with a modified problem formulation and sensor configuration; customizing the observer for surface vessels.

The overall stability of the interconnected observer, where the TMO had fixed gains, was proven to be USGES by Grip et al. (2013). The same stability properties were obtained for the observer structure presented below, while the TMO is extended by introducing time-varying gains. In addition, one of the attitude vector measurements are changed compared to the cited work. The two main contributions of this section can be summarized as:

- In general, the vertical GNSS measurement has relatively low precision. For operations at the (known) sea surface level, this measurement is replaced with a virtual measurement of the integrated height, (4.1)–(4.4), to achieve increased performance related to estimation of heave and vertical specific force.

- Expanding the work of Grip et al. (2013), related to the estimation of translation motion, by introducing time-varying gains[1]. During navigation at sea, such as in DP, time-varying gains are beneficial when GNSS quality changes due to e.g. changes in satellite constellation, obstruction of LOS to satellite(s) when approaching an offshore installation or during temporary loss for differential correction. Applying time-varying gains based on the PosRef's noise level can therefore prevent unnecessary measurement noise to propagate from the sensors to the state estimates, and further to the control system, when GNSS quality is reduced. Such gain strategy has the

[1]The presented algorithm is less general than the TMO of Section 3.3 from the preceding chapter. The TMO of this section was, however, developed earlier.

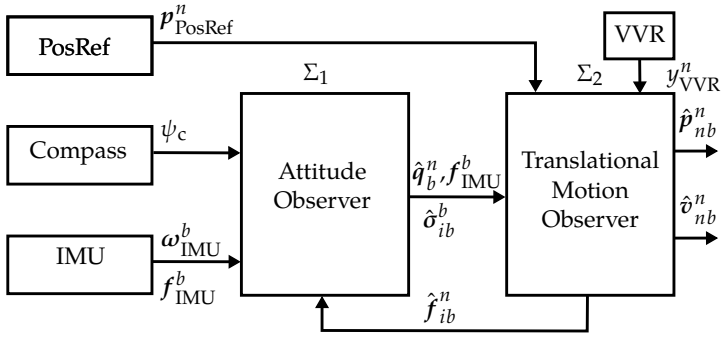

Figure 4.4: Feedback-interconnected observer structure. The attitude observer and TMO are denoted Σ_1 and Σ_2, respectively. Σ_1 provides an estimate of the unit quaternion, $\hat{\boldsymbol{q}}^n_b$, together with an estimate on the gyro bias, $\hat{\boldsymbol{b}}^b_{\text{gyro}}$. The signals $\hat{\boldsymbol{q}}^n_b$ and $\hat{\boldsymbol{\sigma}}^b_{ib}$ are utilized by Σ_2 to estimate the specific force, $\boldsymbol{f}^n_{ib}$. Moreover, $\hat{\boldsymbol{f}}^n_{ib}$ is fed back to Σ_1, and is utilized as a reference vector by the attitude observer.

potential to reduce fuel cost, emissions from engines and wear of mechanical equipment such as thrusters.

This NLO employs two reference frames. The NED and the BODY frames. For marine surface vessels, employing local navigation, NED can be assumed to be nonrotating and fixed to the average sea surface level.

Similar to Chapter 3, the NLO, for loosely coupled GNSS/VVR/INS integration, estimating PVA, is carried out in two steps as illustrated in Figure 4.4. In the first stage the attitude is estimated, represented by the unit quaternion $\boldsymbol{q}^n_b$, together with the gyro bias $\boldsymbol{b}^b_{\text{gyro}}$. The second stage provides estimates of specific force, linear velocity and the position decomposed in NED by exploiting the attitude estimate, $\hat{\boldsymbol{q}}^n_b$, and the injection term of the attitude observer, $\hat{\boldsymbol{\sigma}}^b_{ib}$. The result is based on the kinematic model formulation presented next.

4.3.1 Model formulation

For local navigation, the following dynamic kinematic model is considered

$$\dot{p}^n_{nb,I} = p^n_{nb,z}, \tag{4.5}$$

$$\dot{\boldsymbol{p}}^n_{nb} = \boldsymbol{v}^n_{nb}, \tag{4.6}$$

$$\dot{\boldsymbol{v}}^n_{nb} = \boldsymbol{f}^n_{ib} + \boldsymbol{g}^n_b, \tag{4.7}$$

$$\dot{\boldsymbol{q}}^n_b = \boldsymbol{q}^n_b \otimes \begin{pmatrix} 0 \\ \boldsymbol{\omega}^b_{ib} \end{pmatrix}, \tag{4.8}$$

$$\dot{\boldsymbol{b}}^b_{\text{gyro}} = \boldsymbol{0}_{3\times 1}, \tag{4.9}$$

being in compliance with Section 2.2.1 and (4.3)[2]. Moreover, $\boldsymbol{g}_b^n$, is assumed to be known. This is valid in DP since the operation is confined to a small geographical area on the sea surface.

The overall feedback-interconnected observer structure, illustrated in Figure 4.4, similar to Figure 3.1a, is described in Section 4.3.3–Section 4.3.4.

4.3.2 Sensor configuration

The result obtained in Bryne et al. (2014) was based on the following sensor configuration of IMU, GNSS, compass and VVR measurements:

1. Horizontal position measurement from GNSS given in NED: $\boldsymbol{p}_{\text{GNSS}}^n = (p_{nb,x}^n,\, p_{nb,y}^n)^\intercal$
2. VVR measurement: $y_{\text{VVR}}^n = p_{nb,I}^n = 0$, for all $t \geq 0$, motivated by Section 4.2.
3. Angular velocity measurements in BODY from a tri-axial rate gyro with bias: $\boldsymbol{\omega}_{\text{IMU}}^b = \boldsymbol{\omega}_{ib}^b + \boldsymbol{b}_{\text{gyro}}^b$. The bias components, $\boldsymbol{b}_{\text{gyro}}^b$, in (4.9) are assumed to be slowly time-varying. In an observer, (4.9) is deemed to be sufficient together with an injection term to compensate for the gyro bias.
4. Specific force measurements in BODY from a tri-axial accelerometer: $\boldsymbol{f}_{\text{IMU}}^b = \boldsymbol{f}_{ib}^b$. Accelerometer biases are assumed to be compensated at system startup or by online estimation, utilizing e.g. Grip et al. (2012a, Sec. VI), if the motion is persistently exciting.
5. Heading measurement from a compass: $\psi_c = \psi$.

4.3.3 Attitude observer using compass vector measurements

The attitude observer Σ_1, similar to Chapter 3, Section 3.2, based on the sensor configuration of Section 4.3.2, is given as Grip et al. (2013)

$$\Sigma_1 : \begin{cases} \dot{\hat{\boldsymbol{q}}}_b^n = \frac{1}{2}\hat{\boldsymbol{q}}_b^n \otimes \begin{pmatrix} 0 \\ \hat{\boldsymbol{\omega}}_{ib}^b \end{pmatrix}, & \text{(4.10a)} \\ \hat{\boldsymbol{\omega}}_{ib}^b = \boldsymbol{\omega}_{\text{IMU}}^b - \hat{\boldsymbol{b}}_{\text{gyro}}^b + \hat{\boldsymbol{\sigma}}_{ib}^b, & \text{(4.10b)} \\ \dot{\hat{\boldsymbol{b}}}_{\text{gyro}}^b = \text{Proj}\left(\hat{\boldsymbol{b}}_{\text{gyro}}^b, -k_I(t)\hat{\boldsymbol{\sigma}}_{ib}^b\right), & \text{(4.10c)} \end{cases}$$

where $\text{Proj}(\star,\star)$, as earlier, denotes the angular rate bias projection algorithm, ensuring that $\|\hat{\boldsymbol{b}}_{\text{gyro}}^b\|_2 \leq M_{\hat{b}_{\text{gyro}}}$ for $M_{\hat{b}_{\text{gyro}}} > M_{b_{\text{gyro}}}$ (Grip et al., 2012a), and $k_I(t) > 0$ is the potentially time-varying gain associated with the rate gyro bias estimation. The NLO is structurally the same as in Grip et al. (2013) where the attitude between

[2] In Bryne et al. (2014), the attitude differential equation (4.7) was described according to (B.8). This is equivalent to (4.7).

the $\{b\}$ and the $\{e\}$ frame was estimated. However, here the Earth's rotation is neglected since $\boldsymbol{\omega}_{in}^{b}$ is assumed to be negligible. The injection term, $\hat{\boldsymbol{\sigma}}_{ib}^{b}$, with a compass vector measurement, is given by,

$$\hat{\boldsymbol{\sigma}}_{ib}^{b} = k_1(t)\underline{\boldsymbol{v}}_1^b \times \boldsymbol{R}^\intercal(\hat{\boldsymbol{q}}_b^n)\underline{\boldsymbol{v}}_1^n + k_2(t)\underline{\boldsymbol{v}}_2^b \times \boldsymbol{R}^\intercal(\hat{\boldsymbol{q}}_b^n)\underline{\boldsymbol{v}}_2^n, \tag{4.11}$$

with the gains which satisfy $k_1(t), k_2(t) \geq k_P$ for some $k_P > 0$. Moreover, the measurement vectors $\underline{\boldsymbol{v}}_{1,2}^b$ and reference vectors $\underline{\boldsymbol{v}}_{1,2}^n$ are calculated using

$$\underline{\boldsymbol{v}}_1^b = \underline{\boldsymbol{f}}^b, \qquad \underline{\boldsymbol{v}}_1^n = \underline{\boldsymbol{f}}^n, \tag{4.12}$$

$$\underline{\boldsymbol{v}}_2^b = \underline{\boldsymbol{f}}^b \times \underline{\boldsymbol{c}}^b, \quad \underline{\boldsymbol{v}}_2^n = \underline{\boldsymbol{f}}^n \times \underline{\boldsymbol{c}}^n, \tag{4.13}$$

where the measurement vector $\underline{\boldsymbol{c}}^b$ is based on ψ_c, from the compass, in contrast to the magnetometer-based vector $\boldsymbol{m}_{\text{mag}}^b$, used in Section 3.2 in the previous chapter. Furthermore, the measurement and corresponding reference vector pairs in (4.12)–(4.13) are constructed as

$$\underline{\boldsymbol{f}}^b = \frac{\boldsymbol{f}_{\text{IMU}}^b}{\|\boldsymbol{f}_{\text{IMU}}^b\|_2}, \qquad \underline{\boldsymbol{f}}^n = \frac{\text{sat}_{M_f}(\hat{\boldsymbol{f}}_{ib}^n)}{\|\text{sat}_{M_f}(\hat{\boldsymbol{f}}_{ib}^n)\|_2}, \tag{4.14}$$

$$\underline{\boldsymbol{c}}^b = \begin{pmatrix} \cos\psi_c & -\sin(\psi_c) & 0 \end{pmatrix}^\intercal, \quad \underline{\boldsymbol{c}}^n = \begin{pmatrix} 1 & 0 & 0 \end{pmatrix}^\intercal, \tag{4.15}$$

where $\hat{\boldsymbol{f}}_{ib}^n$ is the estimated specific force, provided by the TMO as depicted in Figure 4.4, presented next in Section 4.3.4. The benefit of using normalized vectors is that the vector pairs only provide direction, hence these are dimensionless, such that the gains $k_{1,2}$ can be considered as cutoff frequencies of the complementary filter Σ_1, cf. Section 3.2.1. Since the gains have unit rad/s, $\hat{\boldsymbol{\sigma}}_{ib}^b$ obtains the same unit as $\boldsymbol{\omega}_{\text{IMU}}^b$.

The estimation error is defined as $\tilde{\boldsymbol{q}} := \boldsymbol{q}_b^n \otimes \hat{\boldsymbol{q}}_b^{n*}$ and $\tilde{\boldsymbol{b}}^b = \boldsymbol{b}_{\text{gyro}}^b - \hat{\boldsymbol{b}}_{\text{gyro}}^b$. Furthermore, we define $\boldsymbol{\chi} := (\tilde{\boldsymbol{r}}; \tilde{\boldsymbol{b}}^b)$, where $\tilde{\boldsymbol{r}}$ denotes the vector part of $\tilde{\boldsymbol{q}}$. The constraint of the unit quaternion yield zero estimation error when $|\tilde{s}| = 1$ or equivalently $\|\tilde{\boldsymbol{r}}\|_2 = 0$. Hence, $\tilde{s} = 0$ corresponds to the maximum attitude error of 180°. Uniform semiglobal exponential stability of the origin $\boldsymbol{\chi} = \boldsymbol{0}$ of the attitude observer's error dynamics can be established under the following three assumptions for $\hat{\boldsymbol{f}}_{ib}^n = \boldsymbol{f}_{ib}^n$:

Assumption 4.1. *The angular rate $\boldsymbol{\omega}_{ib}^b$, the specific force $\boldsymbol{f}_{ib}^b$ and its rate $\dot{\boldsymbol{f}}_{ib}^b$ are uniformly bounded.*

Assumption 4.2. *There exist a constant $c_{\text{obs}} > 0$ such that $\|\underline{\boldsymbol{f}}^b \times \underline{\boldsymbol{c}}^b\|_2 \geq c_{\text{obs}}$ for all $t \geq 0$, resulting in the attitude being uniformly observable.*

Assumption 4.3. *The initial condition is contained in the set $\mathcal{D}(\epsilon) = \{\tilde{\boldsymbol{q}} \mid |\tilde{s}| > \epsilon\}$, i.e. $\hat{\boldsymbol{q}}_b^n(0) \in \mathcal{D}$, representing attitude errors bounded away from 180° by a margin*

determined by $\epsilon \in (0, \frac{1}{2})$. *Furthermore, it is assumed that* $\hat{\boldsymbol{b}}^b_{\text{gyro}}(0)$ *is projected to the ball* $\mathcal{B} \in \{\boldsymbol{b}^b_{\text{gyro}} \mid \|\boldsymbol{b}^b_{\text{gyro}}\|_2 \leq M_{b_{\text{gyro}}}\}$.

Then from Assumptions 4.1–4.3, we use the result of Grip et al. (2012a), where, for each $\epsilon \in (0, \frac{1}{2})$, there exist a $k_P > 0$ such that if $k_1(t), k_2(t) > k_P$ and a $k_I(t) > 0$, then

$$\|\boldsymbol{\chi}(t)\|_2 \leq \kappa_a \mathrm{e}^{-\lambda_a t}\|\boldsymbol{\chi}(0)\|_2, \quad \forall t \geq 0, \tag{4.16}$$

for some $\kappa_a, \lambda_a > 0$ and $\boldsymbol{\chi}(0) \in \{\mathcal{D}(\epsilon), \mathcal{B}\}$, yielding that the origin of $\boldsymbol{\chi}$ is USGES. $\boldsymbol{f}^n_{ib}$ is however not known and needs to be estimated. This is carried out next.

4.3.4 Translation motion observer with time-varying gains applying the VVR as vertical aiding sensor

The TMO of Bryne et al. (2014) is obtained by extending the work of Grip et al. (2013) with

1. The state space augmentation, $p^n_{nb,I} = \int_0^t p^n_{nb,z}\,\mathrm{d}t$
2. Introduction of time-varying observer gains by replacing the combined gain, $\boldsymbol{K}$, of Grip et al. (2013) with $\boldsymbol{K}(t) = \varphi(t)\boldsymbol{K}$, where $\varphi(t) \in \mathbb{R}^1$ is a positive time-varying scaling factor.

The total augmented observer Σ_2 is given as

$$\Sigma_2{}^3 : \begin{cases} \dot{\hat{p}}^n_{nb,I} = \hat{p}^n_{nb,z} + \varphi(t)\vartheta K_{p_I p_I}\tilde{p}^n_{nb,I}, & (4.17a)\\ \dot{\hat{\boldsymbol{p}}}^n_{nb} = \hat{\boldsymbol{v}}^n_{nb} + \varphi(t)\vartheta^2\begin{pmatrix}\boldsymbol{0}_{2\times 1}\\ K_{pp_I}\end{pmatrix}\tilde{p}^n_{nb,I} + \varphi(t)\vartheta\begin{pmatrix}\boldsymbol{0}_{1\times 2}\\ \boldsymbol{K}_{pp}\end{pmatrix}\tilde{\boldsymbol{p}}^n_{nb,xy}, & (4.17b)\\ \dot{\hat{\boldsymbol{v}}}^n_{nb} = \hat{\boldsymbol{f}}^n_{ib} + \boldsymbol{g}^n_b + \varphi(t)\vartheta^3\begin{pmatrix}\boldsymbol{0}_{2\times 1}\\ K_{vp_I}\end{pmatrix}\tilde{p}^n_{nb,I} + \varphi(t)\vartheta^2\begin{pmatrix}\boldsymbol{0}_{1\times 2}\\ \boldsymbol{K}_{vp}\end{pmatrix}\tilde{\boldsymbol{p}}^n_{nb,xy}, & (4.17c)\\ \dot{\boldsymbol{\xi}}^n_{ib} = -\boldsymbol{R}(\hat{\boldsymbol{q}}^n_b)\boldsymbol{S}(\hat{\boldsymbol{\sigma}}^b_{ib})\boldsymbol{f}^b_{\text{IMU}} \\ \qquad\qquad + \varphi(t)\vartheta^4\begin{pmatrix}\boldsymbol{0}_{2\times 1}\\ K_{\xi p_I}\end{pmatrix}\tilde{p}^n_{nb,I} + \varphi(t)\vartheta^3\begin{pmatrix}\boldsymbol{0}_{1\times 2}\\ \boldsymbol{K}_{\xi p}\end{pmatrix}\tilde{\boldsymbol{p}}^n_{nb,xy}, & (4.17d)\\ \hat{\boldsymbol{f}}^n_{ib} = \boldsymbol{R}(\hat{\boldsymbol{q}}^n_b)\boldsymbol{f}^b_{\text{IMU}} + \boldsymbol{\xi}^n_{ib}, & (4.17e)\end{cases}$$

where $\tilde{p}^n_{nb,I} = y^n_{\text{VVR}} - \hat{p}^n_{nb,I} = p^n_{nb,I} - \hat{p}^n_{nb,I}$ and $\tilde{\boldsymbol{p}}^n_{nb,xy} = \boldsymbol{p}^n_{\text{GNSS}} - \hat{\boldsymbol{p}}^n_{nb,xy}$ are the innovation signals. $\boldsymbol{\xi}^n_{ib}$ is an auxiliary state used to estimate $\boldsymbol{f}^n_{ib}$ by relating the angular and translation motion. The signals $\hat{\boldsymbol{q}}^n_b$ and $\hat{\boldsymbol{\sigma}}^b_{ib}$ are provided by Σ_1 of Section 4.3.3. Moreover, ϑ is a high-gain-like parameter used to guarantee stability. Furthermore, by defining the state space

$$\boldsymbol{x}^* := \left(p^n_{nb,I};\, \boldsymbol{p}^n_{nb};\, \boldsymbol{v}^n_{nb};\, \boldsymbol{\xi}^n_{ib}\right), \tag{4.18}$$

[3] Σ_2 was presented with a slightly different structure w.r.t. the time-scale separation using the ϑ term in Bryne et al. (2014). The correct structure is utilized here.

the TMO (4.17) can be written on compound form as:

$$\dot{\hat{\boldsymbol{x}}}^* = \boldsymbol{A}^*\hat{\boldsymbol{x}}^* + \boldsymbol{B}^*\boldsymbol{u}^* + \boldsymbol{D}^* + \varphi(t)\boldsymbol{K}^*\left(\boldsymbol{y} - \boldsymbol{C}\hat{\boldsymbol{x}}^*\right), \tag{4.19}$$

where $\boldsymbol{y} = (y^n_{\text{VVR}}; \boldsymbol{p}^n_{\text{GNSS}})$, with the system matrices

$$\begin{aligned}
\boldsymbol{A}^* &= \left(\begin{array}{c|ccc} 0 & 0\,0\,1 & \boldsymbol{0}_{1\times3} & \boldsymbol{0}_{1\times3} \\ \hline \boldsymbol{0}_{3\times1} & \boldsymbol{0}_{3\times3} & \boldsymbol{I}_3 & \boldsymbol{0}_{3\times3} \\ \boldsymbol{0}_{3\times1} & \boldsymbol{0}_{3\times3} & \boldsymbol{0}_{3\times3} & \boldsymbol{I}_3 \\ \boldsymbol{0}_{3\times1} & \boldsymbol{0}_{3\times3} & \boldsymbol{0}_{3\times3} & \boldsymbol{0}_{3\times3} \end{array}\right), \quad \boldsymbol{B}^* = \left(\begin{array}{cc} \boldsymbol{0}_{1\times3} & \boldsymbol{0}_{1\times3} \\ \hline \boldsymbol{0}_{3\times3} & \boldsymbol{0}_{3\times3} \\ \boldsymbol{I}_{3\times3} & \boldsymbol{0}_{3\times3} \\ \boldsymbol{0}_{3\times3} & \boldsymbol{I}_{3\times3} \end{array}\right), \\
\boldsymbol{C}^* &= \left(\begin{array}{c|ccc} 1 & 0 & 0 & \boldsymbol{0}_{1\times7} \\ \hline 0 & 1 & 0 & \boldsymbol{0}_{1\times7} \\ 0 & 0 & 1 & \boldsymbol{0}_{1\times7} \end{array}\right), \qquad \boldsymbol{D}^* = \left(\begin{array}{c} 0 \\ \hline \boldsymbol{0}_{3\times1} \\ \boldsymbol{g}^n_b \\ \boldsymbol{0}_{3\times1} \end{array}\right),
\end{aligned} \tag{4.20}$$

and the time-invariant gain

$$\boldsymbol{K}^* = \begin{pmatrix} K_{p_1p_I} & \boldsymbol{0}_{1\times2} \\ \boldsymbol{0}_{2\times1} & \boldsymbol{K}_{pp} \\ K_{pp_I} & \boldsymbol{0}_{1\times2} \\ \boldsymbol{0}_{2\times1} & \boldsymbol{K}_{vp} \\ K_{vp_I} & \boldsymbol{0}_{1\times2} \\ \boldsymbol{0}_{2\times1} & \boldsymbol{K}_{\xi p} \\ K^0_{\xi p_I} & \boldsymbol{0}_{1\times2} \end{pmatrix} = \begin{pmatrix} \vartheta K^0_{p_1p_I} & \boldsymbol{0}_{1\times2} \\ \boldsymbol{0}_{2\times1} & \vartheta\boldsymbol{K}^0_{pp} \\ \vartheta^2 K^0_{pp_I} & \boldsymbol{0}_{1\times2} \\ \boldsymbol{0}_{2\times1} & \vartheta^2\boldsymbol{K}^0_{vp} \\ \vartheta^3 K^0_{vp_I} & \boldsymbol{0}_{1\times2} \\ \boldsymbol{0}_{2\times1} & \vartheta^3\boldsymbol{K}^0_{\xi p} \\ \vartheta^4 K^0_{\xi p_I} & \boldsymbol{0}_{1\times2} \end{pmatrix} \tag{4.21}$$

Finally, the input $\boldsymbol{u}^*$ is given as

$$\boldsymbol{u}^* = \begin{pmatrix} \boldsymbol{R}(\hat{\boldsymbol{q}}^n_b)\boldsymbol{f}^b_{\text{IMU}} \\ -\boldsymbol{R}(\hat{\boldsymbol{q}}^n_b)\boldsymbol{S}(\hat{\boldsymbol{\sigma}}^b_{ib})\boldsymbol{f}^b_{\text{IMU}} \end{pmatrix}. \tag{4.22}$$

Moreover, the error states of the TMO (4.17) can be defined

$$\tilde{\boldsymbol{x}}^* := \left(\tilde{p}^n_{nb,I};\, \tilde{\boldsymbol{p}}^n_{nb};\, \tilde{\boldsymbol{v}}^n_{nb};\, \tilde{\boldsymbol{f}}^n_{ib}\right), \tag{4.23}$$

where $\tilde{\boldsymbol{f}}^n_{ib}$, instead of $\boldsymbol{\xi}^n_{ib}$, is utilized as error state. Then, the error dynamics of the origin of Σ_2 can be obtained as

$$\dot{\tilde{\boldsymbol{x}}}^* = \left(\boldsymbol{A}^* - \varphi(t)\boldsymbol{K}^*\boldsymbol{C}^*\right)\tilde{\boldsymbol{x}}^* + \boldsymbol{\rho}(t,\boldsymbol{\chi}) \tag{4.24}$$

where,

$$\boldsymbol{\rho}(t,\boldsymbol{\chi}) = \left(0; \boldsymbol{0}_{3\times1}; \boldsymbol{0}_{3\times1}; \tilde{\boldsymbol{d}}(t,\boldsymbol{\chi})\right), \tag{4.25}$$

with

$$\tilde{\boldsymbol{d}}(t,\boldsymbol{\chi}) = \left(\boldsymbol{I}_3 - \boldsymbol{R}^\intercal(\tilde{\boldsymbol{q}})\right)\boldsymbol{R}^n_b\left(\boldsymbol{S}(\boldsymbol{\omega}^n_{ib})\boldsymbol{f}^b_{ib} + \dot{\boldsymbol{f}}^b_{ib}\right) - \boldsymbol{R}^\intercal(\tilde{\boldsymbol{q}})\boldsymbol{R}^n_b\boldsymbol{S}(\tilde{\boldsymbol{b}}^b_{\text{gyro}})\boldsymbol{f}^b_{ib}, \tag{4.26}$$

similar to Grip et al. (2013), except here the Earth's rotation is neglected since $\boldsymbol{\omega}_{in}^{b} = \mathbf{0}_{3\times1}$ is assumed. Also here $\vartheta \geq 1$ is applied to assert some time-scale separation in order to estimate the specific force in the navigation frame and guarantee stability and robustness in the presence of the disturbance $\tilde{\boldsymbol{d}}(t, \boldsymbol{\chi})$, induced by Σ_1, and the unknown signal $\dot{\boldsymbol{f}}_{ib}^{n}$. The time-varying scalar $\varphi(t) \geq \tau > 0$, can e.g. be chosen by taking into account the horizontal GNSS accuracy such as the horizontal dilution of precision (Farrell, 2008, Ch. 8.5), reported by the GNSS receiver.

4.3.5 Stability analysis

In order to obtain some stability properties of the error dynamics of Σ_2, the linear time-invariant (LTI) systems $(\boldsymbol{A}^*, \boldsymbol{C}^*)$ must be observable. The observability of $(\boldsymbol{A}^*, \boldsymbol{C}^*)$ is trivial to verify since the gravity is constant and known using the Kalman rank condition on the observability matrix

$$\boldsymbol{O}^* = \begin{pmatrix} \boldsymbol{C}^* \\ \boldsymbol{C}^*\boldsymbol{A}^* \\ \vdots \\ \boldsymbol{C}^*\boldsymbol{A}^{*m-1} \end{pmatrix}, \tag{4.27}$$

where $m = \dim(\boldsymbol{A}^*) = 10$ such that $\boldsymbol{O}^*$ will have rank m. Then we continue with the compounded gain from (4.21) and (4.24) which can be defined by [4]

$$\boldsymbol{K}^* := \vartheta \boldsymbol{L}_{\vartheta}^{*\,-1} \boldsymbol{K}_0^* \boldsymbol{E}_{\vartheta}^*, \tag{4.28}$$

where $\boldsymbol{L}_{\vartheta}^*$ is given as

$$\boldsymbol{L}_{\vartheta}^* = \text{blockdiag}\left(1,\ \frac{1}{\vartheta}\boldsymbol{I}_3,\ \frac{1}{\vartheta^2}\boldsymbol{I}_3,\ \frac{1}{\vartheta^3}\boldsymbol{I}_3\right), \tag{4.29}$$

and

$$\boldsymbol{E}_{\vartheta}^* = \boldsymbol{C}^* \boldsymbol{L}_{\vartheta}^* \boldsymbol{C}^{*\dagger}, \tag{4.30}$$

which satisfy Lemma. 4.1.

Lemma 4.1. *$\boldsymbol{E}_{\vartheta}^* = \boldsymbol{C}^* \boldsymbol{L}_{\vartheta}^* \boldsymbol{C}^{*\dagger}$ satisfy $\boldsymbol{E}_{\vartheta}^* \boldsymbol{C}^* = \boldsymbol{C}^* \boldsymbol{L}_{\vartheta}^*$.*

Proof: See Appendix A.2.1.

Now by considering the non-singular transform

$$\boldsymbol{\eta} := \boldsymbol{L}_{\vartheta}^* \tilde{\boldsymbol{x}}^*, \tag{4.31}$$

we obtain the time-scaled error state space $\boldsymbol{\eta}$

$$\boldsymbol{\eta} = \begin{pmatrix} \eta_1 \\ \boldsymbol{\eta}_2 \\ \boldsymbol{\eta}_3 \\ \boldsymbol{\eta}_4 \end{pmatrix} = \begin{pmatrix} \tilde{\boldsymbol{p}}_{nb,I}^{n} \\ \frac{1}{\vartheta}\tilde{\boldsymbol{p}}_{nb}^{n} \\ \frac{1}{\vartheta^2}\tilde{\boldsymbol{v}}_{nb}^{n} \\ \frac{1}{\vartheta^3}\tilde{\boldsymbol{f}}_{ib}^{n} \end{pmatrix}. \tag{4.32}$$

[4] $\boldsymbol{E}_{\vartheta}^*$ was not included in Bryne et al. (2014)

Furthermore, the dynamics of $\boldsymbol{\eta}$ may be obtained as

$$\dot{\boldsymbol{\eta}} = \dot{\boldsymbol{L}}^*_\vartheta \tilde{\boldsymbol{x}}^* + \boldsymbol{L}^*_\vartheta \dot{\tilde{\boldsymbol{x}}}^* = \boldsymbol{L}^*_\vartheta \dot{\tilde{\boldsymbol{x}}}^*. \tag{4.33}$$

Moreover, by considering the term $(\boldsymbol{A}^* - \varphi(t)\boldsymbol{K}^*\boldsymbol{C}^*)\tilde{\boldsymbol{x}}^*$ from (4.24), and exploiting that $\dot{\boldsymbol{\eta}} = \boldsymbol{L}^*_\vartheta \dot{\tilde{\boldsymbol{x}}}^*$ and $\tilde{\boldsymbol{x}}^* = \boldsymbol{L}^{*^{-1}}_\vartheta \boldsymbol{\eta}$ one obtains

$$\boldsymbol{L}^*_\vartheta (\boldsymbol{A}^* - \varphi(t)\boldsymbol{K}^*\boldsymbol{C}^*)\boldsymbol{L}^{*^{-1}}_\vartheta = \vartheta(\boldsymbol{A} - \varphi(t)\boldsymbol{K}^*_0\boldsymbol{C}^*) \tag{4.34}$$

due to

$$\begin{aligned} \boldsymbol{L}^*_\vartheta \boldsymbol{A}^* \boldsymbol{L}^{*^{-1}}_\vartheta &= \vartheta \boldsymbol{A}^*, \\ \varphi(t)\boldsymbol{L}^*_\vartheta \boldsymbol{K}^* \boldsymbol{C} \boldsymbol{L}^{*^{-1}}_\vartheta &= \varphi(t)\vartheta \boldsymbol{K}^*_0 \boldsymbol{C}, \end{aligned}$$

where

$$\boldsymbol{L}^*_\vartheta \boldsymbol{K}^* \boldsymbol{C}^* \boldsymbol{L}^{*^{-1}}_\vartheta = \vartheta \boldsymbol{L}^*_\vartheta \boldsymbol{L}^{*^{-1}}_\vartheta \boldsymbol{K}^*_0 \boldsymbol{E}^*_\vartheta \boldsymbol{C}^* \boldsymbol{L}^{*^{-1}}_\vartheta = \vartheta \boldsymbol{K}^*_0 \boldsymbol{C}^* \boldsymbol{L}^*_\vartheta \boldsymbol{L}^{*^{-1}}_\vartheta = \vartheta \boldsymbol{K}^*_0 \boldsymbol{C}^* \tag{4.35}$$

which follows from Lemma 4.1. In addition, since

$$\boldsymbol{L}^*_\vartheta \boldsymbol{\rho}(t, \tilde{\boldsymbol{\chi}}) = \frac{1}{\vartheta^4} \boldsymbol{\rho}(t, \tilde{\boldsymbol{\chi}}), \tag{4.36}$$

the transformed error dynamics become

$$\frac{1}{\vartheta}\dot{\boldsymbol{\eta}} = (\boldsymbol{A}^* - \varphi(t)\boldsymbol{K}^*_0\boldsymbol{C}^*)\boldsymbol{\eta} + \boldsymbol{\rho}(t, \tilde{\boldsymbol{\chi}}). \tag{4.37}$$

The nominal stationary gain $\boldsymbol{K}^*_0$ can be chosen freely in order to ensure that $\boldsymbol{A}^* - \boldsymbol{K}^*_0\boldsymbol{C}^*$ Hurwitz. $\vartheta \geq 1$ is a tuning parameter used to guarantee stability and robustness with respect to the uncertainties in $\tilde{\boldsymbol{d}}(t, \boldsymbol{\chi})$. However, one may choose

$$\boldsymbol{K}^*_0 = \boldsymbol{P}\boldsymbol{C}^\intercal, \tag{4.38}$$

where $\boldsymbol{P} = \boldsymbol{P}^\intercal > 0$ is the solution of the stationary algebraic Riccati equation

$$\boldsymbol{A}^*\boldsymbol{P} + \boldsymbol{P}\boldsymbol{A}^{*\intercal} + \boldsymbol{Q} - 2\tau \boldsymbol{P}\boldsymbol{C}^{*\intercal}\boldsymbol{C}^*\boldsymbol{P} = \boldsymbol{0}_{10\times 10}. \tag{4.39}$$

Below the conditions for semiglobal exponential stability of the origin of the estimation error dynamics is analysed.

Assumption 4.4. *Initial conditions are in the following sets:*

- $\mathcal{X} \subset \mathbb{R}^{10}$ *is a ball containing the origin* $\tilde{\boldsymbol{x}}^* = \boldsymbol{0}_{10\times 1}$.
- $\mathcal{D}(\bar{\epsilon}) = \{\tilde{\boldsymbol{q}} \mid |\tilde{s}| > \bar{\epsilon}\}$ *presents a set of attitude errors bounded away from* $180°$ *by a small margin determined by an arbitrary constant* $\bar{\epsilon} \in \left(0, \frac{1}{2}\right)$.
- $\mathcal{B} \in \{\boldsymbol{b}^b_{\text{gyro}} \mid \|\boldsymbol{b}^b_{\text{gyro}}\|_2 \leq M_{b_{\text{gyro}}}\}$.

Assumption 4.5. *Observer gains are chosen according to*

- $k_1(t), k_2(t) > k_P$ *being sufficiently large, for* $k_P > 0$, *cf. Grip et al. (2013).*
- $k_I(t) > 0$ *is arbitrary.*
- $\boldsymbol{K}^*(t) = \varphi(t)\boldsymbol{K}_0^*$ *is chosen according to* (4.38)–(4.39), *where* $\varphi(t) \geq \tau$, *for all* $t \geq 0$, *from some constant* $\tau \geq 0$ *and where* $\boldsymbol{K}_0^*$ *is determined using* (4.39) *with the tuning matrix* $\boldsymbol{Q} = \boldsymbol{Q}^\intercal > 0$.

Under the conditions in Assumptions 4.1–4.2 and 4.4–4.5, the error dynamics of Sections 4.3.3 and 4.3.4, the origin, $(\tilde{\boldsymbol{x}}^*; \boldsymbol{\chi}) = \boldsymbol{0}$, of the error dynamics of the feedback-interconnected observers $\Sigma_1 - \Sigma_2$, is USGES according to Theorem 4.1.

Theorem 4.1. *Let* $\mathcal{X}$, $\mathcal{D}(\bar{\epsilon})$ *and* $\mathcal{B}$ *satisfy Assumption 4.4. Furthermore, let* k_P *be chosen to satisfy Assumption 4.5 and ensure stability, according to Grip et al. (2012a, Theorem 1), for* Σ_1 *with known* $\boldsymbol{f}_{ib}^n$. *Also let* $\boldsymbol{P} = \boldsymbol{P}^\intercal > 0$, *being the solution of the algebraic Riccati equation* (4.39) *for a* $\boldsymbol{Q} = \boldsymbol{Q}^\intercal > 0$. *Then, there exist a* $\vartheta^* \geq 1$, *a scalar* $\tau > 0$ *and a* $\varphi(t) \geq \tau$ *such that for* $\vartheta \geq \vartheta^*$, *some nominal gain* (4.38) *and for some constants* $\kappa^*, \lambda^* > 0$, *then*

$$\sqrt{\|\tilde{\boldsymbol{x}}^*(t)\|_2^2 + \|\boldsymbol{\chi}(t)\|_2^2} \leq \kappa^* \mathrm{e}^{-\lambda^* t} \sqrt{\|\tilde{\boldsymbol{x}}^*(0)\|_2^2 + \|\boldsymbol{\chi}(0)\|_2^2}, \tag{4.40}$$

rendering the origin, $(\tilde{\boldsymbol{x}}^*; \boldsymbol{\chi}) = \boldsymbol{0}$, *uniformly semiglobally exponentially stable (USGES).*

Proof: See Appendix A.2.2.

Remark 4.1. *The stability result of Theorem 4.1 is achieved for sufficiently large* ϑ *and* k_P, *respectively. This in combination with* $\mathcal{D}(\bar{\epsilon}) = \{\tilde{\boldsymbol{q}} \mid |\tilde{s}| > \bar{\epsilon}\}$ *ensuring that* (4.40) *always holds. By studying the proof one can calculate the explicit minimum values of* ϑ *and* k_P. *However,* ϑ *and* $k_1(t), k_2(t) \geq k_P$ *will probably be unnecessary large due to the conservative nature of the proof. Therefore, the choice of gains should be based on careful tuning also taking into account noise levels such that unnecessary amplification of sensor noise is prevented. Moreover, high gains in discretized systems can result in numerical instability. Hence, the gains should be chosen with care.*

4.3.6 Case study: TMO aided by VVR versus GNSS

In order to illustrate the effect of the VVR compared to using vertical GNSS or dGNSS measurements, the TMO above is compared to the time-invariant equivalent of the TMO of Section 3.3. In the reminder of the section, this is referred to as the nominal TMO and denoted $\Sigma_{2,\mathrm{nom}}$. The simulation of motion data is described in Appendix C.3. Vertical measurements from standard GNSS and from dGNSS were simulated based on Appendix C.1. A case study with time-varying gains, $\varphi(t)$, $k_1(t)$, $k_2(t)$, $k_I(t)$, can be found in Appendix C.3.2.

Table 4.1: GNSS error-model parameters.

	Std. dev. of w [m]	**Corr. time T [s]**	T_s **[Hz]**
North	0.21	1100	1.0
East	0.21	1100	1.0
Down	0.40	1100	1.0

Table 4.2: dGNSS error-model parameters.

	Std. dev. of w [m]	**Corr. time T [s]**	T_s **[Hz]**
North	0.1	480	1.0
East	0.1	480	1.0
Down	0.2	480	1.0

Table 4.3: GNSS and dGNSS RMS errors related to the performance illustration in Figure 4.1.

Measurement Component	**GNSS RMS error [m]**	**dGNSS RMS error [m]**
North	4.4963	1.7300
East	4.8527	1.4609
Down	9.1083	3.2377

Colored GNSS noise

Typical noise of a standalone GNSS receiver and a receiver with differential corrected positioning solution were simulated. Examples of both transient GNSS and dGNSS error realizations are shown in Figure 4.1 earlier. The parameters of noise process (C.1) for the standalone receiver (Beard and McLain, 2012, Ch. 7.5) is presented in Table 4.1. The dGNSS receiver correlation time is based on the results of Rankin (1994) and Mohleji and Wang (2010), where the former suggests a correlation time of 10 minutes for a simulated dGPS receiver, while the latter suggest a correlation time in the range of $4-8$ minutes. Since the results presented in Mohleji and Wang (2010) are recent, and hence more up to date with respect to hardware and software solutions, this recommendation constituted the basis of the choice for the dGNSS noise realization of (C.1). The driving noise was selected such that the RMS errors of the noise, $z[k]$, over a large time horizon was between 1 and 2 meters in North and East, while the vertical component was in the range of $2-4$ meters. The chosen model parameters related to the dGNSS colored noise are presented in Table 4.2. The RMS errors of the realizations of Figure 4.1 are further given in Table 4.3.

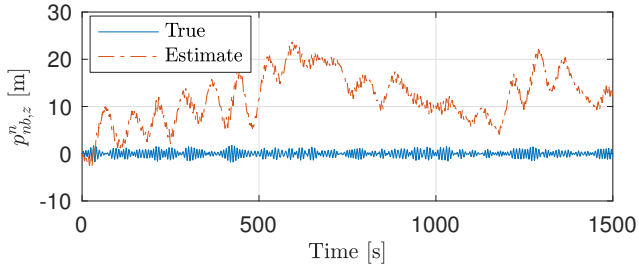

Figure 4.5: Heave estimates obtained using a standalone GNSS receiver as vertical position reference.

Tuning

The gains associated with the horizontal axes were chosen equal for both observers: $\boldsymbol{K}^0_{pp,xy} = 0.4190 \cdot \boldsymbol{I}_2$, $\boldsymbol{K}^0_{vp,xy} = 0.0878 \cdot \boldsymbol{I}_2$ and $\boldsymbol{K}^0_{\xi p,xy} = 0.0091 \cdot \boldsymbol{I}_2$, while the gains associated with the vertical axes of $\Sigma_{2,\text{nom}}$ and Σ_2 are given in Table 4.4. Thus, the gains of the nominal TMO was chosen as $\boldsymbol{K}^0_{pp} = \text{blockdiag}(\boldsymbol{K}_{pp,xy}, K^0_{p_z p_z})$, $\boldsymbol{K}^0_{vp} = \text{blockdiag}(\boldsymbol{K}^0_{vp,xy}, K^0_{v_z p_z})$ and $\boldsymbol{K}^0_{\xi p} = \text{blockdiag}(\boldsymbol{K}^0_{\xi p,xy}, K^0_{\xi_z p_z})$. The gains associated with the same states were chosen similar for both observers such that the comparison would be relevant. In addition, $\vartheta = 1$ was chosen for both $\Sigma_{2,\text{nom}}$ and Σ_2. Regarding the attitude observer, the measurement/reference vector pairs were given equal weights using $k_1 = k_2 = 0.55$, while $k_I = 0.01$ was chosen.

Simulation results

Heave accuracy:

The respective heave estimates obtained, from applying the three simulated vertical position references, are shown in Figures 4.5–4.7. The heave estimate, obtained with aiding from the simulated standalone GNSS receiver, is shown in Figure 4.5 together with the actual heave motion of the ship. Figure 4.6 shows the transient performance of the heave estimate obtained from utilizing the simulated dGNSS

Table 4.4: Vertical Gains Tuning of Σ_2.

TMO			
$\Sigma_{2,\text{nom}}$		Σ_2	
-	-	$K^0_{p_I p_I}$	0.4655
K^0_{pp}	0.1083	$K^0_{pp_I}$	0.1083
K^0_{vp}	0.0148	$K^0_{vp_I}$	0.0148
$K^0_{\xi_z p}$	0.0010	$K^0_{\xi p_I}$	0.0010

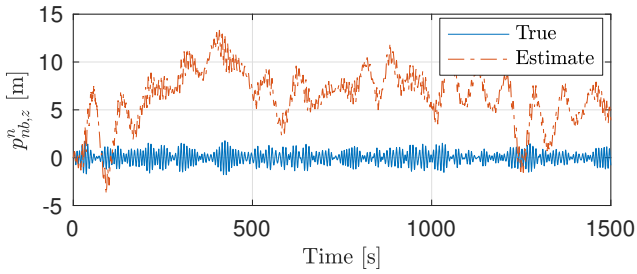

Figure 4.6: Heave estimates obtained using a dGNSS receiver as vertical position reference.

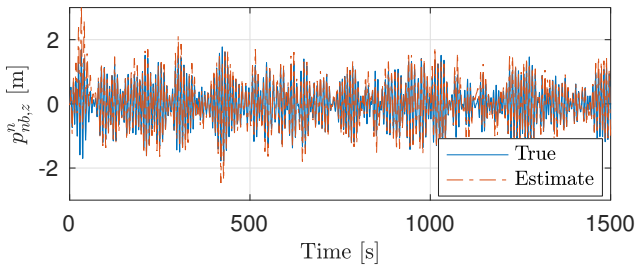

Figure 4.7: Heave estimates obtained using the VVR as vertical position reference.

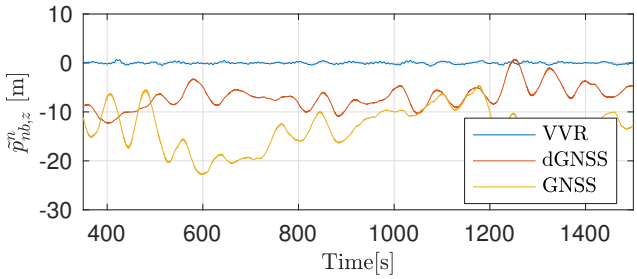

Figure 4.8: Steady-state heave estimation error.

receiver. An improvement in heave estimation performance, when compared to Figure 4.5, is observed. The heave estimate, using the VVR measurement as vertical aiding is shown in Figure 4.7. One can clearly observe the increase in heave estimation accuracy by utilizing Σ_2 as TMO with the VVR aiding concept. This is also observed in Figure 4.8, comparing the respective heave estimation errors. Figure 4.8 show the steady state estimation error utilizing the three vertical position references as INS aid. It is evident that the VVR aiding gave the highest

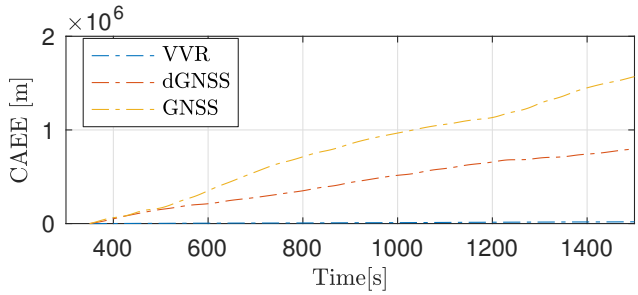

Figure 4.9: Heave CAEE. Calculations started after 350 seconds.

heave estimation accuracy and that standalone GNSS aiding yielded the lowest. This is also confirmed by Table 4.5 where the heave estimation RMS errors together with the mean square errors (MSEs) and the cumulative absolute estimation errors (CAEEs) at time 1500 seconds are presented. The MSE is defined as:

$$MSE := \frac{1}{N}\sum_{k=1}^{N}\left(x(k) - \hat{x}(k)\right)^2, \tag{4.41}$$

while the CAEE is defined as

$$CAEE := \sum_{k=1}^{N}\left|x(k) - \hat{x}(k)\right|, \tag{4.42}$$

where $x = p^n_{nb,z}$ when evaluating the heave estimation error. Figure 4.9 shows how

Table 4.5: Heave: Estimation error statistics.

Vertical Aiding	RMS error [m]	MSE [m^2]	CAEE [m] (at time 1500 s)
VVR	0.1889	0.0357	20753.80
dGNSS	1.5063	2.2691	403155.62
GNSS	7.3705	60.1101	1569456.65

the heave CAEEs evolves over time. The heave CAEE obtained when using the VVR is significantly smaller than the CAEE obtained with a GNSS-based vertical INS aiding. The statistics presented in Table 4.5 are calculated in steady state (between 350 and 1500 seconds of simulation), i.e. after the attitude estimate had converged.

Roll and pitch accuracies:
Since the observers Σ_1–$\Sigma_{2,\text{nom}}$ and Σ_1–Σ_2 are feedback interconnected, the accuracy

Table 4.6: Roll: Estimation error statistics.

Vertical Aiding	RMS error [deg]	MSE [deg^2]	CAEE [deg] (at time 1500 s)
VVR	0.0394	0.0016	3627.1
dGNSS	0.0416	0.0017	3896.6
GNSS	0.0553	0.0031	4965.2

of the translational motion estimates will affect the attitude estimates through the feedback. To show the relationship between the vertical translational motion estimates and the roll and pitch estimates, we start with the term,

$$k_2 \boldsymbol{f}^b_{\text{IMU}} \times \boldsymbol{R}(\hat{\boldsymbol{q}}^n_b)^\intercal \hat{\boldsymbol{f}}^n_{ib},$$

from the attitude observer injection term, $\hat{\boldsymbol{\sigma}}^b_{ib}$, given in (4.11). Moreover, we express the transposed estimated attitude, $\boldsymbol{R}(\hat{\boldsymbol{q}}^n_b)^\intercal$, in terms of Euler angles with

$$\boldsymbol{R}(\hat{\boldsymbol{q}}^n_b)^\intercal = \left(\hat{\boldsymbol{R}}^n_b\right)^\intercal (\phi, \theta, \psi) = \begin{pmatrix} R_{11} & R_{12} & R_{13} \\ R_{21} & R_{22} & R_{23} \\ -\mathrm{s}\hat{\theta} & \mathrm{c}\hat{\theta}\mathrm{s}\hat{\phi} & \mathrm{c}\hat{\theta}\mathrm{c}\hat{\phi} \end{pmatrix}^\intercal = \begin{pmatrix} R_{11} & R_{21} & -\mathrm{s}\hat{\theta} \\ R_{12} & R_{22} & \mathrm{c}\hat{\theta}\mathrm{s}\hat{\phi} \\ R_{13} & R_{23} & \mathrm{c}\hat{\theta}\mathrm{c}\hat{\phi} \end{pmatrix} \tag{4.43}$$

with $\mathrm{s}\cdot = \sin(\cdot)$ and $\mathrm{c}\cdot = \cos(\cdot)$, where $R_{\star\star}$ is found in Fossen (2011, Ch. 2.1.1). By only considering the vertical component of $\hat{\boldsymbol{f}}^n_{ib}$ and relating this to $\hat{\boldsymbol{R}}^b_n$, one obtains

$$\hat{\boldsymbol{R}}^b_n \cdot \begin{bmatrix} 0 \\ 0 \\ \hat{f}^n_{ib,z} \end{bmatrix} = \begin{bmatrix} -\mathrm{s}\hat{\theta} \\ \mathrm{c}\hat{\theta}\mathrm{s}\hat{\phi} \\ \mathrm{c}\hat{\theta}\mathrm{c}\hat{\phi} \end{bmatrix} \hat{f}^n_{ib,z}. \tag{4.44}$$

Hence, it is evident from (4.44) that the roll and pitch estimates are strongly coupled with the vertical component of $\hat{\boldsymbol{f}}^n_{ib}$ from the TMO. Furthermore, one can also argue that if the precision of the vertical reference measurement, which updates the specific force estimate, increases, the roll and pitch estimate accuracy is potentially also increased. This effect can be observed in Figures 4.10–4.11 where the conventional GNSS aiding results in the lowest roll and pitch estimate accuracy compared to those obtained using the VVR or dGNSS as vertical aiding. The statistics of the steady state roll and pitch estimation errors are given in Tables 4.6–4.7, respectively. The highest accuracy is obtained with the VVR and dGNSS aiding. Figures 4.12–4.13, presenting the evolution of CAEEs for the respective roll and pitch estimates, show that the CAEEs are significantly less over time when utilizing VVR and dGNSS, as vertical aiding measurement, compared to the respective counterpart when utilizing a standalone GNSS receiver.

Additional comments

It should be mentioned that the heave estimation precision of Figure 4.7 and the metrics associated with the VVR in Table 4.5 are sea state dependent. For sea states

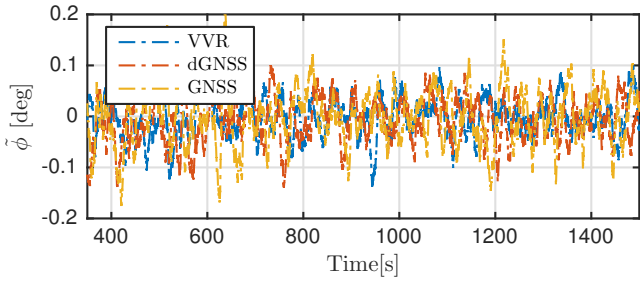

Figure 4.10: Steady-state roll estimation error.

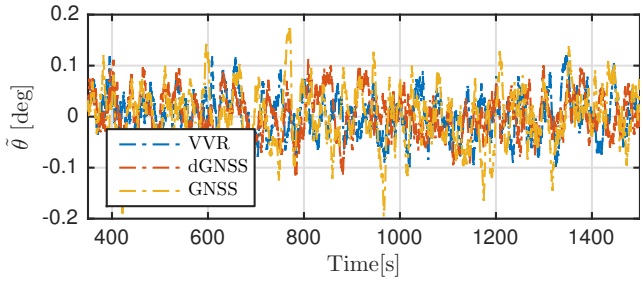

Figure 4.11: Steady-state pitch estimation error.

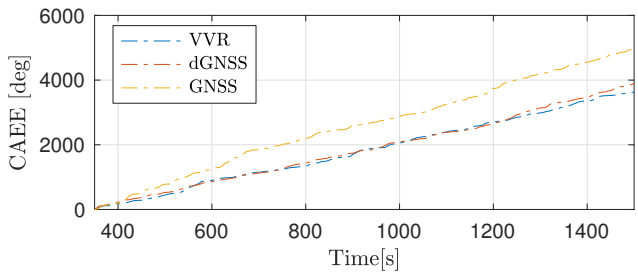

Figure 4.12: Roll CAEE. Calculations started after 350 seconds.

where the wave spectra has a low peak frequency, ω_0, the precision of the heave estimate with the VVR measurement update will decrease if the gains of Σ_2 is not modified accordingly. This is due to the low-pass characteristics of the observer combined with the low-frequency estimated acceleration input, $\hat{\boldsymbol{a}}^n_{ib} = \hat{\boldsymbol{f}}^n_{ib} + \boldsymbol{g}^n_b$, together will inflict phase error on the heave estimates.

Regarding tightly coupled integration schemes where pseudoranges are the observables, the VVR concept also has the potential to increase the GNSS accuracy in the horizontal plane with similar effects as differential correction. This is due to the heave estimates, from the INS, are fed back to the pseudorange resolver during the calculation of the estimated observation vector $\boldsymbol{h}(\hat{\boldsymbol{x}})$ w.r.t. (3.58) of Section 3.4

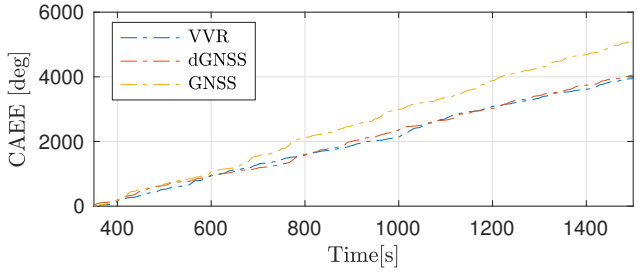

Figure 4.13: Pitch CAEE. Calculations started after 350 seconds.

Table 4.7: Pitch: Estimation error statistics.

Vertical Aiding	**RMS error [deg]**	**MSE [deg^2]**	**CAEE [deg] (at time 1500 s)**
VVR	0.0422	0.0019	3956.6
dGNSS	0.0448	0.0020	4016.0
GNSS	0.0567	0.0032	5117.9

and the calculation of the linearized observation matrix, $\boldsymbol{C}(t, \hat{\boldsymbol{x}})$. By emphasizing that VVR measurement, in general, is more accurate than the pseudoranges (user equivalent range error (UERE) RMS is typically $\sim$ 6 meters, Misra and Enge (2011, Ch. 5.4), for single-frequency receivers), common-mode errors affecting the position both in the horizontal and vertical axes, may be interpreted as a receiver-clock error. In addition, tightly coupled integration will always have some aiding in the vertical axis from the GNSS pseudoranges even though the VVR is the primary vertical aiding. This has the potential to combat some of the phase errors induced by high sea states. For details related to GNSS/INS integration, Titterton and Weston (2004), Grewal et al. (2013) or Groves (2013) can be advised.

4.3.7 Summary

A USGES nonlinear observer for aided INS tailored for ships was developed by introducing a concept for accurate vertical aiding. The main idea is to use the mean surface level of the ocean as a virtual measurement since this will be zero on average. A nonlinear feedback-interconnected observer for estimation of the attitude and translational motion has been developed to utilize the VVR measurement together with horizontal position measurements, obtained e.g. from a GNSS receiver. In addition time-varying gains were introduced to improve convergence and to increase performance and robustness.

Computer simulations of a offshore vessels verify that strapdown inertial navigation systems aided VVR improves the accuracy of the navigation system significantly when compared to conventional loosely coupled GNSS aiding techniques.

The heave, roll and pitch estimates are more accurate with VVR-based aiding compared to the performance obtained with a vertical reference with precision equivalent to that of a standalone GNSS receiver. The VVR is also a simple concept, being self contained and independent of differential corrections.

The simulations indicate that using time-varying gains in estimating translational and angular motion are beneficial for fast convergence and suppression of sensor noise in the event of changes in sensor precision. The time-varying multiplicative scalar gain component $\varphi(t)$ is, however, not optimal since the time-varying component has equal effect on all three axes of the TMO regardless of which gain components that should be modified. In Chapter 3, the results of Johansen and Fossen (2015) were utilized such that time-varying gains in the TMO could be resolved using Riccati-based tuning, of Kalman and Bucy (1961), allowing for multivariable tuning without $\varphi(t)$. This is also applied next, where the VVR concept is improved.

4.4 Extended VVR Concept: Improved Heave Estimation

This section extends the former by:

- Allowing for the NLO design to based on a tangent frame realization of the strapdown equation based on Section 2.3.1.
- Improving the VVR concept by introducing an error model, containing time-varying parameters describing the wave induced motion of a vessel, improving the heave estimates, while the performance of the attitude estimation, obtained in the preceding section, is maintained.
- A generalization of the preceding TMO of Section 4.3 is presented allowing for both time-varying and individual tuning of each axis of the TMO, similar to the strategy from Section 3.3 of the preceding chapter.

As earlier, the motion of the marine surface craft is estimated using a two part feedback-interconnected nonlinear observer strategy as depicted in Figure 4.14, similar to Figure 4.4 though with an additional estimators providing the parameters $\omega_e(t)$ and $\lambda_w(t)$, being the encounter frequency of the waves and the relative damping factor of the approximated wave-response model (Section 4.4.1), respectively.

The PVA estimation is carried out in two steps. First the attitude is estimated by using rate gyro, specific force and compass measurements. The attitude observer is further aided by the second step, consisting of a TMO providing specific force estimates in the navigation frame, together with 3-DOF position and velocity estimates using the estimated attitude, specific force, PosRef and VVR measurements.

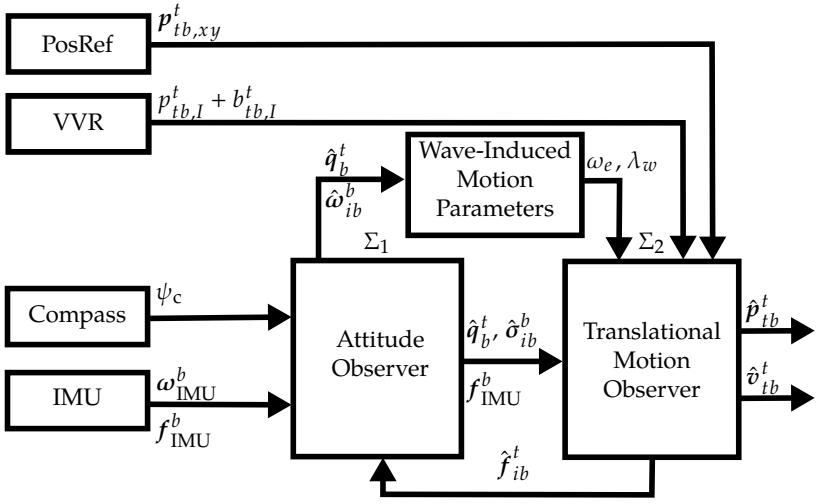

Figure 4.14: Extended observer structure: NLO-based INS aided by VVR, compass and PosRef systems. Estimated attitude and bias compensated angular rate measurements are utilized to estimated parameters related to the wave-induced motion of the vessel. These parameters are further utilized in a VVR error model.

The tangent frame, $\{t\}$, is utilized as navigation frame. Therefore, the VVR measurement is now defined as

$$y^t_{VVR} := 0, \quad \forall t \geq 0. \tag{4.45}$$

similar to (4.2) and (4.4). However, as mentioned in Section 4.2, this measurement is only measuring the average of the signal of $p^t_{tb,I}$ relating to the heave, $p^t_{tb,z}$, according to

$$\dot{p}^t_{tb,I} = p^t_{tb,z}, \tag{4.46}$$

equivalent to (4.3). To compensate for this, an error model in introduced.

4.4.1 Vertical vertical reference error model

As indicated in (4.2), of Section 4.2, choosing the VVR measurement

$$y^t_{\text{VVR}} = p^t_{tb,I} = 0, \tag{4.47}$$

similar to (4.4), would only be valid on average even though it is perfect w.r.t. to noise. Thus being suboptimal w.r.t. to heave peak-to-peak precision even when applying small gains associated with the VVR innovations in the aided INS cf. the case study of Section 4.3.6. Hence, the heave estimation performance obtained in Bryne et al. (2014, 2015b) may be improved, while maintaining the 6-DOF vessel motion estimates from the INS. Especially so in high sea states where the amplitude

of the wave-induced craft motion is high and the frequency of the motion is low (Fossen, 2011, Ch. 8), resulting in $y^t_{\text{VVR}} = p^t_{tb,I}$ is required to be valid for longer time horizons. This is due to the time constant of the wave-induced heave motion is larger for high sea states. Therefore, applying $y^t_{\text{VVR}} = p^t_{tb,I}$ would be less desirable in such conditions. This issue is not dealt with in the previous works (Bryne et al., 2014, 2015b), presented earlier in the chapter.

Fossen and Perez (2009) states that all onboard sensors measure both low-frequency (LF) and wave-frequency (WF) motion components. However, y^t_{VVR} of (4.47) only contains the former; see Figure 4.2. This makes it, in some sense, biased. In order to improve the general accuracy of $y^t_{\text{VVR}} = 0$, additional sensor parameters are introduced by using

$$y^t_{VVR} = p^t_{tb,I} + b^t_{tb,I} = 0, \tag{4.48}$$

instead of (4.47), where the dynamics of $b^t_{tb,I}$ is inspired by the works on wave-filtering of estimated vessel motion such as Sælid et al. (1983), Fossen and Strand (1999) and Fossen and Perez (2009). The VVR error model takes the form of

$$\dot{\zeta}^t_{tb} = b^t_{tb,I}, \tag{4.49}$$

$$\dot{b}^t_{tb,I} = -\omega_e^2(t)\zeta^t_{tb} - 2\lambda_w(t)\omega_e(t)b^t_{tb,I} + \sigma_{b,\text{VVR}}\varepsilon_u, \tag{4.50}$$

for some auxiliary state ζ^t_{tb}, where $0 < \lambda_w(t) < 1$ is the relative damping ratio of the wave-induced motion and

$$\omega_e(t, U, \omega_0, \beta) = \left|\omega_0 - U\frac{\omega_0^2}{g_b}\cos(\beta),\right| \tag{4.51}$$

being the encounter frequency of the waves experienced by the ship (Fossen, 2011, Ch. 8.2.3). Here U is the horizontal speed of the vessel, ω_0 is the peak frequency of the wave spectrum, $g_b = \|\boldsymbol{g}^t_b\|_2$ and β is the angle between the heading of the vessel and the direction of the waves. $\sigma_{b,\text{VVR}}$ is the standard deviation of the process noise and is consider a tuning parameter related to the heave amplitude. In practice, its magnitude is also a measure of how much the model structure and its parameters are trusted. Finally, ε_u represents unity white noise.

4.4.2 Model formulation

The INS, used to estimate the vessel's motion, will be realized based upon the tangent frame realization of the strapdown equations of Section 2.2.3. Thus, the problem formulation is obtained by augmenting the kinematic model of (2.13)–(2.14) and (2.18) with (4.46), the error model (4.49)–(4.50) and the gyro bias model

of Section 2.3.1,

$$\dot{p}^t_{tb,I} = p^t_{tb,z}, \tag{4.52}$$
$$\dot{\boldsymbol{p}}^t_{tb} = \boldsymbol{v}^t_{tb}, \tag{4.53}$$
$$\dot{\boldsymbol{v}}^t_{tb} = -2\boldsymbol{S}(\boldsymbol{\omega}^t_{ie})\boldsymbol{v}^t_{tb} + \boldsymbol{R}^t_b \boldsymbol{f}^b_{ib} + \boldsymbol{g}^t_b, \tag{4.54}$$
$$\dot{\boldsymbol{q}}^t_b = \frac{1}{2}\boldsymbol{q}^t_b \otimes \begin{pmatrix} 0 \\ \boldsymbol{\omega}^b_{ib} \end{pmatrix} - \frac{1}{2}\begin{pmatrix} 0 \\ \boldsymbol{\omega}^t_{it} \end{pmatrix} \otimes \boldsymbol{q}^t_b, \tag{4.55}$$
$$\dot{\boldsymbol{b}}^b_{\text{gyro}} = \boldsymbol{0}_{3\times 1}, \tag{4.56}$$
$$\dot{\zeta}^t_{tb} = b^t_{tb,I}, \tag{4.57}$$
$$\dot{b}^t_{tb,I} = -\omega^2_e(t)\zeta^t_{tb} - 2\lambda_w(t)\omega_e(t)b^t_{tb,I}. \tag{4.58}$$
$$\tag{4.59}$$

Before moving on to the observer design, a similar sensor configuration to that of Section 4.3.1 is introduced.

4.4.3 Attitude observer

The NLO used to estimate the attitude between the $\{b\}$ and $\{t\}$ frame is given by,

$$\Sigma_1 : \begin{cases} \dot{\hat{\boldsymbol{q}}}^t_b = \frac{1}{2}\hat{\boldsymbol{q}}^t_b \otimes \begin{pmatrix} 0 \\ \hat{\boldsymbol{\omega}}^b_{ib} \end{pmatrix} - \frac{1}{2}\begin{pmatrix} 0 \\ \boldsymbol{\omega}^t_{it} \end{pmatrix} \otimes \hat{\boldsymbol{q}}^t_b, & \text{(4.60a)} \\ \hat{\boldsymbol{\omega}}^b_{ib} = \boldsymbol{\omega}^b_{\text{IMU}} - \hat{\boldsymbol{b}}^b_{\text{gyro}} + \hat{\boldsymbol{\sigma}}^b_{ib}, & \text{(4.60b)} \\ \dot{\hat{\boldsymbol{b}}}^b_{\text{gyro}} = \text{Proj}\left(\hat{\boldsymbol{b}}^b_{\text{gyro}}, -k_I(t)\hat{\boldsymbol{\sigma}}^b_{ib}\right). & \text{(4.60c)} \end{cases}$$

Also here, Proj$(\star,\star)$ denotes the angular rate bias projection algorithm ensuring that $\|\hat{\boldsymbol{b}}^b_{\text{gyro}}\|_2 \leq M_{\hat{b}_{\text{gyro}}}$ for $M_{\hat{b}_{\text{gyro}}} > M_{b_{\text{gyro}}}$ (Grip et al., 2012a), and $k_I(t)$ is the gain associated with the rate gyro bias estimation. The NLO is structurally the same as in Chapter 3 and Grip et al. (2013), where the attitude between the $\{b\}$ and the $\{e\}$ frame was estimated. Moreover, the observer's nonlinear injection term, $\hat{\boldsymbol{\sigma}}^b_{ib}$, is given as

$$\hat{\boldsymbol{\sigma}}^b_{ib} = k_1(t)\underline{\boldsymbol{v}}^b_1 \times \boldsymbol{R}^\intercal(\hat{\boldsymbol{q}}^t_b)\underline{\boldsymbol{v}}^t_1 + k_2(t)\underline{\boldsymbol{v}}^b_2 \times \boldsymbol{R}^\intercal(\hat{\boldsymbol{q}}^t_b)\underline{\boldsymbol{v}}^t_2, \tag{4.61}$$

where the measurement vectors $\underline{\boldsymbol{v}}^b_{1,2}$ and reference vectors $\underline{\boldsymbol{v}}^t_{1,2}$ are calculated using

$$\underline{\boldsymbol{v}}^b_1 = \underline{\boldsymbol{f}}^b, \qquad \underline{\boldsymbol{v}}^t_1 = \underline{\boldsymbol{f}}^t, \tag{4.62}$$
$$\underline{\boldsymbol{v}}^b_2 = \underline{\boldsymbol{f}}^b \times \underline{\boldsymbol{c}}^b, \quad \underline{\boldsymbol{v}}^t_2 = \underline{\boldsymbol{f}}^t \times \underline{\boldsymbol{c}}^t. \tag{4.63}$$

Furthermore, the measurement and corresponding reference vector pairs in (4.62)–(4.63) are constructed as

$$\underline{f}^b = \frac{f^b_{\text{IMU}}}{\|f^b_{\text{IMU}}\|_2}, \qquad \underline{f}^t = \frac{\text{sat}_{M_f}(\hat{f}^t_{ib})}{\|\text{sat}_{M_f}(\hat{f}^t_{ib})\|_2}, \tag{4.64}$$

$$\underline{c}^b = \begin{pmatrix} \cos\psi_c & -\sin(\psi_c) & 0 \end{pmatrix}^\mathsf{T}, \quad \underline{c}^t = \begin{pmatrix} 1 & 0 & 0 \end{pmatrix}^\mathsf{T}. \tag{4.65}$$

As before $\hat{f}^t_{ib}$ is the estimated specific force, provided by the TMO as depicted in Figure 4.4.

Similar to Section 4.3.3, the estimation error is defined as $\tilde{q} := q^t_b \otimes \hat{q}^{t*}_b$ and $\tilde{b}^b = b^b_{\text{gyro}} - \hat{b}^b_{\text{gyro}}$. Furthermore, we define $\chi := (\tilde{r}; \tilde{b}^b)$, where $\tilde{r}$ denotes the vector part of $\tilde{q}$. Semiglobal exponential stability of the origin $\chi = \mathbf{0}$ (the scalar part of $\tilde{q}$, $\tilde{s} = 1$) of the attitude observer's error dynamics can be established if Assumptions 4.1–4.2 and 4.6 are satisfied when $\hat{f}^t_{ib} = f^t_{ib}$.

Assumption 4.6. *We assumed that the initial condition in contained in the set* $\mathcal{D}(\epsilon) = \{\tilde{q} \mid |\tilde{s}| > \epsilon\}$, *i.e.* $\hat{q}^t_b(0) \in \mathcal{D}$, *representing attitude errors bounded away from* $180°$ *by a margin determined by* $\epsilon \in (0, \frac{1}{2})$. *Furthermore, it is assumed that* $\hat{b}^b_{\text{gyro}}(0)$ *is projected to the ball* $\mathcal{B} \in \{b^b_{\text{gyro}} \mid \|b^b_{\text{gyro}}\|_2 \leq M_{b_{\text{gyro}}}\}$.

Assumption 4.6 is equivalent to Assumption 4.3 here, however, related to $\hat{q}^t_b(0)$. The same argument as in Section 4.3.3 is utilized, yielding that (4.16) is satisfied and the origin of χ is USGES if $\hat{f}^t_{ib} = f^t_{ib}$, (Grip et al., 2012a). Estimation of f^t_{ib} is carried out next.

4.4.4 Translational motion observer

The TMO is an extension of the preceding TMO of Section 4.3.4 based on Bryne et al. (2014, 2015b) and the results of Grip et al. (2012b, 2013). Then augmentation of the preceding TMO is done by introducing an error model, presented earlier in Section 4.4.1, in order to capture the short term inaccuracies in the VVR measurement. Since the tangent frame realization of the strapdown equations is utilized,

the extended TMO becomes

$$\Sigma_2 : \begin{cases} \dot{\hat{p}}^t_{tb,I} = \hat{p}^t_{tb,z} + \vartheta K^0_{p_I p_I} \tilde{y}^t_{tb,I} & (4.66a) \\ \dot{\hat{\boldsymbol{p}}}^t_{tb} = \hat{\boldsymbol{v}}^t_{tb} + \vartheta^2 \begin{pmatrix} \boldsymbol{0}_{2\times 1} \\ K^0_{pp_I} \end{pmatrix} \tilde{y}^t_{tb,I} + \vartheta \begin{pmatrix} \boldsymbol{K}^0_{pp} \\ \boldsymbol{0}_{1\times 2} \end{pmatrix} \tilde{\boldsymbol{y}}^t_{tb,xy} & (4.66b) \\ \dot{\hat{\boldsymbol{v}}}^t_{tb} = -2\boldsymbol{S}(\boldsymbol{\omega}^t_{ie})\boldsymbol{v}^t_{tb} + \hat{\boldsymbol{f}}^t_{ib} + \boldsymbol{g}^t_b + \vartheta^3 \begin{pmatrix} \boldsymbol{0}_{2\times 1} \\ K^0_{vp_I} \end{pmatrix} \tilde{y}^t_{tb,I} + \vartheta^2 \begin{pmatrix} \boldsymbol{K}^0_{vp} \\ \boldsymbol{0}_{1\times 2} \end{pmatrix} \tilde{\boldsymbol{y}}^t_{tb,xy} & (4.66c) \\ \dot{\hat{\boldsymbol{\xi}}}^t_{ib} = -\boldsymbol{R}(\hat{\boldsymbol{q}}^t_b)\boldsymbol{S}(\hat{\boldsymbol{\sigma}}^b_{ib})\boldsymbol{f}^b_{\text{IMU}} + \vartheta^4 \begin{pmatrix} \boldsymbol{0}_{2\times 1} \\ K^0_{\xi p_I} \end{pmatrix} \tilde{y}^t_{tb,I} + \vartheta^3 \begin{pmatrix} \boldsymbol{K}^0_{\xi p} \\ \boldsymbol{0}_{1\times 2} \end{pmatrix} \tilde{\boldsymbol{y}}^t_{tb,xy} & (4.66d) \\ \hat{\boldsymbol{f}}^t_{ib} = \boldsymbol{R}(\hat{\boldsymbol{q}}^t_b)\boldsymbol{f}^b_{\text{IMU}} + \hat{\boldsymbol{\xi}}^t_{ib} & (4.66e) \\ \dot{\hat{\zeta}}^t_{tb} = \hat{b}^t_{tb,I} + K^0_{\zeta p_I} \tilde{y}^t_{tb,I} & (4.66f) \\ \dot{\hat{b}}^t_{tb,I} = -\omega_e^2(t)\hat{\zeta}^t_{tb} - 2\lambda_w(t)\omega_e(t)\hat{b}^t_{tb,I} + K^0_{b_I p_I} \tilde{y}^t_{tb,I} & (4.66g) \end{cases}$$

where $\tilde{y}^t_{tb,I} = y^t_{\text{VVR}} - \hat{p}^t_{tb,I} - \hat{b}^t_{tb,I}$ and $\tilde{\boldsymbol{y}}^t_{tb,xy} = \boldsymbol{p}^t_{\text{PosRef}} - \hat{\boldsymbol{p}}^t_{tb,xy}$, while $K^0_\star$ and $\boldsymbol{K}^0_\star$ are gains associated with the VVR and the horizontal PosRef measurements, respectively. As earlier, $\boldsymbol{\xi}^t_{ib}$ is an auxiliary state used to estimate $\boldsymbol{f}^t_{ib}$ and where ϑ is a high-gain-like parameter used to guarantee stability. In contrast to the cited works on wave filtering, where the LF motion is estimated from measurements containing LF and WF motion, Σ_2 estimates the WF heave motion based on the inherent LF zero VVR measurement. Furthermore, by noting the LTV structure of (4.66) and defining

$$\boldsymbol{x} := \left(p^t_{tb,I}; \quad \boldsymbol{p}^t_{tb}; \quad \boldsymbol{v}^t_{tb}; \quad \boldsymbol{\xi}^t_{ib}; \quad \zeta^t_{tb}; \quad b^t_{tb,I} \right), \tag{4.67}$$

the TMO can be written on LTV form as

$$\dot{\hat{\boldsymbol{x}}} = \boldsymbol{A}(t)\hat{\boldsymbol{x}} + \boldsymbol{B}(t, \hat{\boldsymbol{q}}^t_b)\boldsymbol{u} + \boldsymbol{D}(t, \hat{\boldsymbol{x}}) + \boldsymbol{K}(t)(\boldsymbol{y} - \boldsymbol{C}\hat{\boldsymbol{x}}), \tag{4.68}$$

with the system matrices

$$\boldsymbol{A}(t) = \text{blockdiag}\left(\boldsymbol{A}^*, \boldsymbol{F}_{\text{VVR}}(t)\right), \tag{4.69a}$$

$$\boldsymbol{A}^* = \begin{pmatrix} 0 & 0\,0\,1 & \boldsymbol{0}_{1\times 3} & \boldsymbol{0}_{1\times 3} \\ \boldsymbol{0}_{3\times 1} & \boldsymbol{0}_{3\times 3} & \boldsymbol{I}_3 & \boldsymbol{0}_{3\times 3} \\ \boldsymbol{0}_{3\times 1} & \boldsymbol{0}_{3\times 3} & \boldsymbol{0}_{3\times 3} & \boldsymbol{I}_3 \\ \boldsymbol{0}_{3\times 1} & \boldsymbol{0}_{3\times 3} & \boldsymbol{0}_{3\times 3} & \boldsymbol{0}_{3\times 3} \end{pmatrix}, \tag{4.69b}$$

$$\boldsymbol{F}_{\text{VVR}}(t) = \begin{pmatrix} 0 & 1 \\ -\omega_e^2(t) & -2\lambda_w(t)\omega_e(t) \end{pmatrix}, \tag{4.69c}$$

input matrices

$$\boldsymbol{B}(t, \hat{\boldsymbol{q}}^t_b) = \begin{pmatrix} \boldsymbol{B}^*(t, \hat{\boldsymbol{q}}^t_b) \\ \boldsymbol{0}_{2\times 6} \end{pmatrix}, \quad \boldsymbol{B}^*(t, \hat{\boldsymbol{q}}^t_b) = \begin{pmatrix} \boldsymbol{0}_{1\times 3} & \boldsymbol{0}_{1\times 3} \\ \boldsymbol{0}_{3\times 3} & \boldsymbol{0}_{3\times 3} \\ \boldsymbol{R}(\hat{\boldsymbol{q}}^t_b) & \boldsymbol{0}_{3\times 3} \\ \boldsymbol{0}_{3\times 3} & \boldsymbol{R}(\hat{\boldsymbol{q}}^t_b) \end{pmatrix}, \tag{4.70}$$

the measurement matrices,

$$\boldsymbol{C} = \begin{pmatrix} \boldsymbol{C}^* & \boldsymbol{H}_{\text{VVR}} \\ \boldsymbol{0}_{2\times 2} & \end{pmatrix}, \boldsymbol{C}^* = \begin{pmatrix} \boldsymbol{I}_3 & \boldsymbol{0}_{3\times 7} \end{pmatrix}, \boldsymbol{H}_{\text{VVR}} = \begin{pmatrix} 0 & 1 \end{pmatrix}, \tag{4.71}$$

the vector

$$\boldsymbol{D}(t, \hat{\boldsymbol{x}}) = \begin{pmatrix} 0; & \boldsymbol{0}_{3\times 1}; & -2\boldsymbol{S}(\boldsymbol{\omega}_{ie}^t)\hat{\boldsymbol{v}}_{tb}^t + \boldsymbol{g}_b^t; & \boldsymbol{0}_{3\times 1}; & \boldsymbol{0}_{2\times 1} \end{pmatrix}, \tag{4.72}$$

and the gain matrix,

$$\boldsymbol{K}(t) = \begin{pmatrix} K_{p_I p_I} & \boldsymbol{0}_{1\times 2} \\ \boldsymbol{0}_{2\times 1} & \boldsymbol{K}_{pp} \\ K_{pp_I} & \boldsymbol{0}_{1\times 2} \\ \boldsymbol{0}_{2\times 1} & \boldsymbol{K}_{vp} \\ K_{vp_I} & \boldsymbol{0}_{1\times 2} \\ \boldsymbol{0}_{2\times 1} & \boldsymbol{K}_{\xi p} \\ K_{\xi p_I} & \boldsymbol{0}_{1\times 2} \\ K_{\zeta p_I} & \boldsymbol{0}_{1\times 2} \\ K_{b_I p_I} & \boldsymbol{0}_{1\times 2} \end{pmatrix} = \begin{pmatrix} \vartheta K_{p_I p_I}^0 & \boldsymbol{0}_{1\times 2} \\ \boldsymbol{0}_{2\times 1} & \vartheta \boldsymbol{K}_{pp}^0 \\ \vartheta^2 K_{pp_I}^0 & \boldsymbol{0}_{1\times 2} \\ \boldsymbol{0}_{2\times 1} & \vartheta^2 \boldsymbol{K}_{vp}^0 \\ \vartheta^3 K_{vp_I}^0 & \boldsymbol{0}_{1\times 2} \\ \boldsymbol{0}_{2\times 1} & \vartheta^3 \boldsymbol{K}_{\xi p}^0 \\ \vartheta^4 K_{\xi p_I}^0 & \boldsymbol{0}_{1\times 2} \\ K_{\zeta p_I}^0 & \boldsymbol{0}_{1\times 2} \\ K_{b_I p_I}^0 & \boldsymbol{0}_{1\times 2} \end{pmatrix}. \tag{4.73}$$

Finally, the input then becomes $\boldsymbol{u} = (\boldsymbol{f}_{\text{IMU}}^b; -\boldsymbol{S}(\hat{\boldsymbol{\delta}}_{ib}^b)\boldsymbol{f}_{\text{IMU}}^b)$. Moreover, the error states of the TMO can be defined as $\tilde{p}_{tb,I}^t := p_{tb,I}^t - \hat{p}_{tb,I}^t$, $\tilde{\boldsymbol{p}}_{tb}^t := \boldsymbol{p}_{tb}^t - \hat{\boldsymbol{p}}_{tb}^t$, $\tilde{\boldsymbol{v}}_{tb}^t := \boldsymbol{v}_{tb}^t - \hat{\boldsymbol{v}}_{tb}^t$, and $\tilde{\boldsymbol{f}}_{tb}^t := \boldsymbol{f}_{ib}^t - \hat{\boldsymbol{f}}_{ib}^t$, where the latter is obtained through a combination of (4.66d)–(4.66e). By including the auxiliary states, associated with the VVR error, $\tilde{\zeta}_{tb}^t := \zeta_{tb}^t - \hat{\zeta}_{tb}^t$ and $\tilde{b}_{tb,I}^t := b_{tb,I}^t - \hat{b}_{tb,I}^t$, one obtains the resulting the error state space

$$\tilde{\boldsymbol{x}} := \begin{pmatrix} \tilde{p}_{tb,I}^t; & \tilde{\boldsymbol{p}}_{tb}^t; & \tilde{\boldsymbol{v}}_{tb}^t; & \tilde{\boldsymbol{f}}_{ib}^t; & \tilde{\zeta}_{tb}^t; & \tilde{b}_{tb,I}^t \end{pmatrix}. \tag{4.74}$$

The error dynamics of the origin of Σ_2 is then given as

$$\dot{\tilde{\boldsymbol{x}}} = (\boldsymbol{A}(t) - \boldsymbol{K}(t)\boldsymbol{C})\tilde{\boldsymbol{x}} + \boldsymbol{\rho}_1(t, \tilde{\boldsymbol{x}}) + \boldsymbol{\rho}_2(t, \boldsymbol{\chi}), \tag{4.75}$$

with

$$\boldsymbol{\rho}_1(t, \tilde{\boldsymbol{x}}) = \begin{pmatrix} 0; & \boldsymbol{0}_{3\times 1}; & -2\boldsymbol{S}(\boldsymbol{\omega}_{ie}^t)\tilde{\boldsymbol{v}}_{tb}^t; & \boldsymbol{0}_{3\times 1}; & \boldsymbol{0}_{2\times 1} \end{pmatrix}, \tag{4.76}$$

$$\boldsymbol{\rho}_2(t, \boldsymbol{\chi}) = \begin{pmatrix} 0; & \boldsymbol{0}_{3\times 1}; & \boldsymbol{0}_{3\times 1}; & \tilde{\boldsymbol{d}}(t, \boldsymbol{\chi}); & \boldsymbol{0}_{2\times 1} \end{pmatrix}, \tag{4.77}$$

and where,

$$\begin{aligned} \tilde{\boldsymbol{d}}(t, \boldsymbol{\chi}) = &\left(\boldsymbol{I}_3 - \boldsymbol{R}^\intercal(\tilde{\boldsymbol{q}})\right) \boldsymbol{R}_b^t \left(\boldsymbol{S}(\boldsymbol{\omega}_{ib}^b)\boldsymbol{f}_{ib}^b + \dot{\boldsymbol{f}}_{ib}^b\right) \\ &- \boldsymbol{S}(\boldsymbol{\omega}_{it}^t)\left(\boldsymbol{I}_3 - \boldsymbol{R}^\intercal(\tilde{\boldsymbol{q}})\right) \boldsymbol{R}_b^t \boldsymbol{f}_{ib}^b - \boldsymbol{R}^\intercal(\tilde{\boldsymbol{q}}) \boldsymbol{R}_b^t \boldsymbol{S}(\tilde{\boldsymbol{b}}_{\text{gyro}}^b)\boldsymbol{f}_{ib}^b, \end{aligned} \tag{4.78}$$

similar to Grip et al. (2013) and Johansen et al. (2017). In order to apply $\vartheta \geq 1$ to estimate $\boldsymbol{f}_{ib}^t$ in the presence of the disturbance (4.78), the system much be left invertible. This was verified using Grip and Saberi (2010) and the accompanying Maple toolbox.

4.4.5 Stability analysis

As in Grip et al. (2013), Bryne et al. (2014, 2015b), Johansen et al. (2017), a parameter $\vartheta \geq 1$ is used in order to assign a certain time-scale structure to the error dynamics of (4.75). For this purpose, similar to Section 4.3.5, the non-singular transform

$$\boldsymbol{L}_\vartheta = \text{blockdiag}\left(1,\ \frac{1}{\vartheta}\boldsymbol{I}_3,\ \frac{1}{\vartheta^2}\boldsymbol{I}_3,\ \frac{1}{\vartheta^3}\boldsymbol{I}_3,\ \boldsymbol{I}_2\right), \tag{4.79}$$

of the state $\tilde{\boldsymbol{x}}$ is introduced such that the transformed state space is obtained using $\boldsymbol{\eta} := \boldsymbol{L}_\vartheta \tilde{\boldsymbol{x}}$ yielding

$$\boldsymbol{\eta} = \begin{pmatrix} \eta_1 \\ \boldsymbol{\eta}_2 \\ \boldsymbol{\eta}_3 \\ \boldsymbol{\eta}_4 \\ \boldsymbol{\eta}_5 \end{pmatrix} = \begin{pmatrix} \tilde{p}^t_{tb,I} \\ \frac{1}{\vartheta}\tilde{\boldsymbol{p}}^t_{tb} \\ \frac{1}{\vartheta^2}\tilde{\boldsymbol{v}}^t_{tb} \\ \frac{1}{\vartheta^3}\tilde{\boldsymbol{f}}^t_{ib} \\ (\tilde{\zeta}^t_{tb}; \tilde{b}^t_{tb,I}) \end{pmatrix}. \tag{4.80}$$

Moreover, the compounded gain (4.73) can further be defined

$$\boldsymbol{K}(t) := \boldsymbol{\vartheta}\boldsymbol{L}_\vartheta^{-1}\boldsymbol{K}_0(t)\boldsymbol{E}_\vartheta, \tag{4.81}$$

with $\boldsymbol{\vartheta} = \text{blockdiag}\,(\vartheta \cdot \boldsymbol{I}_{10}, \boldsymbol{I}_2)$, and where the nominal gain $\boldsymbol{K}_0(t)$ and $\boldsymbol{E}_\vartheta$ is obtained with

$$\boldsymbol{K}_0(t) = \boldsymbol{P}(t)\boldsymbol{C}^\intercal \boldsymbol{R}^{-1}(t), \tag{4.82}$$

and

$$\boldsymbol{E}_\vartheta = \boldsymbol{C}\boldsymbol{L}_\vartheta \boldsymbol{C}^\dagger, \tag{4.83}$$

respectively. Moreover, $\boldsymbol{P}(t) = \boldsymbol{P}^\intercal(t) > 0$ is the solution of the time-scaled algebraic Riccati equation,

$$\vartheta^{-1}\dot{\boldsymbol{P}}(t) = \boldsymbol{A}(t)\boldsymbol{P}(t) + \boldsymbol{P}(t)\boldsymbol{A}^\intercal(t) - \boldsymbol{P}(t)\boldsymbol{C}^\intercal\boldsymbol{R}^{-1}(t)\boldsymbol{C}\boldsymbol{P}(t) + \boldsymbol{G}(t)\boldsymbol{Q}(t)\boldsymbol{G}^\intercal(t). \tag{4.84}$$

In addition,

$$\boldsymbol{G}(t) = \begin{pmatrix} \boldsymbol{B}(t, \hat{\boldsymbol{q}}^t_b) & \boldsymbol{0}_{10\times 1} \\ & \boldsymbol{G}_{\text{VVR}}(t) \end{pmatrix}, \tag{4.85}$$

with $\boldsymbol{G}_{\text{VVR}}(t) = \big(0,\ \sigma_{b,\text{VVR}}(t)\big)^\intercal$, and the positive definite tuning matrices $\boldsymbol{Q}(t) = \boldsymbol{Q}^\intercal(t) > 0$, $\boldsymbol{R}(t) = \boldsymbol{R}^\intercal(t) > 0$, $\boldsymbol{P}(0) = \boldsymbol{P}^\intercal(0) > 0$. Finally, (4.83) follows from Lemma 4.2.

Lemma 4.2. *$\boldsymbol{E}_\vartheta = \boldsymbol{C}\boldsymbol{L}_\vartheta\boldsymbol{C}^\dagger$ satisfy $\boldsymbol{E}_\vartheta\boldsymbol{C} = \boldsymbol{C}\boldsymbol{L}_\vartheta$.*

Proof: See Appendix A.2.4.

Now, the error dynamics of (4.75) is transformed onto $\boldsymbol{\eta}$ yielding

$$\vartheta^{-1}\dot{\boldsymbol{\eta}} = (\boldsymbol{A}(t) - \boldsymbol{K}_0(t)\boldsymbol{C})\,\boldsymbol{\eta} + \frac{1}{\vartheta}\rho_1(t, \boldsymbol{\eta}) + \frac{1}{\vartheta^4}\rho_2(t, \chi), \tag{4.86}$$

where $\boldsymbol{\rho}_1(t,\boldsymbol{\eta}) = \left(0; \mathbf{0}_{3\times1}; -2\boldsymbol{S}(\boldsymbol{\omega}_{ie}^t)\boldsymbol{\eta}_3; \mathbf{0}_{3\times1}; \mathbf{0}_{2\times1}\right)$. With the transform, we obtain $\boldsymbol{L}_\vartheta \boldsymbol{A}(t)\tilde{\boldsymbol{x}} = \vartheta \boldsymbol{A}(t)\boldsymbol{\eta}$ and $\boldsymbol{L}_\vartheta \boldsymbol{K}(t)\boldsymbol{C}\tilde{\boldsymbol{x}} = \vartheta \boldsymbol{L}_\vartheta \boldsymbol{L}_\vartheta^{-1}\boldsymbol{K}_0(t)\boldsymbol{E}_\vartheta \boldsymbol{C}\tilde{\boldsymbol{x}} = \vartheta \boldsymbol{K}_0(t)\boldsymbol{C}\boldsymbol{L}_\vartheta\tilde{\boldsymbol{x}} = \vartheta \boldsymbol{K}_0(t)\boldsymbol{C}\boldsymbol{\eta}$, similar to Section 4.3.5.

First we consider the nominal transformed dynamics

$$\vartheta^{-1}\dot{\boldsymbol{\eta}} = (\boldsymbol{A}(t) - \boldsymbol{K}_0(t)\boldsymbol{C})\,\boldsymbol{\eta}, \tag{4.87}$$

and the accompanying observability and controllability properties that must be satisfied in order to obtain the desired stability properties.

Lemma 4.3. *Considering the measurement covariance matrix $\boldsymbol{R}(t)$ and the process noise covariance matrix $\boldsymbol{Q}(t)$, the system $\left(\boldsymbol{A}(t), \boldsymbol{R}^{-1/2}(t)\boldsymbol{C}\right)$ is uniformly completely observable (UCO) and the system $\left(\boldsymbol{A}(t), \boldsymbol{Q}^{1/2}(t)\boldsymbol{G}(t)\right)$ is uniformly completely controllable (UCC) for all $0 < \lambda_w < 1$ and positive, bounded $\omega_e(t)$.*

Proof: See Appendix A.2.5.

Remark 4.2. *As stated in Chapter 3, Section 3.3.1, the term $-2\boldsymbol{S}(\boldsymbol{\omega}_{ie}^t)\hat{\boldsymbol{v}}_{tb}^t$, in the time-varying vector $\boldsymbol{D}(t,\hat{\boldsymbol{x}})$, does not affect the observability properties. This follows from the fact that the term could have been included in the $\boldsymbol{A}^*$-matrix* (4.69b) *without affecting the observability of $(\boldsymbol{A}^*, \boldsymbol{C}^*)$.*

Since UCO and UCC is established, the stability results of the origin of (4.87) can be obtained.

Lemma 4.4. *Let the nominal gain $\boldsymbol{K}_0$ be calculated according to* (4.82) *where $\boldsymbol{P}(t) = \boldsymbol{P}^\intercal(t) > 0$ is the solution of the time-scaled Riccati equation* (4.84) *with the positive definite matrices $\boldsymbol{Q}(t) = \boldsymbol{Q}^\intercal(t) > 0$, $\boldsymbol{R}(t) = \boldsymbol{R}^\intercal(t) > 0$, $\boldsymbol{P}(0) = \boldsymbol{P}^\intercal(0) > 0$. Then, $\boldsymbol{P}(t)$ is uniformly bounded and the origin of* (4.87) *is globally exponentially stable (GES) for any $\vartheta \geq 1$.*

Proof: See Appendix A.2.6.

Now semiglobal exponential stability of the origin of the feedback-interconnected observer design is considered.

Assumption 4.7. *Initial conditions are in the following sets:*

- $\mathcal{X} \subset \mathbb{R}^{12}$ *is a ball containing the origin $\tilde{\boldsymbol{x}} = \mathbf{0}$.*
- $\mathcal{P} \subset \mathbb{R}^{(12)\times(12)}$ *is an arbitrary compact set of symmetric positive definite matrices $\boldsymbol{P}(0)$.*
- $\mathcal{D}(\bar{\epsilon}) = \{\tilde{\boldsymbol{q}} \mid |\tilde{s}| > \bar{\epsilon}\}$ *presents a set of attitude errors bounded away from* 180° *by a small margin determined by an arbitrary constant $\bar{\epsilon} \in \left(0, \frac{1}{2}\right)$.*
- $\mathcal{B} \in \{\boldsymbol{b}_{\text{gyro}}^b \mid \|\boldsymbol{b}_{\text{gyro}}^b\|_2 \leq M_{b_{\text{gyro}}}\}$.

Assumption 4.8. *Observer gains are chosen according to*

- $k_1(t), k_2(t) > k_P$ *being sufficiently large, for* $k_P > 0$, *cf. Grip et al. (2013).*
- $k_I(t) > 0$ *is arbitrary.*
- $\boldsymbol{K}(t)$ *is chosen according to* (4.81)–(4.83) *and is tuned using* (4.84) *with the matrices* $\boldsymbol{Q}(t) = \boldsymbol{Q}^\top(t), \boldsymbol{R}(t) = \boldsymbol{R}^\top(t), \boldsymbol{P}(0) = \boldsymbol{P}^\top(0) > 0$.

Under the conditions in Assumptions 4.1–4.2 and 4.7–4.8, the main result of the chapter, which is an extension and generalization of Theorem 4.1, can now be established.

Proposition 4.1. *There exists a* $\vartheta^\star \geq 1$ *such that for all* $\vartheta \geq \vartheta^\star$, *that* $\boldsymbol{P}(t)$ *is uniformly bounded and*

$$\sqrt{\|\tilde{\boldsymbol{x}}(t)\|_2^2 + \|\boldsymbol{\chi}(t)\|_2^2} \leq \kappa e^{-\lambda t} \sqrt{\|\tilde{\boldsymbol{x}}(0)\|_2^2 + \|\boldsymbol{\chi}(0)\|_2^2}, \tag{4.88}$$

for some $\kappa > 0$ *and* $\lambda > 0$ *rendering the origin* $(\tilde{\boldsymbol{x}}; \boldsymbol{\chi}) = 0$ *uniformly semiglobally exponentially stable (USGES).*

Proof: See Appendix A.2.7.

4.4.6 Obtaining ω_e and λ_w

The parameters, $\omega_e(t)$ and $\lambda_w(t)$ in the VVR error model are generally unknown and have to be estimated online. Although $\lambda_w(t)$ is often chosen as 0.1 for wave-filtering in dynamic positioning (DP) operations, (Fossen, 2011, Ch. 8.2.6, 11.3.6), (Perez, 2005, Ch 12.5). However, during e.g. vessel transit, with changing sea states, and other situations, estimating $\lambda_w(t)$ might increase performance compared to compensating for the uncertainty in $\lambda_w(t)$ with gain-scheduling dependent on operation and/or sea state. $\omega_e(t)$ can be obtained with a variety of online methods. Here, three methods for finding $\omega_e(t)$ is presented and compared, where one of them also estimates $\lambda_w(t)$.

Wave frequency estimator

The encounter frequency $\omega_e(t)$ may be obtained using the GES wave frequency estimator of Belleter et al. (2015), with

$$\dot{\zeta}_1 = \zeta_2 \tag{4.89}$$

$$\dot{\zeta}_2 = -2\omega_f \zeta_2 - \omega_f^2 \zeta_1 + \omega_f^2 y_w \tag{4.90}$$

$$\dot{\hat{\varphi}} = k(t)\zeta_1(\dot{\zeta}_2 - \hat{\varphi}\zeta_1) \tag{4.91}$$

where y_w is the input signal, ω_f is the embedded lowpass filter's cutoff frequency, $k(t)$ is a positive, smooth time-varying gain and the parameter φ relates to $\hat{\omega}_e(t)$ with $\hat{\omega}_e(t) = \sqrt{|\varphi|}$ such that $\hat{\omega}_e(t)$ converges to $\omega_e(t)$ exponentially fast. Since

$\hat{\omega}_e(t)$ is supposed to be used to improve the heave estimate, the pitch estimate is employed as the driving signal, i.e. $y_w = \hat{\theta}(t)$, due to the strong coupling with heave. $\hat{\theta}(t)$ is obtained from $\hat{\boldsymbol{q}}_b^t(t)$.

Kalman filter based estimation of $\omega_e(t)$ and $\lambda_w(t)$

The encounter frequency $\omega_e(t)$ and the relative damping factor of the wave spectra $\lambda_w(t)$ may be obtained using the algorithm of Perez (2005, Ch. 12.5), here however, based on the estimated pitch $\hat{\theta}$ and estimated pitch rate $\hat{q} = \omega^b_{\text{IMU},y} - \hat{b}^b_{\text{gyro},y}$, compared to using roll and roll rate as in the cited work. The algorithm is deduced by exploiting that pitch is mainly affected by the wave-induced motion such that we can write

$$\begin{pmatrix}\dot{\theta}\\ \dot{q}\end{pmatrix} = \begin{pmatrix}0 & 1\\ -\omega_e^2 & -2\lambda_w\omega_e\end{pmatrix}\begin{pmatrix}\theta\\ q\end{pmatrix} + \begin{pmatrix}w_\theta\\ w_q\end{pmatrix}, \tag{4.92}$$

where $w_\star$ represents white noise processes independent of each other and independent of ω_e and λ_w. In order to estimate λ_w (and ω_e) online, we first apply forward Euler discretization algorithm with step length T_s such that

$$\begin{pmatrix}\theta[k+1]\\ q[k+1]\end{pmatrix} = \begin{pmatrix}1 & T_s\\ -\omega_e^2 T_s & 1-2\lambda_w\omega_e T_s\end{pmatrix}\begin{pmatrix}\theta[k]\\ q[k]\end{pmatrix} + \begin{pmatrix}w_\theta[k]\\ w_q[k]\end{pmatrix} \tag{4.93}$$

is a first-order discretization of (4.92). Furthermore, be writing the system like

$$\begin{pmatrix}\theta[k+1]\\ q[k+1]\end{pmatrix} = \begin{pmatrix}\varphi_{11} & \varphi_{12}\\ \varphi_{21} & \varphi_{22}\end{pmatrix}\begin{pmatrix}\theta[k]\\ q[k]\end{pmatrix}, \tag{4.94}$$

where φ_{jl}, $j, l \in [1,2]$ are unknown parameters, one can reformulate the estimation problem of (4.93) to estimate λ_w and ω_e indirectly. By defining a new state vector, $\boldsymbol{\varphi} := (\varphi_{11}; \varphi_{12}; \varphi_{21}; \varphi_{22})$, and assuming that φ_{jl} are constant or slowly varying ($\dot{\boldsymbol{\varphi}} = \mathbf{0}$ or $\dot{\boldsymbol{\varphi}} \approx \mathbf{0}$), (4.93) is reformulated to the parameter estimation problem

$$\boldsymbol{\varphi}[k+1] = \boldsymbol{\varphi}[k], \tag{4.95}$$

$$\begin{pmatrix}\theta[k]\\ q[k]\end{pmatrix} = \begin{pmatrix}\theta[k-1] & q[k-1] & 0 & 0\\ 0 & 0 & \theta[k-1] & q[k-1]\end{pmatrix}\boldsymbol{\varphi}[k] + \begin{pmatrix}w_\theta[k]\\ w_q[k]\end{pmatrix}. \tag{4.96}$$

Now by defining the measurement vector and measurement matrix

$$\boldsymbol{y}_\varphi[k] := \begin{pmatrix}\theta[k]\\ q[k]\end{pmatrix}, \tag{4.97}$$

$$\boldsymbol{C}_\varphi[k] := \begin{pmatrix}\theta[k-1] & q[k-1] & 0 & 0\\ 0 & 0 & \theta[k-1] & q[k-1]\end{pmatrix}, \tag{4.98}$$

one can estimate $\boldsymbol{\varphi}[k]$ with the discrete-time KF

$$\boldsymbol{K}_{\varphi} = \bar{\boldsymbol{P}}_{\varphi}[k]\boldsymbol{C}_{\varphi}^{\intercal}[k]\left(\boldsymbol{C}_{\varphi}[k]\bar{\boldsymbol{P}}_{\varphi}[k]\boldsymbol{C}_{\varphi}^{\intercal}[k] + \boldsymbol{R}_{\varphi}[k]\right)^{-1}, \tag{4.99a}$$

$$\hat{\boldsymbol{\varphi}}[k] = \bar{\boldsymbol{\varphi}}[k] + \boldsymbol{K}_{\varphi}\left(\boldsymbol{y}_{\varphi}[k] - \boldsymbol{C}_{\varphi}[k]\right), \tag{4.99b}$$

$$\boldsymbol{M}_{\varphi}[k] = \boldsymbol{I}_4 - \boldsymbol{K}_{\varphi}[k]\boldsymbol{C}_{\varphi}[k], \tag{4.99c}$$

$$\hat{\boldsymbol{P}}_{\varphi}[k] = \boldsymbol{M}_{\varphi}[k]\bar{\boldsymbol{P}}_{\varphi}[k]\boldsymbol{M}_{\varphi}^{\intercal}[k] + \boldsymbol{K}_{\varphi}\boldsymbol{R}_{\varphi}\boldsymbol{K}_{\varphi}^{\intercal}[k], \tag{4.99d}$$

$$\bar{\boldsymbol{\varphi}}[k+1] = \hat{\boldsymbol{\varphi}}[k], \tag{4.99e}$$

$$\bar{\boldsymbol{P}}_{\varphi}[k+1] = \hat{\boldsymbol{P}}_{\varphi}[k] + \boldsymbol{Q}_{\varphi}[k]. \tag{4.99f}$$

For each k we obtain $\hat{\omega}_e[k]$, $\hat{\lambda}_w[k]$ with

$$\hat{\omega}_e[k] = \sqrt{-\frac{\hat{\varphi}_{21}[k]}{\hat{\varphi}_{12}[k]}}, \quad \hat{\lambda}_w[k] = \frac{\hat{\varphi}_{11}[k] - \hat{\varphi}_{22}[k]}{2\sqrt{-\hat{\varphi}_{12}[k]\hat{\varphi}_{21}[k]}}, \tag{4.100}$$

or

$$\hat{\omega}_e[k] = \sqrt{-\frac{\hat{\varphi}_{21}[k]}{T_s}}, \quad \hat{\lambda}_w[k] = \frac{1 - \hat{\varphi}_{22}[k]}{2\hat{\omega}_e[k]T_s}, \tag{4.101}$$

by exploiting how (4.96) relates to (4.93). In this study, $T_s = 0.2$ was chosen. Since neither $\hat{\omega}_e[k]$ or $\hat{\lambda}_w[k]$ are states, the possibility of negative square-roots of the output (4.100)–(4.101) can be solved without projection algorithms by choosing predefined minimum values of $\hat{\omega}_e[k]$ or $\hat{\lambda}_w[k]$ if the evaluation of (4.100)–(4.101) yield an imaginary result, at a certain k, in the transient phase.

Estimation of ω_e based on fast Fourier transform (FFT)

The encounter frequency $\omega_e(t)$ may also be estimated using a window of data to estimate the power spectral destiny (PSD). By choosing a window of some frequency dependent data, the estimate of $\omega_e(t)$ may be chosen as the peak frequency of the PSD. In this work, the PSD calculations were based on a 15 minute window of the estimated pitch, with five minutes of overlapping data, while applying Welch (1967)'s method in doing so. However, approaches like this are dependent on the amount of the historic data and are not necessarily adequately capturing transient frequency changes in the wave-induced motion. Perez (2005, Ch. 12.6) state that the sea state can typically be considered stationary for about 20 minutes. Hence, if the window length is chosen in the vicinity of 20 minutes (or shorter), estimation of $\omega_e(t)$ using fast Fourier transform (FFT) may be sufficient capturing transient effects.

4.4.7 Simulation study

For evaluation of the proposed observer structure and to perform a comparison study relative the preceding observer of Section 4.3 (Bryne et al., 2015b), Monte

Carlo (MC) simulations of a supply ship employing DP were conducted, using three different sea states, with 250 runs, at 50 Hz integration frequency. The MSS toolbox (Fossen and Perez, 2010) was used to generate the ship data. The JONSWAP Spectrum, (Fossen, 2011, Ch. 8.2.1) was chosen to generate the wave-induced ship motions with the sea state parameters of Table 4.8 and the peak-shape parameter $\gamma = 3.3$ in all three cases. For all simulations the rate gyro bias was chosen to $\boldsymbol{b}^b_{\text{gyro}} = (-0.04, 0.06, -0.05)^\intercal$. The statistical parameters associated with the sensor noise are presented in Table 4.9. The inertial sensors parameters are in compliance with the datasheet of the ADIS16485 IMU from Analog Devices with RMS noise of 0.067 mg/$\sqrt{\text{Hz}}$ for the accelerometers and 0.0066 °/$\sqrt{\text{Hz}}$ for the rate gyros. For position sensing, the parameters were chosen in compliance with Mohleji and Wang (2010), appropriate for dGNSS.

The observers were implemented with exact discretization similar to Bryne et al. (2017a) at 50 Hz. On the other hand, the measurement corrections associated with the simulated dGNSS, VVR, compass and accelerometer readings, were carried out at 1, 5, 5 and 50 Hz, respectively.

The attitude observer was tuned with $k_1 = 0.3$, $k_2 = 0.1$ and $k_I = 0.008$ in all three sea states using both VVR concepts (with and without the error model). Both the presented and the preceding TMO was tuned in discrete time with

$$\boldsymbol{R}_k = \text{blokdiag}\left(\sigma^2_{y_k,\text{VVR}}, 2.4^2, 2.4^2\right),$$

based on the PosRef error model of Section 2.3.2 and thereby using an ad hoc tuning

Table 4.8: Sea State Parameters Using the Jonswap Spectrum.

Sea state	**Significant wave height H_s**	**Peak frequency ω_0 of wave spectrum**
Slight	1 m	0.9 rad/s
Moderate	2.5 m	0.75 rad/s
High	7 m	0.6 rad/s

Table 4.9: Sensor Parameters.

Sensor	**Gaussian White Noise Std.**	**Gauss-Markov** (Time cont./ driving noise std.)
Acc.	0.0046[a] m/s^2	–
Rate gyro	0.0467[a] °/s	–
dGNSS	–	$8 \cdot 60$ s/1.2 m
Compass	0.1118[b] °	600 s/$\frac{0.5°}{\cos(\mu)}$

[a] Calculated at 50 Hz.
[b] Calculated at 5 Hz ($0.05 \cdot \sqrt{5}^\circ$ RMS).

to reflect the colored noise of the simulated dGNSS, motivated by the results of Section 3.3.5. Moreover, the process noise of the presented TMO was based on the continuous-time parameters

$$\begin{aligned}\boldsymbol{Q}(t) &= \text{blockdiag}\left(\sigma_{\text{acc}}^2 \cdot \boldsymbol{I}_3, \sigma_{\text{acc}}^2 \cdot \boldsymbol{S}_Q, Q_{\text{VVR}}\right),\\ \boldsymbol{S}_Q &= \text{blockdiag}(1.5, 1.5, 0.1),\\ Q_{\text{VVR}} &= 1,\\ \sigma_{b,\text{VVR}} &= 0.6,\end{aligned}$$

and where $\boldsymbol{A}(t)$, $\boldsymbol{G}(t)$ and step length $T_s = 1/Hz$ where used to calculate $\boldsymbol{Q}_k$, the discrete-time equivalent of $\boldsymbol{G}(t)\boldsymbol{Q}(t)\boldsymbol{G}^\intercal(t)$, using van Loan's method (van Loan, 1978). The preceding observer was tuned with

$$\boldsymbol{Q}(t) = \text{blockdiag}\left(\sigma_{\text{acc}}^2 \cdot \boldsymbol{I}_3, \sigma_{\text{acc}}^2 \cdot \boldsymbol{S}_Q\right).$$

The tuning covariance $R_{k,VVR} = \sigma_{y_k,\text{VVR}}^2$ associated with the VVR measurements was chosen based on

$$\sigma_{y_k,\text{VVR}} = \sigma_{y,\text{VVR}} \cdot \frac{1}{\sqrt{1/Hz}},$$

for the proposed observer, while using the more ad hoc formula

$$\sigma_{y_k,\text{VVR}} = \sigma_{y,\text{VVR}} \cdot \sqrt{\frac{S_z}{1/Hz}},$$

for the preceding observer emphasizing the VVR more or less depending on the desired noise level of the driving noise associated with estimating $\boldsymbol{f}_{ib}^t$ in order to scale $\boldsymbol{R}_k$ dependent on the chosen $\boldsymbol{Q}_k$. This is done to maintain an appropriate scale of $\boldsymbol{R}_k$ relative $\boldsymbol{Q}_k$, in order to ad hoc compensate for the short-term inaccuracy of the VVR since this is not taken into account using an error model.

The ad hoc choice of $\boldsymbol{Q}_k$ using $\boldsymbol{S}_Q$ is carried out in order to tune the heave performance almost independent of the tuning associated with the horizontal position due to roll and pitch amplitudes on marine vessels (usually) are small. For the proposed observer $\sigma_{y,\text{VVR}} = 0.0005$ was chosen, where the low value was granted by the zero noise of the VVR measurement and the usage of the error model. For the preceding observer $\sigma_{y,\text{VVR}}$ was chosen ad hoc, $\sigma_{y,\text{VVR}} = 2.15$, yielding fair results in the slight and moderate seas since these are more common than the higher sea states (Fossen, 2011, Ch. 8.2.1) (the worldwide probability of moderate sea state or lower is at 83,13 per cent). Moreover, $\sigma_{y,\text{VVR}}$ is a suboptimal tuning parameter, when applying the observer of Bryne et al. (2015b), since it will be sea state dependent implying that gain-scheduled tuning is preferable. This however is not simple to perform since such tuning preferably would be based on the heave amplitude, which again is directly affected by the chosen tuning creating a loop since re-tuning will affect the heave estimates directly. An alternative would

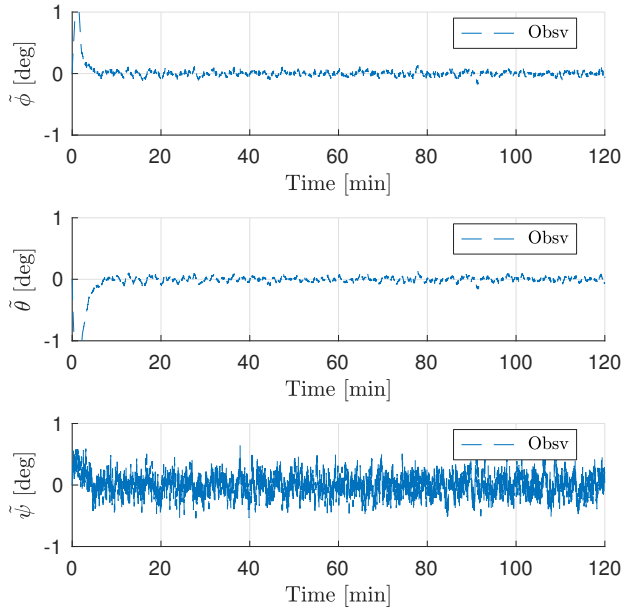

Figure 4.15: Attitude estimation error in moderate sea state.

be to develop tuning rules linked to the pitch amplitude due to the kinematic heave-pitch coupling. The benefit of the newly proposed algorithm is that it implicitly re-tunes the observer based on the time-varying $\boldsymbol{A}$-matrix, due to the online update of $\omega_e(t)$ and $\lambda_w(t)$ in the VVR's error model, which again affect the gain through (4.84). In every scenario, for both TMOs, $\vartheta = 1$ was chosen.

The statistics obtained from the MC simulations are generated based on 5 Hz evaluation of the last 90 minutes of each simulation run. The performance metrics applied are mean estimation error, RMS estimation error

$$RMS = \sqrt{\frac{1}{N}\sum_{k=1}^{N}(x_k - \hat{x}_k)^2}, \tag{4.102}$$

and CAEE

$$CAEE = \sum_{k=1}^{N}|x_k - \hat{x}_k|, \tag{4.103}$$

as before.

Examples of the attitude, horizontal position and heave estimation performance obtained in the moderate sea state are shown in Figures 4.15–4.17. The position error observer in Figure 4.16 is due to the dGNSS receiver simulated with colored noise of Table 4.9. The resulting statistics are presented in Tables 4.10–4.12. It is seen that performance of the heave estimation is improved approximately, 26.4,

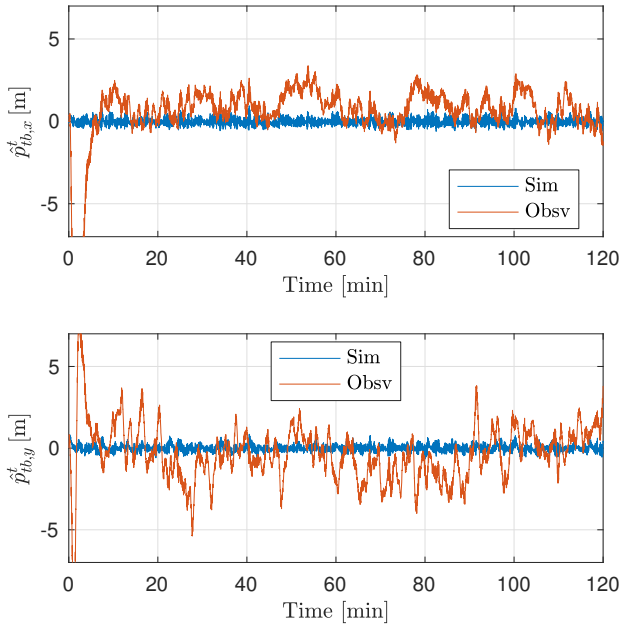

Figure 4.16: Position estimates in moderate sea state.

62.3 and 72.1 percent w.r.t. RMS error, in the slight, moderate and high sea state, respectively, using the presented nonlinear observer structure including the VVR error model, compared to the observer of Bryne et al. (2015b). The presented algorithm, with the chosen tuning, also achieves the industry standard specification of "the five cm or five per cent" RMS error in all three sea states. Regarding the attitude, the statistics indicate that the two algorithms (with or without VVR error model) are practically identical performance-wise.

The performance of the three wave-frequency estimators is illustrated in Figure 4.18. One can observe that the FFT-based estimator of $\omega_e(t)$ proved to be the most robust in detecting the peak-frequency of the wave spectra in DP (where $\omega_e = \omega_0$ due to zero vessel velocity). The reason for the two other estimators being slightly biased to the higher end of the spectrum might be understood from Figure 4.19, showing the estimated PSD of the last 90 minutes of data, from one of the MC simulations runs in moderate sea state, using both the heave reference and the estimated pitch, depicted in blue and red, respectively. One can observe that both signals also had one frequency component around 0.8 rad/s and one slightly above 0.8 rad/s being almost as dominant as the peak-frequency of $\omega_0 = 0.75$ of the simulated wave spectrum. One of these are probably tracked by the two time-domain-based wave frequency estimators. This reasoning stems from the fact that both algorithm are intrinsically based on single frequency identification. Moreover, from Figure 4.18b one can see that the stationary value of $\hat{\lambda}_w$ is quite

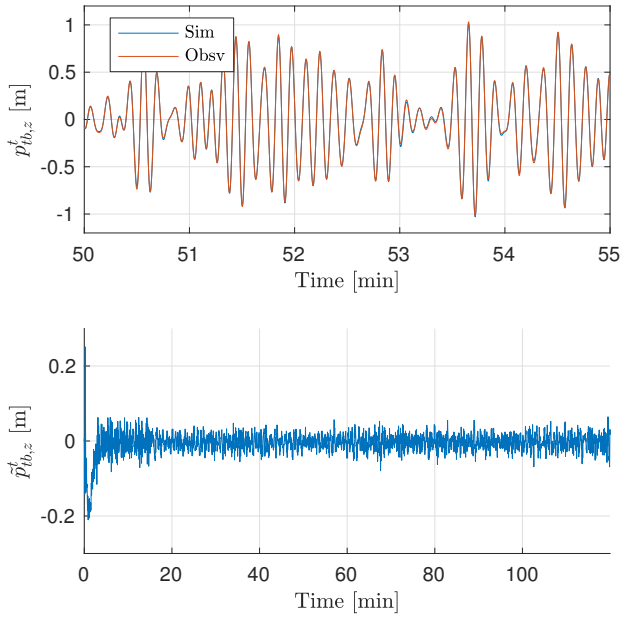

Figure 4.17: Heave estimates in moderate sea state.

far from the recommended value of 0.1 (Fossen, 2011, Ch. 8.2.1), indicating that the relative damping factor of the wave-induced motion not necessarily should be chosen to that of the wave spectrum's own damping factor.

A summary of the simulation study is that the attitude estimation performance of the observer posed is equal to the preceding observer, while the heave estimation performance is increased significantly. The performance improvement is most apparent in the high state yielding that the observer posed is robust to changing sea states with constant tuning matrices $\boldsymbol{Q}$ and $\boldsymbol{R}$ compared to the preceding observer.

Table 4.10: Monte Carlo statistics obtained in slight sea state.

Bryne et al. (2015b)	**Roll**	**Pitch**	**Heave**
Avg. mean error	$-2.1 \cdot 10^{-5^\circ}$	$-3.0 \cdot 10^{-5^\circ}$	−0.0515 cm
Avg. RMS error	0.0366°	0.0370°	1.8668[a] cm
Avg. CAEE	789.3°	798.5°	402.4 m
Proposed Observer	**Roll**	**Pitch**	**Heave**
Avg. mean error	$-2.5 \cdot 10^{-5^\circ}$	$-2.2 \cdot 10^{-6^\circ}$	−0.0480 cm
Avg. RMS error	0.0368°	0.0371°	1.3741[a] cm
Avg. CAEE	794.1°	801.9°	296.2 m

[a] 5% RMS error margin: 0.92 cm.

Table 4.11: Monte Carlo statistics obtained in moderate sea state state.

Bryne et al. (2015b)	**Roll**	**Pitch**	**Heave**
Avg. mean error	$-1.6 \cdot 10^{-4^\circ}$	$-4.0 \cdot 10^{-4^\circ}$	−0.3218 cm
Avg. RMS error	0.0382°	0.0374°	5.1349[a] cm
Avg. CAEE	824.8°	807.0°	1,105.2 m
Proposed Observer	**Roll**	**Pitch**	**Heave**
Avg. mean error	$-2.5 \cdot 10^{-4^\circ}$	$-3.9 \cdot 10^{-4^\circ}$	−0.3217 cm
Avg. RMS error	0.0383°	0.0374°	1.9341[a] cm
Avg. CAEE	825.3°	806.7°	416.3 m

[a] 5% RMS error margin: 2.65 cm.

Table 4.12: Monte Carlo statistics obtained in high sea state.

Bryne et al. (2015b)	**Roll**	**Pitch**	**Heave**
Avg. mean error	0.0013°	−0.0535°	−2.7377 cm
Avg. RMS error	0.0686°	0.0874°	23.9277[a] cm
Avg. CAEE	1,484.9°	1,685.7°	5,128.8 m
Proposed Observer	**Roll**	**Pitch**	**Heave**
Avg. mean error	$2.5 \cdot 10^{-4}$°	−0.0365°	−2.6902 cm
Avg. RMS error	0.0688∘	0.0662°	6.6656[a] cm
Avg. CAEE	1,489.1°	1,318.3°	1,394.1 m

[a] 5% RMS error margin: 7.78 cm.

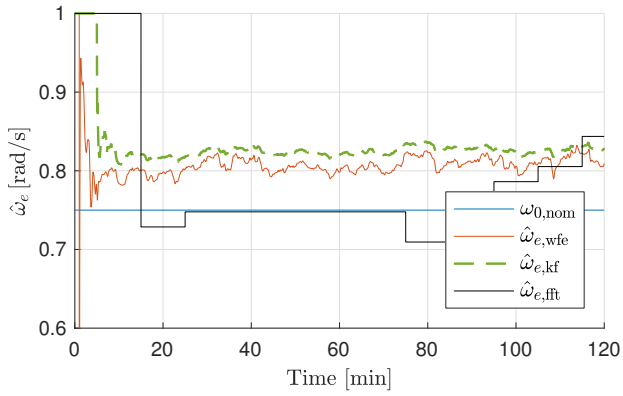

(a) Estimate of $\omega_e(t)$.

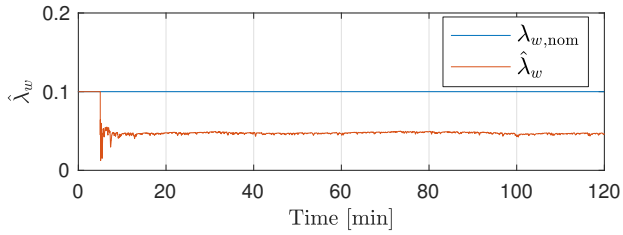

(b) Estimate $\lambda_w(t)$.

Figure 4.18: Wave-induced motion parameter estimates in moderate sea state.

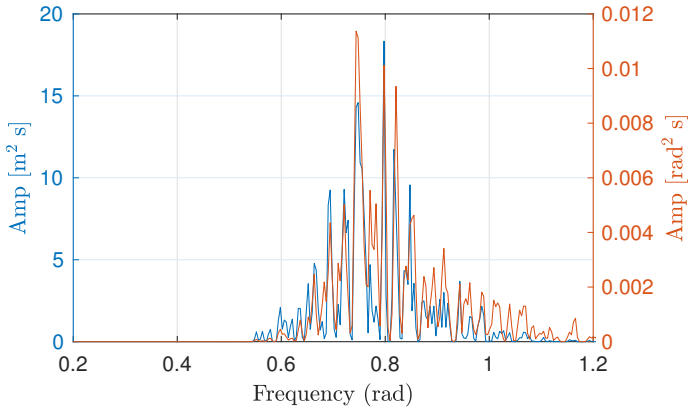

Figure 4.19: PSD of pitch estimate (red) relative the PSD of the true heave (blue) in moderate sea state.

4.4.8 Validation: Experimental results

The nonlinear observer structures of Section 4.4.3 and Section 4.4.4 are further validated using data obtained from an ADIS16485 MEMS IMU, by Analog Devices, installed on an operational offshore vessel, owned and operated by Farstad Shipping; see Appendix E.1. The IMU was interfaced at 1000 Hz, aided by VVR, dGNSS, and gyrocompass measurements. Of the data gathered, two data sets of 120 minutes are used in the validation. The data is of two different operations, illustrated in Figure 4.20, depicting the vessel's respective tracks. One track is of the offshore vessel entering DP and then performing stationkeeping and one is of the vessel during maneuvering.

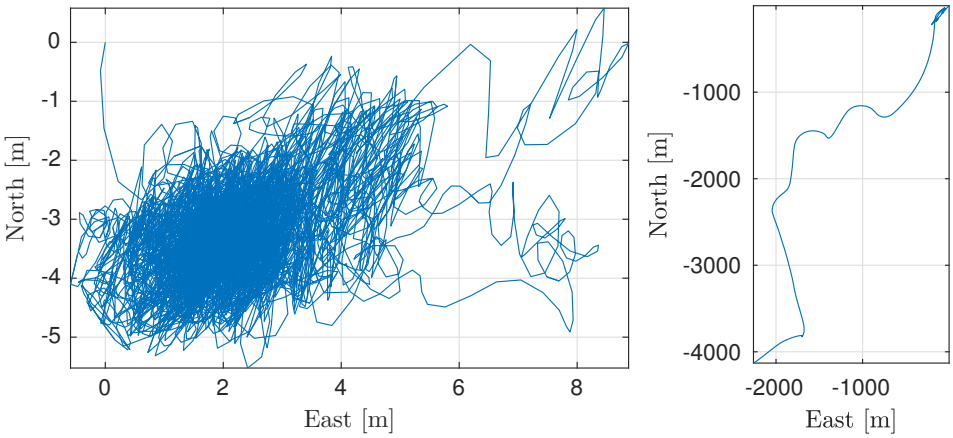

(a) DP/stationkeeping (b) Maneuvering

Figure 4.20: Track of two operations conducted in the Norwegian Sea. Path track is obtained from the onboard dGNSS.

The attitude observer and the TMO was implemented at 1000 Hz. The NLO structure from Sections 4.4.3–4.4.4 was validated using the same measurement corrections rates as in the simulation case study. The observers were tuned similar to that of the simulation study. Also for the validation, the encounter frequency was estimated using the FFT-based method, presented in Section 4.4.6, using 15 minutes of estimated pitch data with a five minute overlap from the previous window. The roll, pitch and heave estimates are compared to the solution provided by the onboard industry standard VRU. The specification of the VRU is presented in Table E.2 of Appendix E.1.

Validation in DP

The statistics of the estimation performance in DP is shown in Table 4.13. Furthermore, in Figure 4.23a, as with the simulation study, one can observe that the

Table 4.13: Statistics obtained based on data gathered during DP in the Norwegian Sea.

	Roll	Pitch	Heave
Mean error	$-1.3 \cdot 10^{-4}$°	0.0053°	0.1461 cm
RMS error	0.0923[a]°	0.1274[a]°	6.1489[a,b] cm
CAEE	1,982.8°	2,667.7°	1,305.3 m

[a] RMS error using Bryne et al. (2015b): Roll 0.0919°, pitch 0.1274°, heave 6.2736 cm.
[b] 5% RMS error margin: 2.1724 cm.

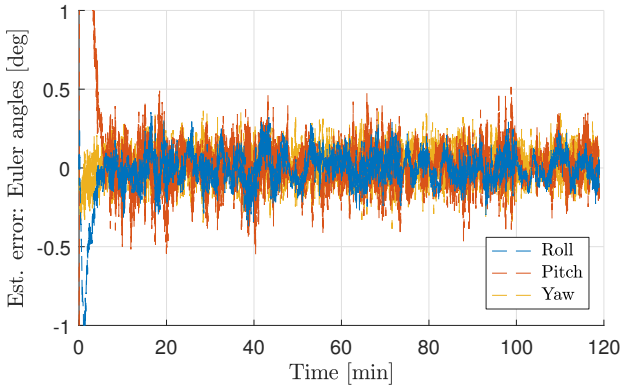

Figure 4.21: Stationkeeping: Attitude estimation error.

three methods for obtaining $\omega_e(t)$ differ from each other and where the FFT-based method is the one that is the best in estimating ω_e compared to reference $\omega_{0,\text{nom}}$, obtained using FFT of the heave signal from the VRU using the entire data set. The reason for the discrepancy in the methods can be understood from Figure 4.24, presenting the estimated PSD using Welch's method (Welch, 1967) of the estimated pitch compared to that of the VRU heave reference, where the PSD of the estimated pitch have two peaks just low of 0.8 rad/s. It seems that the wave frequency estimator of Belleter et al. (2015) converges to a frequency in this area. Nevertheless, one can see that the main peaks of the PSDs, based upon estimated pitch and the heave reference signal, coincides indicating that the FFT-based estimation of $\omega_e(t)$, using pitch, in aiding the heave estimation, have merit.

From the statistics one can read that the performance of the roll estimation is better than that of the pitch compared to the VRU. As with the simulation study, the proposed observer and the preceding observer provide similar results. The data of the two operations are gathered 45 hours and 49 minutes apart. The accelerometer bias compensation was carried out three days before the end of

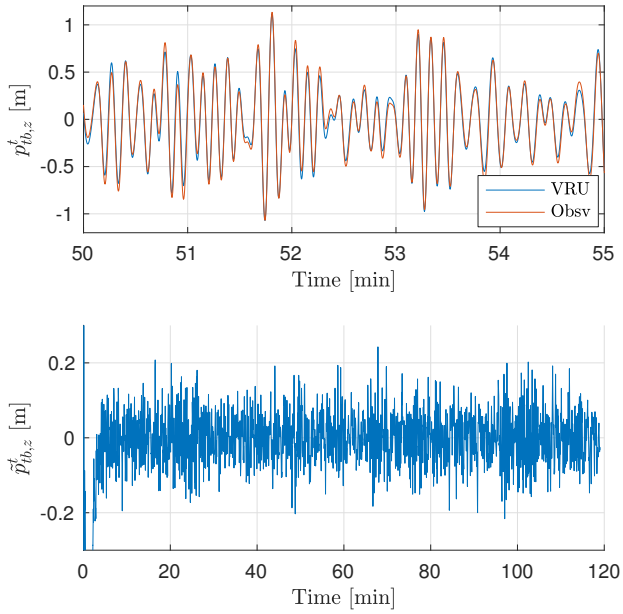

Figure 4.22: Stationkeeping: Heave estimates.

the last data set, indicating that the applied approach is sufficient for attitude estimation. Regarding the heave estimation, the proposed observer provides a heave estimate two per cent closer to the heave signal from the onboard VRU compared to the preceding observer. This is not close to the numbers obtained in the MC simulation. However, distinct conclusions are hard to draw since the comparison is not done relative ground truth, but to a black-box containing its own estimator, nor do we know the exact relative latency between the collected IMU data and the onboard VRU.

Validation during maneuvering

The statistics of the estimation performance obtained during maneuvering are shown in Table 4.14. Also here one can read from the statistics that both observer structures provide attitude estimates with similar error, while the heave estimates have 15.7 per cent less RMS error relative the VRU than the preceding observer. The heave estimate relative that of the VRU can be seen in Figure 4.25. Furthermore, the estimates of $\omega_e(t)$ and $\lambda_w(t)$ can be observed in Figure 4.26. The nominal encounter frequency $\omega_{e,\text{nom}}$ is slot-wise calculated using the heave reference signal from the VRU to obtain some benchmark value when the vessel moves with forward velocity in the south-west direction as seen in Figure 4.20b. In this scenario the FFT-based algorithm had marginally better performance expect between 25 and 35 minutes where the two other algorithms provided outputs closer to the peak

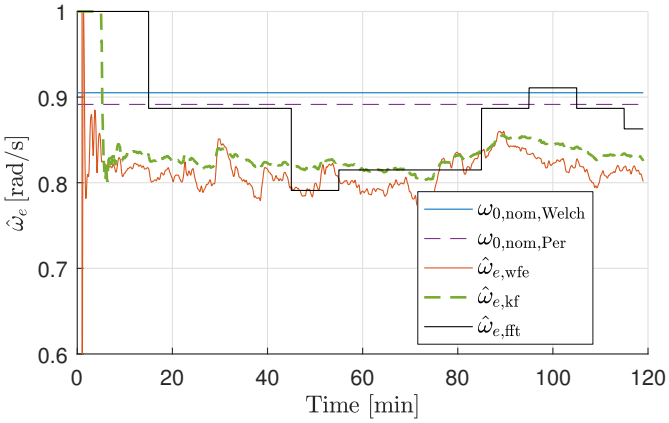

(a) Estimate of $\omega_e(t)$.

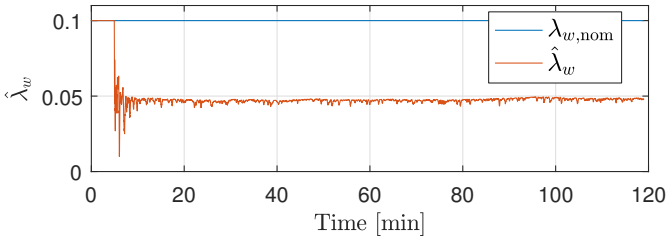

(b) Estimate $\lambda_w(t)$.

Figure 4.23: Stationkeeping: Estimates of wave-induced motion parameters.

Table 4.14: Statistics obtained based on data gathered during maneuvering in the Norwegian Sea.

	Roll	**Pitch**	**Heave**
Mean error	−0.0023°	−0.0246°	0.2047 cm
RMS error error	0.1183[a]°	0.1489[a]°	5.0210[a,b] cm
CAEE	2,368.9°	3,095.9°	1,074.8 m

[a] RMS error using Bryne et al. (2015b): Roll 0.1180°, pitch 0.1489°, heave 5.9561 cm.
[b] 5% RMS error margin: 2.0311 cm.

frequency of the heave reference signal. Furthermore, from the output of the time-domain algorithms one can clearly observe the slowly-varying change in the encounter frequency. The increase of $\hat{\omega}_e(t)$ observed in Figure 4.26, together with the information in Figure 4.27, indicate some degree of following seas.

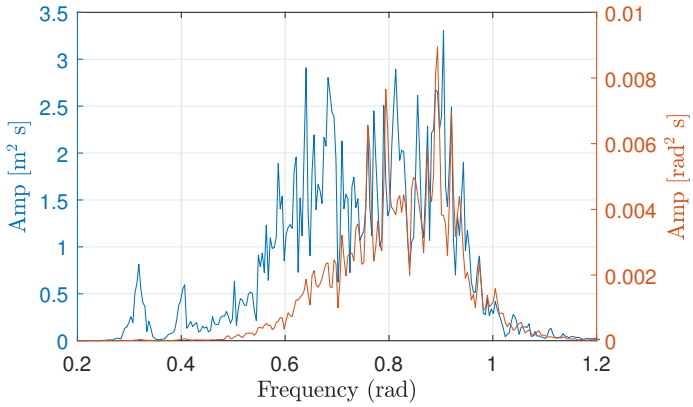

Figure 4.24: Stationkeeping: PSD of estimated pitch (red) compared to the PSD of the VRU's heave reference signal (blue).

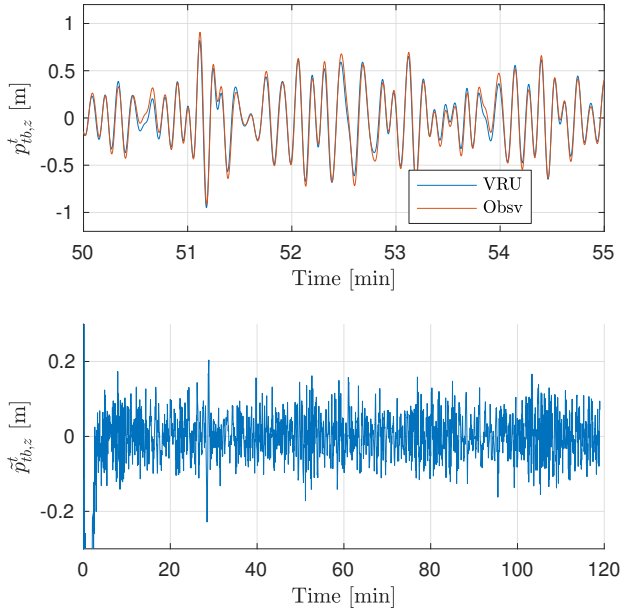

Figure 4.25: Maneuvering: Heave estimates.

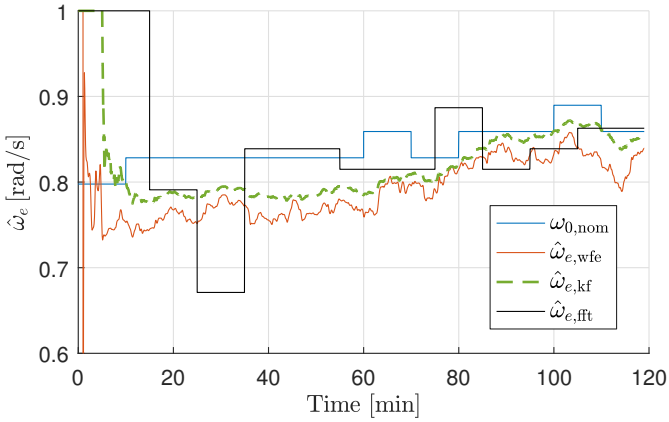

(a) Estimate of $\omega_e(t)$.

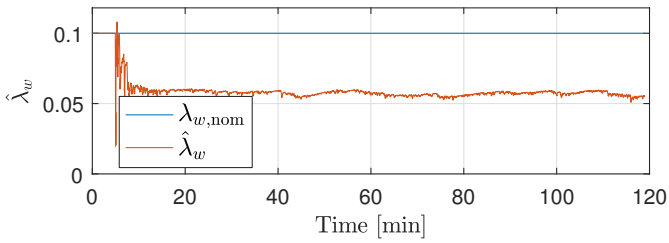

(b) Estimate $\lambda_w(t)$.

Figure 4.26: Maneuvering: Estimates of wave-induced motion parameters.

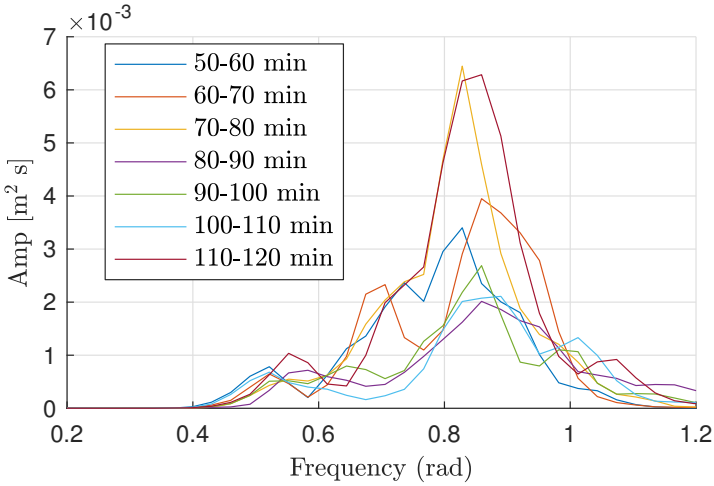

Figure 4.27: Maneuvering: Slot-wise PSD calculation of the heave reference signal. Peaks indicate the nominal encounter frequency $\omega_{e,\text{nom}}$.

Discussion

Since the comparison is not done relative absolute truth, there may be situations where the proposed solution is more accurate than the VRU 's estimates. Moreover, one can further observe that the spectrum of the heave reference signal is quite wide, indicating that the wave-induced motion in heave is quite far from being represented by a pure sine motion, which often VRUs are subjected to during validation testing.

4.4.9 Summary

Obtaining high-quality motion data of a marine vessel is both beneficial and a necessity in order to successfully and safely execute marine operations, oceanographic observations and transportation at sea. In the section six-degree-of-freedom vessel motions were estimated using a MEMS-based strapdown inertial navigation system, applying nonlinear theory, specifically tailored for marine surface vessels, aided by differential corrected global navigation satellite systems, compass and virtual vertical reference measurements. This included the introduction an error model in addition to using the zero VVR as aiding measurement to the vertical axes of the INS. Moreover, the model parameters are updated online.

The origin of the observer's error dynamics was proven to be USGES. The performance of the observer's attitude and heave estimates were evaluated using Monte Carlo simulations and validated with industry standard vertical reference units using data collected as sea. The results obtained are in compliance with industry standard specifications of roll, pitch and heave estimation. Furthermore, the heave estimation performance was improved compared to the work where the virtual vertical reference principle was introduced. In addition, both simulation and experimental results indicate online update of the error model is preferable compared to using fixed model parameters.

Further work could possible go into a in-depth study on the estimation of λ_w. Even though the results from the simulation study indicate that the algorithm used shows promise, both the simulation study and the experimental validation indicate some discrepancies in the estimation of the encounter frequency using the algorithm estimating λ_w compared to using Belleter et al. (2015) and the FFT-based algorithm. This may indicate that also the estimate of λ_w could be improved.

4.5 Conclusions

This chapter has presented two INSs using a feedback-interconnected nonlinear observer framework specifically tailored for marine surface vessels. The main contribution of the chapter, and the thesis, has been the use of a VVR concept to aid the vertical axes of the translational motion observer, the second of the two observers constituting the INS. The first INS utilized a Earth-fixed, non-rotating, NED frame

as navigation frame. The second INS utilized a tangent frame implementation. The origin of both nonlinear observers' error dynamics were proven to be USGES.

The benefit of using the VVR as an alternative to vertical GNSS aiding measurements was illustrated in simulations. The usage of the VVR resulted in significantly improved performance of both the attitude and the heave estimates. The former was a result of the latter due to kinematics couplings between the attitude and translational motion observer. Moreover, in the event changing GNSS noise characteristics, effects on the roll, pitch and heave estimation is minimized by using the VVR as vertical aiding.

The first VVR concept introduced in Bryne et al. (2014, 2015b) (Section 4.3) was later extended by including an VVR error model in Bryne et al. (n.d.) (Section 4.4) containing time-varying parameters related to the wave-induced motion of a surface vessel. This error model improved the heave estimation without affecting the performance of the attitude estimation. The results were evaluated using Monte Carlo simulations and validation using data gather at sea on an offshore vessel. The results indicate that the industry standard specification of five centimeters or five per cent heave root-mean-square estimation error is achievable by including the error model. Moreover, by including the error model, the TMO tuning becomes more intuitive, compared to the initial concept, since the measurement covariance can be chosen based on fact that the VVR is noise free. This in contrast to the initial concept where an ad hoc tuning approach was utilized.

Future works may include studying how adaptive tuning strategies based on the heave amplitude can be developed. In applications where absolute altitude above the seabed is of interest, the VVR concept should be modified to also include absolute vertical aiding from GNSS or HPR, e.g. in order to compensate for changes in altitude due to tides.

5 *INS on Ships*

This chapter covers additional aspects of INS, and in particular MEMS-based INS, on ships. This include choice of sensors, observer structures and tuning together with wave filtering of navigation systems data which is a vital part of the ship's control system.

Section 5.1 covers sensors and observer structures and is based upon Bryne et al. (2016) and Rogne et al. (n.d.b), and presents the outcome of the full-scale validation of MEMS-based INSs using NLOs. Section 5.2 covers the INS-based wave filtering of Bryne et al. (2015a).

5.1 Strapdown MEMS Sensor and Nonlinear Observers

This section is based on Bryne et al. (2016) and Rogne et al. (n.d.b), and presents results on full-scale verification of different NLOs for attitude estimation for ships, comparing two low-cost MEMS IMUs. The results are acquired by comparing the estimation result to well-proven industrial sensor systems providing roll, pitch and heave measurements for marine surface vessels. The verification consist of:

- Applying two NLOs —Mahony et al. (2008) and Bryne et al. (2015b), similar to that presented in Section 4.3 — for ship attitude estimation.
- Applying the NLOs and IMUs during two operational scenarios: Station-keeping with DP and turning maneuvers.
- Evaluation of heave estimation performance based on VVR aiding, presented in Chapter 4, using different sensors.

This work is based on Rogne et al. (n.d.b) and the preliminary work presented by Bryne et al. (2016). Rogne et al. (n.d.b) expanded the work with new tuning to better reflect performance achievable with NLOs, comparison with EKF, applying the VVR to a new observer, and an analysis of vibration and mechanical noise afflicting the IMUs.

A method for evaluating the aggregate performance of one's navigation solution (combination of sensor quality and algorithm) is to evaluate the INS's DR properties. Some results related to DR are presented in Appendix E.2.1. In addition a short discussion regarding the mentioned ship vibrations and other high-frequency motion picked up by the MEMS sensors is provided in Appendix E.2.2. Some ways to reduce or mitigate effects due to these vibrations are provided in this chapter, while a short presentation on how the sensed vibrations also might be taken advantage of is given in Appendix E.2.2.

5.1.1 IMU and ship sensor configuration

IMU and error sources

In addition to the specific forces and angular velocity, each of IMU measurements are contaminated with sensor biases, errors and noise as presented in Section 1.1.2. Furthermore, external noise may arise due to e.g. electrical and magnetic interference or stem from mechanical sources in the form of vibrations. In this work, it is assumed that error sources related to sensor nonlinearity, scale factors, misalignment, cross-coupling and g-sensitivity are compensated for in calibration by the manufacturer, or are otherwise neglectable. Sensor biases may also be calibrated for by the manufacturer or compensated for by in-silico temperature sensors. Nevertheless, some time-varying bias instability and run-to-run instability is often present with MEMS IMUs. Therefore, in contrast to Section 2.3.1, the accelerometer and rate gyro measurements are modeled as

$$\boldsymbol{f}^b_{\text{IMU}} = \boldsymbol{f}^b_{ib} + \boldsymbol{b}^b_{\text{acc}} + \boldsymbol{w}^b_{\text{acc}}, \tag{5.1}$$

$$\boldsymbol{\omega}^b_{\text{IMU}} = \boldsymbol{\omega}^b_{ib} + \boldsymbol{b}^b_{\text{gyro}} + \boldsymbol{w}^b_{\text{gyro}}, \tag{5.2}$$

where $\boldsymbol{f}^b_{ib}$ and $\boldsymbol{\omega}^b_{ib}$ are the true specific forces and angular rates, respectively. Moreover, the respective sensors biases are denoted $\boldsymbol{b}^b_{\text{acc}}$ and $\boldsymbol{b}^b_{\text{gyro}}$, while $\boldsymbol{w}^b_{\text{acc}}$ and $\boldsymbol{w}^b_{\text{gyro}}$ represent the sensor noise and vibration induced noise contained in the respective measurements. Both the accelerometer and gyro biases are assumed slowly time-varying,

$$\dot{\boldsymbol{b}}^b_{\text{gyro}} = \boldsymbol{w}^b_{b,\text{acc}}, \quad \dot{\boldsymbol{b}}^b_{\text{acc}} = \boldsymbol{w}^b_{b,\text{gyro}}, \tag{5.3}$$

where $\boldsymbol{w}^b_{b,\text{acc}}$ and $\boldsymbol{w}^b_{b,\text{gyro}}$ represent small variations in the biases (zero mean).

Ship sensor configuration

Several IMUs were installed on an offshore vessel operating in the Norwegian sea, equipped with a Rolls–Royce Marine DP system. The ship in question is owned and operated by Farstad Shipping. See Appendix E.1 for details. In this work the validation results presented are obtained using ADIS16485 and STIM300 MEMS IMUs. The sensor configuration used in the aided strapdown INS on board the offshore vessel was:

- 1x dGNSS PosRef system providing horizontal position measurements, $\boldsymbol{p}^t_{\text{GNSS}} = (p^t_{tb,x}, p^t_{tb,y})^\intercal$ at 1 Hz.
- VVR: $p^t_{tb,I} = 0$, for all $t \geq 0$ at 1000 Hz.
- 2x IMUs (ADIS16485 and STIM300) providing
  - Tri-axial accelerometer-based specific force measurements, $\boldsymbol{f}^b_{\text{IMU}}$,

  - Tri-axial angular rate measurements, $\boldsymbol{\omega}^b_{\text{IMU}}$,

  both interfaced at 1000 Hz

- Yaw measurements from a triple-redundant gyrocompasses solution, ψ_c, at 5 Hz.

The IMU measurements are filtered with a 6th order lowpass Butterworth filter with a cutoff frequency of 5 Hz. The specifications of the IMUs installed on the offshore vessel are presented in Table E.1. The sensors were fused using the tangent frame mechanization of the strapdown equations (Section 2.2.3) in addition to the kinematic augmentation, (4.46), motivated by the introduction of the VVR measurement as presented Section 4.4, for fusing IMU, compass, GNSS and VVR measurements. In addition, roll (ϕ) and pitch (θ) signals, obtained from a VRU at 5 Hz, are used for comparison. See Table E.2, Appendix E, for manufacturer specifications.

Effects of sensor biases and mounting errors on the attitude estimation

The IMU sensor biases have direct effects on the attitude estimates. The gyro bias influences the attitude dynamically, implying that the unit rotates slower or faster than what is physically happening. The accelerometer biases affect the attitude estimation statically. As stated in e.g. Fossen (2011, Ch. 11.5.2), roll and pitch angles may be obtained in static conditions using accelerometers or inclinometers,

$$\phi = \tan^{-1}\left(\frac{f^b_{\text{IMU},y}}{f^b_{\text{IMU},z}}\right), \tag{5.4}$$

$$\theta = -\tan^{-1}\left(\frac{f^b_{\text{IMU},x}}{\sqrt{{f^b_{\text{IMU},y}}^2 + {f^b_{\text{IMU},z}}^2}}\right), \tag{5.5}$$

making the initialization of roll and pitch (known as leveling) susceptible to accelerometer biases. Similar to accelerometer bias, mounting errors also contribute to static roll and pitch errors. Table 5.1 describe how the different IMU noise and error sources affect the attitude estimation. Similar to using accelerometers in static condition, also using them as measurement vectors in the attitude estimation below, in Section 5.1.2, may be problematic since the angular rate sensor biases and accelerometer biases are not mutually uniformly observable (Farrell, 2008, Ch. 11.9). However, in most situations it is the only option to obtain a roll and pitch like reference. The theory of Grip et al. (2012a, 2013, 2016) either assumes zero accelerometer bias or that it is possible to compensate for it through estimation if the motion is PE, making it possible to differentiate the effects affecting the attitude and the bias estimation. Accelerometer bias compensation for the attitude estimation, using the bias estimate $\bar{\boldsymbol{b}}^b_{\text{acc}}$, can be done statically based on calibration

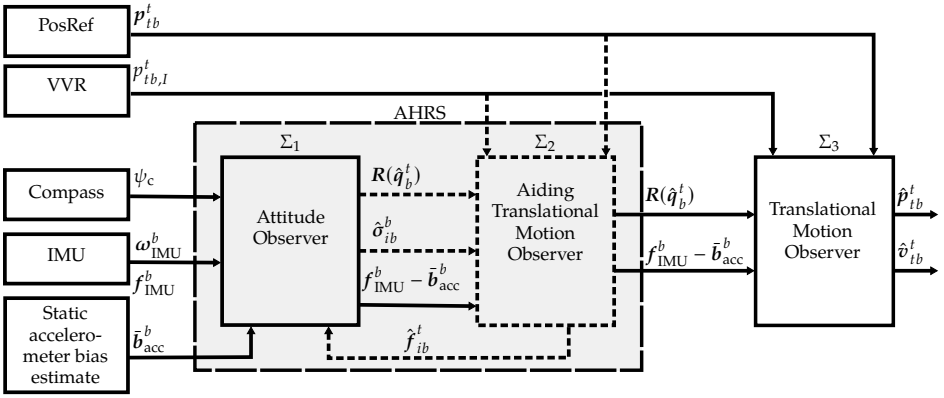

Figure 5.1: Observer structure. Depending on configuration, the AHRS may be aided by a TMO, itself aided by PosRefs and VVR measurements.

results or by online estimation. Here, a constant accelerometer bias compensation is applied, obtained in port, based on the VRU references available, prior to the attitude observer verification scenarios. As presented in Bryne et al. (2016), static accelerometer bias compensation proved successful for at least several days after the initial calibration. This was due to the accelerometer bias in-run stability of the MEMS IMUs installed onboard the vessel.

5.1.2 Nonlinear observers

The sensor configuration was tested and compared using two nonlinear attitude observers, here denoted A and B, respectively. NLO A (Mahony et al., 2008) receives no aiding from a TMO unlike NLO B (Grip et al., 2013; Bryne et al., 2015b). An overview of the observer structures is shown in Figure 5.1. Both attitude observers estimates the attitude between the $\{b\}$ and the $\{t\}$ frame, as in Section 4.4, and the gyro bias, based on model of (5.3), resulting in the observer

Table 5.1: Main error sources that affect the attitude estimation.

Error source	**Effect on attitude estimate**
Gyro bias	Dynamic
Accelerometer bias	Static
Mounting errors	Static
Vibrations	Dynamic[a]

[a] Not necessarily oscillatory. If coning (Groves, 2013, Ch. 5.5.4) occurs, the attitude estimates will drift.

Table 5.2: NLO reference vectors configuration.

	Vector $\underline{c}^t$	Vector $\underline{f}^t$
NLO A	Unit vector North	$-\boldsymbol{g}_b^t/\| - \boldsymbol{g}_b^t\|_2$
NLO B	Unit vector North	$\hat{\boldsymbol{f}}_{ib}^t/\|\hat{\boldsymbol{f}}_{ib}^t\|_2$ through feedback from VVR and PosRef injection

equations,

$$\Sigma_1 : \begin{cases} \dot{\hat{\boldsymbol{q}}}_b^t = \frac{1}{2}\hat{\boldsymbol{q}}_b^t \otimes \begin{pmatrix} 0 \\ \hat{\boldsymbol{\omega}}_{ib}^b \end{pmatrix} - \frac{1}{2}\begin{pmatrix} 0 \\ \boldsymbol{\omega}_{it}^t \end{pmatrix} \otimes \hat{\boldsymbol{q}}_b^t, & (5.6a) \\ \hat{\boldsymbol{\omega}}_{ib}^b = \boldsymbol{\omega}_{\text{IMU}}^b - \hat{\boldsymbol{b}}_{\text{gyro}}^b + \hat{\boldsymbol{\sigma}}_{ib,j}^b, & (5.6b) \\ \dot{\hat{\boldsymbol{b}}}_{\text{gyro}}^b = \text{Proj}\left(\hat{\boldsymbol{b}}_{\text{gyro}}^b, -k_I(t)\hat{\boldsymbol{\sigma}}_{ib,j}^b\right), & (5.6c) \end{cases}$$

where, as earlier, the gain $k_I(t)$ is associated with the gyro bias estimation, and Proj$(\star, \star)$ denotes the gyro bias projection algorithm of Grip et al. (2012a) and the reference therein. The index j represents the respective attitude observer. The difference between the two observers lies in the injection term, $\hat{\boldsymbol{\sigma}}_{ib}^b$, j, given as

$$\hat{\boldsymbol{\sigma}}_{ib}^b = k_1(t)\underline{\boldsymbol{v}}_1^b \times \boldsymbol{R}^\intercal(\hat{\boldsymbol{q}}_b^t)\underline{\boldsymbol{v}}_1^t + k_2(t)\underline{\boldsymbol{v}}_2^b \times \boldsymbol{R}^\intercal(\hat{\boldsymbol{q}}_b^t)\underline{\boldsymbol{v}}_2^t, \tag{5.7}$$

where $\underline{\boldsymbol{v}}_1^b$ and $\underline{\boldsymbol{v}}_2^b$ are the measurement vectors and $\underline{\boldsymbol{v}}_1^t$ and $\underline{\boldsymbol{v}}_2^t$ are the reference vectors, calculated using

$$\underline{\boldsymbol{v}}_1^b = \underline{\boldsymbol{f}}^b, \quad \underline{\boldsymbol{v}}_2^b = \underline{\boldsymbol{f}}^b \times \underline{\boldsymbol{c}}^b,$$
$$\underline{\boldsymbol{v}}_1^t = \underline{\boldsymbol{f}}^t, \quad \underline{\boldsymbol{v}}_2^t = \underline{\boldsymbol{f}}^t \times \underline{\boldsymbol{c}}^t.$$

An overview of the main differences between NLO A and B can be found in Table 5.2. For both observers, $\underline{\boldsymbol{c}}^b = \left(\cos(\psi_c), -\sin(\psi_c), 0\right)^\intercal$ and $\underline{\boldsymbol{c}}^t = (1, 0, 0)^\intercal$ are chosen as in Chapter 4. Both $\underline{\boldsymbol{c}}^b$ and $\underline{\boldsymbol{c}}^t$ are naturally normalized. As stated earlier, by using normalized measurement/reference vector pairs, the gains k_1 and k_2 can be considered as the NLO's complimentary filter cutoff frequencies. Hence, for motion frequencies higher than k_1 and k_2, the angular rate measurements are the primary source of attitude information, while for frequencies lower than k_1 and k_2, the respective measurement/reference vectors are the primary source of attitude information.

Nonlinear attitude observer A

For attitude observer A, $\hat{\boldsymbol{\sigma}}_{ib,A}^b$ is implemented with $\underline{\boldsymbol{f}}^b$ and $\underline{\boldsymbol{f}}^t$ based on the injection term similar to Mahony et al. (2008) by choosing

$$\underline{\boldsymbol{f}}^b = \frac{\boldsymbol{f}_{\text{IMU}}^b - \bar{\boldsymbol{b}}_{\text{acc}}^b}{\|\boldsymbol{f}_{\text{IMU}}^b - \bar{\boldsymbol{b}}_{\text{acc}}^b\|_2}, \quad \underline{\boldsymbol{f}}^t = \frac{-\boldsymbol{g}_b^t}{\| - \boldsymbol{g}_b^t\|_2}, \tag{5.8}$$

where the local gravity vector is utilized as reference vector based on the assumption that the specific force in the navigation frame is dominated by $-\boldsymbol{g}_b^t$.

Nonlinear attitude observer B

Regarding attitude observer B, the reference vector $\underline{\boldsymbol{f}}^t$, in the calculation of $\hat{\boldsymbol{\sigma}}_{ib,B}^b$, is chosen as

$$\underline{\boldsymbol{f}}^t = \frac{\text{sat}_{M_f}(\hat{\boldsymbol{f}}_{ib}^t)}{\|\text{sat}_{M_f}(\hat{\boldsymbol{f}}_{ib}^t)\|_2}, \tag{5.9}$$

where $\hat{\boldsymbol{f}}_{ib}^t$ is estimated using a modified version of the feedback-interconnected observer framework Grip et al. (2013), using the TMOs of Bryne et al. (2014, 2015b), where the VVR-aiding concept is applied. Moreover, by providing the specific force estimate $\hat{\boldsymbol{f}}_{ib}^t$, to Σ_1, the attitude estimation is potentially more accurate when the vessel is accelerated compared to using $-\boldsymbol{g}_b^t$ as reference vector. $\hat{\boldsymbol{f}}_{ib}^t$, provided to attitude observer B, is estimated using the TMO Σ_2, see Figure 5.1, which has injection from a PosRef in addition to the VVR measurement. The TMO used to estimate $\hat{\boldsymbol{f}}_{ib}^t$, utilized by NLO B, takes the form of

$$\Sigma_2 : \begin{cases} \dot{\hat{p}}_{tb,I}^t = \hat{p}_{tb,z}^t + \vartheta K_{p_I p_I} \tilde{p}_{tb,I}^t, & \text{(5.10a)} \\ \dot{\hat{\boldsymbol{p}}}_{tb}^t = \hat{\boldsymbol{v}}_{tb}^t + \vartheta^2 \begin{pmatrix} \boldsymbol{0}_{2\times 1} \\ K_{pp_I} \end{pmatrix} \tilde{p}_{tb,I}^t + \vartheta \begin{pmatrix} \boldsymbol{K}_{pp} \\ \boldsymbol{0}_{1\times 2} \end{pmatrix} \tilde{\boldsymbol{p}}_{tb}^t, & \text{(5.10b)} \\ \dot{\hat{\boldsymbol{v}}}_{tb}^t = -2\boldsymbol{S}(\boldsymbol{\omega}_{ie}^t)\boldsymbol{v}_{tb}^t + \hat{\boldsymbol{f}}_{ib}^t + \boldsymbol{g}_b^t + \vartheta^3 \begin{pmatrix} \boldsymbol{0}_{2\times 1} \\ K_{vp_I} \end{pmatrix} \tilde{p}_{tb,I}^t + \vartheta^2 \begin{pmatrix} \boldsymbol{K}_{vp} \\ \boldsymbol{0}_{1\times 2} \end{pmatrix} \tilde{\boldsymbol{p}}_{tb}^t, & \text{(5.10c)} \\ \dot{\hat{\boldsymbol{\xi}}}_{ib}^t = -\boldsymbol{R}(\hat{\boldsymbol{q}}_b^t)\boldsymbol{S}(\hat{\boldsymbol{\sigma}}_{ib,B}^b)\left(\boldsymbol{f}_{\text{IMU}}^b - \bar{\boldsymbol{b}}_{\text{acc}}^b\right) \\ \qquad\qquad + \vartheta^4 \begin{pmatrix} \boldsymbol{0}_{2\times 1} \\ K_{\xi p_I} \end{pmatrix} \tilde{p}_{tb,I}^t + \vartheta^3 \begin{pmatrix} \boldsymbol{K}_{\xi p} \\ \boldsymbol{0}_{1\times 2} \end{pmatrix} \tilde{\boldsymbol{p}}_{tb}^t, & \text{(5.10d)} \\ \hat{\boldsymbol{f}}_{ib}^t = \boldsymbol{R}(\hat{\boldsymbol{q}}_b^t)\left(\boldsymbol{f}_{\text{IMU}}^b - \bar{\boldsymbol{b}}_{\text{acc}}^b\right) + \boldsymbol{\xi}_{ib}^t, & \text{(5.10e)} \end{cases}$$

similar to Section 4.4.4, however, here without the VVR error model, where $\tilde{p}_{tb,I}^t = p_{tb,I}^t - \hat{p}_{tb,I}^t$, $\tilde{\boldsymbol{p}}_{tb}^t = \boldsymbol{p}_{\text{GNSS}}^t - (\hat{p}_{tb,x}^t, \hat{p}_{tb,y}^t)^\intercal$. $K_{[\cdot]p_I}$ and $\boldsymbol{K}_{[\cdot]p}$ are fixed gains, while $\vartheta \geq 1$ is a tuning parameter used to guarantee stability. The gains may be chosen such that the feedback interconnection $\Sigma_1 - \Sigma_2$ possesses uniform semiglobal exponential stability properties, cf. Section 4.3.5. Here, Σ_2 is referred to as the *aiding* TMO, cf. Figure 5.1, since it is primarily used to aid NLO B by providing an estimate of $\boldsymbol{f}_{ib}^t$.

In state-space form, the TMO is represented as:

$$\dot{\hat{\boldsymbol{x}}}_a = \boldsymbol{A}_a \hat{\boldsymbol{x}}_a + \boldsymbol{B}_a \boldsymbol{u}_a + \boldsymbol{D}_a + \vartheta \boldsymbol{L}_\vartheta^{-1} \boldsymbol{K}_a \boldsymbol{E}_\vartheta \left(\boldsymbol{y} - \boldsymbol{C}\hat{\boldsymbol{x}}_a\right) \tag{5.11}$$

with the state vectors, output measurement and input

$$\begin{aligned}\hat{\boldsymbol{x}}_a &= \left(\hat{p}^t_{tb,I}; \hat{\boldsymbol{p}}^t_{tb}; \hat{\boldsymbol{v}}^t_{tb}; \hat{\boldsymbol{\xi}}^t_{ib}\right),\\ \boldsymbol{y} &= \left(p^n_I; \boldsymbol{p}^t_{\text{GNSS}}\right),\\ \boldsymbol{u} &= \begin{pmatrix} \boldsymbol{f}^b_{\text{IMU}} - \bar{\boldsymbol{b}}^b_{\text{acc}} \\ -\boldsymbol{S}\left(\hat{\boldsymbol{\sigma}}^b_{ib,B}\right)(\boldsymbol{f}^b_{\text{IMU}} - \bar{\boldsymbol{b}}^b_{\text{acc}}) \end{pmatrix},\end{aligned}$$

the system matrices

$$\boldsymbol{A}_a = \begin{pmatrix} 0 & \begin{pmatrix}0 & 0 & 1\end{pmatrix} & \boldsymbol{0}_{1\times3} & \boldsymbol{0}_{1\times3} \\ \boldsymbol{0}_{3\times1} & \boldsymbol{0}_{3\times3} & \boldsymbol{I}_3 & \boldsymbol{0}_{3\times3} \\ \boldsymbol{0}_{3\times1} & \boldsymbol{0}_{3\times3} & \boldsymbol{0}_{3\times3} & \boldsymbol{I}_3 \\ \boldsymbol{0}_{3\times1} & \boldsymbol{0}_{3\times3} & \boldsymbol{0}_{3\times3} & \boldsymbol{0}_{3\times3} \end{pmatrix}, \quad \boldsymbol{B}_a = \begin{pmatrix} \boldsymbol{0}_{1\times3} & \boldsymbol{0}_{1\times3} \\ \boldsymbol{0}_{3\times3} & \boldsymbol{0}_{3\times3} \\ \boldsymbol{R}(\hat{\boldsymbol{q}}^t_b) & \boldsymbol{0}_{3\times3} \\ \boldsymbol{0}_{3\times3} & \boldsymbol{R}(\hat{\boldsymbol{q}}^t_b) \end{pmatrix},$$

$$\boldsymbol{C}_a = \begin{pmatrix} \boldsymbol{I}_3 & \boldsymbol{0}_{3\times7} \end{pmatrix}, \quad \boldsymbol{D}_a = \begin{pmatrix} 0 & \boldsymbol{0}_{3\times1}; & -2\boldsymbol{S}(\boldsymbol{\omega}^t_{ie})\boldsymbol{v}^t_{tb} + \boldsymbol{g}^t_b & \boldsymbol{0}_{3\times1} \end{pmatrix},$$

and the gain related matrices

$$\begin{aligned}\boldsymbol{K}_a &= \begin{pmatrix} K_{p_Ip_I} & \boldsymbol{0}_{1\times2} \\ \boldsymbol{0}_{2\times1} & \boldsymbol{K}_{pp} \\ K_{pp_I} & \boldsymbol{0}_{1\times2} \\ \boldsymbol{0}_{2\times1} & \boldsymbol{K}_{vp} \\ K_{vp_I} & \boldsymbol{0}_{1\times2} \\ \boldsymbol{0}_{2\times1} & \boldsymbol{K}_{\xi p} \\ K_{\xi p_I} & \boldsymbol{0}_{1\times2} \end{pmatrix},\\ \boldsymbol{L}_\vartheta &= \text{blockdiag}\left(1, \frac{1}{\vartheta}\boldsymbol{I}_3, \frac{1}{\vartheta^2}\boldsymbol{I}_3, \frac{1}{\vartheta^3}\boldsymbol{I}_3\right),\\ \boldsymbol{E}_\vartheta &= \boldsymbol{C}_a\boldsymbol{L}_\vartheta\boldsymbol{C}_a^\dagger,\end{aligned}$$

where the latter term always satisfies Lemma 4.1.

Translational motion observer

Even though the gyro and accelerometer biases are not mutually uniformly observable without the vessel accelerating and rotating (Farrell, 2008, Ch. 11.9), some accelerometer bias compensation has to be performed in order to obtain an INS with reasonable DR capabilities. For $\Sigma_1 - \Sigma_2$, a fixed pre-compensated accelerometer bias $\bar{\boldsymbol{b}}^b_{\text{acc}}$ is applied for attitude estimation. However, some acceleration errors may be present owing to some in-run bias instability, w.r.t. Table E.1 of Appendix E. To atone for this, an additional TMO, Σ_3, was utilized including an estimate of the residual accelerometer bias $\hat{\boldsymbol{b}}^b_{\text{acc}}$, inspired by the observer of Fossen (2011, Ch. 11.5.1). Observer Σ_3 for additional accelerometer bias estimation can

be described as follows:

$$\dot{\hat{\boldsymbol{x}}} = \boldsymbol{A}(t, \hat{\boldsymbol{q}}_b^t)\hat{\boldsymbol{x}} + \boldsymbol{B}(t, \hat{\boldsymbol{q}}_b^t)\boldsymbol{u} + \boldsymbol{D}(t, \hat{\boldsymbol{x}}) + \boldsymbol{K}(t)\left(\boldsymbol{y} - \boldsymbol{C}\hat{\boldsymbol{x}}\right). \tag{5.12}$$

with the state space,

$$\hat{\boldsymbol{x}} = \left(p_{tb,I}^t; \hat{\boldsymbol{p}}_{tb}^t; \hat{\boldsymbol{v}}_{tb}^t; \hat{\boldsymbol{b}}_{\text{acc}}^b\right),$$

measurement $\boldsymbol{y}$ and input $\boldsymbol{u}$,

$$\begin{aligned}\boldsymbol{y} &= \left(p_{tb,I}^n; \boldsymbol{p}_{\text{GNSS}}^t\right),\\ \boldsymbol{u} &= \boldsymbol{f}_{\text{IMU}}^b - \bar{\boldsymbol{b}}_{\text{acc}}^b,\end{aligned}$$

and the system matrices and vector

$$\boldsymbol{A}(t, \hat{\boldsymbol{q}}_b^t) = \begin{pmatrix} 0 & \begin{pmatrix}0 & 0 & 1\end{pmatrix} & \boldsymbol{0}_{1\times3} & \boldsymbol{0}_{1\times3} \\ \boldsymbol{0}_{3\times1} & \boldsymbol{0}_{3\times3} & \boldsymbol{I}_3 & \boldsymbol{0}_{3\times3} \\ \boldsymbol{0}_{3\times1} & \boldsymbol{0}_{3\times3} & \boldsymbol{0}_{3\times3} & -\boldsymbol{R}(\hat{\boldsymbol{q}}_b^t) \\ \boldsymbol{0}_{3\times1} & \boldsymbol{0}_{3\times3} & \boldsymbol{0}_{3\times3} & \boldsymbol{0}_{3\times3} \end{pmatrix}, \quad \boldsymbol{B}(t, \hat{\boldsymbol{q}}_b^t) = \begin{pmatrix} \boldsymbol{0}_{1\times3} \\ \boldsymbol{0}_{3\times3} \\ \boldsymbol{R}(\hat{\boldsymbol{q}}_b^t) \\ \boldsymbol{0}_{3\times3} \end{pmatrix},$$

$$\boldsymbol{C} = \begin{pmatrix}\boldsymbol{I}_3 & \boldsymbol{0}_{3\times7}\end{pmatrix}, \quad \boldsymbol{D}(t, \hat{\boldsymbol{x}}) = \begin{pmatrix}0; & \boldsymbol{0}_{3\times1}; & -2\boldsymbol{S}(\boldsymbol{\omega}_{ie}^t)\hat{\boldsymbol{v}}_{tb}^t + \boldsymbol{g}_b^t; & \boldsymbol{0}_{3\times1}\end{pmatrix},$$

considering $\boldsymbol{R}(\hat{\boldsymbol{q}}_b^t)$ as an external signal provided to Σ_3 by Σ_1. Thus, $\boldsymbol{A}(t, \hat{\boldsymbol{q}}_b^t)$ is treated as time-varying system matrix and the TMO's error dynamics is rendered exponentially stable by employing a Riccati-equation and gain similar to the Kalman and Bucy (1961) filter,

$$\boldsymbol{K}(t) = \boldsymbol{P}(t)\boldsymbol{C}^\intercal\boldsymbol{R}^{-1}(t), \tag{5.13}$$

$$\dot{\boldsymbol{P}}(t) = \boldsymbol{A}(t)\boldsymbol{P}(t) + \boldsymbol{P}(t)\boldsymbol{A}^\intercal(t) - \boldsymbol{K}(t)\boldsymbol{R}(t)\boldsymbol{K}^\intercal(t) + \boldsymbol{G}(t)\boldsymbol{Q}(t)\boldsymbol{G}^\intercal(t), \tag{5.14}$$

with

$$\boldsymbol{G}(t) = \begin{pmatrix} \boldsymbol{0}_{1\times3} & \boldsymbol{0}_{1\times3} \\ \boldsymbol{0}_{3\times3} & \boldsymbol{0}_{3\times3} \\ \boldsymbol{R}(\hat{\boldsymbol{q}}_b^t) & \boldsymbol{0}_{3\times3} \\ \boldsymbol{0}_{3\times3} & \boldsymbol{I}_3 \end{pmatrix}, \tag{5.15}$$

where the explicite dependency of $\hat{\boldsymbol{q}}_b^t$ have been omitted in (5.13)–(5.15). By using (5.14)–(5.15), the process noise associated with the accelerometer in $\boldsymbol{Q}(t)$ is related to the navigation frame, $\{t\}$, through $\boldsymbol{R}(\hat{\boldsymbol{q}}_b^t)$. The actual implementation of the observer is done in discrete time, as in for instance Bryne et al. (2017a), cf. Chapter 3 and Section 3.3.6, using the discrete time versions of the Riccati equation and Kalman gain. Furthermore, $\boldsymbol{Q}(t)$ and $\boldsymbol{R}(t)$ are covariance matrices chosen according to sensor noise and desired tuning, considered next.

5.1.3 Observer tuning

Σ_1 was tested with the $k_1 = 0.1, k_2 = 0.1, k_I = 0.05$. For Σ_2, the parameter $\vartheta = 1$ was chosen. In order to calculate the gains $K_{[\cdot]p_I}$ and $\boldsymbol{K}_{[\cdot]p}$, the continuous-time steady-state Riccati equation, similar to the (Kalman and Bucy, 1961) filter, and akin to Σ_3,

$$\begin{aligned}\boldsymbol{K}_a &= \boldsymbol{P}_{a,\infty}\boldsymbol{C}_a^\intercal \boldsymbol{R}_a^{-1} \\ \boldsymbol{0} &= \boldsymbol{A}_a\boldsymbol{P}_{a,\infty} + \boldsymbol{P}_{a,\infty}\boldsymbol{A}_a^\intercal - \boldsymbol{K}_a\boldsymbol{R}_a\boldsymbol{K}_a^\intercal + \boldsymbol{B}_a\boldsymbol{Q}_a\boldsymbol{B}_a^\intercal\end{aligned}$$

was employed using the following covariance matrices for process and measurement noise

$$\begin{aligned}\boldsymbol{Q}_a &= \text{blockdiag}(0.1^2 \cdot \boldsymbol{I}_3, 0.15^2 \cdot \boldsymbol{I}_3), \\ \boldsymbol{R}_a &= \text{blockdiag}(35^2, 2^2 \cdot \boldsymbol{I}_2),\end{aligned}$$

where the first element of $\boldsymbol{Q}_a$ is the variance associated with the input $\boldsymbol{f}^b_{\text{IMU}}$, and the second element is associated with the cross product of $\hat{\boldsymbol{\sigma}}^b_{ib,B}$ and $\boldsymbol{f}^b_{\text{IMU}}$ as seen in (5.10d). Furthermore, the first element of $\boldsymbol{R}_a$ is a value representing VVR measurement uncertainty, and the second element is the GNSS horizontal measurement variance. This results in the following gains:

$$\begin{aligned}K_{p_Ip_I} &= 0.6368, \\ K_{pp_I} &= 0.2028, \boldsymbol{K}_{pp} = 0.7950 \cdot \boldsymbol{I}_2, \\ K_{vp_I} &= 0.0378, \boldsymbol{K}_{vp} = 0.3160 \cdot \boldsymbol{I}_2, \\ K_{\xi p_I} &= 0.0035, \boldsymbol{K}_{\xi p} = 0.0612 \cdot \boldsymbol{I}_2.\end{aligned}$$

For Σ_3, the covariance matrices,

$$\begin{aligned}\boldsymbol{Q} &= \text{blockdiag}(0.1^2 \cdot \boldsymbol{I}_3,\ 0.001^2 \cdot \boldsymbol{I}_3), \\ \boldsymbol{R} &= \text{blockdiag}(20^2,\ 2^2 \cdot \boldsymbol{I}_2),\end{aligned}$$

were chosen w.r.t. (5.13)–(5.14) and the calculation of the gain $\boldsymbol{K}$. As for Σ_2, the first element of $\boldsymbol{Q}$ is the variance associated with $\boldsymbol{f}^b_{\text{IMU}}$, but the second element is the driving process noise associated with the accelerometer bias estimate, $\hat{\boldsymbol{b}}^b_{\text{acc}}$. $\boldsymbol{R}$ represents exactly the same as $\boldsymbol{R}_a$, albeit tuned a bit differently for the VVR measurement. In addition, all matrices were tuned in continuous time, and then converted to discrete time equivalents in the actual implementation.

5.1.4 Full-scale testing: Attitude estimation

In this section, the results related of the attitude estimation using the two distinct attitude observers and two particular MEMS IMUs, during two different operations undertaken by the offshore vessel, are presented. The first operation

is stationkeeping during DP. The second is a maneuvering operation, where the vessel changes heading while surging forward. Plots of the respective path tracks over two hours are shown in Figures 4.20a and 4.20b in Section 4.4.8, respectively.

The attitude estimation is evaluated using the mean error, RMS error and CAEE metrics, where the latter is defined in (4.42) on page 71, using the onboard VRU as reference. Also, a comparison with the output of NavLab (Gade, 2004) is provided. NavLab is a navigation software suite based on the EKF, and has been applied in the industry on a wide range of systems, including in defense and maritime application. The metrics were calculated based on the last 90 minutes of the data sets.

DP

An excerpt of the attitude estimates obtained using the STIM300 IMU and NLO B in DP is shown in Figure 5.2a. The estimation errors relative the VRU and gyrocompass measurements over two hours are shown in Figure 5.2b. The statistics obtained using NLO A as attitude estimator in DP are presented in Table 5.3. Similar statistics obtained using NLO B and NavLab are presented in Table 5.4 and 5.5, respectively. Examples of typical angular rate bias estimates are shown in Figure 5.3.

Results

From Tables 5.3–5.5 one can see that the choice of estimator, to perform the attitude estimation, in DP is more important than the choice of sensor, at least when it comes to our selection of IMUs. It is evident from the results that both the RMS error and CAEE is improved using NLO B and NavLab compared to the results obtained with A. This is particularly noticeable in roll. The mean errors are approximately the same, where the differences are on such a scale that the practical effects of such errors, for instance in lever arm compensation, are negligible. For NavLab, larger differences are observed between the IMUs than is the case for the NLOs.

Table 5.3: Attitude error statistics using NLO A in DP.

	ADIS16485	**STIM300**
Roll mean error [deg]	0.0036	0.0003
Pitch mean error [deg]	0.0090	0.0070
Roll RMS error [deg]	0.1113	0.1151
Pitch RMS error [deg]	0.1080	0.1071
Roll CAEE [deg]	2361.8	2442.7
Pitch CAEE [deg]	2254.9	2239.7

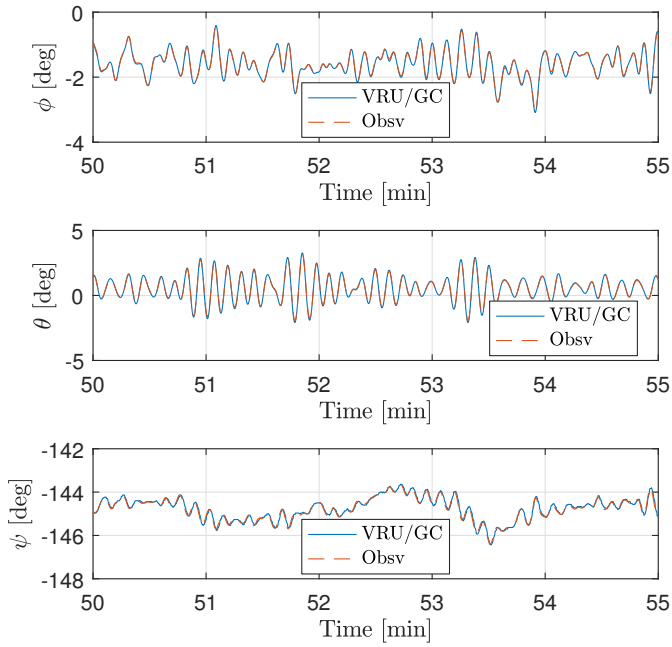

(a) Attitude estimates.

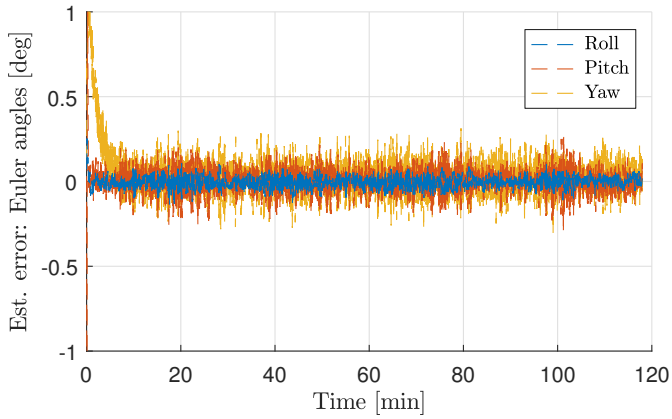

(b) Attitude estimation error.

Figure 5.2: Attitude estimation using NLO B and STIM300.

This could mean that the tuning of NavLab is more sensitive to sensor changes. In Bryne et al. (2016) even larger differences in the RMS errors were observed between NLO A and B were the gains were chosen to be $k_1 = 0.5, k_2 = 0.5, k_I = 0.08$. In addition, the results related to the RMS error obtained here with NLO B is improved compared to the results obtained in Section 4.4.8, which utilized the extended VVR concept, exploiting an error model (Sections 4.4.3–4.4.4) and

Table 5.4: Attitude error statistics using NLO B in DP.

	ADIS16485	**STIM300**
Roll mean error [deg]	-0.0007	-0.0044
Pitch mean error [deg]	0.0047	0.0016
Roll RMS error [deg]	0.0363	0.0299
Pitch RMS error [deg]	0.0670	0.0649
Roll CAEE [deg]	759.80	628.99
Pitch CAEE [deg]	1406.0	1357.5

Table 5.5: Attitude error statistics using Navlab in DP.

	ADIS16485	**STIM300**
Roll mean error [deg]	-0.0193	-0.0094
Pitch mean error [deg]	0.0463	0.0063
Roll RMS error [deg]	0.0417	0.0287
Pitch RMS error [deg]	0.0813	0.0628
Roll CAEE [deg]	881.89	610.79
Pitch CAEE [deg]	1731.1	1233.3

unfiltered measurements from the ADIS16485 IMU. However the results obtained in Section 4.4.8 yield less RMS error relative the VRUs than those obtained using NLO A based on filtered inertial measurements.

Maneuvering

The statistics obtained using attitude NLO A during the turning maneuvers are presented in Table 5.6. Similar statistics obtained using NLO B and NavLab are presented in Table 5.7 and in Table 5.8, respectively.

Results

Comparable results to what were obtained in DP, are achieved during the maneuvers as shown in Tables 5.6–5.8. NLO B and NavLab outperforms NLO A considering RMS error and CAEE in roll and pitch, but not as much as in the DP case. As opposed to the DP case, NavLab yielded virtually no difference in output between the two sensors. Similar to the results from DP, the estimation RMS error is reduced using filtered IMU measurements and NLO B compared to Section 4.4.8 when applying the same ADIS16485 IMU.

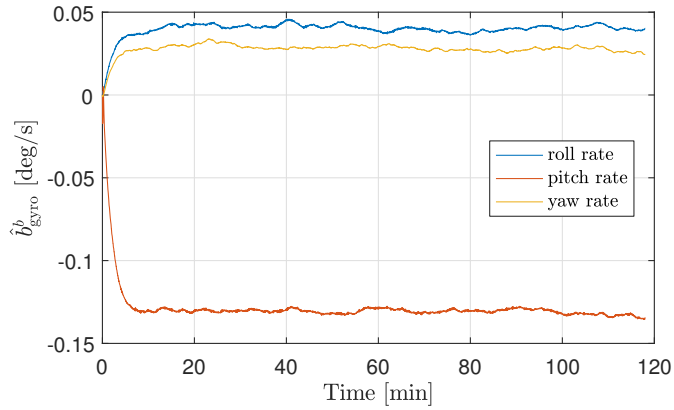

(a) ADIS16485

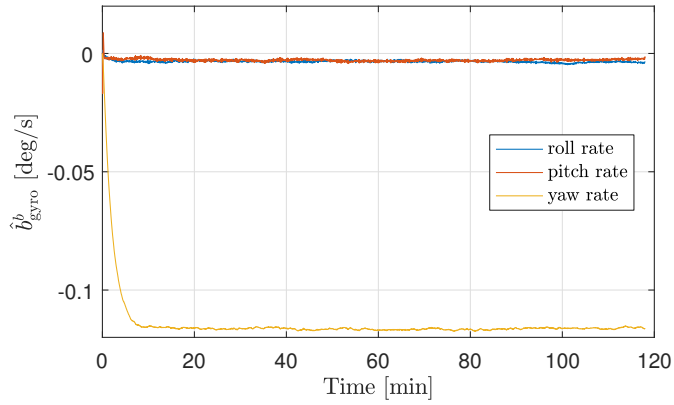

(b) STIM300

Figure 5.3: Typical angular rate bias estimates.

High-speed turning

Statistics for the yaw estimation error is not generated as this is somewhat meaningless exercise considering that the gyrocompass, which was the only available heading reference, also was used to aid the attitude observers. However, some qualitative results are portrayed in Figure 5.4 which illustrates what happens during a sharp turn while the ship had forward velocity (Figure 5.4b). The estimation error increases, most likely because of the IMU gyros' greater dynamic range compared to that of the mechanical gyrocompass.

Discussion

The results obtained during the two vessel operations gave approximately similar results for both IMUs. The two different NLOs however provided varied results

Table 5.6: Attitude error statistics using NLO A during turning maneuvers.

	ADIS16485	**STIM300**
Roll mean error [deg]	-0.0089	-0.0134
Pitch mean error [deg]	-0.0245	-0.0041
Roll RMS error [deg]	0.1102	0.1122
Pitch RMS error [deg]	0.1161	0.1139
Roll CAEE [deg]	2442.6	2484.0
Pitch CAEE [deg]	2638.6	2582.6

Table 5.7: Attitude error statistics using NLO B during turning maneuvers.

	ADIS16485	**STIM300**
Roll mean error [deg]	-0.008	-0.0115
Pitch mean error [deg]	-0.0188	0.0022
Roll RMS error [deg]	0.0870	0.0848
Pitch RMS error [deg]	0.1113	0.1193
Roll CAEE [deg]	1636.3	1575.8
Pitch CAEE [deg]	2446.2	2500.2

Table 5.8: Attitude error statistics using Navlab during turning maneuvers.

	ADIS16485	**STIM300**
Roll mean error [deg]	-0.0345	-0.0301
Pitch mean error [deg]	0.0311	0.0081
Roll RMS error [deg]	0.0847	0.0817
Pitch RMS error [deg]	0.1078	0.1154
Roll CAEE [deg]	1613.3	1433.3
Pitch CAEE [deg]	2135.6	2123.5

when compared to the onboard VRUs. Since injection from the respective accelerometers and the gyrocompass heading were enabled during the entire study, the mean attitude estimation error is primarily dependent on the vector measurement/reference pairs. Signals with frequencies below the NLO's internal cutoff frequencies, k_1 and k_2, affects the attitude estimates through the measurement vectors. Hence, the mean error is over time dependent on the measurement vectors' sensor biases, not the angular rate measurement biases. Since both IMUs gave approximately the same performance, one can assume that the accelerometer biases are highly in-run stable in the environment they were located, considering the three days between the end of the bias compensation done in port and the

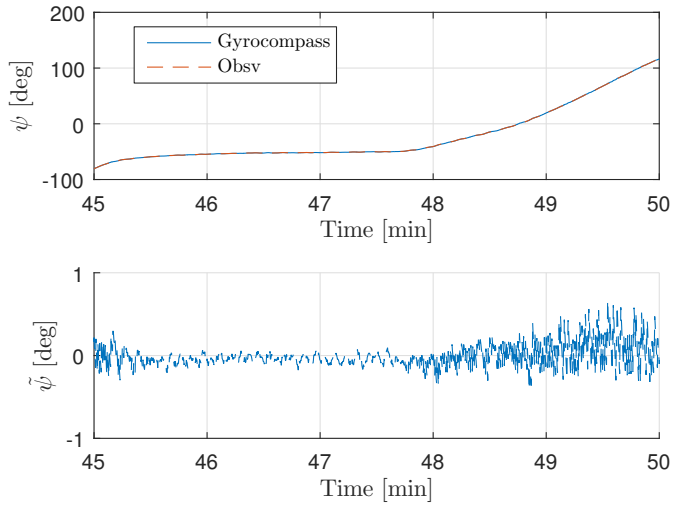

(a) Yaw estimation and estimation error.

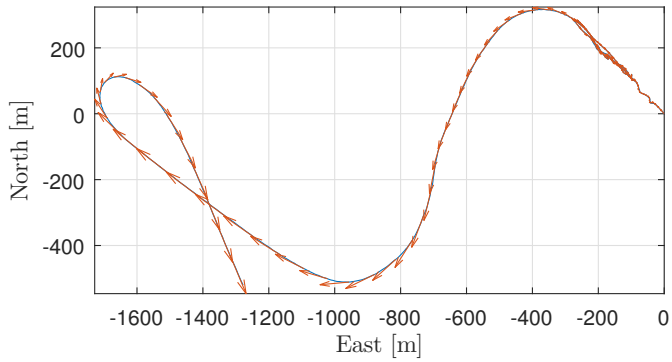

(b) XY plot. Arrows indicate velocity.

Figure 5.4: Heading estimation in high-speed turning using gyrocompass as aiding.

beginning of the second vessel operation presented here.

During both cases, the attitude estimation errors relative to the VRU were smaller using NLO B, compared to using NLO A, particularly in roll. The latter NLO has a static specific force injection, (see Section 5.1.2 and Table 5.2) using $-\boldsymbol{g}_b^t$ as reference vector. $-\boldsymbol{g}_b^t$ is not equal to $\boldsymbol{f}_{ib}^t$, even in DP, due to the wave-induced motions of the vessel. The effect of using $\hat{\boldsymbol{f}}_{ib}^t$ as reference vector is considerable, as expected from the results of Bryne et al. (2015b), due to the kinematic coupling between roll, pitch and heave obtained using VVR as vertical reference in TMO Σ_2. The performance of NLO B was comparable to what achieved with NavLab. In addition, the results obtained indicate that pre-filtering of the IMU measurements are beneficial w.r.t. to roll and pitch estimation when comparing to the VRU since

the validation results are improved compared to those obtained in Section 4.4.8. This study unlike that of the previous chapter did not utilize the extended VVR concept. However, the simulation study of Section 4.4.7 indicates that the attitude estimates obtained with or without the VVR error model have similar performance. Thus one can argue that pre-filtering is beneficial even though different TMOs were utilized in the respective studies.

When turning, larger yaw errors can be observed compared to when the ship is in stationkeeping. Figure 5.4 shows an example of NLO yaw estimates and errors during a sharp turn with high forward speed. The estimate from the NLO starts by being ahead of the gyrocompass, but is ultimately "corrected" because of aiding. This is due to the slow dynamics of the gyrocompass during sharp turns, such that the angular rate measurements from the IMUs about the BODY z-axis is the primary source of yaw information for turns with rates faster than k_2. Hence, larger discrepancies between the NLOs and the gyrocompass is expected in dynamic conditions, underlining that the MEMS IMU is more capable than the traditional mechanical gyrocompass in capturing this motion.

It should also be emphasized the performance comparison was carried out by comparing the NLOs' output to the VRU's equivalent signals and not to absolute truth. Hence, there may exist situations where the NLOs provide more accurate estimates than the VRU. The VRU manufacture specifications are presented in Table E.2.

5.1.5 Full-Scale testing: Heave Estimation

DP

A selection of the heave estimates obtained using the STIM300 and Σ_2 and Σ_3 is shown in Figure 5.5. The heave estimation error statistics obtained using the same observers are presented in Tables 5.9–5.10. By comparing Table 5.9 with Table 4.13 of Section 4.4.8 one can observe that the heave RMS error is reduced by applying filtered ADIS16485 IMU measurements when using the TMO of (5.10), originally from Bryne et al. (2015b), to estimate heave.

Table 5.9: Heave error statistics using Σ_2 in DP.

	ADIS16485	**STIM300**
Mean heave error [cm]	-0.6511	-0.6005
RMS heave error [cm]	5.7766	10.523
Heave CAEE [m]	1215.0	2207.3

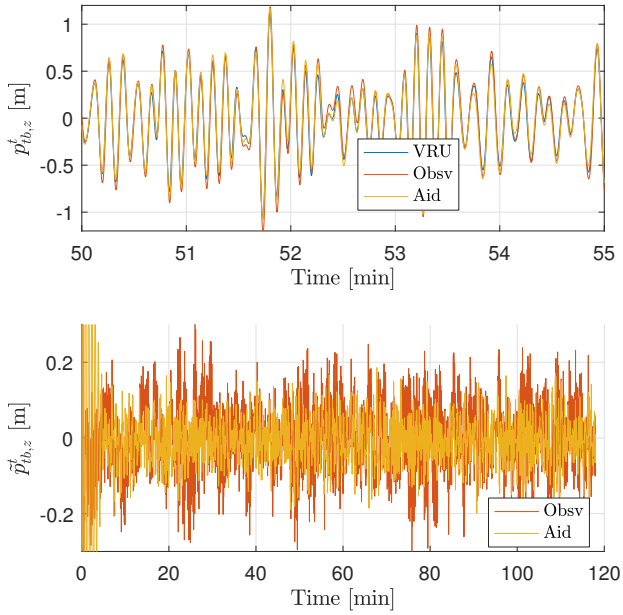

Figure 5.5: Heave estimates and heave estimation error obtained in DP using the aiding TMO Σ_2 (yellow), to aid Σ_1, and Σ_3 (red) vs. the onboard VRU (blue).

Table 5.10: Heave error statistics using Σ_3 in DP.

	ADIS16485	**STIM300**
Mean heave error [cm]	0.2288	0.1339
RMS heave error [cm]	8.0644	10.274
Heave CAEE [m]	1706.2	2112.6

Maneuvering

The heave estimation error statistics obtained during the turning maneuvers using the Σ_2 and Σ_3 are presented in Table 5.11 and 5.12, respectively. From Table 4.14 one can observe that the RMS error actually is larger in Tables 5.11–5.12 compared to the same study carried out using a TMO equivalent to (5.10) (VVR-based heave estimation without using the error model) based on unfiltered ADIS16485 IMU measurements in Section 4.4.8.

Discussion

Considering the heave estimation performance, the usage of Σ_2, the TMO used to aid Σ_1 using NLO B, was benifical compared to Σ_3. While the attitude estimates showed practically no difference between the IMUs, the use of ADIS16485 gave

Table 5.11: Heave error statistics using Σ_2 during turning maneuvers.

	ADIS16485	**STIM300**
Mean heave error [cm]	-0.2982	-0.2689
RMS heave error [cm]	6.3318	9.8799
Heave CAEE [m]	1462.5	2275.0

Table 5.12: Heave error statistics using Σ_3 during turning maneuvers.

	ADIS16485	**STIM300**
Mean heave error [cm]	0.3831	0.7008
RMS heave error [cm]	8.5277	12.308
Heave CAEE [m]	1907.4	2699.1

better heave estimates than obtained with STIM300, with the methods used. In addition, the sensors' effect on performance is more evident than the choice of TMO. This might be due to the ADIS16485's accelerometers having better velocity-random walk and in-run bias stability characteristics than those of the STIM300 and since both TMOs have forms of (residual) accelerometer bias estimation, directly or indirectly, as illustrated in Figure 5.6. Also, it should be mentioned that the STIM300 unit, provided by Sensonor, is an engineering sample. Such units are made for testing and do not necessarily fulfill all of the specifications in the datasheet under all environmental conditions. Therefore, one cannot guarantee that the results obtained is representative for a commercially available STIM300. The results obtained with pre-filtering of the IMU measurements were more inconclusive than those obtained related to attitude estimation. Generally, the heave estimation might be improved with tuning emphasizing heave specifically, or using alternative algorithms, such as the one in Section 4.4.4 (Bryne et al., n.d.). The heave estimates obtained with the TMO of Section 4.4.4 had significantly lower RMS error and CAEE relative the VRU than presented in this chapter.

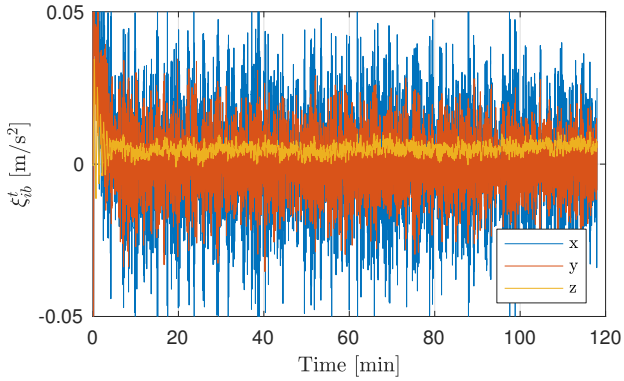

(a) ξ_{ib}^t of TMO Σ_2.

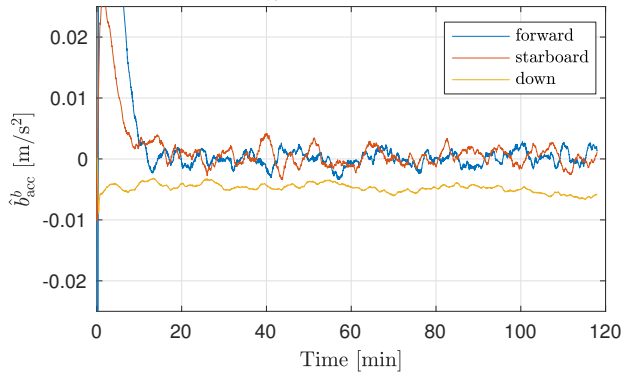

(b) Accelerometer bias estimate $\hat{\boldsymbol{b}}_{\text{acc}}^b$ of TMO Σ_3.

Figure 5.6: Accelerometer bias estimation. Both TMOs have embedded accelerometer bias estimation. Σ_2 estimates the bias indirectly through $\boldsymbol{\xi}_{ib}^t$ where the (negative) bias estimate is added to the rotated specific force measurement, (5.10e), since $\boldsymbol{\xi}_{ib}^t$ acts as an integral effect w.r.t. $\hat{\boldsymbol{f}}_{ib}^t$. Σ_3 of (5.12) has a standard (and more correct) approach where the bias estimate is subtracted directly from the specific force measurement in BODY.

5.1.6 Summary

A successful verification of two nonlinear observers was carried out, employing two different MEMS IMUs, namely the ADIS16485 and STIM300. The full-scale experimental data was collected on an offshore vessel operating outside the Norwegian coast. Comparing the observer output to industry standard VRUs and navigation software based on EKF showed that favorable performance could be achieved. Moreover, considering the attitude estimation performance, the type of NLO was more important than the choice IMU. The results also showed that estimating specific force in the navigation frame, and using this estimate as ref-

erence vector instead of assuming that the vessel is not accelerated, improves the attitude estimation when applying NLOs. If the vessel is assumed to be not be accelerated, tuning can mitigate some of the performance loss, however, at price of slower convergence due to lower gains. The results also indicate that attitude estimation can be improved with pre-filtering of the IMU measurements. Heave estimation was also compared, revealing more differences between the IMUs. Seemingly ADIS16485 had a better accelerometer than STIM300, in compliance with the restrictive specifications, cf. Table E.1.

The results indicate that the heave estimation performance is closely linked to the quality of the accelerometer. Furthermore, it also seems that using a feedback-interconnected NLO structure is favorable over a cascaded structure in order to maximize the attitude estimation performance. The same goes for the heave estimation performance.

5.2 INS-based Wave Filtering

Wave filtering is a vital part of DP and marine autopilot systems and is applied such that only the low frequency (LF) components of the vessel's surge, sway and heading motions are considered by the control system. Fossen (2011, Ch. 11) defines:

Definition 5.1. *Wave filtering can be defined as the reconstruction of the low-frequency motion components from noisy measurements of position, heading and in some cases velocity and acceleration by means of a state observer or a filter.*

Wave-induced craft motion, also known as the wave frequency (WF) motion, oscillates about the vessel's LF motion as indicated in Figure 5.7. By preventing the WF

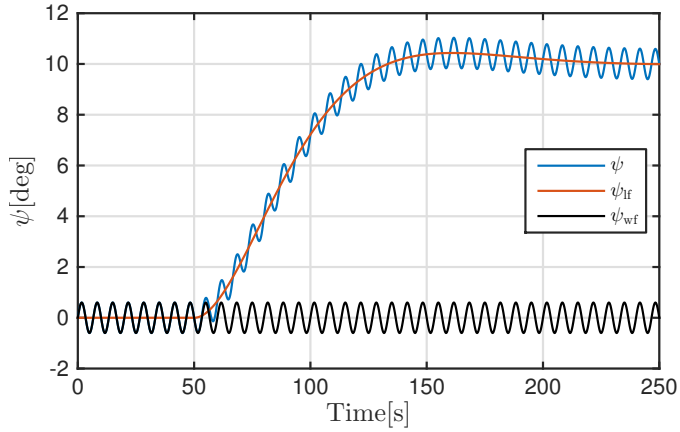

Figure 5.7: Illustration of the total (blue), LF (red) and WF (black) motion of the vessel's heading, ψ.

motion to enter the control loop, only the mean vessel motion is considered by the controller which will result in less fluctuations of thrust. Hence, from a practical point of view, wave filtering has the potential to reduce wear of mechanical equipment, such as thrusters and engines, together with reducing the fuel consumption and emissions from the vessel's engines.

5.2.1 Background

Observer-based wave filtering was first introduced by Balchen et al. (1976) and later extended by Sælid et al. (1983) utilizing the vessel model and applying the EKF. This wave-filtering technique makes use of the knowledge of the encounter frequency, ω_e, to separate the LF and WF motion components. The encounter frequency, as given in Section 4.4.1, (4.51), is the peak frequency of the wave spectra, ω_0, shifted due to the forward speed of the vessel, U, and the angle between the craft's heading and the direction of the waves, β. Fossen and Perez

(2009) presented an overview of KF and model-based techniques for wave filtering in DP and autopilot designs. One potential shortcoming of the EKF is that global stability and robustness properties are nontrivial to prove.

Another non-EKF-model-based design followed with Vik and Fossen (1997), who developed an USGES observer including wave filtering. Lauvdal and Fossen (1998) presented an autopilot design with an adaptive controller in cascade with a notch filter where the latter performed the wave filtering. Furthermore, Fossen and Strand (1999) developed a nonlinear GES observer, with wave filtering of horizontal position and heading measurements. The passivity result of Fossen and Strand (1999) is valid for a constant encounter frequency. Strand and Fossen (1999) extended their work to include online estimation of the encounter frequency. Torsetnes et al. (2004) handled time-varying encounter frequencies with a globally contracting observer employing gain scheduling. Nguyen et al. (2007) and Brodtkorb et al. (2014) dealt with time-varying encounter frequencies using four passive observers, based on Fossen and Strand (1999), parameterized with four different and constant encounter frequencies employed in a hybrid framework.

Hassani et al. (2012) presented an adaptive wave filtering scheme utilizing the KF and a linearized vessel model, yielding a local result, where the encounter frequency candidates had to be chosen in advance. Later, these results were extended by Hassani et al. (2013a,b) to include estimation of the dominating wave frequency with a discrete-time gradient-based algorithm and with a maximum likelihood algorithm together with a bank of KFs, respectively.

In Chapter 4, based upon Bryne et al. (2014), presented time-varying NLOs for INSs, estimating 6-DOF vessel motions, with USGES stability properties, exploiting the PosRef system's quality indicator, customized for marine surface vessels, based on the results of Grip et al. (2013). However, either works considered wave filtering. Results related to inertial sensor-based wave filtering of both position and heading, in part except from Lindegaard and Fossen (2001) which utilized acceleration measurements in a model-based regime, is a gap in the literature.

A radically different approach with a wave-filtering effect is provided in Veksler et al. (2012). By allowing a dynamics window in the thrust allocation system, the thrust variation due to the wave-induced motion, and other high-frequency consumer power variations, is reduced. This leads to less wear on machinery, as well as reduced fuel consumption and emissions by and from the vessel's engines.

5.2.2 Wave filter modeling

All the sensor measurements contain both the LF and WF motions of the vessel. Therefore the estimates from an INS will contain both motion components. In order to separate the LF motion from the WF motion, linear models, exploiting the superposition principle, can be utilized to capture the main dynamics of the oscillatory wave-induced motion due to first-order wave-induced forces on the hull. The

models are parameterized with the dominant wave encounter frequency, $\omega_e(t)$, the relative damping ratio, λ_w, and the gain, K_{w_i}, where the latter is a measure of the wave excitation intensity. The WF component of the i^{th} measurement can be written as $y_{\text{wf}_i} = h_{\text{wf}_i}(s)w_i$ with

$$h_{\text{wf}_i}(s) = \frac{K_{w_i} s}{s^2 + 2\lambda_w \omega_e s + \omega_e^2}, \tag{5.16}$$

as in Fossen (2011, Ch. 8.2.6), similar to Section 4.4.1, where $w_i \in \mathbb{R}^1$ is assumed to be the driving noise of the WF model and being white Gaussian noise.

The wave encounter frequency is time dependent, continuous, positive, and uniformly bounded, $0 < \omega_{e,\min} \leq \omega_e(t) \leq \omega_{e,\max} < \infty$. The relative damping ratio can be considered as a known constant. (Fossen, 2011, Ch 8.2) recommends $\lambda_w = 0.1$ and $\lambda_w = 0.26$ for the JONSWAP and the Modified Pierson–Moskowitz (MPM) spectra, respectively. λ_w can also be estimated online as in Section 4.4.6, (4.92)–(4.101). Furthermore, the time variation of $\omega_e(t)$ is dealt with using a state-space representation given by:

$$\dot{\xi}_{\text{wf}_i} = y_{\text{wf}_i} \tag{5.17}$$

$$\dot{y}_{\text{wf}_i} = -\omega_e^2(t)\, \xi_{\text{wf}_i} - 2\lambda_w\, \omega_e(t)\, y_{\text{wf}_i} + E_i w_i \tag{5.18}$$

where (5.17)–(5.18) is a realization of (5.16) with $E_i = K_{w_i}$. On the other hand, the dynamics of the LF measurement component is given as:

$$\dot{y}_{\text{lf}_i} = u_i \tag{5.19}$$

where u_i is a given input signal. Finally, the measurement, y_i, is given by:

$$y_i = y_{\text{lf}_i} + y_{\text{wf}_i}. \tag{5.20}$$

Eqs. (5.17)–(5.20) can be written in matrix form as:

$$\dot{\boldsymbol{x}}_i = \boldsymbol{A}(t)\boldsymbol{x}_i + \boldsymbol{B}u_i + \boldsymbol{E}_i w_i \tag{5.21}$$

$$y_i = \boldsymbol{C}\boldsymbol{x}_i \tag{5.22}$$

with $\boldsymbol{x}_i = (\xi_{\text{wf}_i},\ y_{\text{wf}_i},\ y_{\text{lf}_i})^\intercal$ and

$$\boldsymbol{A}(t) = \begin{pmatrix} 0 & 1 & 0 \\ -\omega_e^2(t) & -2\lambda_w\omega_e(t) & 0 \\ 0 & 0 & 0 \end{pmatrix}, \quad \boldsymbol{B} = \begin{pmatrix} 0 \\ 0 \\ 1 \end{pmatrix}, \quad \boldsymbol{C} = \begin{pmatrix} 0 & 1 & 1 \end{pmatrix}, \quad \boldsymbol{E}_i = \begin{pmatrix} 0 \\ K_{w_i} \\ 0 \end{pmatrix}. \tag{5.23}$$

5.2.3 Observer design

This work addresses a similar problem as the nonlinear adaptive wave filter of Strand and Fossen (1999). The wave-filtering design to be presented is based

upon inertial sensors and an INS, as opposed to exploiting the vessel model and auxiliary sensors together with mathematical models to obtain thruster and wind generated forces and moments. The main contributions is:

- Development of a vessel-model-free INS with wave filtering. The design incorporates an exogenous time-varying encounter frequency, $\omega_e(t)$, which can be estimated using an adaptive algorithm based on signal processing such as Belleter et al. (2015), as presented in Section 4.4.6, or using an algorithm based on FFT.

The objective of the wave-filtering design is to construct LF estimates of position, velocity and heading from the sensor measurements available. The objective is carried out with a modular observer design as seen in Figure 5.8. First, two feedback-interconnected observers, $\Sigma_1 - \Sigma_2$, are utilized to estimate the vessel's position, attitude, linear velocity and gyro bias, (Bryne et al., 2014, 2015b). These two observers constitutes the strapdown INS and are the attitude observer of Section 4.4.3 and the TMO of Section 4.3.4 with similar sensor configuration as presented in Section 4.3.1. Furthermore, the LF estimates are constructed utilizing the estimates from $\Sigma_1 - \Sigma_2$ and the time-varying encounter frequency, $\omega_e(t)$.

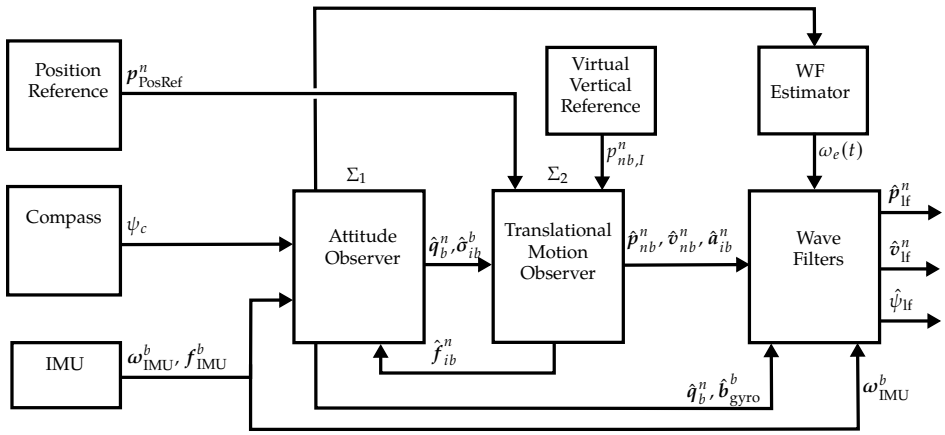

Figure 5.8: Feedback-interconnected observer structure with wave filtering. The observers $\Sigma_1 - \Sigma_2$ are aided by a compass, position reference system and the virtual vertical reference. The outputs of Σ_1 and Σ_2, together with the estimated encounter frequency, $\omega_e(t)$, are provided to the wave-filtering block. The outputs of the wave-filtering block are the LF estimates $\boldsymbol{p}^n_{\text{lf}}$, $\boldsymbol{v}^n_{\text{lf}}$ and ψ_{lf}.

The wave-filtering strategy is based on adaptive notch filtering and a time-varying observer design utilizing the model structure from Section 5.2.2 by utilizing the time-varying encounter frequency, $\omega_e(t)$, obtained from (4.89)–(4.91), and the estimates provided by $\Sigma_1 - \Sigma_2$. With respect to the model (5.17)–(5.19), similar to that of (4.49)–(4.50) of Section 4.4.6, the estimates from Σ_1 and Σ_2 are utilized

both as input and measurements in the wave-filtering observer design as illustrated in Figure 5.9. Reconstructing the LF signals employing observers, together with notch filters, has the potential to yield less phase-shift compared to utilization of pure notch filters. In addition, the WF components can also be estimated when employing observers. Pure filtering strategies do not have this capability.

Five time-varying observers are proposed to reconstruct the LF motion for horizontal positions, horizontal linear velocities and heading, as indicated in Figure 5.9. The observers are structurally similar and given by:

$$\dot{\hat{\boldsymbol{x}}}_i = \boldsymbol{A}(t)\hat{\boldsymbol{x}}_i + \boldsymbol{B}u_i + \boldsymbol{K}_i(t)\tilde{y}_i, \quad \tilde{y}_i = y_i - \boldsymbol{C}\hat{\boldsymbol{x}}_i \tag{5.24}$$

where $\hat{\boldsymbol{x}} = (\hat{\xi}_{\text{wf}}, \hat{y}_{\text{wf}}, \hat{y}_{\text{lf}})^\top$. The matrices $\boldsymbol{A}(t)$, $\boldsymbol{B}$ and $\boldsymbol{C}$ are given in (5.23). The term $\boldsymbol{E}_i w_i$ in (5.23) is neglected in the design since the observers are solely driven by the innovation signal $\tilde{y}_i$ and the given $\omega_e(t)$ at time $t \geq t_0$. The LF input u_i is obtained by notch filtering the given signal r_i obtained from $\Sigma_1 - \Sigma_2$, as:

$$u_i = h_{n_i}(s) r_i, \tag{5.25}$$

with

$$h_{n_i}(s) = \frac{s^2 + 2\zeta_{n_i}\omega_n s + \omega_n^2}{(s + \omega_n)^2}. \tag{5.26}$$

The overview of the given input r_i and outputs y_i is presented in Table 5.13. In order to allow for the notch filter to be adaptive, (5.25)–(5.26) is realized in state-space form as

$$\dot{\boldsymbol{x}}_{n_i} = \boldsymbol{A}_n(t)\boldsymbol{x}_{n_i} + \boldsymbol{B}_n r_i \tag{5.27}$$

$$u_i = \boldsymbol{C}_{n_i}(t)\boldsymbol{x}_{n_i} + D_n r_i \tag{5.28}$$

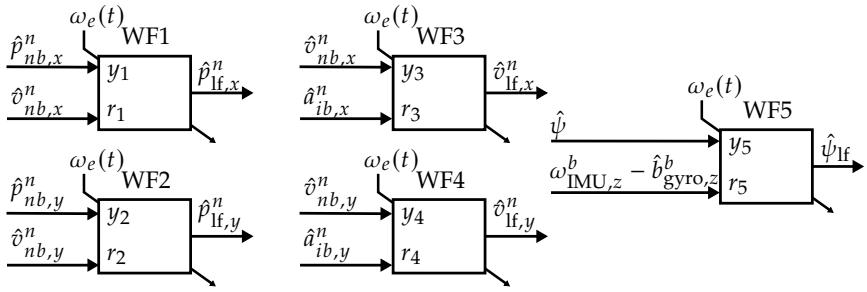

Figure 5.9: Wave filtering concept. The wave filtering is performed with five time-varying observers. For each signal to be wave filtered the total motion estimate from Σ_1 or Σ_2 is utilized as the observer measurement and the corresponding derivative, estimate or measurement, is utilized as input to the observer.

Table 5.13: Input r_i and output y_i of the wave-filtering observers.

Observer Number	Measurement y_i	Input r_i
1	$\hat{p}^n_{nb,x}$	$\hat{v}^n_{nb,x}$
2	$\hat{p}^n_{nb,y}$	$\hat{v}^n_{nb,y}$
3	$\hat{v}^n_{nb,x}$	$\hat{a}^n_{ib,x}$
4	$\hat{v}^n_{nb,y}$	$\hat{a}^n_{ib,y}$
5	$\hat{\psi}$	$\omega^b_{\text{IMU},z} - \hat{b}^b_{\text{gyro},z}$

where

$$\begin{aligned} \boldsymbol{A}_n(t) &= \begin{pmatrix} -2\omega_n(t) & -\omega_n^2(t) \\ 1 & 0 \end{pmatrix}, \boldsymbol{B}_n = \begin{pmatrix} 1 \\ 0 \end{pmatrix}, \\ \boldsymbol{C}_{n_i}(t) &= \begin{pmatrix} 2(\zeta_{n_i} - 1)\omega_n(t) & 0 \end{pmatrix}, D_n = 1. \end{aligned} \tag{5.29}$$

with constant ζ_{n_i}. Then, by choosing $\omega_n(t) = \omega_e(t)$, the input signal, r_i, will be adaptively notch filtered by (5.27)–(5.28).

The observer gains are given as $\boldsymbol{K}_i(t) = \boldsymbol{P}_i(t)\boldsymbol{C}^\intercal$ where $\boldsymbol{P}_i = \boldsymbol{P}_i^\intercal > 0$ is the positive-definite solution of

$$\dot{\boldsymbol{P}}_i(t) = \boldsymbol{A}(t)\boldsymbol{P}_i(t) + \boldsymbol{P}_i(t)\boldsymbol{A}^\intercal(t) + \boldsymbol{Q}_i(t) \tag{5.30}$$

with $\boldsymbol{Q}_i(t) = \boldsymbol{Q}_i^\intercal(t) > 0$ as the positive-definite matrix utilized as tuning parameter. By defining $\tilde{\boldsymbol{x}}_i := \boldsymbol{x}_i - \hat{\boldsymbol{x}}_i$, the corresponding observer error dynamics becomes:

$$\dot{\tilde{\boldsymbol{x}}}_i = (\boldsymbol{A}(t) - \boldsymbol{K}_i(t)\boldsymbol{C})\tilde{\boldsymbol{x}}_i. \tag{5.31}$$

If $\boldsymbol{Q}_i(t)$, $\boldsymbol{A}(t)$ and $\boldsymbol{B}$ are uniformly bounded and the pair $(\boldsymbol{A}(t), \boldsymbol{C})$ is UCO, then $\boldsymbol{P}_i(t)$ will be uniformly bounded, that is $c_1\boldsymbol{I}_3 \leq \boldsymbol{P}_i(t) \leq c_2\boldsymbol{I}_3$ for all $t \geq 0$, with the constants $c_1, c_2 > 0$, (Anderson, 1971, Lemma 3.2). Furthermore, this will render the origin of (5.31) to be GES. $\boldsymbol{A}(t)$ and $\boldsymbol{B}$ are naturally bounded from the model definition of (5.17)–(5.19) due to the physical properties of $\omega_e(t)$ and that λ_w can be chosen as a positive constant. In addition, $\boldsymbol{Q}_i(t)$ will always be bounded by choice since it is a tuning parameter. The following intermediate result insures that the pair $(\boldsymbol{A}(t), \boldsymbol{C})$ is UCO:

Lemma 5.1. *Assume that λ_w and $\omega_e(t)$ are positive and uniformly bounded. Then, the pair $(\boldsymbol{A}(t), \boldsymbol{C})$ is uniformly completely observable.*

Proof: See Appendix A.2.8.

Uniform boundedness of $\boldsymbol{P}_i(t)$ follows since $(\boldsymbol{A}(t), \boldsymbol{C})$ is UCO. Hence, the error dynamics (5.31) is GES.

Remark 5.1. *The gain of the observer* (5.24) *is calculated similar to using the continuous Riccati equation of the Kalman-Bucy filter (Kalman and Bucy, 1961). However, since the given measurement y_i is a smooth estimate from $\Sigma_1 - \Sigma_2$ rather than a sensor reading with additive white Gaussian noise, the measurement covariance, is omitted from the observer design. Then eq. (23) of Anderson (1971) takes the form of*

$$\dot{V}_i = -2\tilde{y}_i^2 - \tilde{\boldsymbol{x}}_i^\top \boldsymbol{P}_i^{-1}(t)\boldsymbol{Q}_i(t)\boldsymbol{P}_i^{-1}(t)\tilde{\boldsymbol{x}}_i < 0.$$

Since $\dot{V}$ remains uniformly negative, the results of Anderson also apply for (5.30)–(5.31).

5.2.4 Case study

Some simulations results illustrating the time-varying INS-based wave filtering, presented above, are shown.

The encounter frequency was obtained using Belleter et al. (2015). The pitch estimate, $\hat{\theta}$, obtained through $\hat{\boldsymbol{q}}_b^n$ from Σ_1, is chosen as the driving input signal such that $y = \hat{\theta}$ of Belleter et al. (2015) similar to Section 4.4.6. The implementation of time-varying wave filters were carried out with exact discretization at 100 Hz. The design parameter ζ_{n_i} of (5.27)–(5.29) was chosen $\zeta_{n_i} = 0.05$ for all five adaptive notch filters. Details related to the simulations are available in Appendix C.3.2.

The two position wave filters were tuned with $\boldsymbol{Q}_i = \text{diag}(0.01, 2.5^2, 0.5)$, while the velocity and heading wave filters were tuned as $\boldsymbol{Q}_i = \text{diag}(0.01, 2^2, 0.5)$.

Figure 5.10 shows the estimated pitch, from Σ_1, feeding the WF estimator together with output of the WF estimator, $\omega_e(t)$. The fast convergence of the pitch estimate, seen in Figure 5.10a, was due to the time-varying tuning scheme presented in Appendix C.3.2. The estimate of $\omega_e(t)$ began to settle at the encounter frequency after 250 seconds as seen in Figure 5.10b. In Figure 5.11, the wave-filtered heading, $\hat{\psi}_{\text{lf}}$, together with the adaptive notch-filtered gyro measurement,

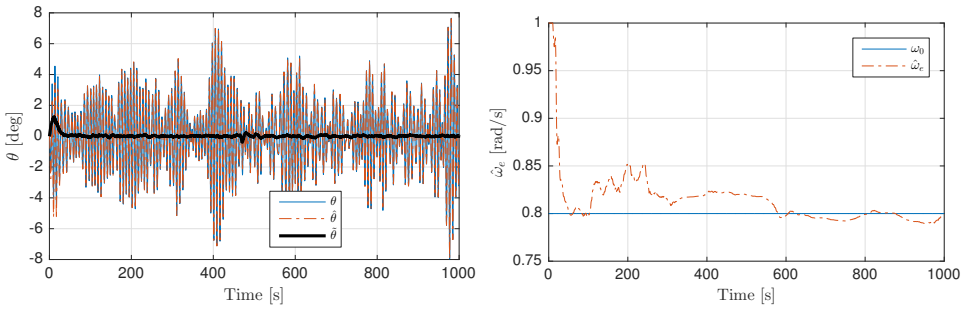

(a) Pitch estimate provided by Σ_1.

(b) Estimate of ω_e from the WF estimator.

Figure 5.10: Evolution of the pitch estimate which acts as the driving signal in the estimation of $\omega_e(t)$ together with the encounter frequency provided by (4.89)–(4.91).

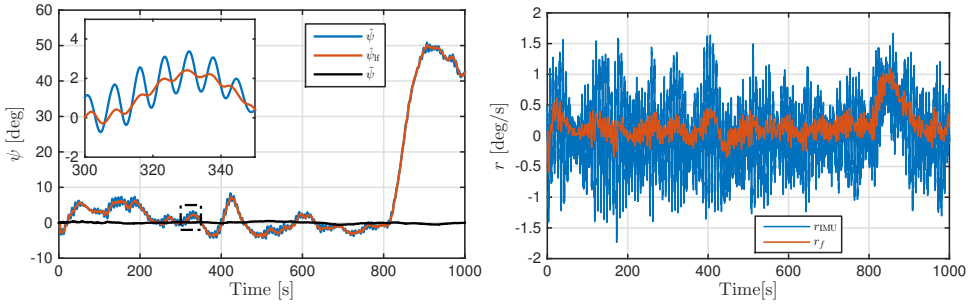

(a) Estimated heading vs estimated LF heading.

(b) Measured yaw rate (blue) versus filtered yaw rate (red).

Figure 5.11: The estimated yaw angle together with the wave-filtered yaw estimate and gyro bias compensated filtered yaw rate.

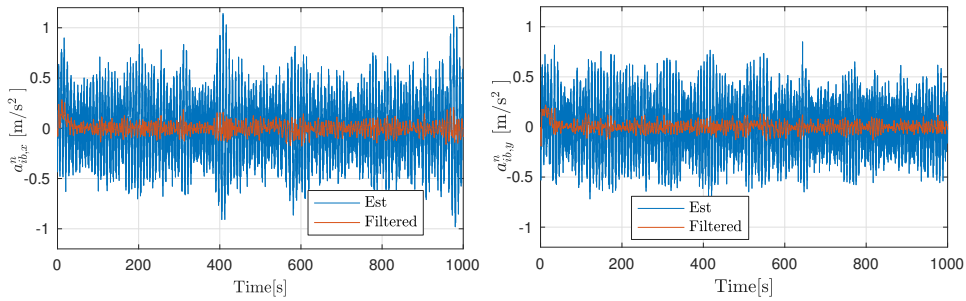

(a) North

(b) East

Figure 5.12: Estimated and filtered estimated acceleration in North and East where the filtered estimates enter the linear velocity wave filters. Blue: Estimated. Red: Filtered.

r_f is presented. The effect of the heading wave filtering, seen in Figure 5.11a, is evident since the majority of the WF motion is not present in the LF estimates. The bias-compensated and notch-filtered yaw rate measurements are shown in Figure 5.11b.

The adaptive notch-filtered acceleration input to the velocity wave filters is shown in Figure 5.12 together with the estimated acceleration, $\hat{\boldsymbol{a}}^n_{ib} = \hat{\boldsymbol{f}}^n_{ib} + \boldsymbol{g}^n_b$. The effect of the adaptive notch filter is obvious where the filtered acceleration estimates are significantly smoother than the signals which they are based upon.

This leads to the wave filtering of velocity and position. Figure 5.13 show the LF estimates of position, $\hat{\boldsymbol{p}}^n_{\text{lf}}$, and linear velocity, $\hat{\boldsymbol{v}}^n_{\text{lf}}$, versus the estimated vessel position and linear velocity, respectively provided by the INS. The initial transients of the LF estimates are due to $\hat{\omega}_e(t)$, at the time, not having converged to the encounter frequency, resulting in the observers of (5.24) and the notch filters

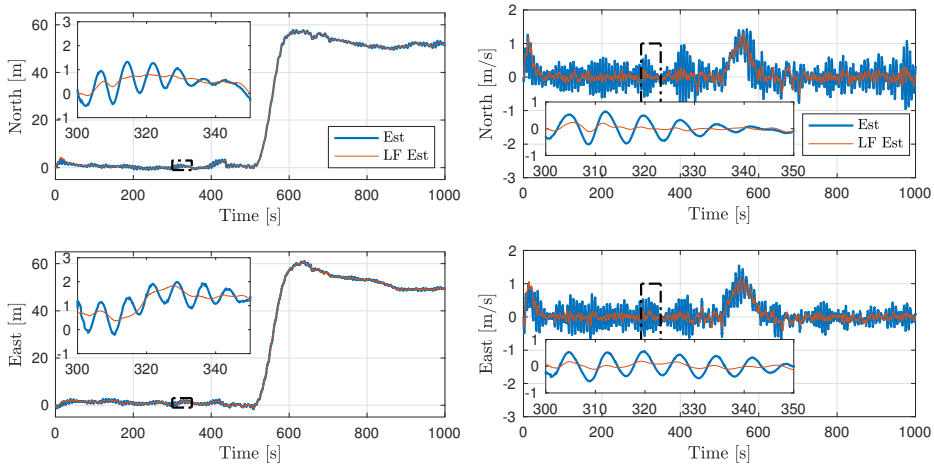

(a) LF position estimates versus the estimated position provided by Σ_2.

(b) LF velocity estimates versus the estimated velocity provided by Σ_2.

Figure 5.13: LF position and velocity estimates versus the estimates provided by the INS.

of (5.27)–(5.28) to not perform optimally before $\hat{\omega}_e(t)$ converged to $\omega_e(t)$. After the transients settled, one can clearly observe that the wave filters reconstructed the LF positions and velocities adequately.

5.2.5 Summary

A marine craft wave-filtering strategy for inertial navigation systems aided by a VVR concept together with position and heading reference systems has been presented. The navigation systems consist of two feedback-interconnected observers with USGES properties, cf. Chapter 4. The wave filtering is performed with five time-varying GES observers, based on signals from the navigation system and sensor measurements, to separate the LF and WF motion components of the craft's position, linear velocity and heading estimates. The time-varying encounter frequency, used in the wave-filtering design, was obtained using an adaptive signal-based algorithm. Simulations show how the time-varying wave-filtering strategy successfully generates low-frequency vessel motion estimates from the inertial navigation system and noisy measurements.

Further developments should look into optimizing the choice of input filters with respect to mitigation of wave-frequency motion while minimizing phase lag. Also extending the wave filtering framework to handle two-peaked wave spectra is a possible extension.

5.3 Conclusions

This chapter has presented the results related to specific combinations of nonlinear observers and MEMS inertial sensors for estimating the motion of a marine surface vessel. Verification studies related to attitude and heave estimates using data collected at sea have been carried out. In addition, wave filtering, specific to surface craft, have been develop based on an inertial navigation system. This thesis is the first in doing so, where such design previously have exploited vessel models.

The verification study of the sensors in question indicate that the choice of nonlinear observer is more important that the choice of sensor in order to obtain high-accuracy roll and pitch estimates. The heave estimation however is more reliant on high-quality accelerometers. In addition, pre-filtering of the IMU measurements can improve the attitude estimation. Pre-filtering related to heave estimation was inconclusive.

The wave-filtering based purely on an inertial navigation system and inertial sensors proved successful in attenuating the wave-frequency motions. Improvements and extensions are however possible such as optimizing the filters with respect to mitigation of wave-frequency motion while minimizing phase lag. Also extending the wave filtering framework to handle two-peaked wave spectra is a possible extension.

6 Sensor Redundancy and Fault Tolerance

6.1 Overview and Motivation

Fault-tolerance is vital in marine control applications. Equipment such as sensors can fail or provide erroneous measurements during operation. Hence, the navigation system must be able to handle such events. This include incidents such as sensor outliers, jumps/bias, drift and dropouts. Thus considering the GNC framework, depicted in Figure 1.1 on page 1, sensor fault and failure handling is imperative in order to guarantee safe, robust and efficient marine operations involving automatic control.

The navigation system need functions for self-diagnostics and fault management. Especially so for autonomous vessels, in order for these vehicles to operate safely and autonomously in areas potentially far from possible human intervention. In this regard, sensor redundancy is a necessity in order to detect sensors errors, faults and failures and for the navigation system to continue to provide PVA data in the event of sensor faults. According to DNV GL (2011) redundancy is defined as

Definition 6.1. *The ability of a component or system to maintain its function when one failure has occurred. Redundancy can be achieved, for instance, by installation of multiple components, systems or alternative means of performing a function.*

In this chapter sensor configuration concepts is presented utilizing multiple PosRef systems and IMUs to fully the redundancy requirement regarding the navigation system. Section 6.2 takes on redundancy and fault tolerance w.r.t. PosRefs and heading reference systems and is based on Bryne et al. (2015a). Section 6.3 presents concepts related to redundant MEMS IMUs utilizing NLOs. The section is based on Rogne et al. (n.d.a).

6.2 Redundant Position Reference and Heading References

6.2.1 Concept

In order to ensure that the INS, cf. $\Sigma_1 - \Sigma_2$ (Sections 4.3.3–4.3.4 or Sections 4.4.3–4.4.4) of Chapter 4 and the wave filters of Section 5.2 have acceptable performance and are fault tolerant, sensor monitoring and sensor weighting should be performed. The respective measurements from the triple-redundant sensors are monitored and processed as illustrated in Figure 6.1. The signal processing consist of two main components; Signal monitoring and signal weighting. However, first the modeling of sensor noise, which the design is based upon, is presented.

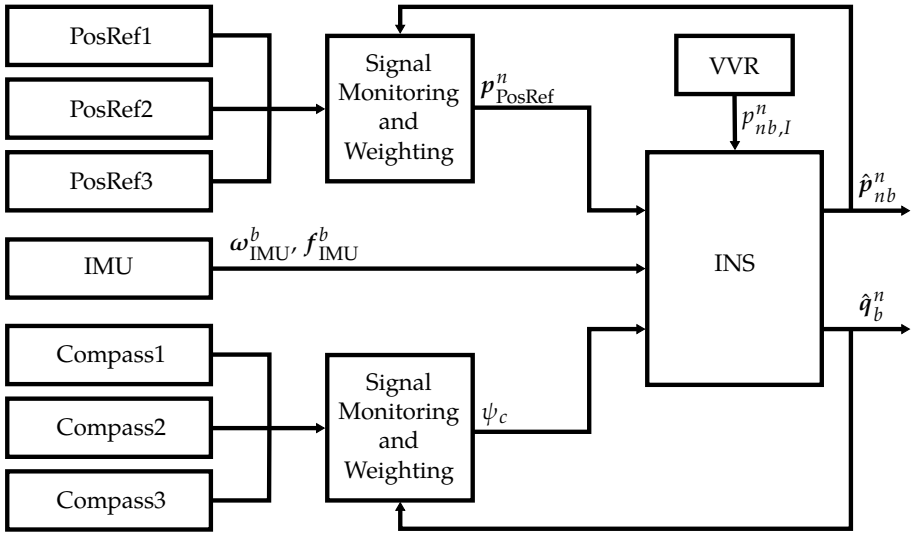

Figure 6.1: Structure of the triple-redundant signal processing. The sensor voting and sensor weighting takes place in the two respective *Signal Monitoring and Weighting* blocks. The output of each blocks is utilized by the INS to estimated the position, $\hat{p}^n_{nb}$ and the attitude, $\hat{q}^n_b$. Furthermore, the prediction of these signal between sampling are utilized by the sensor-monitoring algorithms. After passing the monitoring test, the weighted measurements, p^n_{PosRef} and ψ_c, are applied in aiding the INS.

6.2.2 Sensor error modeling and sensor faults

The work focused on fault detection and isolation (FDI) of three types of errors and faults in a single sensor utilizing the structural properties of the triple-redundant sensor packages together with a high-rate strapdown INS. The typical errors and faults in question are:

- Outliers

- Fixed bias
- Drift

According to Chen et al. (2009), drift of dGNSS PosRef systems can be due to differential link error, being a critical error considering dGNSS is the primary PosRef in DP systems. Therefore, the rationale was based on this PosRef system.

Detection of the considered sensor errors can be nontrivial due to the dynamics of the PosRefs' measurement errors. The transient behavior of the dGNSS measurement error closely resembles a Gauss-Markov process, as stated by Mohleji and Wang (2010, p. 5), due to correlation of the dGNSS observation errors in time. In discrete time, this noise model is given by:

$$e_i(k+1) = a[k]e_i[k] + w_i[k], \tag{6.1}$$

where $w_i[k]$ is the white Gaussian driving noise of the i^{th} measurement and $a[k]$ is the transition parameter

$$a[k] = \mathrm{e}^{-\frac{1}{T}T_s}, \tag{6.2}$$

where T is the time constant and T_s is the sensor's sampling interval. For GNSS systems, with differential correction the time constant usually lie between 4-8 minutes as suggested in Mohleji and Wang (2010). For other DP PosRefs such as HPR systems, similar time-correlated noise can be assumed. This is due to the noise is time correlated due to the speed of sound in water will vary with time due to e.g. changes in sea temperature and ocean currents. Arguments akin to those above can also be made for a mechanical gyrocompass, which is the nominal heading reference in DP due to class notations such as DNV GL (2011), since in essence the north seeking procedure is a mechanical system exposed to disturbances.

6.2.3 Sensor monitoring and voting based upon fault detection, isolation and identification

The fault detection and isolation together with partial diagnosis are performed by modeling the respective faults in discrete time and exploiting the information available from the redundant sensor packages in a stochastic estimation setup without taking into account the vessel motions.

First, the sensor information is modified by utilizing the available information from the INS. A given fault-free measurement $y_i[k]$, at time k, contains information on the vessel's motion in addition to the noise of (6.1) for each respective sensor. In order to analyze the sensor readings for faults separately from the motion of the vessel, the predicted signals from the feedback-interconnected NLO $\Sigma_1 - \Sigma_2$ are utilized to remove the craft's motion components from the respective measurement at each sampling time k. Since the INS provides estimates at significantly higher

rate than the respective aiding sensors do, the vessel motion components can be removed by subtracting the INS prediction $\bar{y}_i$, at time k, from the measurement $y_i[k]$ such as,

$$z_i[k] = y_i[k] - \bar{y}_i, \tag{6.3}$$

where $\bar{y}_i$ is the INS's last available prediction of y_i before time k. Now, ideally z_i contains only sensor noise and faults, i.e $z_i[k] = e_i[k] + f_i[k]$, since the estimates from $\Sigma_1 - \Sigma_2$ are smooth and based on DR from IMU data between each of the samples from the respective sensor packages.

The dynamics of transformed measurements $z_i[k], z_i(k+1), \ldots, z_i(k+m)$ can be modeled, for each i^{th} sensor reading, in discrete time as

$$\boldsymbol{x}(k+1) = \boldsymbol{\Phi}[k]\boldsymbol{x}[k] + \begin{pmatrix} w[k] \\ 0 \\ 0 \end{pmatrix} + u(k-\tau_f)\begin{pmatrix} 0 \\ f_b \\ f_r \end{pmatrix}, \tag{6.4}$$

$$z[k] = \boldsymbol{H}[k]\boldsymbol{x}[k] + e[k], \tag{6.5}$$

similar to Gustafsson (2000, p. 296) with,

$$\boldsymbol{\Phi}[k] = \begin{pmatrix} a[k] & 0 & 0 \\ 0 & 1 & 1 \\ 0 & 0 & 1 \end{pmatrix}, \quad \boldsymbol{H}[k] = \begin{pmatrix} 1 & 1 & 0 \end{pmatrix}, \tag{6.6}$$

where the subscript i is omitted for simplicity. Furthermore, $a[k]$ is given by (6.2) and $w[k]$ is the driving noise of (6.1). $e[k]$ is presumed to be white Gaussian measurement noise, while $u(k-\tau_f)$ is the step function

$$u(k-\tau_f) = \begin{cases} 1 & \text{for } k > \tau_f \\ 0 & \text{else} \end{cases}. \tag{6.7}$$

Moreover, f_b is the sensor bias or drift and f_r is the rate of the bias/drift. Hence, f_r is zero for a fixed bias and is a constant for a drift with constant rate. Then, a measurement sample is deemed fault free if f_b and f_r is contained to a neighborhood around zero. All this implies that $x_1[k]$ corresponds to the sensor noise, while $x_2[k]$ and $x_3[k]$ is the given sensor bias/drift and drift rate, respectively. The system (6.4)-(6.5) is observable for $0 < a[k] < 1$ which can be verified with Kalman's rank condition test.

The sensor monitoring is conducted by running a discrete-time KF with the measurement update

$$\boldsymbol{S}[k] = \boldsymbol{H}[k]\bar{\boldsymbol{P}}[k]\boldsymbol{H}[k] + r[k], \tag{6.8}$$

$$\boldsymbol{K}[k] = \bar{\boldsymbol{P}}[k]\boldsymbol{C}[k]^\intercal \boldsymbol{S}[k]^{-1}, \tag{6.9}$$

$$\hat{\boldsymbol{x}}[k] = \bar{\boldsymbol{x}}[k] + \boldsymbol{K}[k](z[k] - \boldsymbol{H}[k]\bar{\boldsymbol{x}}[k], \tag{6.10}$$

$$\hat{\boldsymbol{P}}[k] = (\boldsymbol{I} - \boldsymbol{K}[k]\boldsymbol{H}[k])\bar{\boldsymbol{P}}[k](\boldsymbol{I} - \boldsymbol{K}[k]\boldsymbol{H}[k])^\intercal + \boldsymbol{K}[k]r[k]\boldsymbol{K}[k]^\intercal, \tag{6.11}$$

and the time update

$$\bar{\boldsymbol{x}}[k+1] = \boldsymbol{\Phi}[k]\hat{\boldsymbol{x}}[k], \tag{6.12}$$

$$\bar{\boldsymbol{P}}[k+1] = \boldsymbol{\Phi}[k]\hat{\boldsymbol{P}}[k]\boldsymbol{\Phi}^{\intercal}[k] + \boldsymbol{\Gamma}[k]\bar{\boldsymbol{Q}}[k]\boldsymbol{\Gamma}^{\intercal}[k], \tag{6.13}$$

respectively, where $\hat{\boldsymbol{P}}[k] = \hat{\boldsymbol{P}}^{\intercal}[k] > 0$ and $\bar{\boldsymbol{P}}[k+1] = \bar{\boldsymbol{P}}^{\intercal}[k+1] > 0$. Even though $w[k]$ only enters the upper state, the process noise of the filter $\boldsymbol{w}[k]$ is chosen $\boldsymbol{w}[k] = (w[k]; w_b[k]; w_r[k])$, such that the states associated with the faults will be more sensitive to changes in the innovation sequence. In addition, $r = E[e^2[k]]$ is the reported covariance of the sensor noise and $\boldsymbol{Q}[k] = E[\boldsymbol{w}[k]\boldsymbol{w}[k]^{\intercal}]$ is the covariance of the process noise. This again leads to the modified process noise covariance matrix $\bar{\boldsymbol{Q}}[k]$ which can be given by:

$$\bar{\boldsymbol{Q}}[k] = \boldsymbol{Q}[k] - \frac{1}{r}\boldsymbol{M}[k]\boldsymbol{M}[k]^{\intercal} \tag{6.14}$$

motivated by

$$\mathrm{E}\left[\begin{pmatrix}\boldsymbol{w}[k]\\ e[k]\end{pmatrix}(\boldsymbol{w}^{\intercal}[k]\, e[k])\right] = \begin{pmatrix}\boldsymbol{Q}[k] & \boldsymbol{M}[k]\\ \boldsymbol{M}^{\intercal}[k] & r[k]\end{pmatrix}, \tag{6.15}$$

as given in Gustafsson (2012, Sec. 7.2.3), taking into account the cross correlation between the process noise, $\boldsymbol{w}[k]$ and measurement noise $e[k]$ with respect to the model (6.1) and the measurement (6.3). In this case, $\boldsymbol{M}[k] = [m[k], 0, 0]^{\intercal}$ is the cross covariance of the measurement and process noise, where $m[k]$ can be calculated offline as:

$$m[k] = \frac{1}{n-1}\sum_{l=k-n-1}^{k-1}\big(w[l] - \mu_w\big)\big(e[l] - \mu_e\big), \tag{6.16}$$

and stored in a look-up table where n is the length of a window based on fault-free data. μ_w and μ_e are the respective means over the same window. The choice of $a[k]$, in $\boldsymbol{\Phi}[k]$, $w[k-n-1], \ldots, w[k-1]$ and $e[k-n-1], \ldots, e[k-1]$ can be calculated prior to the operation based upon previous data collected from the sensor in question. Moreover, this offline analysis should take in account the possibility of changing sensor precision over time. Hence, the look-up table containing $\bar{\boldsymbol{Q}}$ should be based upon process noise data $w[k-n-1], \ldots, w[k-1]$ and measurement noise data $e[k-n-1], \ldots, e[k-1]$ corresponding to a variety of sensor covariances $r[k-n-1], \ldots, r[k-1]$ and $a[k]$ such that the $m[k-n-1], \ldots, m[k-1]$ are valid for changing sensor precision.

Sensor outlier detection:

Outlier detection can then be performed with innovation monitoring of the KF (6.8)–(6.13) with

$$T[k] = \big(z[k] - \boldsymbol{H}[k]\bar{\boldsymbol{x}}[k]\big)^{\intercal}\boldsymbol{S}^{-1}[k]\big(z[k] - \boldsymbol{H}[k]\bar{\boldsymbol{x}}[k]\big) \tag{6.17}$$

as in Gustafsson (2012, eq. (7.71)). If $T[k]$ is exceeds a predefined threshold, $z[k]$ is deemed to be an outlier. For instance if $T(k)$ exceeds $\chi^2_{\alpha,\nu}$, where χ^2 indicates the chi-squared distribution, α the significance level and ν the degrees of freedom.

Sensor bias and sensor drift detection:

Sudden changes in the mean of $z[k]$, corresponding to an emerging sensor bias, will be detectable with (6.17) yielding $T[k]$ to spike. The same effect will present itself if the sensor recovers. Then, monitoring of $\hat{\boldsymbol{x}}_2[k]/\bar{\boldsymbol{x}}_2[k]$ should be done in parallel with outlier detection to detect a sensor bias.

Sensor drift is in general the most difficult fault to detect and identify since it is not necessarily noticeable in the innovation monitoring of (6.17) due to a possibly low drift rate, f_r. For the same reason, only monitoring of $\hat{\boldsymbol{x}}_3[k]/\bar{\boldsymbol{x}}_3[k]$, the state associated with the drift rate, can be insufficient to detect sensor drift since the rate may be lower than the process noise of the filter (6.8)-(6.12). Therefore, drift detection is performed by monitoring the estimate/prediction $\hat{\boldsymbol{x}}_2[k]/\bar{\boldsymbol{x}}_2[k]$, associated with the sensor bias. Then, sensor drift is detected if the sensor bias estimate surpasses a given threshold regardless of the result from the innovation monitoring. The fault estimation ensures that partial fault diagnosis is obtained.

By following the methodology above instead of a typical voting strategy enables the possibility to detect an erroneous sensor also when only two PosRefs are available. This is due to the IMU measurements are provided at significantly higher rates than the PosRef and compass measurements. This again, allows for $z_i[k]$ to be generated and performing the fault estimation with (6.8)–(6.12). However, with only two position and heading references available, this strategy will only work for faster emerging errors. For slowly drifting position reference measurement, an alternative algorithm is presented by Rogne et al. (2014). An other framework for detecting similar faults based on particle filtering is presented by Zhao and Skjetne (2014).

6.2.4 Sensor weighting

The second step of the redundant signal processing is measurement weighting. If the given measurement was deemed healthy by the fault-detection algorithms of Section 6.2.3, the measurements should be weighted. By assuming that sensors have independent noise components, the weighted measurement, $\boldsymbol{x}_w$, of dimension p from N sensors can be obtained from e.g. Gustafsson (2012, Ch. 2.2) by minimizing the object function

$$V^{LS} = \big(\boldsymbol{y}[k] - \boldsymbol{H}_w[k]\boldsymbol{x}_w[k]\big)^\intercal \boldsymbol{R}^{-1}[k]\big(\boldsymbol{y}[k] - \boldsymbol{H}_w[k]\boldsymbol{x}_w[k]\big), \tag{6.18}$$

where $\boldsymbol{y}[k] \in \mathbb{R}^{p \cdot N}$ is the vector of measurements at time k. $\boldsymbol{x}_w[k] \in \mathbb{R}^p$ represents the weighted measurement while $\boldsymbol{H}_w[k] = \left(\boldsymbol{I}_{p_1}, \ldots, \boldsymbol{s}I_{p_N}\right)^\intercal$ yielding,

$$\boldsymbol{x}_w[k] = \boldsymbol{R}_w[k]\boldsymbol{H}_w^\intercal[k]\boldsymbol{R}^{-1}[k]\boldsymbol{y}[k]. \tag{6.19}$$

Here $\boldsymbol{R}[k]$ is a block-diagonal matrix of the reported covariance matrices from the respective sensors. Furthermore, these covariances are $E[e_{c_i}^2[k]]$ and $E[\boldsymbol{e}_{\text{PosRef},i}[k]\,\boldsymbol{e}_{\text{PosRef},i}^\intercal][k]$ with respect to the possible sensor components of (6.5). Then, $\boldsymbol{x}_w$ is the weighted measurement, in a least squares sense with covariance

$$\boldsymbol{R}_w[k] = \left(\boldsymbol{H}_w[k]^\intercal \boldsymbol{R}^{-1}[k]\boldsymbol{H}_w[k]\right)^{-1}, \tag{6.20}$$

and utilized in the INS's measurement updates.

Remark 6.1. *The assumption of independent sensor noise is not true for PosRefs based on satellite navigation and for HPR systems. This is due to the noise being time correlated for dGNSS receivers within the same geographical area and for each pair of HPR transponders and transducers. In DP, differential correction of GNSS is applied to reduce common-mode errors, however there are still some residual common-mode errors present after the correction. Nevertheless, this assumption have still be proven to be useful in KF-based observer designs with position measurements from such position references.*

6.2.5 Case study

This section presents a simulation case study of the combined INS triple-redundant signal processing. The feedback interconnected observers $\Sigma_1 - \Sigma_2$ of Sections 4.3.3–4.3.4 constituted the INS. As stated in Section 6.2.2 dGNSS contained colored noise. Hence, the dGNSSs were were simulated with the first-order Gauss-Markov. The same was the gyrocompasses. Details related to the simulations are found in Appendix C.3.2. The following errors and fault were introduced to illustrate the triple-redundant FDI concept introduced above:

- At time 350 and 400 seconds the position of dGNSS3 spiked with minus five meters north and five meters south.
- Between 400-500 seconds the precision of dGNSS2 was reduced where the standard deviation doubled as described in Appendix C.3.2. In addition, dGNSS2 began to drift 0.1 m/s in the same time period.
- Between 450-500 seconds dGNSS3 did not provide any measurements.
- Between 600-700 seconds the quality of all three dGNSSs deteriorated as described in Appendix C.3.2, Table C.1.
- At 800 seconds the third gyrocompass began to lag before recovering when time approached 1000 seconds.

- At 1000 seconds all three dGNSS reference were lost due to e.g. powerful ionospheric scintillation.

Results regarding the dGNSS sensor package, related to signal monitoring and weighting can be seen in Figures 6.2–6.3. In Figure 6.2a one can observe that the measurements from dGNSS3 at time 300 seconds and at 350 seconds are outliers. Furthermore, from Figure 6.2b one notices that measurements from dGNSS2 slowly drifts between 400 and 500 seconds. The outliers of dGNSS3 and the drift of dGNSS2 were detected with the innovation monitoring and bias/drift detection, respectively. This is indicated by Figure 6.2d, showing how the status of the respective dGNSS receivers evolved with the faults described above. The results of the dGNSS wild-point detection is seen in Figure 6.2c, while the drift estimation of dGNSS2 is seen in Figures 6.2e–6.2f, respectively. dGNSS2 was rejected when the drift estimate surpassed the bias/drift thresholds level of Table C.2. In addition, one can observe in Figure 6.2c that the innovation monitoring spikes multiple times after the measurements from dGNSS2 were rejected. This is due to $\bar{y}_i$ of (6.3), now only is based on fault-free information since the INS estimates are only aided with non-erroneous dGNSS measurements. Then, $z_i[k]$ will have an offset compared to $\bar{y}_i$ since $y_i[k]$, related to dGNSS2 drifts. This again verifies that it was correct to dismiss the measurements from dGNSS2 in the given time period. In addition, the rejections of dGNSS3, seen in Figure 6.2d at approximate 650 and 700 seconds, respectively were due to the bias monitoring incorrectly estimated biases/drift at these instances in time since the transient dGNSS measurement error surpassed the bias/drift threshold.

Figure 6.3 shows the weighted dGNSS measurements and the weighed covariance. The former is almost unaffected by the simulated errors as seen in Figure 6.3. The resulting effects of the sensor monitoring related to the weighted dGNSS covariance can be seen in Figure 6.3b. An increase is seen when dGNSS2 and dGNSS3 were rejected. Furthermore, it can be seen that the weighted covariance increases at 450 seconds since dGNSS3 fails to provide measurements. At approximately 500 seconds both dGNSS2 and dGNSS3 recovered, as seen in Figure 6.2d, such that the weighted dGNSS covariance decreased. Figure 6.3b also shows an increase in the weighted dGNSS covariance in the time frame of 600 to 700 seconds, however, with larger magnitude than before. This is due to the increase in noise magnitude in the measurements provided by all three receivers. In addition, Figure 6.3b also shows the evolution of the time-varying gain $\varphi(t)$ based on the weighted covariance provided by the triple-redundant dGNSS sensor package. One can observe that $\varphi(t)$ decreases when the weighted covariance increases and vice versa.

Figure 6.4 illustrates signal monitoring and weighting of the triple-redundant gyrocompass sensor package. Figure 6.4a shows how the third gyrocompass begins to lag after 800 seconds, while the weighted measurements in Figure 6.4d are unaffected by the this fault. This is due to the sensor monitoring excludes the third gyrocompass approximately 30 seconds after the compass fails to capture the

change in heading, as seen in Figure 6.4c, since the bias/drift estimate surpassed the threshold of Table C.2. The bias/drift estimates related to the compass measurements are presented in Figure 6.4b. In addition, one can see that compass1 was rejected at approximately 200 and 280 seconds and the compass3 was rejected at approximately 150 seconds. These are falsely detected compass errors induced by the low threshold value in Table C.2 and the transient measurement errors of the compasses at the given instances in time.

Figure 6.5 present the position, velocity and attitude estimation errors. One can observe that the vertical position and velocity errors are considerably smaller than then horizontal counterparts. This is due to the usage of the VVR measurement to stabilize the vertical axes. The horizontal axes are dependent on dGNSS quality, with the respective colored measurement noise (and errors) resulting in the horizontal estimation errors are bigger then the vertical. The velocity error is less affected by the transient dGNSS error since the gains, associated with the velocity, are smaller than the position gains (Appendix C.3.2). The transient heading error in Figure 6.5c is due to the colored noise of gyrocomass measurement errors. The spikes seen in Figure 6.5b are due to the transient effect when dGNSS2 is excluded due to drift, while the largest transient errors of Figure 6.5a are due to the fault detection not instantaneously detect the drift of dGNSS2. The residual transient error is due to the colored noise of all three PosRefs.

Results related to loss of PosRefs is presented in Appendix C.3.2. It is shown that heading estimation is robust to loss of PosRefs. This follows from the INS-based FDI, in contrast to vessel-model-based designs, since the sway-yaw couplings of the kinetics are avoided with an approach based on kinematics.

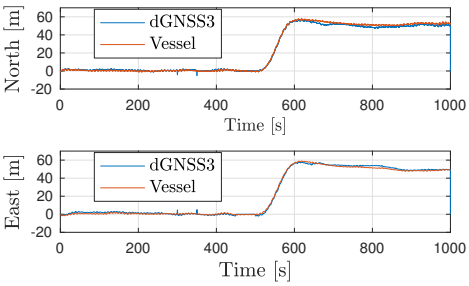

(a) Position measurements from dGNSS3 versus the vessel's position. Outliers are observed at 350 and 400 seconds.

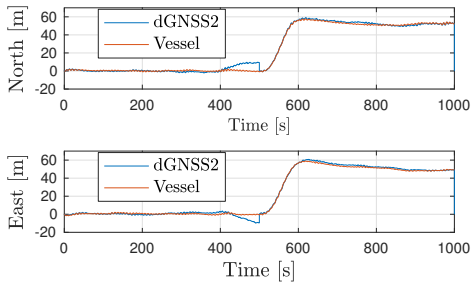

(b) Positions measurements from dGNSS2 versus the vessel's positions. dGNSS2 drifts between 400 and 500 seconds.

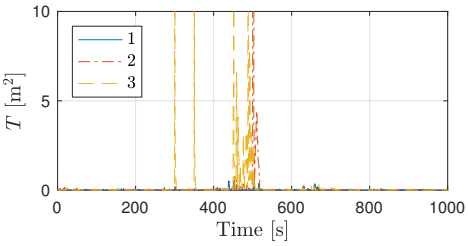

(c) Outlier monitoring of the east components of the dGNSS sensor package.

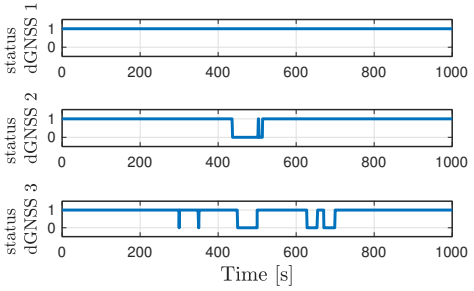

(d) GNSS status. Accepted and rejected measurements are represented by 1 and 0, respectively.

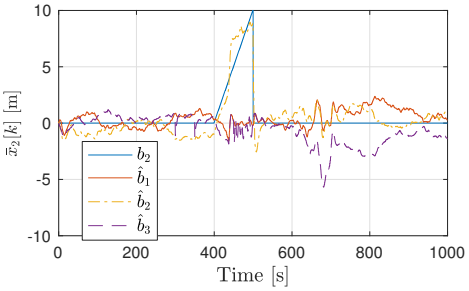

(e) Estimates of the bias/drift of the north dGNSS measurement component.

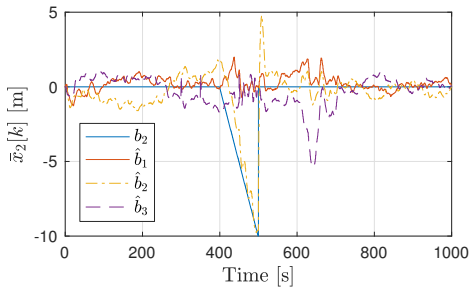

(f) Estimates of the bias/drift of the east dGNSS measurement component.

Figure 6.2: dGNSS faults and fault monitoring. dGNSS2 provided erroneous measurements between 400-500 seconds of simulation, while the dGNSS3 measurements spiked at 350 and 400 seconds of simulation. All of the GNSS measurements becomes less accurate between 600-700 seconds of simulation.

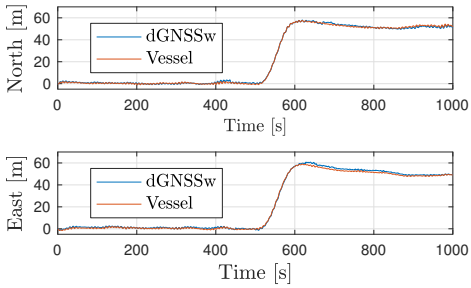

(a) Weighted position measurements from the dGNSS sensor package versus the vessel's positions.

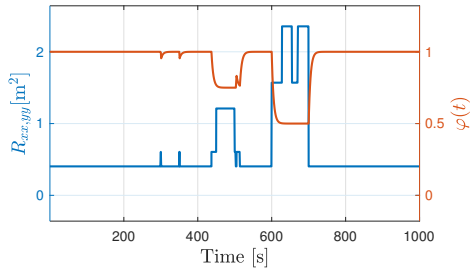

(b) Covariance of the weighted dGNSS measurements versus the time-varying gain $\vartheta(t)$.

Figure 6.3: Results of the dGNSS sensor weighting.

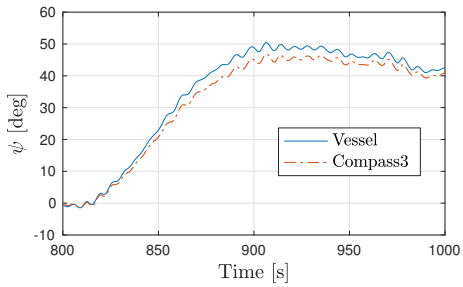

(a) The lagging heading measurements from the third gyrocompass versus the vessel's heading.

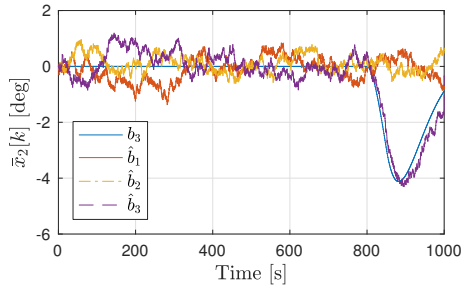

(b) Compass bias/drift estimates.

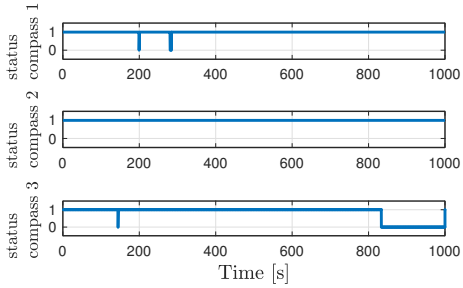

(c) Compass sensor status. Accepted and rejected measurements are represented by 1 and 0, respectively.

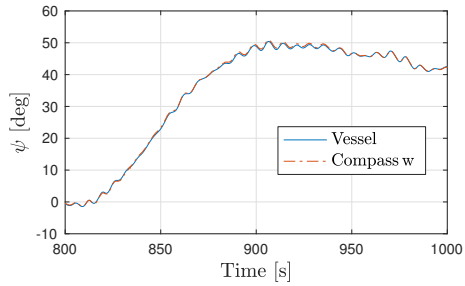

(d) Weighted measurements from the gyrocompass heading reference sensor package versus the vessel's heading.

Figure 6.4: Results of the triple-redundant signal possessing of the heading reference sensor package where compass3 provided lagging measurements after 800 seconds of simulation.

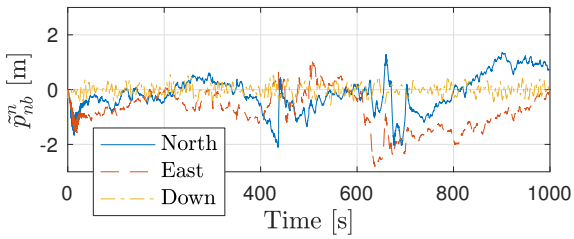

(a) Position estimation error.

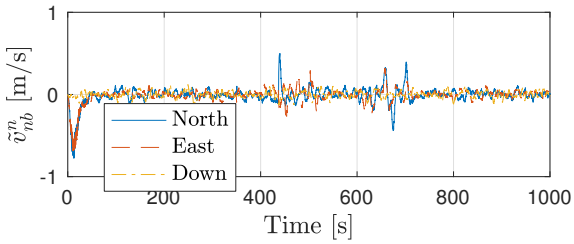

(b) Velocity estimation error.

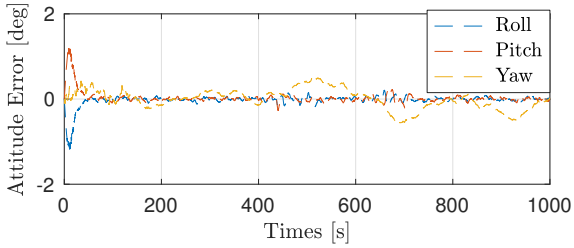

(c) Attitude estimation error.

Figure 6.5: Position, velocity and attitude estimation errors.

6.2.6 Summary

A sensor monitoring and weighting scheme for triple-redundant position and heading references was developed, applying multiple KFs, in order to detect faulty sensor measurements, employing the possibility to detect and isolate biased and drifting sensor readings and outliers. By doing so, potentially preventing the faulty measurements from entering the inertial navigation system. Measurements deemed fault-free were weighted using a least squares approach before provided to the INS. The FDI approach was based on access to an IMU and an accompanying INS.

The IMU-based triple-redundant sensor monitoring and weighting scheme, presented here, was shown to be successful in detecting and estimating realistic sensor faults in presence of colored noise. In particular, the detection of slowly drifting position and heading measurements is shown to be feasible with the design proposed. Fault tolerance of the heading estimate related to position reference loss is achieved since the heading was maintained independent of position with the observer structure proposed. This independence is not achieved with a vessel-model-based design due to the sway-yaw coupling of the kinetics.

6.3 Redundant Inertial Sensors

The main contributions of this section are methods for fusing redundant MEMS inertial measurements in the context of nonlinear attitude observers, which have not previously been covered in the litterateur. Usage of redundant IMUs allows for both fault detection and automatic fault management. The latter is achieved by relying on the remaining sensors when experiencing inertial sensor faults in one of the available IMUs. Achieving such capabilities have received little attention when applying NLOs in INSs. Usage of the redundant sensors also have the capability to reduce the impact of sensor noise.

6.3.1 Background

Fault detection and isolation (FDI) in inertial units is well established. A FDI method based on the generalized likelihood ratio test (Willsky and Jones, 1976) has prevailed for decades. The ratio is based on the likelihood given that the data fits under two models or hypotheses. These are the zero hypothesis, H_0, representing non-failure or the H_1 hypothesis representing erroneous/faulty measurements in the context of sensor readings. In the adaptation for inertial sensors, the classical discrete methods by Daly et al. (1979); Sturza (1988), and the continuous-time case of Medvedev (1995), employ parity equations to generate residuals, upon which the FDI is based. The admitted inaccuracies of MEMS IMUs prove to be a challenge when applying classical methods for FDI on inertial sensors, (Waegli et al., 2008; Guerrier et al., 2012). In this context Guerrier et al. (2012) proposed an improved method based on the Mahalanobis distance with promising results. FDI in INSs using NLOs have up to day received limited attention, except for results such as Rogne et al. (2014); Bryne et al. (2015a); Rogne et al. (2015, 2016b). However, these works have not considered IMU faults, primarily focusing on faults in aiding sensors.

Redundant IMUs have traditionally been applied in safety-critical systems such as passenger jets, military aircraft and spacecraft. In the maritime domain, DP vessels are required to have several gyrocompasses and VRUs, both forms of INSs, on board. However, autonomous vehicles are on the horizon, not only in the air (Sukkarieh et al., 2000), but also on land and at sea. In order for these vehicles to operate safely and autonomously in areas potentially far from possible human intervention, they need functions for self-diagnostics and fault management. To be feasible and competitive in the nascent consumer and commercial markets, it is not viable to fit all these vehicles with expensive high-end gyroscopes and accelerometers. Therefore, an investigation on how to improve the FDI performance with MEMS sensors is of interest.

6.3.2 Concepts

Two concepts for redundant MEMS IMU configuration using NLOs, employed for PVA estimation, are presented. Both concepts are based on the nominal observer structure with a single IMU, as illustrated in Figure 6.6, applying the tangent frame as navigation frame. The design, however, allows for alternative realizations based on e.g. ECEF or NED observer implementations. Both concepts utilize the same TMO.

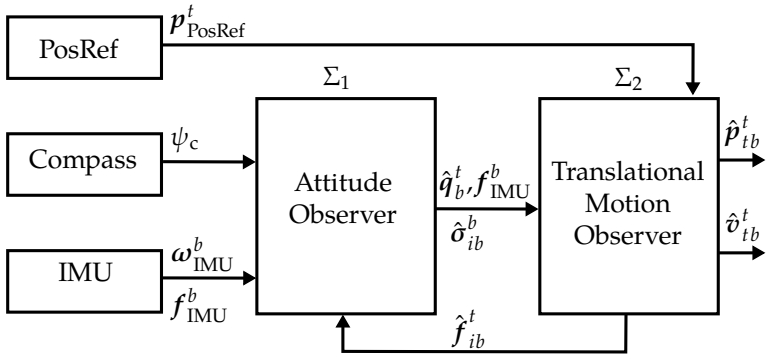

Figure 6.6: Nominal nonlinear observer structure applicable with a single IMU.

Concept 1

In alternative 1 the gyro and accelerometer outputs from the IMUs are combined into single measurements via the parity space method, presented in Section 6.3.5, before being fed into the observer as shown in Figure 6.7. In this approach, no modification of the original observer structure of Grip et al. (2013) is necessary (only one Σ_1 is used) such that $\bar{q}^t_b$, $\bar{\omega}^b_{\text{IMU}}$ and $\bar{f}^b_{\text{IMU}}$ are utilized instead of $\hat{q}^t_b$, ω^b_{IMU} and f^b_{IMU} cf. Figure 6.6. $\bar{(\cdot)}$ indicates weighted measurements or estimates.

Concept 2

In concept 2, portrayed in Figure 6.8, only the accelerometer measurements are combined beforehand, while the angular rate measurements, $\omega^b_{\text{IMU},j}$, where j is the respective IMU's index, are sent to m different instances of the nonlinear attitude observer, (6.25), presented in Section 6.3.4. The outputs of these observers are then merged and forwarded to the TMO, (6.33).

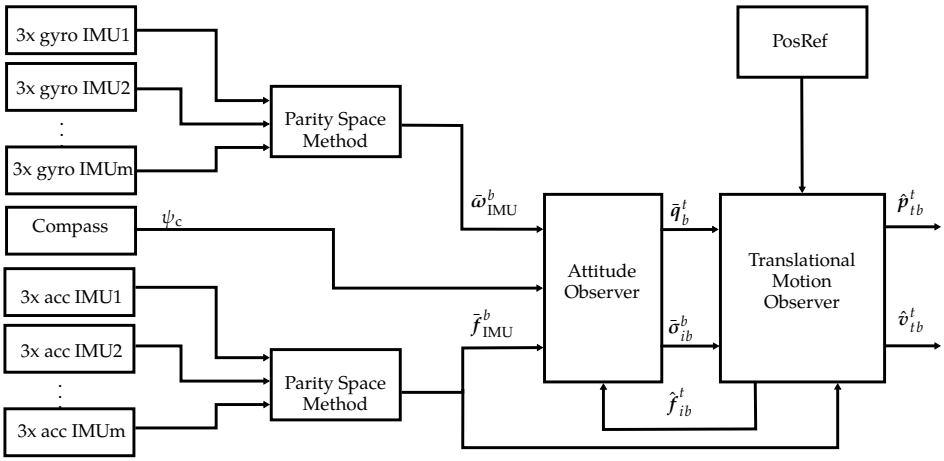

Figure 6.7: Redundant IMU concept 1 – Observer structure.

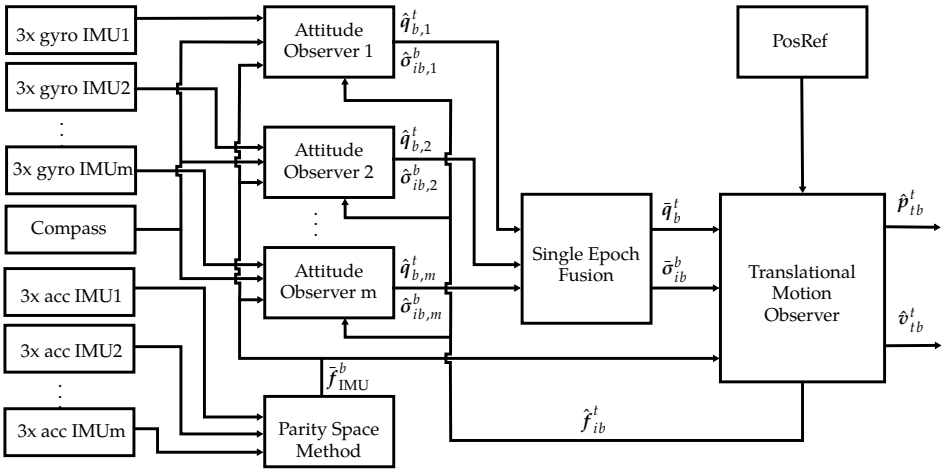

Figure 6.8: Redundant IMU concept 2 – Observer structure.

6.3.3 Inertial and heading sensors

IMU model

A similar IMU model as (5.1)–(5.2), Section 5.1.1 is considered. Now, however, sensor faults $\boldsymbol{d}^b_\star$ are also included,

$$\boldsymbol{f}^b_{\text{IMU}} = \boldsymbol{f}^b_{ib} + \boldsymbol{b}^b_{\text{acc}} + \boldsymbol{w}^b_{\text{acc}} + \boldsymbol{d}^b_{\text{acc}}, \tag{6.21}$$

$$\boldsymbol{\omega}^b_{\text{IMU}} = \boldsymbol{\omega}^b_{ib} + \boldsymbol{b}^b_{\text{gyro}} + \boldsymbol{w}^b_{\text{gyro}} + \boldsymbol{d}^b_{\text{gyro}}, \tag{6.22}$$

where

$$\boldsymbol{d}^b_\star = \begin{cases} \left(d^b_{\star,x},\, d^b_{\star,y},\, d^b_{\star,z}\right)^\mathsf{T} & \text{if fault has occured,} \\ \boldsymbol{0}_{3\times 1} & \text{otherwise.} \end{cases} \tag{6.23}$$

Heading reference

In addition to the MEMS IMUs, it is assumed that there is a heading reference available, typically in the form of a gyrocompass providing the heading ψ_c, or derived from a magnetometer yielding a tri-axial measurement of the earth's magnetic field $\boldsymbol{m}^b_{tb}$ in the body frame, which can be related to the earth's magnetic field vector $\boldsymbol{m}^t_{tb}$, decomposed in the tangent frame at the vehicle's location, thus potentially providing a true-north heading. If ECEF is used as navigation frame, $\boldsymbol{m}^b_{eb}$ can be related to $\boldsymbol{m}^e_{eb}$, similar to that presented in Section 3.2, in order to obtained the heading.

Multiple IMUs

Combining multiple IMUs should in the ideal case reduce the noise levels and bias magnitudes. Indeed, for the combined inertial sensor output $\bar{x}$ from m independent measurements $\bar{x} = \left(y_1 + y_2 + \ldots + y_m\right)/m$, with equal standard deviation $\sigma_{y,j} = \sigma_y$ results in

$$\begin{aligned} \text{Var}(\bar{x}) &= \text{Var}\left(\frac{1}{m}\sum_{j=1}^{m} y_j\right) = \frac{1}{m^2}\sum_{j=1}^{m}\sigma^2_{y,j} \\ \Rightarrow \sigma_{\bar{x}} &= \frac{\sigma_y}{\sqrt{m}}, \end{aligned} \tag{6.24}$$

assuming the same zero-mean distribution for each of the measurement errors. However, when it comes to sensor noise, common-mode disturbances like vibrations, mentioned in the previous chapter, could void the advantageous property of (6.24). Regardless, the bias magnitude in the aggregated measurement will be reduced compared to the magnitude of the of largest bias of the m measurements.

In Guerrier et al. (2012) it was found that for sensor triads, their relative orientation does not matter when it comes to optimality, but in the case of sensor failures

a skewed configuration is preferred when using less than four sensor triads. In the upcoming Section 6.3.7, three sensor triads in an orthogonal configuration, arguably below the recommended number, are utilized. However, it was shown that FDI results still are attainable using this structure.

6.3.4 Nonlinear observers

Attitude observer

When utilizing multiple attitude observer, these takes the form of

$$\Sigma_{1,j}: \begin{cases} \dot{\hat{\boldsymbol{q}}}_{b,j}^{t} = \frac{1}{2}\hat{\boldsymbol{q}}_{b,j}^{t} \otimes \begin{pmatrix} 0 \\ \hat{\boldsymbol{\omega}}_{ib,j}^{b} \end{pmatrix} - \frac{1}{2}\begin{pmatrix} 0 \\ \boldsymbol{\omega}_{it}^{t} \end{pmatrix} \otimes \hat{\boldsymbol{q}}_{b,j}^{t}, & \text{(6.25a)} \\ \hat{\boldsymbol{\omega}}_{ib,j}^{b} = \boldsymbol{\omega}_{\text{IMU},j}^{b} - \hat{\boldsymbol{b}}_{\text{gyro},j}^{b} + \hat{\boldsymbol{\sigma}}_{ib,j}^{b}, & \text{(6.25b)} \\ \dot{\hat{\boldsymbol{b}}}_{\text{gyro},j}^{b} = \text{Proj}\left(\hat{\boldsymbol{b}}_{\text{gyro},j}^{b}, -k_I(t)\hat{\boldsymbol{\sigma}}_{ib,j}^{b}\right), & \text{(6.25c)} \end{cases}$$

where the j^{th} NLO is similar to that of Section 4.4.3 and with the injection terms,

$$\hat{\boldsymbol{\sigma}}_{ib,j}^{b} = k_1(t)\underline{\boldsymbol{v}}_1^b \times \boldsymbol{R}^{\intercal}(\hat{\boldsymbol{q}}_{b,j}^{t})\underline{\boldsymbol{v}}_1^t + k_2(t)\underline{\boldsymbol{v}}_2^b \times \boldsymbol{R}^{\intercal}(\hat{\boldsymbol{q}}_{b,j}^{t})\underline{\boldsymbol{v}}_2^t. \tag{6.26}$$

These are implemented such that the j^{th} observer uses its own attitude estimate $\hat{\boldsymbol{q}}_{b,j}^{t}$, and

$$\underline{\boldsymbol{v}}_1^b = \underline{\boldsymbol{f}}^b, \quad \underline{\boldsymbol{v}}_2^b = \underline{\boldsymbol{f}}^b \times \underline{\boldsymbol{c}}^b, \tag{6.27}$$

$$\underline{\boldsymbol{v}}_1^t = \underline{\boldsymbol{f}}^t, \quad \underline{\boldsymbol{v}}_2^t = \underline{\boldsymbol{f}}^t \times \underline{\boldsymbol{c}}^t, \tag{6.28}$$

in order to calculate (6.26). The respective measurement and reference vectors are defined as

$$\underline{\boldsymbol{f}}^b := \frac{\bar{\boldsymbol{f}}_{\text{IMU}}^{b}}{\|\bar{\boldsymbol{f}}_{\text{IMU}}^{b}\|_2}, \tag{6.29}$$

$$\underline{\boldsymbol{c}}^b := \begin{pmatrix} \cos(\psi_c) & -\sin(\psi_c) & 0 \end{pmatrix}^{\intercal}, \tag{6.30}$$

$$\underline{\boldsymbol{f}}^t := \frac{\text{sat}_{M_f}(\hat{\boldsymbol{f}}_{ib}^{t})}{\|\text{sat}_{M_f}(\hat{\boldsymbol{f}}_{ib}^{t})\|_2}, \tag{6.31}$$

$$\underline{\boldsymbol{c}}^t := \begin{pmatrix} 1 & 0 & 0 \end{pmatrix}^{\intercal}, \tag{6.32}$$

similar to the chosen configuration in Section 4.4.3. $\bar{\boldsymbol{f}}_{\text{IMU}}^{b}$ is a fused accelerometer signal. This is obtained as described Section 6.3.5. The measurement and reference vector pairs $\underline{\boldsymbol{c}}^b$ and $\underline{\boldsymbol{c}}^t$ could easily be replaced with magnetometer equivalents, as described in Section 6.3.3, similar to Section 3.2.

Translational motion observer

The TMO estimates position, linear velocity and specific forces $\hat{\boldsymbol{p}}_{tb}^{t} \in \mathbb{R}^3$, $\hat{\boldsymbol{v}}_{tb}^{t} \in \mathbb{R}^3$ and $\hat{\boldsymbol{f}}_{ib}^{t} \in \mathbb{R}^3$, with $\{t\}$ as navigation frame. The resulting TMO takes the form,

$$\Sigma_2 : \begin{cases} \dot{\hat{\boldsymbol{p}}}_{tb}^{t} = \hat{\boldsymbol{v}}_{tb}^{t} + \vartheta \boldsymbol{K}_{pp} \tilde{\boldsymbol{p}}_{tb}^{t} & \text{(6.33a)} \\ \dot{\hat{\boldsymbol{v}}}_{tb}^{t} = -2\boldsymbol{S}(\boldsymbol{\omega}_{ie}^{t}) \hat{\boldsymbol{v}}_{tb}^{t} + \hat{\boldsymbol{f}}_{ib}^{t} + \boldsymbol{g}_{b}^{t} + \vartheta^2 \boldsymbol{K}_{vp} \tilde{\boldsymbol{p}}_{tb}^{t} & \text{(6.33b)} \\ \dot{\hat{\boldsymbol{\xi}}}_{ib}^{t} = -\boldsymbol{R}\left(\bar{\boldsymbol{q}}_{b}^{t}\right) \boldsymbol{S}\left(\bar{\boldsymbol{\sigma}}_{ib}^{b}\right) \bar{\boldsymbol{f}}_{\text{IMU}}^{b} + \vartheta^3 \boldsymbol{K}_{\xi p} \tilde{\boldsymbol{p}}_{tb}^{t} & \text{(6.33c)} \\ \hat{\boldsymbol{f}}_{ib}^{t} = \boldsymbol{R}\left(\bar{\boldsymbol{q}}_{b}^{t}\right) \bar{\boldsymbol{f}}_{\text{IMU}}^{b} + \hat{\boldsymbol{\xi}}_{ib}^{t}, & \text{(6.33d)} \end{cases}$$

equivalent to the design of Grip et al. (2013) except for use of the tangent frame, instead of ECEF, as navigation frame and the use of fused signals $\bar{\boldsymbol{f}}_{\text{IMU}}^{b}$, $\bar{\boldsymbol{q}}_{b}^{t}$ and $\bar{\boldsymbol{\sigma}}_{ib}^{b}$, based on the signals $\boldsymbol{f}_{\text{IMU},j}^{b}$, $\hat{\boldsymbol{q}}_{b,j}^{t}$ and $\hat{\boldsymbol{\sigma}}_{ib,j}^{b}$. How $\bar{\boldsymbol{f}}_{\text{IMU}}^{b}$, $\bar{\boldsymbol{q}}_{b}^{t}$ and $\bar{\boldsymbol{\sigma}}_{ib}^{b}$ are generated is presented in the two following sections, Section 6.3.5 and 6.3.6, respectively.

The reason why the accelerometer measurements are not treated similarly as the angular rate measurements in Concept 2 is because of the feedback interconnection where the measured specific force enters the TMO directly through $\bar{\boldsymbol{f}}_{\text{IMU}}^{b}$ and indirectly through $\bar{\boldsymbol{q}}_{b}^{t}$ and $\bar{\boldsymbol{\sigma}}_{ib}^{b}$. Therefore if some faulty accelerometer measurements from IMU j enter the aiding TMO directly through both (6.33c) and (6.33d), the equilibrium of the feedback-interconnected system $\Sigma_{1,j} - \Sigma_2$ will be affected before the FDI algorithms of Section 6.3.6 have had time to react. If so, this might further impair the unit quaternion weighting of Section 6.3.6. This can be understood from the fact that the stability properties of the feedback-interconnected NLO of Grip et al. (2013) only hold for fault-free measurements.

6.3.5 Parity space method

In the parity space method, the detection of faults simply comes down to the choice between two hypotheses, either that an erroneous measurement has presented itself or not (Sturza, 1988). A statistical test is performed, based on a decision variable D_{det} obtained from separating the measurement space, i.e. all the redundant measurements, into two subspaces, namely the parity space and the dimensional state space, the latter of which is essentially the vehicle's body frame.

For $l = 3m$ measurements of a 3-dimensional state vector $\boldsymbol{x}$, where m is the number of triads, the measurement model is given as

$$\boldsymbol{y}_{\text{IMU}}^{b} = \boldsymbol{H}\boldsymbol{x}_{ib}^{b} + \boldsymbol{b}_{\star}^{b} + \boldsymbol{w}_{\star}^{b} + \boldsymbol{d}_{\star}^{b}, \tag{6.34}$$

where $\boldsymbol{H}$ is the measurement matrix

$$\boldsymbol{H} = \begin{pmatrix} \boldsymbol{I}_3 & \boldsymbol{I}_3 & \dots & \boldsymbol{I}_3 \end{pmatrix}^{\mathsf{T}}, \tag{6.35}$$

relating the state space to the measurement space, $\star$ represents either the accelerometers or the gyros, $\boldsymbol{w}_{\star}^{b}$ is a vector of white noise, $\boldsymbol{b}_{\star}^{b}$ is a vector of biases and $\boldsymbol{d}_{\star}^{b}$ is a vector of fault effects. $\boldsymbol{x}_{ib}^{b}$ is the state space vector of interest, in this case either $\boldsymbol{\omega}_{ib}^{b}$ or $\boldsymbol{f}_{ib}^{b}$ as described in Section 6.3.3.

To distinguish between faults and regular IMU biases, one should compensate as much as possible for the biases beforehand, such that the resultant bias $\boldsymbol{b}_{\star}^{b}$ is as close to zero as possible before applying the parity space method.

The least squares estimate of $\boldsymbol{x}_{ib}^{b}$ in (6.34) is

$$\bar{\boldsymbol{x}}_{ib}^{b} = (\boldsymbol{H}^{\intercal}\boldsymbol{H})^{-1}\boldsymbol{H}^{\intercal}\boldsymbol{y}_{\text{IMU}}^{b}, \tag{6.36}$$

while the residual (fault and noise) vector estimate becomes

$$\boldsymbol{f}_{r} = \boldsymbol{S}_{r}\boldsymbol{y}_{\text{IMU}}^{b}, \tag{6.37}$$

where $\boldsymbol{S}_{r}$ is given by

$$\boldsymbol{S}_{r} = (\boldsymbol{I}_{l} - \boldsymbol{H}(\boldsymbol{H}^{\intercal}\boldsymbol{H})^{-1}\boldsymbol{H}^{\intercal}). \tag{6.38}$$

Furthermore, the decision variable for detection can be computed as

$$D_{det} = \boldsymbol{f}_{r}^{\intercal}\boldsymbol{f}_{r}. \tag{6.39}$$

Assuming that the measurement noises are Gaussian, uncorrelated and with equal variance, and that each of the sensors are equally likely to have measurement faults, the threshold T_{det}, to which D_{det} will be compared, is given as Sturza (1988)

$$T_{det}\left(p_{FA}, l-3, \sigma_{n}^{2}\right) = \sigma_{n}^{2}F^{-1}\left(1 - p_{FA}|l-3\right), \tag{6.40}$$

where p_{FA} is the probability of false alarms, $l-3$ is the degree of freedom, σ_{n}^{2} is the measurement noise variance, and $F^{-1}\left(p|v\right)$ is the inverse χ^{2} cumulative distribution function, such that:

$$x = F^{-1}\left(p|v\right) = \{x : F\left(x|v\right) = p\}, \tag{6.41}$$

where

$$p = F\left(x|v\right) = \int_{0}^{x} \frac{t^{(v-2)/2}e^{-t/2}}{2^{v/2}\Gamma(v/2)}, \tag{6.42}$$

and $\Gamma(\cdot)$ is the Gamma function.

For fault isolation, the faulty sensor number k can be identified by

$$k = \arg\max_{j\in[1;l]} \frac{f_{r,j}^{2}}{s_{jj}} \tag{6.43}$$

where $f_{r,j}$ is the j^{th} element of $\boldsymbol{f}_{r}$ and s_{jj} is the j^{th} diagonal element of the matrix $\boldsymbol{S}_{r}$. The parity space method is summarized in Algorithm 1.

Algorithm 1 Parity Space Method

Require: $\boldsymbol{H}$, $\boldsymbol{S}_r$, $\boldsymbol{y}^b_{\text{IMU}}$, T_{det}
b_dont_stop = true
while b_dont_stop **do**
  $\boldsymbol{f}_r = \boldsymbol{S}_r \boldsymbol{y}^b_{\text{IMU}}$
  $D_{det} = \boldsymbol{f}_v^\intercal \boldsymbol{f}_r$
  if $D_{det} > T_{det}$ **then**
    $k = \arg\max_{j \in [1;l]} \frac{f_j^2}{s_{jj}}$
    Remove k^{th} measurement from $\boldsymbol{y}^b_{\text{IMU}}$, $\boldsymbol{H}$
    Recalculate $\boldsymbol{S}_r$
  else
    b_dont_stop = false
  end if
end while
Output: $\bar{x} = (\boldsymbol{H}^\intercal \boldsymbol{H})^{-1} \boldsymbol{H}^\intercal \boldsymbol{y}^b_{\text{IMU}}$

6.3.6 Quaternion averaging and FDI

Averaging quaternions

The estimated unit quaternions from Section 6.3.4 ($\hat{\boldsymbol{q}}^t_{b,1}, \hat{\boldsymbol{q}}^t_{b,2}, \ldots, \hat{\boldsymbol{q}}^t_{b,m}$), when applying Concept 2, can be weighed optimally using a single epoch estimation algorithm solving the optimization problem

$$\bar{\boldsymbol{q}}^t_b := \underset{\boldsymbol{q}^t_b \in \mathcal{S}^3}{\arg\max} \sum_{j=1}^{m} w_j (\boldsymbol{q}^t_b)^\intercal \hat{\boldsymbol{q}}^t_{b,j} (\hat{\boldsymbol{q}}^t_{b,j})^\intercal \boldsymbol{q}^t_b, \tag{6.44}$$

minimizing the quaterion error, equivalent to that posed in Markley (2007) with respect to the definition in (B.2.2) of Appendix B.2.2. Eq. (6.44) is a representation of the objective originally posed by Wahba (1965), where w_j are positive weights. Pure least squares weighting is not applicable for unit quaternions since this procedure alone neither maintains the unity norm of the averaged quaternion nor can guarantee that the correct averaged quaternion is obtained regardless of the sign of the quaternions, $\hat{\boldsymbol{q}}^t_{b,j}$, w.r.t. to the set $\boldsymbol{Q}$ of (B.2.2) in Appendix B.2.2. This is a crucial property of a unit quaternion-based fusing algorithm due to the topology, and the inherit topological obstruction (Bhat and Bernstein, 2000), inferred by (B.2.2), where $\hat{\boldsymbol{q}}^t_{b,j}$ and $-\hat{\boldsymbol{q}}^t_{b,j}$ represents the same rotation.

Using scalar weighted quaternions, for each update of the m attitude observers the averaged/weighted quaternion, $\bar{\boldsymbol{q}}^t_b$, based on the m quaternion estimates $\hat{\boldsymbol{q}}^t_{b,1}, \hat{\boldsymbol{q}}^t_{b,2}, \ldots, \hat{\boldsymbol{q}}^t_{b,m}$, and the respective weights, $w_1, w_2, \ldots, w_m$, may be obtained using Algorithm 2 performing an eigenvalue/eigenvector decomposition of a matrix composed of the given quaternions and weights. Furthermore, in Algorithm 2, $\boldsymbol{E}$ is the matrix of eigenvectors of $\boldsymbol{K}_q$, $\boldsymbol{D}_{\text{eig}}$ is a diagonal matrix of

Algorithm 2 Quaternion Weighting with Scalar Weights

Input: Quaternion estimates $\hat{\boldsymbol{q}}_{b,j}^t$, weights w_j

1: $w_{\text{tot}} = \sum_{j=1}^m w_j$
2: $\boldsymbol{M} = \sum_{j=1}^m w_j \hat{\boldsymbol{q}}_{b,j}^t \left(\hat{\boldsymbol{q}}_{b,j}^t\right)^\intercal$
3: $\boldsymbol{K}_q = 4\boldsymbol{M} - w_{\text{tot}}\boldsymbol{I}_4$
4: $[\boldsymbol{E}, \boldsymbol{D}_{\text{eig}}] = \text{eig}(\boldsymbol{K}_q)$
5: $[\lambda_{\max}, j_{\max}] = \max(\text{diag}(\boldsymbol{D}_{\text{eig}}))$
6: $\bar{\boldsymbol{q}}_b^t = \boldsymbol{E}(:, j_{\max})$

Ensure: $\|\bar{\boldsymbol{q}}_b^t\|_2 = 1$
Output: $\bar{\boldsymbol{q}}_b^t$

the eigenvalues of $\boldsymbol{K}_q$ and $i_{\max}$ is the column index associated with the maximum eigenvalue, $\lambda_{\max}$, of $\boldsymbol{D}_{\text{eig}}$. The algorithm results in a weighted quaternion $\bar{\boldsymbol{q}}_b^t$ providing a unique attitude representation (Markley, 2007). According to Markley (2007), a computationally efficient alternative to Algorithm 2 is the QUaternion ESTtimation (QUEST) algorithm. A detailed study on QUEST is found in Shuster and Oh (1981). Alternatives to employing QUEST are presented in Markley and Mortari (2000). For a matrix weighted alternative to Algorithm 2, see Algorithm 5, Appendix F.

FDI with quaternions

For the detection and isolation of faults in quaternions, the angle between the receptive orientation estimates and the weighted average, $\tilde{\beta}_j$, is employed as the foundation for the FDI. Consider two unit quaternions $\boldsymbol{q}_1 = (s_1; \boldsymbol{r}_1)$ and $\boldsymbol{q}_2 = (s_2; \boldsymbol{r}_2)$, where $\boldsymbol{r}_j = (r_{j_1}; r_{j_2}; r_{j_3})$, the error quaternion between them is described by

$$\tilde{\boldsymbol{q}} := \boldsymbol{q}_1 \otimes \boldsymbol{q}_2^* = \begin{pmatrix} \boldsymbol{q}_2 & \boldsymbol{\Xi}_q(\boldsymbol{q}_2) \end{pmatrix}^\intercal \boldsymbol{q}_1, \tag{6.45}$$

based on Appendix B.2.2, where $*$ denote the unit quaternion conjugate. For unit quaternions, the scalar part of the error quaternion can be calculated

$$\tilde{s} = s_1 s_2 + q_2 p_2 + q_3 p_3 + q_4 p_4, \tag{6.46}$$

which is equal to the dot product $\boldsymbol{q}_1^\intercal \boldsymbol{q}_2$. Now, consider that $\tilde{\beta}$ is the angle of the vector part of the error quaternion. Then, the relationship between the scalar part and the angle is given as

$$\begin{aligned} \tilde{s} &:= \cos\left(\frac{\tilde{\beta}}{2}\right) \\ \Rightarrow \tilde{\beta} &= 2\arccos(\tilde{s}) = 2\arccos\left(\boldsymbol{q}^\intercal \boldsymbol{p}\right), \end{aligned} \tag{6.47}$$

Algorithm 3 Quaternion FDI

Require: $\hat{\boldsymbol{q}}_{b,1}^t \dots \hat{\boldsymbol{q}}_{b,m}^t, w_1 \dots w_m, \alpha_{det}$
b_dont_stop = true
while b_dont_stop **do**
  $\bar{\boldsymbol{q}}_b^t = \text{quat\_avg}(\hat{\boldsymbol{q}}_{b,1}^t \dots \hat{\boldsymbol{q}}_{b,m}^t, w_1 \dots w_m)$
  for $j = 1$ **To** m **do**
    $\tilde{\beta}_j = 2 \arccos\left(\left|(\hat{\boldsymbol{q}}_{b,j}^t)^\intercal \bar{\boldsymbol{q}}_b^t\right|\right)$
  end for
  if $\text{any}(\tilde{\beta})_j > \alpha_{det}$ **then**
    $k = \arg\max_{j \in [1;m]} \tilde{\beta}_j$
    Remove k^{th} quaternion $\hat{\boldsymbol{q}}_{b,k}^t$
  else
    b_dont_stop = false
  end if
end while
Ensure: $\|\bar{\boldsymbol{q}}_b^t\|_2 = 1$
Output: $\bar{\boldsymbol{q}}_b^t$

from Chou (1992). Furthermore, (6.47) may serve as a useful metric for FDI. However, for a $\alpha \in [0, 1]$, due to

$$\beta = 2 \arccos(\alpha) = 2\pi - 2 \arccos(-\alpha), \tag{6.48}$$

one can instead use the absolute value of the dot product to avoid to calculate the absolute error angle. Therefore,

$$\tilde{\beta}_j = 2 \arccos\left(\left|(\hat{\boldsymbol{q}}_{b,j}^t)^\intercal \bar{\boldsymbol{q}}_b^t\right|\right), \tag{6.49}$$

is chosen to serve as basis for FDI. If any of the $\tilde{\beta}_j$ values are over a given threshold α_{det}, the corresponding quaternion is removed from the average, using Algorithm 3. The threshold α_{det} might be chosen as the maximum allowable angle difference between an attitude observer's output and the average output. The value should be as low as possible, but in order to minimize false alarms, a lower bound on α_{det} could be determined by empirical data from a fault-free case.

Fusing $\hat{\boldsymbol{\sigma}}_{ib,j}^b$

In contrast to the unit quaternions, $\hat{\boldsymbol{q}}_{b,j}^t$, the injection terms from the respective attitude observers, $\hat{\boldsymbol{\sigma}}_{ib,j}^b \in \mathbb{R}^3$, may evolve freely on $\mathbb{R}^3$ due to no topological obstruction. Thus, the fused injection term, $\bar{\boldsymbol{\sigma}}_{ib}^b$, to be used in the TMO, is easily

obtained with LS-based weighting,

$$\bar{\boldsymbol{\sigma}}_{ib}^{b} = \left(\sum_{j=1}^{m} w_j \right)^{-1} \sum_{j=1}^{m} w_j \hat{\boldsymbol{\sigma}}_{ib,j}^{b} \tag{6.50}$$

$$= \left(\boldsymbol{H}_{\hat{\sigma}}^{\mathsf{T}} \boldsymbol{R}_{\hat{\sigma}}^{-1} \boldsymbol{H}_{\hat{\sigma}} \right)^{-1} \boldsymbol{H}_{\hat{\sigma}}^{\mathsf{T}} \boldsymbol{R}_{\hat{\sigma}}^{-1} \boldsymbol{y}_{\hat{\sigma}}. \tag{6.51}$$

where

$$\boldsymbol{y}_{\hat{\sigma}} = \left(\hat{\boldsymbol{\sigma}}_{ib,1}^{b}; \quad \hat{\boldsymbol{\sigma}}_{ib,2}^{b}; \quad \ldots \quad ; \quad \hat{\boldsymbol{\sigma}}_{ib,m}^{b} \right), \tag{6.52}$$

$$\boldsymbol{H}_{\hat{\sigma}} = \left(\boldsymbol{I}_3 \quad \boldsymbol{I}_3 \quad \ldots \quad \boldsymbol{I}_3 \right)^{\mathsf{T}}. \tag{6.53}$$

The matrix $\boldsymbol{H}_{\hat{\sigma}}$ and vector $\boldsymbol{y}_{\hat{\sigma}}$ are modified according to the output of the FDI method in Section 6.3.6, meaning that $\hat{\boldsymbol{\sigma}}_{ib,k}^{b}$ from a faulty observer j is removed. Using the scalar weights, the matrix $\boldsymbol{R}_{\hat{\sigma}}$ of (6.51), which can be considered as a covariance matrix, is easily obtained as

$$\boldsymbol{R}_{\hat{\sigma}} = \text{blockdiag} \left(\frac{1}{w_1} \boldsymbol{I}_3, \frac{1}{w_2} \boldsymbol{I}_3, \ldots, \frac{1}{w_m} \boldsymbol{I}_3 \right). \tag{6.54}$$

Similar to the matrix-weighted quaternion procedure, the respective weights of $\boldsymbol{R}_{\hat{\sigma}}$ does not have to be diagonal, allowing for block-diagonal structure for $\boldsymbol{R}_{\hat{\sigma}}$

$$\boldsymbol{R}_{\hat{\sigma}} = \text{blockdiag} \left(\boldsymbol{R}_1, \boldsymbol{R}_2, \ldots, \boldsymbol{R}_m \right), \tag{6.55}$$

based on some design criteria of positive definite matrices, $\boldsymbol{R}_j$.

6.3.7 Case study

A case study on usage of redundant IMUs installed onboard an offshore vessel, cf. Appendix E, is presented. Three IMUs were applied. A modified version of the translational motion observer of Section 6.3.4 was employed in validating the two FDI concepts. This TMO is designed specifically for surface vessels and is the same as described in (5.10), Section 5.1.2, however using the $\bar{\boldsymbol{q}}_b^t$ and $\bar{\boldsymbol{\sigma}}_{ib}^{b}$, similar to that of the TMO (6.33) of Section 6.3.4. The vessel was conducting a dynamic positioning operation at the time of the data acquisition, and the north-east plot of its track is shown in Figure 6.9, equivalent to Figure 4.20a of Section 4.4.8. Artificial faults are added to the signals in order to trigger the FDI methods. The results of the NLO-based concept (Concept 2) are compared with the classical parity space method (Concept 1) commonly used in high-grade redundant inertial systems.

Ship sensor configuration

The sensor configuration for validating the concepts was:

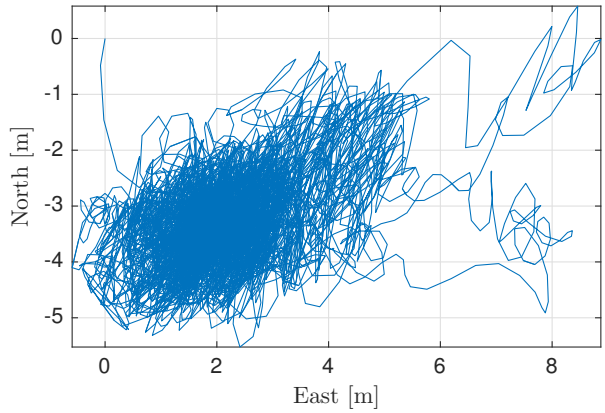

Figure 6.9: Path track obtained from the onboard GNSS.

- 1x differential GNSS position measurement, $\boldsymbol{p}^t_{\text{GNSS}} = (p^t_{tb,x}, p^t_{tb,y})^\intercal$ available at 1 Hz (only horizontal position is used).
- VVR: $p^t_{tb,I} = 0$, for all $t \geq 0$ available at 1000 Hz.
- 3x ADIS 16485 IMUs and 1x STIM300 IMU, each providing
  - Tri-axial accelerometer-based specific force measurements, $\boldsymbol{f}^b_{\text{IMU}}$
  - Tri-axial angular rate measurements, $\boldsymbol{\omega}^b_{\text{IMU}}$

  all interfaced at 1000 Hz.
- Yaw measurements from a triple-redundant gyrocompass (GC) solution, ψ_c, available at 5 Hz.

The STIM300 was utilized for comparison. As in Section 5.1, for the performance and FDI evaluations, the IMU measurements are filtered with a 6th order low-pass Butterworth filter with a cutoff frequency of 5 Hz. The attitude estimates were compared to the 5 Hz VRU roll (ϕ) and pitch (θ) signals. See Table E.2 for specifications from the manufacturer. The specifications of the IMUs installed are presented in Table E.1.

Accelerometer bias estimation

In Bryne et al. (2016), it was found that the accelerometer biases were sufficiently in-run stable over several days for attitude estimation, and a static accelerometer bias estimate $\bar{\boldsymbol{b}}^b_{\text{acc}}$ was used. The same approach was used here, meaning that

$$\boldsymbol{f}^b_{\text{IMU,j}} = \boldsymbol{f}^b_{\text{IMU}^*,\text{j}} - \bar{\boldsymbol{b}}^b_{\text{acc,j}}, \tag{6.56}$$

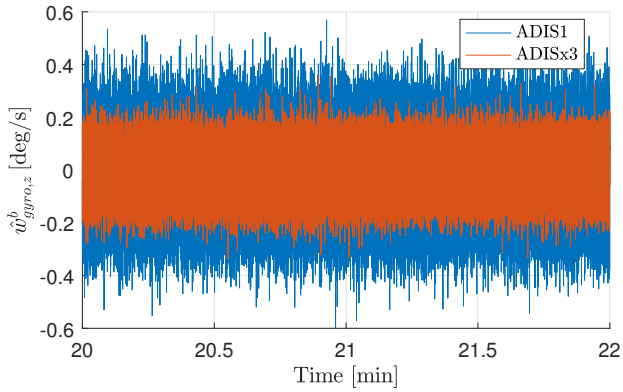

Figure 6.10: Noise estimates: z-axis the angular rate sensor.

Table 6.1: Noise standard deviation (Std) estimates, $\hat{\sigma}_{\text{gyro}}$, for angular rate sensors, in degrees/s.

Std	ADISx3	ADIS1	ADIS2	ADIS3	STIM
$\hat{\sigma}_{\text{gyro},x}$	0.1162	0.1546	0.1545	0.1668	0.1252
$\hat{\sigma}_{\text{gyro},y}$	0.1707	0.2101	0.2037	0.2073	0.1460
$\hat{\sigma}_{\text{gyro},z}$	0.0776	0.1363	0.1194	0.1247	0.0881

where $f^b_{\text{IMU}^*,j}$ is the raw measurement from the j^{th} IMU, was applied. Alternatively, the approach of Grip et al. (2016) could be applied, augmenting (6.33) with an accelerometer bias estimator subject to a PE requirement w.r.t. to the motion.

Full-scale testing: Noise reduction

To obtain some estimates for angular rate sensor and accelerometer noise, high-pass filtering of the raw measurements is performed with a 6th order Butterworth filter to remove bias and the vehicle motion, and calculate the standard deviation of the result. An example of the output is seen in Figure 6.10. This will at least make it possible to compare the individual sensor outputs to each other, and to compare the individual sensors to the aggregated output based on several sensors. The results are presented in Tables 6.1–6.2, and show a slight reduction of noise. According to (6.24), we could have hoped for a reduction by the factor of $\sqrt{m} \approx 1.73$, since $m = 3$, but only the results related to the z-axis of the aggregated angular rate sensor come close to that number. This is due to ship vibrations affecting the IMU noise reduction obtained by the least squares weighting.

Table 6.2: Noise standard deviation (Std) estimates for accelerometers, in m/s^2.

Std	ADISx3	ADIS1	ADIS2	ADIS3	STIM
$\hat{\sigma}_{\text{acc},x}$	0.0557	0.0905	0.0400	0.0611	0.0432
$\hat{\sigma}_{\text{acc},y}$	0.0441	0.0669	0.0343	0.0482	0.0485
$\hat{\sigma}_{\text{acc},z}$	0.0696	0.0749	0.0750	0.0746	0.0616

Table 6.3: Attitude estimation error compared to onboard VRU, in degrees.

	ADISx3 Concept 1	ADISx3 Concept 2	ADIS2 [a]	STIM [a]
Roll mean error	0.0008	0.0011	-0.0007	-0.0044
Pitch mean error	0.0009	0.0009	0.0047	0.0016
Roll RMS error	0.0310	0.0328	0.0363	0.0299
Pitch RMS error	0.0653	0.0662	0.0670	0.0649
Roll CAEE	648.28	687.92	759.80	628.99
Pitch CAEE	1,370.6	1,389.1	1,406.0	1,357.5

[a] Results from Section 5.1.4

Table 6.4: Heave estimation error compared to onboard VRU.

	ADISx3 Concept 1	ADISx3 Concept 2	ADIS2 [a]	STIM [a]
Mean heave error [cm]	-0.6147	-0.6147	-0.6511	-0.6005
Heave RMS error [cm]	4.0515	4.0515	5.7766	10.523
Heave CAEE [m]	855.93	855.93	1,215.0	2,207.3

[a] Results from Section 5.1.5

Full-scale testing: Performance evaluation

Both Concept 1 and 2 are compared with single-IMU solutions for attitude and heave estimation, and the onboard VRU serves as reference. The results are presented in Tables 6.3–6.4, and show that for attitude there really is not much of a difference between the different alternatives and IMUs. This is in compliance with the findings of Rogne et al. (n.d.b), presented in Section 5.1 of the preceding chapter, where it was discovered that the choice of estimator had more impact than the choice of IMU. Even using a significantly more noisy signal yielded approximately the same estimation error compared to the VRU. When it comes to heave estimation, the results vary more, and apparently using a combined accelerometer input is favorable. Figures 6.11–6.13 present example outputs from Concept 2 related to attitude and heave, and Figure 6.14 shows the fault-detection variables for both the parity space method and quaternion averaging in a fault-free case.

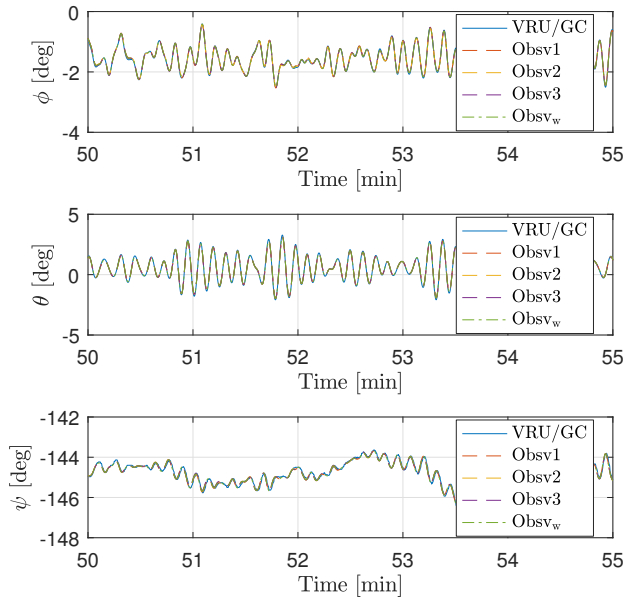

Figure 6.11: Attitude estimates based on redundant ADIS16485 IMUs with quaternion averaging. The weighted result is denoted with subscript w.

Full-scale testing: FDI

Here the same dataset as above was utilized where artificial faults were added to the measurements from one of the accelerometers and one of the angular rate sensors.

Accelerometer fault

An additional bias of 1 m/s^2 is added to the x-axis of ADIS2 at t = 20min. Since the accelerometer FDI for both alternatives is based on the exact same parity space method, the results are expected to be the same. Figure 6.15 shows the fault detection variables and the fault status of the faulty accelerometer. The faulty sensor is removed in an orderly fashion, and practically no effect is seen on the estimates. Since the parity space method only removes one axis, the observers may still make use of the remaining eight axes to full effect.

Angular rate sensor fault

For ADIS3, the gyro bias is increased by 1 deg/s on the y-axis at t = 20min. For Concept 1, one can observe from Figure 6.16 that the attitude estimates deviate when the fault occurs, before converging back to its default state. The reason can be seen in Figure 6.17; when one of the faulty angular rate sensor axis is removed, the aggregated gyro bias, of the combined sensor output, is changed and the observer

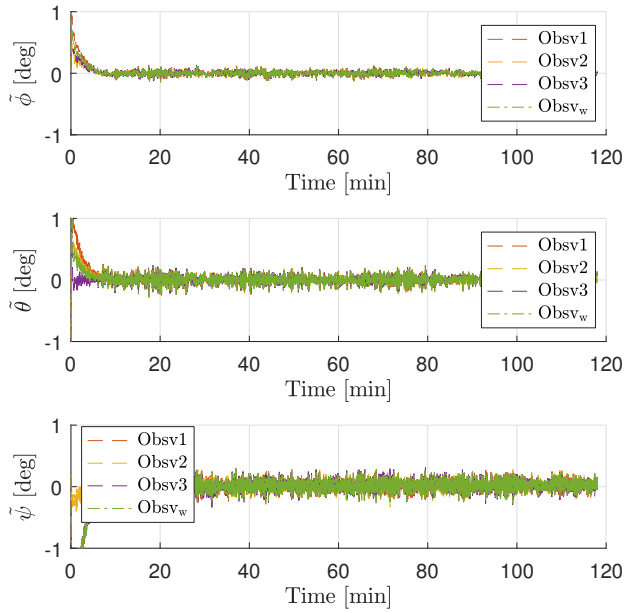

Figure 6.12: Attitude estimation errors based on redundant ADIS16485 IMUs with quaternion averaging. The weighted result is denoted with subscript w.

needs some time to estimate the new combined bias. From Figure 6.18 one can see that the fault is detected and isolated sufficiently.

From Figure 6.19 one can see that the averaged attitude estimates of Concept 2 are not significantly affected by the fault, while the one faulty estimator remains erroneous. Figure 6.20 show the results of the FDI. After a transient period the first five minutes, the $\tilde{\beta}_j$ angles remains under the threshold α_{det}, before the fault occurs at $t = 20$min. The fault is then properly detected and isolated, and the output from the faulty estimator is removed from the quaternion average.

Discussion

For the noise reduction, the theoretical levels from (6.24) were not achieved. This is most likely because much of the noise is not independent from sensor to sensor, but rather common mechanical vibrations or electrical/magnetic disturbances. For the z-axis of the accelerometer the reduction was only around 7%, strongly suggesting that the noise is correlated. The STIM300 IMU was used for comparison relative the triple-redundant solution and had a slightly better noise characteristic than the individual ADIS16485s, w.r.t. to Table 6.2. The triple-redundant solution, however, brought the combined ADIS16485 output to the same levels as obtained with the STIM300.

As far as performance goes, not much was achieved for the attitude estimation

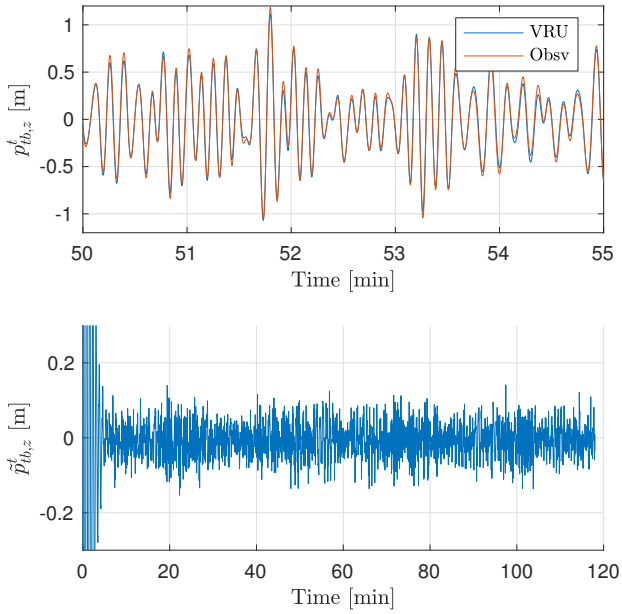

Figure 6.13: Heave estimates and heave estimation error obtained with redundant ADIS16485 IMUs using the parity space method.

by merging the IMUs, while the heave estimation was somewhat improved. The accelerometer plays a major role in this regard, so reducing the noise and bias before using it in the TMO is evidently helpful. Even though the STIM300 measurements gathered at sea had better noise characteristics according to Table 6.2, the results obtained with this IMU proved to be worse than those obtained when both merging three IMUs and only using one of the ADIS16485 IMUs available. This probably has something to do with the STIM300's accelerometer in-run bias stability, which is a bit worse than the ADIS16485's counterpart, considering the manufacture specifications, cf. Table E.1 on page 205.

Fault detection and isolation related to the accelerometer with the parity space method proved successful. With much of the bias removed using (6.56), the detection variable D_{det} clearly indicated a detected fault. Moreover, by using (6.43), the faulty sensor was identified. For the angular rate sensors, however, a problem arose as shown in Figures 6.17–6.18. The bias estimates were disturbed, causing a perturbation in the attitude estimate, as seen in Figure 6.16. The quaternion-based FDI algorithm fared better in this regard, quickly voting out the erroneous (third) IMU/NLO combination. After the estimate of Concept 1 has converged again, this method has the upper hand, since still eight gyro axes are in play, versus only six when using Concept 2, since a whole gyro triad providing input to the faulty observer is removed. Considering the results of Table 6.3, the latter, however, may not impair the attitude estimation performance since a triple-redundant IMU

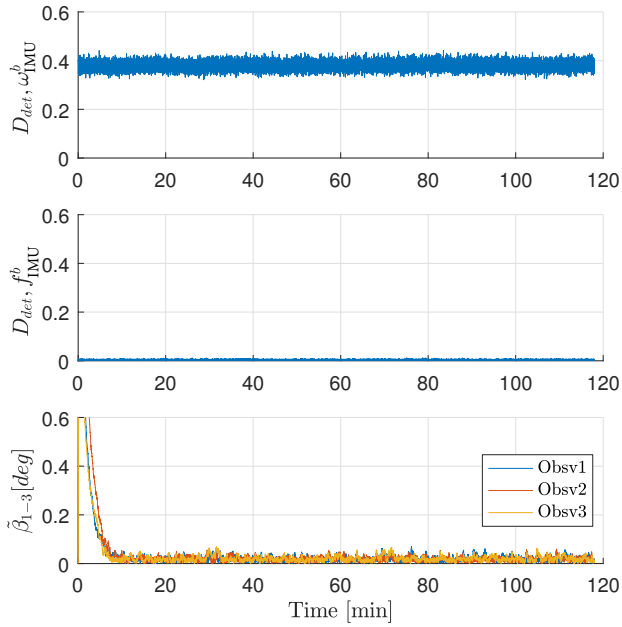

Figure 6.14: Redundant IMUs: Fault detection variables in the fault-free case. Top: Parity space method for angular rate sensor using Concept 1. Middle: Parity space method for accelerometer (Concept 1 and 2). Bottom: Quaternion fault angles using Concept 2.

configuration did not have significant improvements compared to only using one.

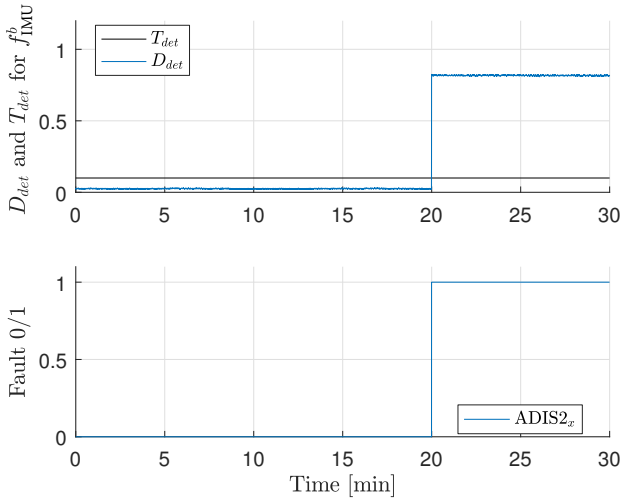

Figure 6.15: Redundant IMUs: Fault detection and isolation when applying the parity space method for accelerometer FDI.

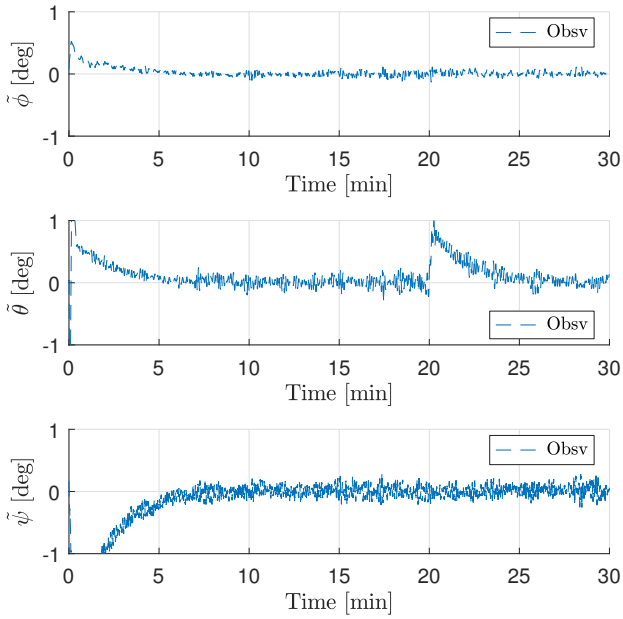

Figure 6.16: Redundant IMUs: Concept 1 – Attitude estimation error when using the parity space method for angular rate FDI.

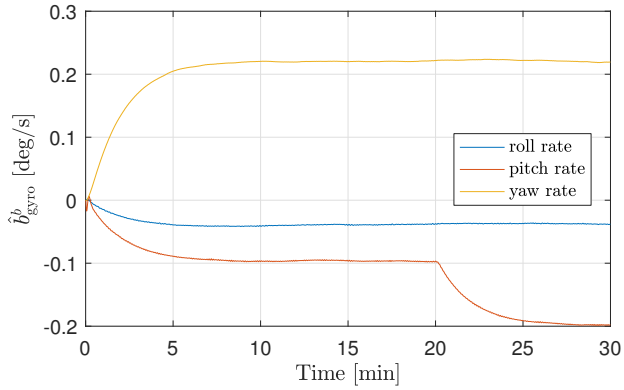

Figure 6.17: Redundant IMUs: Concept 1 – Gyro bias estimates when using the parity space method for angular rate FDI.

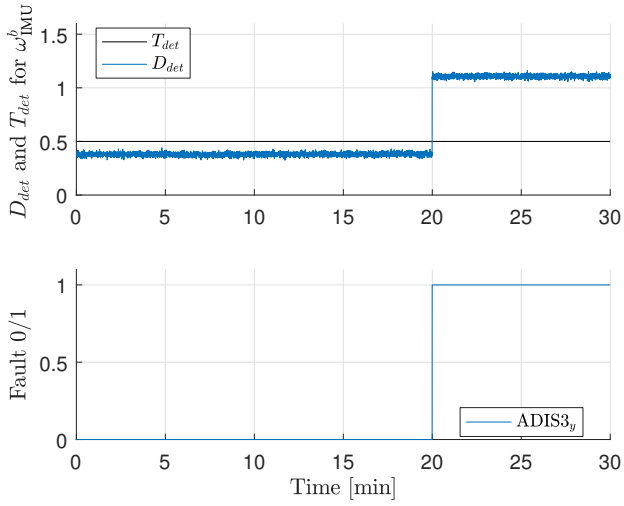

Figure 6.18: Redundant IMUs: Concept 1 – Fault detection and isolation when using the parity space method for angular rate FDI.

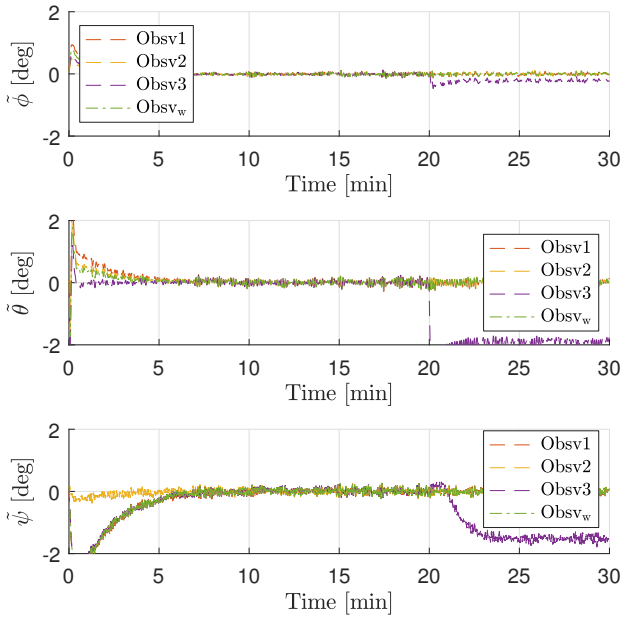

Figure 6.19: Redundant IMUs: Concept 2 – Attitude estimation error when using the quaternion-based algorithm for angular rate FDI.

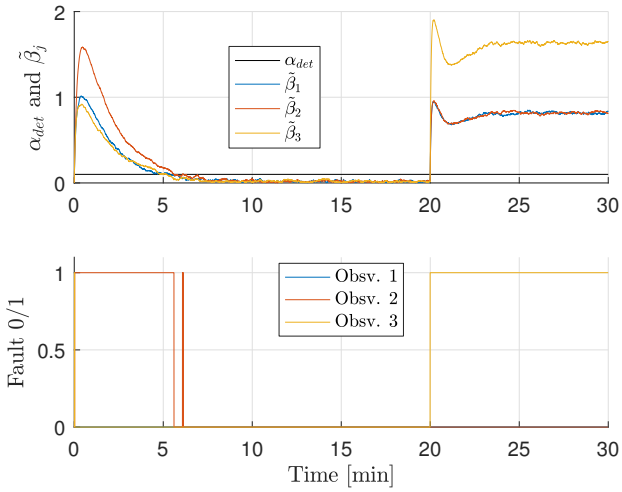

Figure 6.20: Redundant IMUs: Concept 2 – Fault detection and isolation when using the quaternion-based algorithm for angular rate FDI.

6.3.8 Summary

Two concepts for applying redundant MEMS IMUs in the context for nonlinear observers have been presented. One alternative was based on the classic parity space method, while the other also employed a quaternion-based averaging, fault detection and fault isolation scheme. The structural differences between the alternatives were laid out. Algorithms were developed for both concepts. These were further validated using full-scale experimental data acquired from an offshore vessel, using three ADIS16485 IMUs. A STIM300, with a better gyro, w.r.t. to in-run bias stability, was used for comparison. In addition, the ship's industry-proven vertical reference unit sensors were utilized for comparison. In addition, the onboard gyrocompasses were used to aid the attitude observers. For attitude estimation performance, there was little to gain from redundant IMUs in this context, while for heave estimation there were some improvements.

Artificial faults were added to the measurement signals in order to test the fault detection and isolation (FDI) algorithms. In the accelerometer fault situation, the fault was detected and isolated rapidly, and where the FDI in this case was purely based on the parity space method in both alternatives. For the angular rate sensor fault, the parity space method implemented here showed some weaknesses compared to the quaternion-based method. Nonetheless, both methods successfully detected and isolated the fault.

For further work, one could consider finding ways of adding the accelerometer FDI to the quaternion-based scheme as well. This was not done here because of the feedback interconnection between the nonlinear attitude observer and the translational motion observer, that is somewhat sensitive to accelerometer (specific force) disturbances.

6.4 Conclusions

This chapter presented algorithms for FDI of redundant position reference, heading and MEMS inertial sensors based on INSs, designed using nonlinear observer theory.

The algorithms related position and heading sensors was based on applying multiple Kalman filters, to detect faulty measurements, employing the possibility to detect and isolate biased and drifting sensor readings and outliers, preventing the faulty measurements from entering the navigation system. Measurements deemed fault-free were weighted using a least squares approach. The algorithms were evaluated in simulation. The detection of slowly drifting position and heading measurements, from a single sensor, is shown to be feasible with the design proposed.

For redundant MEMS inertial sensors, two alternative concepts for integration of multiple IMUs were presented based on nonlinear observers. The first concept was based on the classic parity space method, while the other also employed a quaternion-based averaging and FDI scheme. The algorithms were validated on full-scale experimental data acquired from an offshore vessel, using three ADIS16485 IMUs. The results were compared to industry-proven VRUs. For attitude estimation performance, there was little to gain from redundant IMUs in this context, while for heave estimation there were some improvements. Simulated faults were added to the signals to test the FDI properties. For FDI of angular rate sensors, the parity space method implemented showed some weaknesses compared to the quaternion-based method.

Further work can focus on validating algorithms for FDI of position and heading sensors. One could also consider investigating FDI designs where the accelerometer is added to the quaternion-based scheme as well. This was not done here because of the feedback interconnection between the nonlinear attitude observer and the translational motion observer, that is somewhat sensitive to accelerometer disturbances.

7 *Concluding Remarks*

This thesis has presented new theoretical results and applications related to strapdown inertial navigation of marine surface vessels. The proposed navigation systems have been based using nonlinear observers (NLOs) in contrast to traditional solutions based on the extended Kalman filter. Furthermore, the designs have utilized a feedback-interconnection framework of an attitude and a translational motion observer where the origins of the observers' error dynamics were proven to be uniformly semiglobally exponentially stable. The presented observers provided position, velocity and attitude together with specific force estimates. The primary focus, however, has been on attitude and heave estimation of marine vessels, related to vertical reference units (VRUs), providing similar signals, which have a widespread utilization on ships, in particular on offshore vessels. The motivation behind this was to facilitate high-quality position estimation, since accelerometers and position measurements are related to each other, using the attitude, through a rotation matrix, and a kinematic model. It is also beneficial that the inertial navigation systems (INSs) provide its own heave estimate without the need of additional VRUs.

The beginning of the thesis focused on extensions and the inclusion of time-varying gains in the nonlinear observer design, motivated by the desire to improve the performance of the estimation of position, velocity and attitude. It was shown that augmenting loosely coupled integration strategies of satellite and inertial navigation systems, in order to compensate for the colored noise of global navigation satellite systems (GNSS), proved to be difficult. Through simulations it was shown that this compensation is feasible with highly accurate velocity measurements, though most likely, not realistic in practice. It was further shown, using data collected during an unmanned aerial vehicle flight, that tightly coupled GNSS/INS integration gave the best performance relative real-time kinematic GNSS when integrating the sensors with nonlinear observers. In addition, algorithms for discrete-time implementation of the observers were presented.

The main contribution of the thesis was the introduction of the virtual vertical reference (VVR) principle as an alternative to GNSS for vertical aiding of inertial navigation systems for marine vessels. This concept is based on exploiting that the averaged heave displacement of a marine vessel is zero on average relative the mean sea surface. The design was first presented with a scalar time-varying gain, affecting the estimation of both the horizontal and the vertical motion. It was shown through simulations that utilizing the VVR principle improved estimation of roll and pitch compared to utilizing GNSS as vertical reference due to kinematic couplings. Moreover, it was also shown through validation of the observers that exploiting the feedback interconnection with the VVR concept resulted in smaller errors relative to the output of industry standard VRUs compared to utilizing a standalone nonlinear observer, with the gravity as reference vector. The latter is

an alternative to applying the estimated specific force, obtained from a feedback interconnection with a translational motion observer (TMO), as reference vector.

The observer structure, aided by VVR, was later extended to allow for a more flexible time-varying design. This included exploiting an error model based on parameters describing the wave-induced motion of a marine vessel. This increased the potential heave estimation performance. Furthermore, the mentioned parameters were obtained using the estimated pitch and measured pitch rate, compensated for gyro bias. It was shown by Monte Carlo simulations that the design has the potential to achieve the industry standard specification related to heave accuracy and precision of five centimeters or five per cent root-mean-square error. Validation using sensor data from a MEMS inertial measurement unit (IMU), collected on an offshore vessel, was carried out by comparing the heave estimate to the output of an industry standard VRU.

The fifth chapter of the thesis focused on aspects of INS specifics related to ships. Sensor configurations, choice of observers and filtering were emphasized. Pre-filtering of the IMU measurements seems promising for attenuating sensor noise and disturbances induced by significant ship vibrations. Such filtering, however, might introduce undesirable phase lag. The attitude estimates obtained using the ship data and the NLOs were compared to the output of a proven navigation suite based on the extended Kalman filter. The NLO aided by a TMO obtained similar performance as the navigation suite in estimating roll and pitch. Moreover, the wave filtering of the estimates from a NLO-based INS was also carried out. This work is the first in doing so unlike traditional designs, which have exploited vessel models in the observer design.

The final chapter focused on sensor redundancy and fault tolerance. It was shown that drift detection of position and heading references is possible if triple-redundant sensors are available. Fault detection and isolation of MEMS inertial sensors were carried out using full-scale data, applying two concepts, exploiting redundant IMU configurations, based on nonlinear observers. The first concept utilized a traditional parity space approach together with one attitude observer and a TMO. The second concept exploited redundant attitude observers as well. Both designs proved to be successful in detecting faults which were artificially injected. However, the concept with redundant attitude observers proved to be the most robust toward faulty rate gyros. Averaging of a triple-redundant IMU did not improve the attitude estimation, however, the heave estimation might be improved by fusing multiple IMUs.

The course of this work showed that the heave estimation performance could be improved by taking sea-state-dependent parameters into account. Further work may explore ways of improving the heave estimation even more. Not necessarily performance-wise, but towards increased robustness. The design with the highest performance, presented in this work, is also the most sensitive to the sea state. Validating the design in sea states with dual-peaked wave spectra is of interest.

Extending the design might be necessary. Moreover, including absolute vertical position reference measurements to the VVR-based TMOs, for increased applicability in situations where knowing absolute altitude over the seabed is necessary, is a possible extension. Also extending the VVR concept to be utilized in tightly coupled GNSS/INS integration would be of interest. Such design has the potential to outperform loosely coupled integration. In addition, the inclusion of the VVR might increase the fault-tolerance properties of the aided INS due to possibly improved pseudorange monitoring, since additional information related to the vessel's motion is introduced to the observer framework.

More focus on the fault tolerance of the proposed INSs is of interest. Fault tolerance properties will receive increased attention in the steps towards more autonomy in marine vessels. Traditionally, sensor and VRU redundancy on offshore vessels have typically been more separated than presented here, where each unit provides its own processed estimate output. The results presented here related to sensor and observer validation indicate that a more integrated design could be beneficial, especially related to the heave estimation. For such strategies to receive industrial attention, extending the framework to handle a wider range of faults is necessary in order to not increase or induce risk. By doing so, sensor costs can potentially by reduced since existing VRU solutions can be replaced. At the same time, the navigation system's performance and its fault-tolerance properties can be increased.

Stability Properties and Detailed Proofs

A

A.1 Stability Properties

This section in based on Loria and Panteley (2005).

Consider a general time-varying nonlinear system

$$\dot{\boldsymbol{x}} = \boldsymbol{f}(t, \boldsymbol{x}, \boldsymbol{u}) \quad \boldsymbol{x}(t_0) := \boldsymbol{x}_0, \tag{A.1a}$$

$$\boldsymbol{y} = \boldsymbol{h}(\boldsymbol{x}), \tag{A.1b}$$

where $\boldsymbol{f} : \mathbb{R}_{\geq 0} \times \mathbb{R}^n \to \mathbb{R}^n$ with initial conditions $(t_0, \boldsymbol{x}_0)$. Moreover, B_r denotes the open ball

$$B_r := \{\boldsymbol{x} \in \mathbb{R}^n \ : \ \|\boldsymbol{x}\|_2 < r\}, \tag{A.2}$$

while $\boldsymbol{x}(t; t_0, \boldsymbol{x}_0)$ denotes the solution $\boldsymbol{x}(t)$ of (A.1), at time t, with initial condition $(t_0, \boldsymbol{x}_0)$.

The stability properties considered in this thesis follows c.f. Loria and Panteley (2005), Definition. 2.7.

Definition A.1 (Uniform Local Exponential Stability). *The origin of the system* (A.1) *is said to be uniformly locally exponentially stable (ULES) if there exist constants* γ_1, γ_2 *and* $r > 0$ *such that for all* $(t_0, \boldsymbol{x}_0 \in \mathbb{R}_{\geq_0} \times B_r)$

$$\|\boldsymbol{x}(t; t_0, \boldsymbol{x}_0)\|_2 \leq \gamma_1 \|\boldsymbol{x}_0\|_2 \mathrm{e}^{-\gamma_2 (t - t_0)}, \quad \forall t \geq t_0. \tag{A.3}$$

Definition A.2 (Uniform Semiglobal Exponentially Stability). *If for each* $r > 0$ *there exist* γ_1, γ_2 *such that* (A.3) *holds for all* $(t_0, \boldsymbol{x}_0) \in \mathbb{R}_{\geq 0} \times B_r$ *then, the system is said to be uniformly semiglobally exponentially stable (USGES).*

Definition A.3 ((Uniform) Global Exponentially Stability). *The origin of the system* (A.1) *is said to be (uniformly) globally exponentially stable (GES) if there exist* $\gamma_1, \gamma_2 > 0$ *such that* (A.3) *holds for all* $(t_0, \boldsymbol{x}_0) \in \mathbb{R}_{\geq_0} \times \mathbb{R}^n$.

A.2 Detailed Proofs

A.2.1 Proof of Lemma 4.1

Proof. From (4.20) we have that

$$\boldsymbol{C}^* = \begin{pmatrix} \boldsymbol{I}_3 & \boldsymbol{0}_{3\times 7} \end{pmatrix}. \tag{A.4}$$

Hence,

$$\boldsymbol{C}^{*\dagger}\boldsymbol{C}^* = \text{blockdiag}\left(\boldsymbol{I}_3, \boldsymbol{0}_{7\times 7}\right), \tag{A.5}$$

and we get

$$\boldsymbol{L}_\vartheta^*\boldsymbol{C}^{*\dagger}\boldsymbol{C}^* = \boldsymbol{C}^{*\dagger}\boldsymbol{C}^*\boldsymbol{L}_\vartheta^*, \tag{A.6}$$

due to $\boldsymbol{C}^{*\dagger}\boldsymbol{C}^*$ and $\boldsymbol{L}_\vartheta^*$ share a block diagonal structure. Then the result follows by $\boldsymbol{E}_\vartheta^*$ of (4.30) post-multiplied with $\boldsymbol{C}^*$, using (A.6) and $\boldsymbol{C}^*\boldsymbol{C}^{*\dagger}\boldsymbol{C}^* = \boldsymbol{C}^*$ (Horn and Johnson, 2013, Ch. 7.3) such that $\boldsymbol{E}_\vartheta^*\boldsymbol{C}^* = \boldsymbol{C}^*\boldsymbol{L}_\vartheta^*\boldsymbol{C}^{*\dagger}\boldsymbol{C}^* = \boldsymbol{C}^*\boldsymbol{C}^{*\dagger}\boldsymbol{C}^*\boldsymbol{L}_\vartheta^* = \boldsymbol{C}^*\boldsymbol{L}_\vartheta^*$. □

A.2.2 Proof of Theorem 4.1

Proof. Consider the Lyapunov function candidate defined as $U(t,\boldsymbol{\eta}) := \frac{1}{\vartheta}\boldsymbol{\eta}^\intercal\boldsymbol{P}^{-1}\boldsymbol{\eta}$, where $\boldsymbol{P} = \boldsymbol{P}^\intercal > 0$ is the solution of (4.39). Differentiation along the trajectories of (4.37) gives

$$\begin{aligned}\dot{U}(t,\boldsymbol{\eta}) &= \frac{1}{\vartheta}\dot{\boldsymbol{\eta}}^\intercal\boldsymbol{P}^{-1}\boldsymbol{\eta} + \frac{1}{\vartheta}\boldsymbol{\eta}^\intercal\boldsymbol{P}^{-1}\dot{\boldsymbol{\eta}},\\ &= \boldsymbol{\eta}^\intercal(\boldsymbol{P}^{-1}\boldsymbol{A}^* + \boldsymbol{A}^{*\intercal}\boldsymbol{P}^{-1})\boldsymbol{\eta} - \varphi(t)\boldsymbol{\eta}^\intercal\boldsymbol{P}^{-1}\boldsymbol{K}_0\boldsymbol{C}^*\boldsymbol{\eta}\\ &\quad - \varphi(t)\boldsymbol{\eta}^\intercal\boldsymbol{C}^\intercal\boldsymbol{K}_0^\intercal\boldsymbol{P}^{-1}\boldsymbol{\eta} + 2\boldsymbol{\eta}^\intercal\boldsymbol{P}^{-1}\boldsymbol{\rho}(t,\boldsymbol{\chi}).\end{aligned} \tag{A.7}$$

By considering (4.38), we have that $\boldsymbol{K}_0^* = \boldsymbol{P}\boldsymbol{C}^{*\intercal}$ and by resolving the transposes and exploiting that $\boldsymbol{P} = \boldsymbol{P}^\intercal$ gives

$$\dot{U}(t,\boldsymbol{\eta}) = \boldsymbol{\eta}^\intercal\boldsymbol{P}^{-1}(\boldsymbol{A}^*\boldsymbol{P} + \boldsymbol{P}\boldsymbol{A}^{*\intercal})\boldsymbol{P}^{-1}\boldsymbol{\eta} - 2\varphi(t)\boldsymbol{\eta}^\intercal\boldsymbol{C}^{*\intercal}\boldsymbol{C}^*\boldsymbol{\eta} + 2\boldsymbol{\eta}^\intercal\boldsymbol{P}^{-1}\boldsymbol{\rho}(t,\boldsymbol{\chi}). \tag{A.8}$$

Furthermore, by inserting (4.39) into (A.8) gives

$$\dot{U}(t,\boldsymbol{\eta}) = -\boldsymbol{\eta}^\intercal\boldsymbol{P}^{-1}\boldsymbol{Q}\boldsymbol{P}^{-1}\boldsymbol{\eta} - 2(\varphi(t)-\tau)\boldsymbol{\eta}^\intercal\boldsymbol{C}^{*\intercal}\boldsymbol{C}^*\boldsymbol{\eta} + 2\boldsymbol{\eta}^\intercal\boldsymbol{P}^{-1}\boldsymbol{\rho}(t,\boldsymbol{\chi}). \tag{A.9}$$

Then, (A.9) can be simplified further since $\varphi(t) \geq \tau > 0$ yielding,

$$\dot{U}(t,\boldsymbol{\eta}) \leq -\boldsymbol{\eta}^\intercal\boldsymbol{P}^{-1}\boldsymbol{Q}\boldsymbol{P}^{-1}\boldsymbol{\eta} + 2\boldsymbol{\eta}^\intercal\boldsymbol{P}^{-1}\boldsymbol{\rho}(t,\boldsymbol{\chi}). \tag{A.10}$$

Moreover, since $\|\boldsymbol{I}_3 - \tilde{\boldsymbol{R}}^\intercal\| = \|\tilde{s}\boldsymbol{S}(\tilde{\boldsymbol{r}}) - \boldsymbol{S}(\tilde{\boldsymbol{r}}^2)\| \leq 2\|\tilde{\boldsymbol{r}}\|_2$, a bound of $\boldsymbol{\rho}(t,\boldsymbol{\chi})$ can be given as $\|\boldsymbol{\rho}(t,\boldsymbol{\chi})\|_2 \leq \frac{1}{\vartheta^4}\gamma_1\|\boldsymbol{\chi}\|_2$, for some $\gamma_1 > 0$ independent of ϑ. Hence, $\dot{U}(t,\boldsymbol{\eta})$ can take the following form

$$\dot{U}(t,\boldsymbol{\eta}) \leq \lambda_{\min}(\boldsymbol{Q})\lambda_{\min}(\boldsymbol{P}^{-1})^2\|\boldsymbol{\eta}\|_2^2 + \frac{2\|\boldsymbol{P}^{-1}\|}{\vartheta^4}\gamma_1\|\boldsymbol{\eta}\|_2\|\boldsymbol{\chi}\|_2. \tag{A.11}$$

Since the reference vector based on $\boldsymbol{f}_{ib}^n$, in (4.60)–(4.61), is not known, but estimated, we turn the attention back to the dynamics of $\tilde{s}$. The attitude observer of (4.60)–(4.61), with the injection term $\boldsymbol{\sigma}_{ib}^b$ based on known $\boldsymbol{f}_{ib}^n$ and the error dynamics,

$$\dot{\tilde{s}} = \frac{1}{2}\tilde{\boldsymbol{r}}^\intercal \boldsymbol{R}(\boldsymbol{q}_b^n)(\tilde{\boldsymbol{b}}^b + \boldsymbol{\sigma}_{ib}^b), \tag{A.12}$$

$$\dot{\tilde{\boldsymbol{r}}} = -\frac{1}{2}(\tilde{s}\boldsymbol{I}_3 - \boldsymbol{S}(\tilde{\boldsymbol{r}}))\boldsymbol{R}(\boldsymbol{q}_b^n)(\tilde{\boldsymbol{b}}^b + \boldsymbol{\sigma}_{ib}^b), \tag{A.13}$$

$$\dot{\tilde{\boldsymbol{b}}} = -\text{Proj}(\hat{\boldsymbol{b}}_{\text{gyro}}^b, -k_I(t)\boldsymbol{\sigma}_{ib}^b), \tag{A.14}$$

was proven to be USGES in Grip et al. (2012a). First, Grip et al. defines $V(t,\tilde{s}) := 1-\tilde{s}^2 = \|\tilde{\boldsymbol{r}}\|_2^2$ and $\dot{V}(t,\tilde{s}) = M_{b_{\text{gyro}}} - k_P c_{\text{obs}}^2 \alpha(\tilde{s})$, where $\alpha(\tilde{s}) = \tilde{s}^2(1-\tilde{s}^2)$. Moreover, from Grip et al. (2012a), a sufficiently large k_P and $|\tilde{s}| = \epsilon$ imply that $\dot{V} = M_{b_{\text{gyro}}} - k_P c_{\text{obs}}^2 \alpha(\epsilon)$. This results in the trajectories not being able to escape the region defined by $|\tilde{s}| \geq \epsilon$. Furthermore, $\dot{\tilde{s}}$ can be expressed as

$$\dot{\tilde{s}} = \frac{1}{2}\tilde{\boldsymbol{r}}^\intercal \boldsymbol{R}(\boldsymbol{q}_b^n)(\tilde{\boldsymbol{b}}^b + \boldsymbol{\sigma}_{ib}^b) + \mu_1, \tag{A.15}$$

where $\mu_1 = \frac{1}{2}\tilde{\boldsymbol{r}}^\intercal \boldsymbol{R}(\boldsymbol{q}_b^n)(\hat{\boldsymbol{\sigma}}_{ib}^b - \boldsymbol{\sigma}_{ib}^b)$, by taking into account (A.12) and that $\hat{\boldsymbol{\sigma}}_{ib}^b$, instead of $\boldsymbol{\sigma}_{ib}^b$, is utilized as the injection term. Moreover, μ_1 has the property

$$|\mu_1| \leq \frac{1}{2}k_1 \|\boldsymbol{f}_{ib}^b\|_2 \, \|\tilde{\boldsymbol{r}}\|_2 \, \|\tilde{\boldsymbol{f}}_{ib}^n\|_2 \leq \gamma_2 \|\tilde{\boldsymbol{r}}\|_2 \, \|\tilde{\boldsymbol{f}}_{ib}^n\|_2, \tag{A.16}$$

for a $\gamma_2 > 0$ independent of ϑ, which can be given as,

$$|\mu_1| \leq \vartheta^3 \gamma_2 \|\tilde{\boldsymbol{r}}\|_2 \, \|\boldsymbol{\eta}\|_2. \tag{A.17}$$

By following the steps of Grip et al. (2013, Proof, Theorem 1) we also have $|\dot{\tilde{s}}| \leq \frac{1}{2}(\|\tilde{\boldsymbol{b}}^b\|_2 + \|\hat{\boldsymbol{\sigma}}_{ib}^b\|_2)$. Since $\|\tilde{\boldsymbol{b}}^b\|_2 \leq M_{b_{\text{gyro}}}$ and $\hat{\boldsymbol{\sigma}}_{ib}^b$ only consist of bounded signals we have $|\dot{\tilde{s}}| \leq M_s$ for a $M_s > 0$ independent of ϑ.

Motivated by Grip et al. (2013, Lemma 2), the bound of $\tilde{\boldsymbol{x}}^*$ can be given as $\|\tilde{\boldsymbol{x}}^*\| \leq \delta$, obtained for all $t \geq T$, for some δ, as presented in Lemma A.1, Appendix A.2.3, on page 178. Furthermore, δ can be defined as $\delta := k_P \, c_{\text{obs}}^2(\alpha(\epsilon + \tilde{\epsilon}/2) - \alpha(\epsilon))/(2\gamma_2) > 0$ and $T = \tilde{\epsilon}/(2\,M_s)$, where $\tilde{\epsilon} := \bar{\epsilon} - \epsilon$, and let ϑ be sufficiently large such that for all $t \geq T$, $\|\tilde{\boldsymbol{x}}\|^* \leq \delta$. Then, as in Grip et al. (2013, Proof, Theorem 1),

$$|\tilde{s}(T)| \geq |\tilde{s}(0)| - \int_0^T |\dot{\tilde{s}}(t)| \, \mathrm{d}t \leq \bar{\epsilon} - M_s\tilde{\epsilon}/(2\,M_s) = \epsilon + \tilde{\epsilon}/2,$$

and for all $t \geq T$, $|\mu_1| \leq \gamma_2 \|\tilde{\boldsymbol{r}}\|_2 \, \|\boldsymbol{\eta}\|_2 \leq \gamma_2 \delta \leq k_P \, c_{\text{obs}}^2(\alpha(\epsilon + \tilde{\epsilon}/2) - \alpha(\epsilon))/2$. Now, it follows for $t \geq T$ that the derivative of $V(\tilde{s})$ yields

$$\begin{aligned} \dot{V} &\leq M_{b_{\text{gyro}}} - k_P \, c_{\text{obs}}^2 \, \alpha(\tilde{s}) + 2|\tilde{s}\mu_1|, \\ &\leq M_{b_{\text{gyro}}} - k_P \, c_{\text{obs}}^2(\alpha(\tilde{s}) - \alpha(\epsilon + \tilde{\epsilon}/2) + \alpha(\epsilon)). \end{aligned} \tag{A.18}$$

Then, with the reference to the proof of Grip et al. (2012a, Theorem 1) it follows for $|\tilde{s}| = \epsilon + \tilde{\epsilon}/2$ that $\dot{V} \leq M_{b_{\text{gyro}}} - k_P\, c_{\text{obs}}^2 \alpha(\epsilon) < 0$. Hence, $\tilde{\boldsymbol{q}}$ cannot escape the set $\mathcal{D}(\epsilon + \tilde{\epsilon}/2) \subset \mathcal{D}(\epsilon)$ and we can assume $|\tilde{s}| \geq \epsilon$ in the remainder of the analysis.

By taking in account (A.13)–(A.14) and that $\hat{\boldsymbol{\sigma}}_{ib}^b$ is the injection term, the error dynamics of $\tilde{\boldsymbol{r}}$ and $\tilde{\boldsymbol{b}}^b$ are written

$$\dot{\tilde{\boldsymbol{r}}} = -\frac{1}{2}\left(\tilde{s}\boldsymbol{I}_3 - \boldsymbol{S}(\tilde{\boldsymbol{r}})\right)\boldsymbol{R}(\boldsymbol{q}_b^n)(\tilde{\boldsymbol{b}}^b + \boldsymbol{\sigma}_{ib}^b) + \boldsymbol{\mu}_2, \tag{A.19}$$

$$\dot{\tilde{\boldsymbol{b}}} = -\text{Proj}(\hat{\boldsymbol{b}}_{\text{gyro}}^b, -k_I(t)\boldsymbol{\sigma}_{ib}^b) + \boldsymbol{\mu}_3. \tag{A.20}$$

Hence, $\boldsymbol{\mu}_2$ and $\boldsymbol{\mu}_3$ take the form,

$$\boldsymbol{\mu}_2 = \frac{1}{2}(\tilde{s}\boldsymbol{I}_3 - \boldsymbol{S}(\tilde{\boldsymbol{r}}))\boldsymbol{R}(\boldsymbol{q}_b^n)(\boldsymbol{\sigma}_{ib}^b - \hat{\boldsymbol{\sigma}}_{ib}^b), \tag{A.21}$$

and

$$\boldsymbol{\mu}_3 = \text{Proj}(\hat{\boldsymbol{b}}_{\text{gyro}}^b, -k_I(t)\boldsymbol{\sigma}_{ib}^b) - \text{Proj}(\hat{\boldsymbol{b}}_{\text{gyro}}^b, -k_I(t)\hat{\boldsymbol{\sigma}}_{ib}^b). \tag{A.22}$$

Then, $\|\boldsymbol{\mu}_2\|_2 \leq \gamma_3 \|\tilde{\boldsymbol{f}}_{ib}^n\|_2 \leq \vartheta^3 \gamma_3 \|\boldsymbol{\eta}\|_2$ for some $\gamma_3 > 0$ independent of ϑ. From the properties of the parameter projection, it can be shown that

$$\|\boldsymbol{\mu}_3\|_2 \leq \gamma_4 \|\tilde{\boldsymbol{f}}_{ib}^n\|_2 \leq \vartheta^3 \gamma_4 \|\boldsymbol{\eta}\|_2, \tag{A.23}$$

for some $\gamma_4 > 0$ independent of ϑ.

Furthermore, Grip et al. (2012a) also presents the Lyapunov function candidate

$$W(t, \tilde{\boldsymbol{r}}, \tilde{s}, \tilde{\boldsymbol{b}}^b) = V(\tilde{s}) + 2\,\ell\,\tilde{s}\,\tilde{\boldsymbol{r}}^\intercal \boldsymbol{R}(\boldsymbol{q}_b^n)\,\tilde{\boldsymbol{b}}^b + \frac{\ell}{2k_I}\left(\tilde{\boldsymbol{b}}^b\right)^\intercal \tilde{\boldsymbol{b}}^b > 0, \quad \forall\, \tilde{\boldsymbol{r}}, \tilde{\boldsymbol{b}}^b \neq 0, \tag{A.24}$$

By following the steps of Grip et al. (2012a, Proof, Theorem 1) result in

$$\dot{W} \leq -\begin{pmatrix} \|\tilde{\boldsymbol{r}}\|_2 & \|\tilde{\boldsymbol{b}}^b\|_2 \end{pmatrix} \begin{pmatrix} k_P\, a - \ell\, M_{b_{\text{gyro}}}^2 & \star \\ -\frac{1}{2}(1 + 2\,\ell\, M_\omega) & l\,\epsilon^2 \end{pmatrix} \begin{pmatrix} \|\tilde{\boldsymbol{r}}\|_2 \\ \|\tilde{\boldsymbol{b}}^2\|_2 \end{pmatrix}, \tag{A.25}$$

where $\star$ indicates symmetry, $a > 0$ and $M_\omega \geq \|\boldsymbol{\omega}_{ib}^b\|_2$. ℓ is given in Grip et al. (2012a). Moreover, from Grip et al. (2012a) for some sufficiently large k_P, can it be shown that $\dot{W} \leq -\kappa\|\boldsymbol{\chi}\|_2^2 < 0$ for some $\kappa > 0$. With the relations above we get that $\dot{W}$ is less or equal than $-\kappa\|\boldsymbol{\chi}\|_2^2$ plus the terms related to μ_1, $\boldsymbol{\mu}_2$ and $\boldsymbol{\mu}_3$, yielding that

$$\begin{aligned} \dot{W} \leq\ & -\kappa\|\boldsymbol{\chi}\|_2^2 - 2\tilde{s}\mu_1 + 2\ell\mu_1\tilde{\boldsymbol{r}}^\intercal \boldsymbol{R}(\boldsymbol{q}_b^n)\tilde{\boldsymbol{b}}^b + 2\ell\tilde{s}\boldsymbol{\mu}_2^\intercal \boldsymbol{R}(\boldsymbol{q}_b^n)\tilde{\boldsymbol{b}}^b \\ & + 2\ell\tilde{s}\tilde{\boldsymbol{r}}^\intercal \boldsymbol{R}(\boldsymbol{q}_b^n)\boldsymbol{\mu}_3 + \frac{\ell}{k_I(t)}\left(\tilde{\boldsymbol{b}}^b\right)^\intercal \boldsymbol{\mu}_3. \end{aligned} \tag{A.26}$$

Furthermore, by taking in account the bounds on μ_1, $\boldsymbol{\mu}_2$ and $\boldsymbol{\mu}_3$, it follows that

$$\begin{aligned} \dot{W} &\leq -\kappa\|\boldsymbol{\chi}\|_2^2 + 2\vartheta^3\gamma_2\|\tilde{\boldsymbol{r}}\|_2\|\boldsymbol{\eta}\|_2 + 2\ell\vartheta^3\gamma_2\|\tilde{\boldsymbol{b}}^b\|_2\|\boldsymbol{\eta}\|_2 \\ &\quad + 2\ell\vartheta^3\gamma_3\|\tilde{\boldsymbol{b}}^b\|_2\|\boldsymbol{\eta}\|_2 + 2\ell\vartheta^3\gamma_4\|\tilde{\boldsymbol{r}}\|_2\|\boldsymbol{\eta}\|_2 + \frac{\ell}{k_I(t)}\vartheta^3\gamma_4\|\tilde{\boldsymbol{b}}^b\|_2\|\boldsymbol{\eta}\|_2, \\ &\leq -\kappa\|\boldsymbol{\chi}\|_2^2 + \gamma_5\vartheta^3\|\boldsymbol{\chi}\|_2\|\boldsymbol{\eta}\|_2, \end{aligned} \tag{A.27}$$

for an appropriate constant γ_5, independent of ϑ.

Now, defining the LFC $Y(t, \boldsymbol{\chi}, \boldsymbol{\eta}) := U + \frac{1}{\vartheta^7} W$ on the form of

$$\beta_1(\|\boldsymbol{\eta}\|_2^2 + \|\boldsymbol{\chi}\|_2^2) \leq Y \leq \beta_2(\|\boldsymbol{\eta}\|_2^2 + \|\boldsymbol{\chi}\|_2^2), \tag{A.28}$$

where $\beta_1, \beta_2 > 0$ are constants. Then, the derivative of Y along the trajectories satisfies

$$\begin{aligned} \dot{Y}(t, \boldsymbol{\chi}, \boldsymbol{\eta}) \leq & -\lambda_{\min}(\boldsymbol{Q})\lambda_{\min}(\boldsymbol{P}^{-1})^2\|\boldsymbol{\eta}\|_2^2 + \frac{2\,\gamma_1}{\vartheta^4}\|\boldsymbol{P}^{-1}\|\|\boldsymbol{\eta}\|_2\|\boldsymbol{\chi}\|_2 \\ & - \frac{1}{\vartheta^7}\kappa\|\boldsymbol{\chi}\|_2^2 + \gamma_5\frac{1}{\vartheta^4}\|\boldsymbol{\chi}\|_2\|\boldsymbol{\eta}\|_2, \end{aligned} \tag{A.29}$$

yielding

$$\dot{Y}(t, \boldsymbol{\chi}, \boldsymbol{\eta}) \leq -\begin{pmatrix} \|\boldsymbol{\eta}\|_2 & \|\boldsymbol{\chi}\|_2 \end{pmatrix} \begin{pmatrix} \lambda_{\min}(\boldsymbol{Q})\lambda_{\min}(\boldsymbol{P}^{-1})^2 & \star \\ -\frac{2\|\boldsymbol{P}^{-1}\|\gamma_1+\gamma_5}{2\vartheta^4} & \frac{\kappa}{\vartheta^7} \end{pmatrix} \begin{pmatrix} \|\boldsymbol{\eta}\|_2 \\ \|\boldsymbol{\chi}\|_2 \end{pmatrix}, \tag{A.30}$$

where $\star$ indicates symmetry. Clearly the first-order principal minor,

$$\lambda_{\min}(\boldsymbol{Q})\lambda_{\min}(\boldsymbol{P}^{-1})^2 > 0,$$

is positive. The second-order principal minor,

$$\frac{1}{\vartheta^7}\lambda_{\min}(\boldsymbol{Q})\lambda_{\min}(\boldsymbol{P}^{-1})^2\kappa - \frac{1}{\vartheta^8}\frac{(2\|\boldsymbol{P}^{-1}\|\gamma_1 + \gamma_5)^2}{4}$$

is positive for $\vartheta > \frac{(2\|\boldsymbol{P}^{-1}\|\gamma_1+\gamma_5)^2}{4\,\lambda_{\min}(\boldsymbol{Q})\lambda_{\min}(\boldsymbol{P}^{-1})^2\,\kappa}$. Inherently

$$\dot{Y}(t, \boldsymbol{\chi}, \boldsymbol{\eta}) \leq -\beta_3(\|\boldsymbol{\eta}\|_2^2 + \|\boldsymbol{\chi}\|_2^2), \tag{A.31}$$

for some $\beta_3 > 0$. By invoking the comparison lemma (Khalil, 2002, Lemma 3.4) with the linear system $\dot{u} = -\beta_3 u$, and the corresponding solution $u(t) = u(0)\mathrm{e}^{-\beta_3 t}$ yields

$$Y(t, \boldsymbol{\chi}, \boldsymbol{\eta}) \leq Y(0, \boldsymbol{\chi}, \boldsymbol{\eta})\mathrm{e}^{-\beta_3 t}, \tag{A.32}$$

for all $t \geq 0$. Consequently, the equilibrium $(\boldsymbol{\eta}; \boldsymbol{\chi}) = \mathbf{0}$ is USGES as defined in Appendix A.1. □

A.2.3 Uniform Attractivity the Origin of the TMO's Error Dynamics

Drawing upon the elements of Grip et al. (2013, Lemma 2), the origin of $\tilde{\boldsymbol{x}}^*$ is proven to be uniformly attractive and stable.

Lemma A.1 (Uniform Attractivity and Stability)**.** *For any $\delta > 0$ and $T > 0$ there exist a $\vartheta_1^* \geq 1$ such that for $\vartheta \geq \vartheta_1^*$ and all initial condition as specified in Theorem 4.1 results in $\|\tilde{\boldsymbol{x}}^*\|_2 \leq \delta$ for all $t \geq T$. Hence, $\tilde{\boldsymbol{x}}^* = \mathbf{0}$ is an uniformly attractive and stable equilibrium point.*

Proof. The proof follows as in (Grip et al., 2013, Proof Lemma 2). The parameter projection in (4.10c) ensures $\|\tilde{\boldsymbol{b}}^b\|_2 \leq M_{\hat{b}_{\text{gyro}}}$ and because $\|\tilde{\boldsymbol{r}}\|_2 \leq 1$, we have that

$$\|\tilde{\boldsymbol{x}}\|_2 \leq \sqrt{M_{\hat{b}_{\text{gyro}}}^2 + 1}.$$

Furthermore, we define the level set $\Omega_\vartheta := \{\boldsymbol{\eta} \,|\, U \leq \frac{\delta^2}{\vartheta^7}\lambda_{\min}(\boldsymbol{P}^{-1})\}$, and note that $\boldsymbol{\eta} \in \Omega_\vartheta \Rightarrow \|\boldsymbol{\eta}\|_2 \leq \frac{\delta}{\vartheta^3} \Rightarrow \|\tilde{\boldsymbol{x}}^*\|_2 \leq \delta$. Outside of Ω_ϑ, we have $\|\boldsymbol{\eta}\|_2 \geq \frac{\delta}{\vartheta^3}\sqrt{\lambda_{\min}(\boldsymbol{P}^{-1})/\lambda_{\max}(\boldsymbol{P}^{-1})}$ which implies that $\dot{U}$ can be stated as

$$\begin{aligned}
\dot{U} \leq & -\frac{1}{2}\lambda_{\min}(\boldsymbol{Q})\lambda_{\min}(\boldsymbol{P}^{-1})^2\|\boldsymbol{\eta}\|_2^2 \\
& -\left(\frac{\delta\sqrt{\lambda_{\min}(\boldsymbol{P}^{-1})}\sqrt{\lambda_{\min}(\boldsymbol{Q})\lambda_{\min}(\boldsymbol{P}^{-1})^2}}{2\vartheta^3\sqrt{\lambda_{\max}(\boldsymbol{P}^{-1})}} - \frac{2\|\boldsymbol{P}^{-1}\|\gamma_1}{\vartheta^4}\sqrt{M^2+1}\right)\|\boldsymbol{\eta}\|_2 \\
= & -\frac{1}{2}\lambda_{\min}(\boldsymbol{Q})\lambda_{\min}(\boldsymbol{P}^{-1})^2\|\boldsymbol{\eta}\|_2^2 \\
& -\left(\frac{\delta\sqrt{\lambda_{\min}(\boldsymbol{Q})}\lambda_{\min}(\boldsymbol{P}^{-1})^{\frac{3}{2}}}{2\vartheta^3\sqrt{\lambda_{\max}(\boldsymbol{P}^{-1})}} - \frac{2\|\boldsymbol{P}^{-1}\|\gamma_1}{\vartheta^4}\sqrt{M^2+1}\right)\|\boldsymbol{\eta}\|_2.
\end{aligned}$$

by utilizing (A.11). The first term is negative definite. The second term can be made negative definite with a sufficiently large ϑ, yielding

$$\begin{aligned}
\dot{U} &\leq -\frac{1}{2}\lambda_{\min}(\boldsymbol{Q})\lambda_{\min}(\boldsymbol{P}^{-1})^2\|\boldsymbol{\eta}\|_2^2 \\
&\leq -\frac{\vartheta}{2}\frac{\lambda_{\min}(\boldsymbol{Q})\lambda_{\min}(\boldsymbol{P}^{-1})^2}{\lambda_{\max}(\boldsymbol{P}^{-1})}U
\end{aligned}$$

outside Ω_ϑ. Defining a as:

$$a := \vartheta\,\lambda_{\min}(\boldsymbol{Q})\lambda_{\min}(\boldsymbol{P}^{-1})^2/(2\lambda_{\max}(\boldsymbol{P}^{-1}))$$

and invoking the comparison lemma (Khalil, 2002, Lemma 3.4) with the linear system $\dot{u} = -au$ and the corresponding solution $u(t) \leq u(0)e^{-a\,t}$, we get $U(t) \leq U(0)e^{-a\,t}$. By letting $L > \delta$ be a bound on $\|\tilde{\boldsymbol{x}}^*(0)\|_2$ for any initial condition as

specified in Theorem 4.1 , then L is also a bound on $\|\boldsymbol{\eta}(0)\|_2$. Then, outside Ω_ϑ we have

$$U(t) \leq \frac{\lambda_{\max}(\boldsymbol{P}^{-1})L^2}{\vartheta} \mathrm{e}^{\left(-\frac{\vartheta}{2}\frac{\lambda_{\min}(\boldsymbol{Q})\lambda_{\min}(\boldsymbol{P}^{-1})^2}{\lambda_{\max}(\boldsymbol{P}^{-1})}t\right)}.$$

Thus, $\boldsymbol{\eta}$ must enter Ω_ϑ before

$$t \geq T = \frac{2\lambda_{\max}(\boldsymbol{P}^{-1})}{\lambda_{\min}(\boldsymbol{Q})\lambda_{\min}(\boldsymbol{P}^{-1})^2\vartheta}\left(6\ln(\vartheta) + \ln\left(\frac{L^2\lambda_{\max}(\boldsymbol{P}^{-1})}{\delta^2\lambda_{\min}(\boldsymbol{P}^{-1})}\right)\right).$$

Hence, for a sufficiency large $\vartheta \geq 1$, $\|\tilde{\boldsymbol{x}}^*\|_2 \leq \delta$ for $t \geq T$. □

A.2.4 Proof of Lemma 4.2

Proof. Let $\boldsymbol{Z} \in \mathbb{R}^{m\times(m-k)}$ be the matrix forming an orthonormal basis for the null space of $\boldsymbol{C}$ where m is the dimension of $\boldsymbol{A}(t)$ and $k = \operatorname{rank}(\boldsymbol{C})$ such that $\boldsymbol{C}\boldsymbol{Z} = \boldsymbol{0}_{3\times m-k}$. Considering the vector $\boldsymbol{z} = (z_1; \boldsymbol{z}_2; z_3; \boldsymbol{z}_4; \boldsymbol{z}_5; z_6; z_7)$ where $z_1, z_3, z_6, z_7 \in \mathbb{R}^1$, $\boldsymbol{z}_2 \in \mathbb{R}^2$ and $\boldsymbol{z}_4, \boldsymbol{z}_5 \in \mathbb{R}^3$, the vector $\boldsymbol{z}$ belongs to the null space of $\boldsymbol{C}$ if $\boldsymbol{C}\boldsymbol{z} = \boldsymbol{0}_{3\times1}$. This is valid for $z_1 = z_7 = 0$ and $\boldsymbol{z}_2 = \boldsymbol{0}_{2\times1}$. z_3, $\boldsymbol{z}_4$ and $\boldsymbol{z}_5$ can be arbitrary.

By considering singular value decomposition of $\boldsymbol{C} = \boldsymbol{U}\boldsymbol{\Sigma}\boldsymbol{V}^\intercal$, where $\boldsymbol{C}^\dagger = \boldsymbol{V}\boldsymbol{\Sigma}^\dagger\boldsymbol{U}^\intercal$. From the characterization of the null space of $\boldsymbol{C}$, we obtain

$$\boldsymbol{C}^\dagger\boldsymbol{C} = \boldsymbol{V}\boldsymbol{\Sigma}^\dagger\boldsymbol{\Sigma}\boldsymbol{V}^\intercal = \begin{pmatrix}\boldsymbol{Z}_{11} & \boldsymbol{Z}_{12}^\intercal \\ \boldsymbol{Z}_{12} & \boldsymbol{Z}_{22}\end{pmatrix}, \tag{A.33}$$

since $\boldsymbol{U}^\intercal = \boldsymbol{U}^{-1}$, such that $\boldsymbol{U}^\intercal\boldsymbol{U} = \boldsymbol{I}_3$, (Horn and Johnson, 2013, Ch. 2.1) and where

$$\boldsymbol{Z}_{11} = \operatorname{blockdiag}\left(\frac{1}{2}, \boldsymbol{Z}_p, \boldsymbol{0}_{3\times3}, \boldsymbol{0}_{3\times3}\right),$$
$$\boldsymbol{Z}_{12} = \begin{pmatrix}0 & \boldsymbol{0}_{1\times9} \\ \frac{1}{2} & \boldsymbol{0}_{1\times9}\end{pmatrix}, \quad \boldsymbol{Z}_{22} = \begin{pmatrix}0 & 0 \\ 0 & \frac{1}{2}\end{pmatrix},$$

and $\boldsymbol{Z}_p = \operatorname{blockdiag}(\boldsymbol{I}_2, 0)$. Then we get

$$\boldsymbol{L}_\vartheta\boldsymbol{C}^\dagger\boldsymbol{C} = \boldsymbol{C}^\dagger\boldsymbol{C}\boldsymbol{L}_\vartheta, \tag{A.34}$$

due to the structure of $\boldsymbol{C}^\dagger\boldsymbol{C}$ and since $\boldsymbol{L}_\vartheta$ is diagonal and has 1 in the upper left and bottom right element such that $1/2$ contained in $\boldsymbol{Z}_{12}$ is distributed equivalent in both sides of (A.34) in the upper and lower, left and right elements, respectively. Then the result follows by $\boldsymbol{E}_\vartheta$ post-multiplied with $\boldsymbol{C}$, using (A.34) and $\boldsymbol{C}\boldsymbol{C}^\dagger\boldsymbol{C} = \boldsymbol{C}$ (Horn and Johnson, 2013, Ch. 7.3) such that $\boldsymbol{E}_\vartheta\boldsymbol{C} = \boldsymbol{C}\boldsymbol{L}_\vartheta\boldsymbol{C}^\dagger\boldsymbol{C} = \boldsymbol{C}\boldsymbol{C}^\dagger\boldsymbol{C}\boldsymbol{L}_\vartheta = \boldsymbol{C}\boldsymbol{L}_\vartheta$. □

A.2.5 Proof of Lemma 4.3

Proof. UCO of the LTV system $\left(\boldsymbol{A}(t), \boldsymbol{R}^{-1/2}(t)\boldsymbol{C}\right)$ can be established with the observability Gramian

$$\boldsymbol{\mathcal{W}}_o(t_0, t_1) = \int_{t_0}^{t_1} \boldsymbol{\Phi}^\intercal(t_0, \tau)\boldsymbol{C}^\intercal \boldsymbol{R}^{-1}\boldsymbol{C}\boldsymbol{\Phi}(t_0, \tau)\,\mathrm{d}\tau, \tag{A.35}$$

while UCC of $\left(\boldsymbol{A}(t), \boldsymbol{Q}^{-1/2}(t)\boldsymbol{G}(t)\right)$ can be established with the controllability Gramian

$$\boldsymbol{\mathcal{W}}_c(t_0, t_1) = \int_{t_0}^{t_1} \boldsymbol{\Phi}(t_0, \tau)\boldsymbol{G}(t)\boldsymbol{Q}(t)\boldsymbol{G}^\intercal(t)\boldsymbol{\Phi}^\intercal(t_0, \tau)\,\mathrm{d}\tau, \tag{A.36}$$

for all $t \geq 0$. Moreover, the system ($\boldsymbol{A}(t)$,$\boldsymbol{G}(t)$,$\boldsymbol{C}$) is UCO and UCC if and only if both $\boldsymbol{\mathcal{W}}_o(t_0, t_1)$ and $\boldsymbol{\mathcal{W}}_c(t_0, t_1)$ are positive definite on every interval $t \in [t_0, t_1]$ for $t_1 > t_0$ for all $t \geq 0$. We omit the explicite time dependency of ω_e, λ_w and $\sigma_{b,\mathrm{VVR}}$ in the reminder of the proof.

We start with the state transition matrix $\boldsymbol{\Phi}(t_0, \tau) = \mathrm{e}^{(\boldsymbol{A}(\tau - t_0))}$ which takes the form of

$$\boldsymbol{\Phi}(\tau) = \begin{pmatrix} 1 & 0\ 0\ (\tau - t_0) & 0\ 0\ \frac{(\tau-t_0)^2}{2} & 0\ 0\ \frac{(\tau-t_0)^3}{6} & \boldsymbol{0}_{1\times 2} \\ \boldsymbol{0}_{3\times 1} & \boldsymbol{I}_3 & (\tau - t_0)\boldsymbol{I}_3 & \frac{(\tau-t_0)^2}{2}\boldsymbol{I}_3 & \boldsymbol{0}_{3\times 2} \\ \boldsymbol{0}_{3\times 1} & \boldsymbol{0}_{3\times 3} & \boldsymbol{I}_3 & (\tau - t_0)\boldsymbol{I}_3 & \boldsymbol{0}_{3\times 2} \\ \boldsymbol{0}_{3\times 1} & \boldsymbol{0}_{3\times 3} & \boldsymbol{0}_{3\times 3} & \boldsymbol{I}_3 & \boldsymbol{0}_{3\times 2} \\ \boldsymbol{0}_{2\times 1} & \boldsymbol{0}_{2\times 3} & \boldsymbol{0}_{2\times 3} & \boldsymbol{0}_{2\times 3} & \mathrm{e}^{(\boldsymbol{F}_{\mathrm{VVR}}(\tau - t_0))} \end{pmatrix}. \tag{A.37}$$

Due to the block-diagonal structure of $\boldsymbol{A}(t)$ we have that

$$\boldsymbol{A}^j(t) = \begin{pmatrix} \boldsymbol{A}_0^j & \boldsymbol{0}_{10\times 2} \\ \boldsymbol{0}_{2\times 10} & \boldsymbol{F}_{\mathrm{VVR}}^j(t) \end{pmatrix}, \quad j \in [1, \dots m-1], \tag{A.38}$$

where m is the dimension of $\boldsymbol{A}(t)$. Therefore, we may study the observability of the subsystems $(\boldsymbol{A}_0, \boldsymbol{C}_0)$, with dimension $m_0 = 10$, and $(\boldsymbol{F}_{\mathrm{VVR}}(t), \boldsymbol{H}_{\mathrm{VVR}})$, with dimension $l = 2$, separately. By consider the nominal LTI system $(\boldsymbol{A}_0, \boldsymbol{C}_0)$, applying the rank condition on $\boldsymbol{\mathcal{O}}_0 = \left(\boldsymbol{C}_0; \boldsymbol{C}_0\boldsymbol{A}_0; \boldsymbol{C}_0\boldsymbol{A}_0^2; \dots; \boldsymbol{C}_0\boldsymbol{A}_0^{m_0-1}\right)$ is trivial, and yields rank m_0. Then if the system $(\boldsymbol{F}_{\mathrm{VVR}}(t), \boldsymbol{H}_{\mathrm{VVR}})$ is UCO, the complete system $(\boldsymbol{A}(t), \boldsymbol{C})$ is UCO. We now consider the observability Gramian for the lower right block of $(\boldsymbol{A}(t), \boldsymbol{C})$,

$$\boldsymbol{\mathcal{W}}_{o_{\mathrm{VVR}}}(t_0, t_1) = \int_{t_0}^{t_1} \boldsymbol{\Upsilon}_{o_{\mathrm{VVR}}}^\intercal(t_0, \tau) R_{\mathrm{VVR}}^{-1} \boldsymbol{\Upsilon}_{o_{\mathrm{VVR}}}(t_0, \tau)\,\mathrm{d}\tau, \tag{A.39}$$

where $\boldsymbol{\Upsilon}_{o_{\mathrm{VVR}}}(t_0, \tau) = \boldsymbol{H}_{\mathrm{VVR}}\boldsymbol{\Phi}_{\mathrm{VVR}}(t_0, \tau)$. Continuing with the non-zero vector $z = (z_1, z_2)^\intercal \in \mathbb{R}^l$, and pre and post multiplying (A.39) with z, we obtain

$$z^\intercal \boldsymbol{\mathcal{W}}_{o_{\mathrm{VVR}}}(t_0, t_1) z = \int_{t_0}^{t_1} z^\intercal \boldsymbol{\Upsilon}_{o_{\mathrm{VVR}}}^\intercal(t_0, \tau) R_{\mathrm{VVR}}^{-1} \boldsymbol{\Upsilon}_{o_{\mathrm{VVR}}}(t_0, \tau) z\,\mathrm{d}\tau, \tag{A.40}$$

for all $t_1 \geq t_0$. Since R_{VVR} is a positive scalar we may write

$$z^\intercal \mathcal{W}_{o_{\text{VVR}}}(t_0, t_1) z \geq R_{\max} \int_{t_0}^{t_1} \|\Upsilon_{o_{\text{VVR}}}(t_0, \tau) z\|_2^2 \, \mathrm{d}\tau \tag{A.41}$$

where $R_{\max}$ is the maximum value of R_{VVR} over the interval $[t_0, t_1]$. Then it is relatively straightforward to obtain

$$\begin{aligned}
\Upsilon_{o_{\text{VVR}}}(t_0, \tau) z = \ldots \\
&- \frac{\omega_e \mathrm{e}^{-\lambda_w}}{2\sqrt{\lambda_w^2 - 1}} \left(\mathrm{e}^{\sqrt{\lambda_w^2 - 1}\omega_e(\tau - t_0)} - \mathrm{e}^{-\sqrt{\lambda_w^2 - 1}\omega_e(\tau - t_0)} \right) z_1 \\
&+ \left(\frac{\mathrm{e}^{-\lambda_w}}{2} \left(\mathrm{e}^{\sqrt{\lambda_w^2 - 1}\omega_e(\tau - t_0)} + \mathrm{e}^{-\sqrt{\lambda_w^2 - 1}\omega_e(\tau - t_0)} \right) \right. \\
&\left. - \frac{\lambda_w \mathrm{e}^{-\lambda_w}}{2\sqrt{\lambda_w^2 - 1}} \left(\mathrm{e}^{\sqrt{\lambda_w^2 - 1}\omega_e(\tau - t_0)} - \mathrm{e}^{-\sqrt{\lambda_w^2 - 1}\omega_e(\tau - t_0)} \right) \right) z_2.
\end{aligned} \tag{A.42}$$

Furthermore, we exploit that $0 < \lambda_w < 1$, resulting in

$$\sqrt{\lambda_w^2 - 1} = \sqrt{1 - \lambda_w^2} i \tag{A.43}$$

such that (A.42) becomes

$$\begin{aligned}
\Upsilon_{o_{\text{VVR}}}(t_0, \tau) z = \ldots \\
&- \frac{\omega_e \mathrm{e}^{-\lambda_w}}{2i\sqrt{1 - \lambda_w^2}} \left(\mathrm{e}^{\sqrt{1 - \lambda_w^2}\omega_e(\tau - t_0)i} - \mathrm{e}^{-\sqrt{1 - \lambda_w^2}\omega_e(\tau - t_0)i} \right) z_1 \\
&+ \left(\frac{\mathrm{e}^{-\lambda_w}}{2} \left(\mathrm{e}^{\sqrt{1 - \lambda_w^2}\omega_e(\tau - t_0)i} + \mathrm{e}^{-\sqrt{1 - \lambda_w^2}\omega_e(\tau - t_0)i} \right) \right. \\
&\left. - \frac{\lambda_w \mathrm{e}^{-\lambda_w}}{2i\sqrt{1 - \lambda_w^2}} \left(\mathrm{e}^{\sqrt{1 - \lambda_w^2}\omega_e(\tau - t_0)i} - \mathrm{e}^{-\sqrt{1 - \lambda_w^2}\omega_e(\tau - t_0)i} \right) \right) z_2,
\end{aligned} \tag{A.44}$$

which again can be written as

$$\begin{aligned}
\Upsilon_{o_{\text{VVR}}}(t_0, \tau) z = z_2 \mathrm{e}^{-\lambda_w} \cos\left(\sqrt{1 - \lambda_w^2} \omega_e (\tau - t_0) \right) \\
- \frac{(\omega_e z_1 + \lambda_w z_2) \mathrm{e}^{-\lambda_w}}{\sqrt{1 - \lambda_w^2}} \sin\left(\sqrt{1 - \lambda_w^2} \omega_e (\tau - t_0) \right).
\end{aligned} \tag{A.45}$$

It follows that $\|\Upsilon_{o_{\text{VVR}}}(t_0, \tau) z\|_2^2$ can be obtained as

$$\begin{aligned}
\|\Upsilon_{o_{\text{VVR}}}(t_0, \tau) z\|_2^2 = \frac{(\omega_e z_1 + \lambda_w z_2)^2 \mathrm{e}^{-2\lambda_w}}{1 - \lambda_w^2} \sin^2(c(\tau - t_0)) \\
- 2 \frac{(\omega_e z_1 z_2 + \lambda_w z_2^2) \mathrm{e}^{-2\lambda_w}}{\sqrt{1 - \lambda_w^2}} \sin(c(\tau - t_0)) \cos(c(\tau - t_0)) \\
+ z_2^2 \mathrm{e}^{-2\lambda_w} \cos^2(c(\tau - t_0)),
\end{aligned} \tag{A.46}$$

for $c := \sqrt{1-\lambda_w^2}\omega_e$. Now (A.46) can be simplified further,

$$\begin{aligned}\|\boldsymbol{\Upsilon}_{o_{\text{VVR}}}(t_0,\tau)\boldsymbol{z}\|_2^2 &= \frac{(\omega_e z_1+\lambda_w z_2)^2 \mathrm{e}^{-2\lambda_w}}{1-\lambda_w^2}\sin^2(c(\tau-t_0)) \\ &- \frac{(\omega_e z_1 z_2+\lambda_w z_2^2)\mathrm{e}^{-2\lambda_w}}{\sqrt{1-\lambda_w^2}}\sin(2c(\tau-t_0)) + z_2^2\mathrm{e}^{-2\lambda_w}\cos^2(c(\tau-t_0)).\end{aligned} \tag{A.47}$$

From (A.47) we notice that for $\tau \geq t_0$ $\|\boldsymbol{\Upsilon}_{o_{\text{VVR}}}(t_0,\tau)\boldsymbol{z}\|_2^2 = 0$ if and only if $\boldsymbol{z} = \boldsymbol{0}_{l\times 1}$. Moreover, since

$$\int_{t_0}^{t_1}\sin^2(c(\tau-t_0))\,\mathrm{d}\tau = \frac{2c(t_1-t_0)+\sin\left(2c(t_0-t_1)\right)}{4c}, \tag{A.48}$$

$$\int_{t_0}^{t_1}\cos^2(c(\tau-t_0))\,\mathrm{d}\tau = \frac{2c(t_1-t_0)+\sin\left(2c(t_1-t_0)\right)}{4c}, \tag{A.49}$$

where $2c(t_1-t_0)$ always is positive and

$$\frac{(\omega_e z_1+\lambda_w z_2)^2\mathrm{e}^{-2\lambda_w}}{1-\lambda_w^2} \neq z_2^2\mathrm{e}^{-2\lambda_w} \quad \forall t\geq 0, \boldsymbol{z}\neq \boldsymbol{0}_{l\times 1}, \tag{A.50}$$

result in $\boldsymbol{z}^\intercal \boldsymbol{\mathcal{W}}_{o_{\text{VVR}}}(t_0,t_1)\boldsymbol{z}$ to be uniformly positive. Hence, for any $t_1 > t_0$, $\boldsymbol{\mathcal{W}}_{o_{\text{VVR}}}(t_0,t_1)$ is positive definite (and therefore invertible), since ω_e is positive and bounded and $0<\lambda_w<1$ on every interval $t\in[t_0,t_1]$. Thus, $(\boldsymbol{A}(t), \boldsymbol{R}^{-1/2}\boldsymbol{C})$ is UCO.

Now we consider controllability, making a similar argument as above. With no loss of generality, we assumed that $\boldsymbol{R}(t,\hat{\boldsymbol{q}}_b^t) = \boldsymbol{I}_3$, for usage in $\boldsymbol{B}_0$ cf. (4.70), due to the rotation matrix having unit norm and rank of 3 uniformly. By considering the nominal LTI system $(\boldsymbol{A}_0,\boldsymbol{B}_0)$, applying the rank condition on $\boldsymbol{\mathcal{C}}_0 = \left(\boldsymbol{B}_0,\, \boldsymbol{A}_0\boldsymbol{B}_0,\, \boldsymbol{A}_0^2\boldsymbol{B}_0,\, \ldots,\, \boldsymbol{A}_0^{m_0-1}\boldsymbol{B}_0\right)$ is trivial, and yields rank m_0. Then if the system $(\boldsymbol{F}_{\text{VVR}}(t), \boldsymbol{G}_{\text{VVR}}(t))$, is UCC, the complete system $(\boldsymbol{A}(t), \boldsymbol{G}(t))$ is UCC. Now we consider the controllability Gramian for the lower right block of $(\boldsymbol{A}(t), \boldsymbol{G}(t))$,

$$\boldsymbol{\mathcal{W}}_{c_{\text{VVR}}}(t_0,t_1) = \int_{t_0}^{t_1}\boldsymbol{\Upsilon}_{c_{\text{VVR}}}^\intercal(t_0,\tau)Q_{\text{VVR}}\boldsymbol{\Upsilon}_{c_{\text{VVR}}}(t_0,\tau)\,\mathrm{d}\tau, \tag{A.51}$$

where $\boldsymbol{\Upsilon}_{c_{\text{VVR}}}(t_0,\tau) = \boldsymbol{G}_{\text{VVR}}^\intercal\boldsymbol{\Phi}_{\text{VVR}}^\intercal(t_0,\tau)$. We continue by proving UCC of $(\boldsymbol{F}_{\text{VVR}}(t), \boldsymbol{G}_{\text{VVR}}(t))$ applying the non-zero vector $\boldsymbol{z} = (z_1,z_2)^\intercal \in \mathbb{R}^l$ similarly as above such that

$$\boldsymbol{z}^\intercal\boldsymbol{\mathcal{W}}_{c_{\text{VVR}}}(t_0,t_1)\boldsymbol{z} = \int_{t_0}^{t_1}\boldsymbol{z}^\intercal\boldsymbol{\Upsilon}_{c_{\text{VVR}}}^\intercal(t_0,\tau)\boldsymbol{\Upsilon}_{c_{\text{VVR}}}(t_0,\tau)\boldsymbol{z}\,\mathrm{d}\tau, \tag{A.52}$$

$$= \int_{t_0}^{t_1}\|\boldsymbol{\Upsilon}_{c_{\text{VVR}}}(t_0,\tau)\boldsymbol{z}\|_2^2\,\mathrm{d}\tau, \tag{A.53}$$

using that $Q_{\text{VVR}} = 1$, for all $t_1 \geq 0$. Then it is relatively straightforward to obtain

$$\begin{aligned}
&\Upsilon_{c_{\text{VVR}}}(t_0, \tau)\boldsymbol{z} = \dots \\
&\frac{\sigma_{b,\text{VVR}} \mathrm{e}^{-\lambda_w}}{2\omega_e\sqrt{\lambda_w^2 - 1}} \left(\mathrm{e}^{-\sqrt{\lambda_w^2-1}\omega_e(\tau - t_0)} - \mathrm{e}^{\sqrt{\lambda_w^2-1}\omega_e(\tau - t_0)} \right) z_1 \\
&+ \left(\frac{\sigma_{b,\text{VVR}} \mathrm{e}^{-\lambda_w}}{2} \left(\mathrm{e}^{\sqrt{\lambda_w^2-1}\omega_e(\tau - t_0)} + \mathrm{e}^{-\sqrt{\lambda_w^2-1}\omega_e(\tau - t_0)} \right) \right. \\
&\left. - \frac{\sigma_{b,\text{VVR}} \lambda_w \mathrm{e}^{-\lambda_w}}{2\sqrt{\lambda_w^2 - 1}} \left(\mathrm{e}^{\sqrt{\lambda_w^2-1}\omega_e(\tau - t_0)} - \mathrm{e}^{-\sqrt{\lambda_w^2-1}\omega_e(\tau - t_0)} \right) \right) z_2.
\end{aligned} \tag{A.54}$$

which is structurally similar to (A.42). By following similar steps as to (A.44)–(A.50) we can state that for any $t_1 > t_0$, $\boldsymbol{\mathcal{W}}_{c_{\text{VVR}}}(t_0, t_1)$ is positive definite since ω_e and $\sigma_{b,\text{VVR}}$ is positive and bounded and $0 < \lambda_w < 1$ on every interval $[t_0, t_1]$. Thus, $(\boldsymbol{A}(t), \boldsymbol{Q}^{-1/2}(t)\boldsymbol{G}(t))$ is UCC. □

A.2.6 Proof of Lemma 4.4

Proof. By considering the Lyapunov function candidate $U(t, \boldsymbol{\eta}) = \boldsymbol{\eta}^\intercal \boldsymbol{\vartheta}^{-1} \boldsymbol{P}^{-1} \boldsymbol{\vartheta}^{-1} \boldsymbol{\eta}$, where $\boldsymbol{P} = \boldsymbol{P}^\intercal > 0$ is the solution of (4.84), the proof follows from Kalman and Bucy (1961); Anderson (1971) and is trivial to obtain. However, the steps of the proof is not necessarily obvious. Therefore, the main steps are still included.

Along the trajectories of (4.87) and (4.84) one obtains

$$\dot{U}(t, \boldsymbol{\eta}) = \dot{\boldsymbol{\eta}}^\intercal \boldsymbol{\vartheta}^{-1} \boldsymbol{P}^{-1} \boldsymbol{\vartheta}^{-1} \boldsymbol{\eta} + \boldsymbol{\eta}^\intercal \boldsymbol{\vartheta}^{-1} \dot{\boldsymbol{P}}^{-1} \boldsymbol{\vartheta}^{-1} \boldsymbol{\eta} + \boldsymbol{\eta}^\intercal \boldsymbol{\vartheta}^{-1} \boldsymbol{P}^{-1} \boldsymbol{\vartheta}^{-1} \dot{\boldsymbol{\eta}} \tag{A.55}$$

Now, inserting for $\dot{\boldsymbol{\eta}}^\intercal \boldsymbol{\vartheta}^{-1}$ and $\boldsymbol{\vartheta}^{-1} \dot{\boldsymbol{\eta}}$, including (4.82), such that (A.55) becomes

$$\begin{aligned}
\dot{U}(t, \boldsymbol{\eta}) = &\boldsymbol{\eta}^\intercal \left(\boldsymbol{A}^\intercal - \boldsymbol{C}^\intercal \boldsymbol{R}^{-1} \boldsymbol{C} \boldsymbol{P} \right) \boldsymbol{\vartheta}^{-1} \boldsymbol{P}^{-1} \boldsymbol{\vartheta}^{-1} \boldsymbol{\eta} \\
&+ \boldsymbol{\eta}^\intercal \boldsymbol{\vartheta}^{-1} \boldsymbol{P}^{-1} \boldsymbol{\vartheta}^{-1} \left(\boldsymbol{A} - \boldsymbol{P} \boldsymbol{C}^\intercal \boldsymbol{R}^{-1} \boldsymbol{C} \right) \boldsymbol{\eta} \\
&- \boldsymbol{\eta}^\intercal \boldsymbol{\vartheta}^{-1} \boldsymbol{P}^{-1} \dot{\boldsymbol{P}} \boldsymbol{P}^{-1} \boldsymbol{\vartheta}^{-1} \boldsymbol{\eta}.
\end{aligned} \tag{A.56}$$

Expanding (A.56) results in

$$\begin{aligned}
\dot{U}(t, \boldsymbol{\eta}) = &\boldsymbol{\eta}^\intercal \boldsymbol{P}^{-1} \left(\boldsymbol{P} \boldsymbol{A}^\intercal - \boldsymbol{P} \boldsymbol{C}^\intercal \boldsymbol{R}^{-1} \boldsymbol{C} \boldsymbol{P} \right) \boldsymbol{P}^{-1} \boldsymbol{\vartheta}^{-1} \boldsymbol{\eta} \\
&+ \boldsymbol{\eta}^\intercal \boldsymbol{\vartheta}^{-1} \boldsymbol{P}^{-1} \left(\boldsymbol{A} \boldsymbol{P} - \boldsymbol{P} \boldsymbol{C}^\intercal \boldsymbol{R}^{-1} \boldsymbol{C} \boldsymbol{P} \right) \boldsymbol{P}^{-1} \boldsymbol{\eta} \\
&- \boldsymbol{\eta}^\intercal \boldsymbol{\vartheta}^{-1} \boldsymbol{P}^{-1} \dot{\boldsymbol{P}} \boldsymbol{P}^{-1} \boldsymbol{\vartheta}^{-1} \boldsymbol{\eta}.
\end{aligned} \tag{A.57}$$

Furthermore, by inserting (4.84) into (A.57) results in

$$\begin{aligned}
\dot{U}(t, \boldsymbol{\eta}) = &\boldsymbol{\eta}^\intercal \boldsymbol{P}^{-1} \left(\boldsymbol{P} \boldsymbol{A}^\intercal - \boldsymbol{P} \boldsymbol{C}^\intercal \boldsymbol{R}^{-1} \boldsymbol{C} \boldsymbol{P} \right) \boldsymbol{P}^{-1} \boldsymbol{\vartheta}^{-1} \boldsymbol{\eta} \\
&+ \boldsymbol{\eta}^\intercal \boldsymbol{\vartheta}^{-1} \boldsymbol{P}^{-1} \left(\boldsymbol{A} \boldsymbol{P} - \boldsymbol{P} \boldsymbol{C}^\intercal \boldsymbol{R}^{-1} \boldsymbol{C} \boldsymbol{P} \right) \boldsymbol{P}^{-1} \boldsymbol{\eta} \\
&- \boldsymbol{\eta}^\intercal \boldsymbol{\vartheta}^{-1} \boldsymbol{P}^{-1} \left(\boldsymbol{\vartheta} \boldsymbol{A} \boldsymbol{P} + \boldsymbol{\vartheta} \boldsymbol{P} \boldsymbol{A}^\intercal - \boldsymbol{\vartheta} \boldsymbol{P} \boldsymbol{C}^\intercal \boldsymbol{R}^{-1} \boldsymbol{C} \boldsymbol{P} + \boldsymbol{\vartheta} \boldsymbol{G} \boldsymbol{Q} \boldsymbol{G}^\intercal \right) \boldsymbol{P}^{-1} \boldsymbol{\vartheta}^{-1} \boldsymbol{\eta}.
\end{aligned} \tag{A.58}$$

Then by expanding (A.58) such that we have ϑ^{-1} on both sides of the parentheses one obtain

$$\begin{aligned}\dot{U}(t,\boldsymbol{\eta}) = \boldsymbol{\eta}^\top \vartheta^{-1}\boldsymbol{P}^{-1}\big(&- \vartheta\boldsymbol{G}\boldsymbol{Q}\boldsymbol{G}^\top + \boldsymbol{P}\vartheta\boldsymbol{A}^\top + \boldsymbol{A}\vartheta\boldsymbol{P} - \vartheta\boldsymbol{A}\boldsymbol{P} - \vartheta\boldsymbol{P}\boldsymbol{A}^\top \\ &- \boldsymbol{P}\vartheta\boldsymbol{C}^\top\boldsymbol{R}^{-1}\boldsymbol{C}\boldsymbol{P} - \boldsymbol{P}\boldsymbol{C}^\top\boldsymbol{R}^{-1}\boldsymbol{C}\vartheta\boldsymbol{P} + \vartheta\boldsymbol{P}\boldsymbol{C}^\top\boldsymbol{R}^{-1}\boldsymbol{C}\boldsymbol{P}\big)\boldsymbol{P}^{-1}\vartheta^{-1}\boldsymbol{\eta}.\end{aligned} \tag{A.59}$$

Now, since ϑ commutes with $\boldsymbol{A}$ and $\boldsymbol{A}^\top$, (A.59) becomes

$$\begin{aligned}\dot{U}(t,\boldsymbol{\eta}) &= \boldsymbol{\eta}^\top \vartheta^{-1}\boldsymbol{P}^{-1}\big(- \vartheta\boldsymbol{G}\boldsymbol{Q}\boldsymbol{G}^\top + \boldsymbol{P}\boldsymbol{A}^\top\vartheta + \vartheta\boldsymbol{A}\boldsymbol{P} - \vartheta\boldsymbol{A}\boldsymbol{P} - \vartheta\boldsymbol{P}\boldsymbol{A}^\top \\ &\quad - \boldsymbol{P}\vartheta\boldsymbol{C}^\top\boldsymbol{R}^{-1}\boldsymbol{C}\boldsymbol{P} - \boldsymbol{P}\boldsymbol{C}^\top\boldsymbol{R}^{-1}\boldsymbol{C}\vartheta\boldsymbol{P} + \vartheta\boldsymbol{P}\boldsymbol{C}^\top\boldsymbol{R}^{-1}\boldsymbol{C}\boldsymbol{P}\big)\boldsymbol{P}^{-1}\vartheta^{-1}\boldsymbol{\eta} \\ &= \boldsymbol{\eta}^\top \vartheta^{-1}\boldsymbol{P}^{-1}\big(- \vartheta\boldsymbol{G}\boldsymbol{Q}\boldsymbol{G}^\top + \boldsymbol{P}\boldsymbol{A}^\top\vartheta - \vartheta\boldsymbol{P}\boldsymbol{A}^\top \\ &\quad - \boldsymbol{P}\vartheta\boldsymbol{C}^\top\boldsymbol{R}^{-1}\boldsymbol{C}\boldsymbol{P} - \boldsymbol{P}\boldsymbol{C}^\top\boldsymbol{R}^{-1}\boldsymbol{C}\vartheta\boldsymbol{P} + \vartheta\boldsymbol{P}\boldsymbol{C}^\top\boldsymbol{R}^{-1}\boldsymbol{C}\boldsymbol{P}\big)\boldsymbol{P}^{-1}\vartheta^{-1}\boldsymbol{\eta}.\end{aligned} \tag{A.60}$$

Since $\vartheta = \vartheta^\top > 0$, $\vartheta \geq 1$, $\|\boldsymbol{P}\boldsymbol{A}^\top\vartheta\| = \|\vartheta\boldsymbol{P}\boldsymbol{A}^\top\|$ and $\boldsymbol{P}\boldsymbol{A}^\top\vartheta$ and $\vartheta\boldsymbol{P}\boldsymbol{A}^\top$ have equal eigenvalues. The same goes for $\boldsymbol{P}\vartheta\boldsymbol{C}^\top\boldsymbol{R}^{-1}\boldsymbol{C}\boldsymbol{P}$ and $\boldsymbol{P}\boldsymbol{C}^\top\boldsymbol{R}^{-1}\boldsymbol{C}\vartheta\boldsymbol{P}$. In addition,

$$\|\boldsymbol{P}\vartheta\boldsymbol{C}^\top\boldsymbol{R}^{-1}\boldsymbol{C}\boldsymbol{P}\| = \|\boldsymbol{P}\boldsymbol{C}^\top\boldsymbol{R}^{-1}\boldsymbol{C}\vartheta\boldsymbol{P}\| \geq \|\vartheta\boldsymbol{P}\boldsymbol{C}^\top\boldsymbol{R}^{-1}\boldsymbol{C}\boldsymbol{P}\|, \tag{A.61}$$

since, $\vartheta\boldsymbol{C}^\top\boldsymbol{R}^{-1}\boldsymbol{C} = (\boldsymbol{C}^\top\boldsymbol{R}^{-1}\boldsymbol{C}\vartheta)^\top$ and $\|\vartheta\boldsymbol{P}\boldsymbol{C}^\top\| \leq \|\boldsymbol{P}\vartheta\boldsymbol{C}^\top\|$, together with

$$\begin{aligned}\max\left(\operatorname{eig}\left(\boldsymbol{P}\vartheta\boldsymbol{C}^\top\boldsymbol{R}^{-1}\boldsymbol{C}\boldsymbol{P}\right)\right) &= \max\left(\operatorname{eig}\left(\boldsymbol{P}\boldsymbol{C}^\top\boldsymbol{R}^{-1}\boldsymbol{C}\vartheta\boldsymbol{P}\right)\right) \\ &\geq \max\left(\operatorname{eig}\left(\vartheta\boldsymbol{P}\boldsymbol{C}^\top\boldsymbol{R}^{-1}\boldsymbol{C}\boldsymbol{P}\right)\right),\end{aligned} \tag{A.62}$$

due to how ϑ possibly scales $\boldsymbol{C}^\top\boldsymbol{R}^{-1}\boldsymbol{C}$ on the inside of $\boldsymbol{P}$, on either side in (A.61), since $\vartheta\boldsymbol{P} \neq \boldsymbol{P}\vartheta$ for $\vartheta > 1$. Moreover, $\vartheta\boldsymbol{P}\boldsymbol{C}^\top\boldsymbol{R}^{-1}\boldsymbol{C}\boldsymbol{P} \geq 0$, and

$$\|\boldsymbol{G}\boldsymbol{Q}\boldsymbol{G}^\top\| \leq \|\vartheta\boldsymbol{G}\boldsymbol{Q}\boldsymbol{G}^\top\|, \tag{A.63}$$

$$\|\boldsymbol{P}\boldsymbol{C}^\top\boldsymbol{R}^{-1}\boldsymbol{C}\boldsymbol{P}\| \leq \|\vartheta\boldsymbol{P}\boldsymbol{C}^\top\boldsymbol{R}^{-1}\boldsymbol{C}\boldsymbol{P}\|. \tag{A.64}$$

Consequently,

$$\begin{aligned}\dot{U}(t,\boldsymbol{\eta}) &\leq -\boldsymbol{\eta}^\top\vartheta^{-1}\boldsymbol{P}^{-1}\big(\boldsymbol{G}\boldsymbol{Q}\boldsymbol{G}^\top + \boldsymbol{P}\boldsymbol{C}^\top\boldsymbol{R}^{-1}\boldsymbol{C}\boldsymbol{P}\big)\boldsymbol{P}^{-1}\vartheta^{-1}\boldsymbol{\eta} \\ &= -\boldsymbol{\eta}^\top\vartheta^{-1}\left(\boldsymbol{P}^{-1}\boldsymbol{G}\boldsymbol{Q}\boldsymbol{G}^\top\boldsymbol{P}^{-1} + \boldsymbol{C}^\top\boldsymbol{R}^{-1}\boldsymbol{C}\right)\vartheta^{-1}\boldsymbol{\eta} < 0\end{aligned} \tag{A.65}$$

In addition, since $\|\vartheta^{-1}\| = 1$, for all $\vartheta \geq 1$, results in

$$\dot{U}(t,\boldsymbol{\eta}) \leq -\gamma_1\|\boldsymbol{\eta}\|_2^2 < 0, \tag{A.66}$$

for some constant $\gamma_1 > 0$ independent of ϑ, (Johansen and Fossen, 2015, Lemma 6), since $\boldsymbol{P}$ is bounded above and below due to UCO of $(\boldsymbol{A}(t), \boldsymbol{C})$, and UCC of $(\boldsymbol{A}(t), \boldsymbol{G}(t))$, with positive definite $\boldsymbol{R}$ and $\boldsymbol{Q}$ matrices, yielding that the origin of the nominal error dynamics is GES. □

A.2.7 Proof of Proposition 4.1

Proof. The proof is mainly based on the proofs of Grip et al. (2013), Bryne et al. (2014) and Johansen et al. (2017). For completeness the main components of the proof are outlined below.

From the proof of Lemma 4.4 we have that $U(t,\boldsymbol{\eta}) = \boldsymbol{\eta}^\top \boldsymbol{\vartheta}^{-1}\boldsymbol{P}^{-1}\boldsymbol{\vartheta}^{-1}\boldsymbol{\eta}$ and that

$$\dot{U} \leq \gamma_1\|\boldsymbol{\eta}\|_2 + \frac{1}{\vartheta}\gamma_2\gamma_4\|\boldsymbol{\eta}\|_2^2 + \frac{1}{\vartheta^4}\gamma_3\gamma_4\|\boldsymbol{\eta}\|_2 \cdot \|\boldsymbol{\chi}\|_2, \tag{A.67}$$

with

$$\frac{2}{\vartheta}\boldsymbol{\eta}^\top \boldsymbol{\vartheta}^{-1}\boldsymbol{P}^{-1}\boldsymbol{\rho}_1(t,\boldsymbol{\eta}) \leq \gamma_1\|\boldsymbol{\eta}\|_2 \tag{A.68}$$

$$\frac{2}{\vartheta^4}\boldsymbol{\eta}^\top \boldsymbol{\vartheta}^{-1}\boldsymbol{P}^{-1}\boldsymbol{\rho}_2(t,\boldsymbol{\chi}) \leq \frac{1}{\vartheta}\gamma_2\gamma_4\|\boldsymbol{\eta}\|_2^2 + \frac{1}{\vartheta^4}\gamma_3\gamma_4\|\boldsymbol{\eta}\|_2 \cdot \|\boldsymbol{\chi}\|_2 \tag{A.69}$$

where $\gamma_1, \gamma_2, \gamma_3, \gamma_4 > 0$ are constants independent of ϑ since $\|\boldsymbol{\vartheta}^{-1}\| = 1$ for all $\vartheta \geq 1$. Moreover, since we known that a uniform bound on $\boldsymbol{P}^{-1}$, cf. proof of Theorem 4.1, can be established independent of ϑ, (Johansen and Fossen, 2015, Lemma 6), we continue with the intermediate results of Grip et al. (2013) where it can be shown that for any $\delta > 0$ and $T > 0$ there exist a $\vartheta_1^* \geq 1$ such that for $\vartheta \geq \vartheta_1^*$ there exist an invariant set $\mathcal{X}_1 \in \mathbb{R}^{12}$ such that for $\|\boldsymbol{\eta}(0)\|_2 \in \mathcal{X}_1$ we have that $\|\boldsymbol{\eta}\|_2 \leq \delta$, for all $t \geq T$, as obtained in Lemma A.1. By further following the cited results we define the function

$$W(t,\tilde{s},\tilde{\boldsymbol{r}},\tilde{\boldsymbol{b}}^b) := \left(1-\tilde{s}^2\right) + 2\ell\tilde{s}\tilde{\boldsymbol{r}}\boldsymbol{R}(\boldsymbol{q}_b^t)\tilde{\boldsymbol{b}}^b + \frac{\ell}{k_I}(\tilde{\boldsymbol{b}}^b)^\top\tilde{\boldsymbol{b}}^b, \tag{A.70}$$

where ℓ is a constant taken from Grip et al. (2012a). Furthermore, in Grip et al. (2013) it was shown that for $|\tilde{s}| > \bar{\epsilon}$, $\dot{W}$ satisfy,

$$\dot{W} \leq \gamma_6\|\boldsymbol{\chi}\|_2^2 + \gamma_5\|\boldsymbol{\chi}\| \cdot \|\boldsymbol{\eta}\|_2, \tag{A.71}$$

for some constants $\gamma_5, \gamma_6 > 0$, independent of ϑ. Moreover, we continue to define the Lyapunov function candidate $V(t,\boldsymbol{\eta},\boldsymbol{\chi}) = U(t,\boldsymbol{\eta}) + \frac{1}{\vartheta_7}W(t,\boldsymbol{\chi})$, resulting in

$$\dot{V} \leq -\boldsymbol{z}^\top \boldsymbol{M}(\vartheta)\boldsymbol{z}, \tag{A.72}$$

with $\boldsymbol{z} = \left(\|\boldsymbol{\eta}\|_2; \|\boldsymbol{\chi}\|_2\right) \in \mathbb{R}^2$ and

$$\boldsymbol{M}(\vartheta) = \begin{pmatrix} \gamma_1 - \frac{\gamma_2\gamma_4}{\vartheta} & \star \\ -\frac{\gamma_3\gamma_4+\gamma_5}{2\vartheta^4} & \frac{\gamma_6}{\vartheta^7} \end{pmatrix}, \tag{A.73}$$

and where $\star$ indicate symmetry. Considering the principal minors of $\boldsymbol{M}(\vartheta)$, we obtain $\boldsymbol{M}(\vartheta) > 0$ with

$$\vartheta \geq \max\left(\frac{\gamma_2\gamma_4}{\gamma_1}, \frac{\gamma_2\gamma_4\gamma_6 + \frac{1}{4}(\gamma_3\gamma_4+\gamma_5)^2}{\gamma_1\gamma_6}\right). \tag{A.74}$$

Thus by choosing ϑ_1^* to satisfy (A.74) and $\vartheta \geq \vartheta_1^*$ accordingly, there exist an invariant set $\mathcal{X}_2$ where for all $\tilde{\boldsymbol{x}} \in \mathcal{X}_2$ and constants α_3, $\alpha_4 > 0$, we have

$$\dot{V} \leq -\alpha_3 \|\boldsymbol{z}\|_2^2 - \alpha_4 \|\boldsymbol{\chi}\|_2^2 \leq -2\beta V, \tag{A.75}$$

for some $\beta > 0$ where $\mathcal{X} \subset \mathcal{X}_1 \cap \mathcal{X}_2$ is chosen as the largest invariant set. The USGES result, applying the definition of Loria and Panteley (2005), of the origin $(\tilde{\boldsymbol{x}}; \boldsymbol{\chi}) = \mathbf{0}$ then follows by applying the comparison lemma (Khalil, 2002, Lemma 3.4), such that

$$V(t) \leq V(0)\mathrm{e}^{-2\beta t}, \quad \forall t \geq 0, \tag{A.76}$$

is obtained. □

A.2.8 Proof of Lemma 5.1

Proof. Since $\boldsymbol{A}(t)$ is time-varying, the rank condition for observability does not directly apply. Observability properties of time-varying systems can, among others, be obtained through calculating the observability co-distribution applying Lie derivatives $L_0, L_1, \ldots, L_{n-1}$ for a system of dimension n. See, e.g. Nijmeijer and der Schaft (1990, Ch. 3.2) for details.

Theorem 3.32 of Nijmeijer and der Schaft (1990, Ch. 3.2) entails that the pair $(\boldsymbol{A}(t), \boldsymbol{C})$ is uniformly observable if and only if the observability co-distribution, $\mathrm{d}\boldsymbol{O}$ has full rank, e.i

$$\operatorname{rank}(\mathrm{d}\boldsymbol{O}) = n \tag{A.77}$$

for all $t \geq 0$.

The observability co-distribution takes the form of

$$\mathrm{d}\boldsymbol{O} = \begin{pmatrix} L_0(t) \\ L_1(t) \\ L_2(t) \end{pmatrix} = \begin{pmatrix} \boldsymbol{C} \\ \boldsymbol{C}\boldsymbol{A}(t) \\ \boldsymbol{C}\boldsymbol{A}^2(t) + \boldsymbol{C}\dot{\boldsymbol{A}}(t) \end{pmatrix} \tag{A.78}$$

$$= \begin{pmatrix} 0 & 1 & 1 \\ -\omega_e^2(t) & -2\lambda_w\omega_e(t) & 0 \\ 2\lambda_w\omega_e^3(t) - 2\omega_e(t)\dot{\omega}_e(t) & 4\lambda_w^2\omega_e^2(t) - 2\omega_e(t) - 2\lambda_w & 0 \end{pmatrix}. \tag{A.79}$$

Suppose that, at an instance in time, $\dot{\omega}_e(t) = \lambda_w\omega_e^2(t)$ such that

$$\mathrm{d}\boldsymbol{O} = \begin{pmatrix} 0 & 1 & 1 \\ -\omega_e^2(t) & -2\lambda_w\omega_e(t) & 0 \\ 0 & 4\lambda_w^2\omega_e^2(t) - 2\omega_e(t) - 2\lambda_w & 0 \end{pmatrix}. \tag{A.80}$$

By investigation of the null space of $\mathrm{d}\boldsymbol{O}$, i.e. $\mathrm{d}\boldsymbol{O}\boldsymbol{x} = 0$, where $\boldsymbol{x}$ is the state vector, yields

$$x_2 + x_3 = 0 \tag{A.81}$$

$$-\omega_e^2(t)x_1 - 2\lambda_w\omega_e(t)x_2 = 0 \tag{A.82}$$

$$\left(4\lambda_w^2\omega_e^2(t) - 2\omega_e(t) - 2\lambda_w\right)x_2 = 0. \tag{A.83}$$

resulting in

$$\begin{aligned}
&\text{eq. (A.83) implies: } x_2 = 0,\\
&\text{eq. (A.81) implies: } x_3 = -x_2 = 0,\\
&\text{eq. (A.82) implies: } x_1 = \frac{2\lambda_w}{\omega_e^2(t)} x_2 = 0
\end{aligned}$$

from the properties of $0 < \omega_{e,\min} \leq \omega_e(t) \leq \omega_{e,\max} < \infty$, and that $\lambda_w > 0$ is a constant. Now suppose that $\dot{\omega}_e(t) = 0$. Then,

$$\mathrm{d}\boldsymbol{\mathcal{O}} = \begin{pmatrix} 0 & 1 & 1 \\ -\omega_e^2(t) & -2\lambda_w\omega_e(t) & 0 \\ 2\lambda_w\omega_e^3(t) & 4\lambda_w^2\omega_e^2(t) - 2\omega_e(t) - 2\lambda_w & 0 \end{pmatrix}. \tag{A.84}$$

Again, investigation of the null space, $\mathrm{d}\boldsymbol{\mathcal{O}}\boldsymbol{x} = 0$, results in

$$x_2 + x_3 = 0 \tag{A.85}$$

$$-\omega_e^2(t)x_1 - 2\lambda_w\omega_e(t)x_2 = 0 \tag{A.86}$$

$$2\lambda_w\omega_e^3(t)x_1 + \left(4\lambda_w^2\omega_e^2(t) - 2\omega_e(t) - 2\lambda_w\right)x_2 = 0. \tag{A.87}$$

The validity of (A.86)–(A.87) hold if and only if $x_1 = x_2 = 0$ which implies that (A.85) can only be zero for $x_3 = -x_2 = 0$. Then, since $\boldsymbol{C}$ is constant, $\omega_e(t)$ is positive and uniformly bounded and λ_w is a positive constant, $\mathrm{d}\boldsymbol{\mathcal{O}}$ cannot take any other form than presented in (A.80) and (A.84). Hence, the pair $(\boldsymbol{A}(t), \boldsymbol{C})$ is uniformly observable for all $t \geq 0$ since

$$\dim \operatorname{null}(\mathrm{d}\boldsymbol{\mathcal{O}}) = 0 \Rightarrow \operatorname{rank}(\mathrm{d}\boldsymbol{\mathcal{O}}) = 3, \forall t \geq 0,$$

for all constellations of $\mathrm{d}\boldsymbol{\mathcal{O}}$. □

B Notations, Representations and Background Material

B.1 General Mathematical Notations

The Euclidean vector norm and the induced matrix norm are denoted $\|\cdot\|_2$ and $\|\cdot\|$, respectively. The set $\mathcal{I}_k$ is a set containing the indices of available measurements at time $t = k \cdot T_s$ where T_s indicates the sampling interval and k is the time index. $E[\cdot]$ denotes statistical expectation, while Gaussian white noise n with mean μ and variance σ^2 is given as $n \sim (\mu, \sigma^2)$. The exponential function is denoted $\mathrm{e}^{(\cdot)}$, while the matrix exponential function is denoted $\mathbf{e}^{(\cdot)}$. Furthermore, the $n \times n$ identity matrix is denoted $\boldsymbol{I}_n$, while a block diagonal matrix is given by $\boldsymbol{M} = \text{blockdiag}(\boldsymbol{M}_1, \boldsymbol{M}_2, \ldots, \boldsymbol{M}_n)$ for square matrices $\boldsymbol{M}_j$. Moreover, the transpose of a vector or a matrix is denoted $(\cdot)^\intercal$. $\boldsymbol{S}(\cdot) \in SS(3)$ represents the skew symmetric matrix such that $\boldsymbol{S}(z_1)z_2 = z_1 \times z_2$ for two vectors $z_1, z_2 \in \mathbb{R}^3$. $z = (z_1; z_2; \ldots; z_n)$ denotes a vector of stacked column vectors $z_1, z_2, \ldots z_n$. Moreover, $\otimes$ denotes the Hamiltonian quaternion product. For a vector $z \in \mathbb{R}^3$, with transpose $z^\intercal$, $\bar{z}$ denotes the quaternion with zero real part and vector part z, that is $\bar{z} = (0; z)$. Saturation is represented by $\text{sat}_\star(\cdot)$, where the subscript indicates the saturation limit. The right Moore-Penrose pseudo inverse is denoted $(\cdot)^\dagger$. The sinc function is defined as

$$\text{sinc}(\alpha) := \begin{cases} 1 & \text{for } \alpha = 0 \\ \frac{\sin(\alpha)}{\alpha} & \text{otherwise,} \end{cases} \tag{B.1}$$

for an angle α.

B.2 Attitude Representation

A general rotation matrix describing the rotation between two given frames $\{a\}$ and $\{b\}$ and is denoted $\boldsymbol{R}_a^b \in SO(3)$. In this thesis two attitude representations, Euler angles and the unit quaternion, respectively, are used to describe orientations. The former is mainly used for illustrations on how the attitude evolves over time, while the unit quaternion is used to estimate the attitude.

B.2.1 Euler Angles

The Euler angles roll, pitch and yaw is denoted ϕ, θ and ψ, respectively together with their angular rates p, q and r in compliance with the SNAME (1950) notations. From Fossen (2011, Ch. 2) and the references therein these relates to the matrix

between the $\{b\}$ and $\{n\}$ frames like

$$\boldsymbol{R}_b^n = \begin{pmatrix} \mathrm{c}\theta\mathrm{c}\psi & -\mathrm{c}\phi\mathrm{s}\psi + \mathrm{s}\phi\mathrm{s}\theta\mathrm{c}\psi & \mathrm{s}\phi\mathrm{s}\psi + \mathrm{s}\theta\mathrm{c}\phi\mathrm{c}\psi \\ \mathrm{c}\theta\mathrm{s}\psi & \mathrm{c}\phi\mathrm{c}\psi + \mathrm{s}\psi\mathrm{s}\theta\mathrm{s}\phi & -\mathrm{s}\phi\mathrm{c}\psi + \mathrm{c}\phi\mathrm{s}\psi\mathrm{s}\theta \\ -\mathrm{s}\theta & \mathrm{s}\phi\mathrm{c}\theta & \mathrm{c}\phi\mathrm{c}\theta \end{pmatrix} \in SO(3), \tag{B.2}$$

where $\mathrm{s}\cdot := \sin(\cdot)$, $\mathrm{c}\cdot := \cos(\cdot)$.

B.2.2 Unit Quaternion

Similar to Euler angles and the rotation matrix, the rotation between $\{a\}$ and $\{b\}$ may be represented using the unit quaternion $\boldsymbol{q}_a^b = (s, \boldsymbol{r}^\intercal)^\intercal$ where $s \in \mathbb{R}^1$ is the real part of the quaternion and $\boldsymbol{r} \in \mathbb{R}^3$ is the vector part. Moreover, its conjugate is denoted $\boldsymbol{q}_a^{b*} = (s, -\boldsymbol{r}^\intercal)^\intercal$.

The unit quaternion $\boldsymbol{q}_a^b = (s, \boldsymbol{r}^\intercal)^\intercal$ where $s \in \mathbb{R}^1$ is the real part of the quaternion and $\boldsymbol{r} \in \mathbb{R}^3$ is the vector part such that $\boldsymbol{q}_a^b \in \mathcal{Q}$, where the set $\mathcal{Q}$ is given as

$$\mathcal{Q} := \left\{ \boldsymbol{q} | \boldsymbol{q}^\intercal \boldsymbol{q} = 1,\ \boldsymbol{q} = (s, \boldsymbol{r}^\intercal)^\intercal \right\}.$$

The rotation matrix $\boldsymbol{R}(\boldsymbol{q}_a^b) := \boldsymbol{R}_a^b$ can be obtained from the unit quaternion, $\boldsymbol{q}_a^b$ using

$$\boldsymbol{R}(\boldsymbol{q}_a^b) = \boldsymbol{I}_3 + 2s\boldsymbol{S}(\boldsymbol{r}) + 2\boldsymbol{S}^2(\boldsymbol{r}), \tag{B.3}$$

Fossen (2011, Eq. 2.56) and the reference therein.

Euler angles may be obtained from $\boldsymbol{q}_a^b$ by relating these through the rotation matrix

$$\boldsymbol{R}(\boldsymbol{q}_a^b) = \boldsymbol{R}_a^b(\phi, \theta, \psi) = \begin{pmatrix} R_{11} & R_{12} & R_{13} \\ R_{21} & R_{22} & R_{23} \\ R_{31} & R_{32} & R_{33} \end{pmatrix}, \tag{B.4}$$

such that

$$\phi = \operatorname{arctan2}(R_{32}, R_{33}), \tag{B.5}$$

$$\theta = -\arcsin(R_{32}) = -\arctan\left(\frac{R_{31}}{\sqrt{1 - R_{31}^2}}\right), \quad \text{for } \theta \neq \pm 90^\circ \tag{B.6}$$

$$\psi = \operatorname{arctan2}(R_{31}, R_{11}). \tag{B.7}$$

The unit quaternion rate of change, $\dot{\boldsymbol{q}}_a^b$, can be calculated in numerous ways. Three different notation are used in this thesis, all equivalent. The first takes the form of

$$\dot{\boldsymbol{q}}_a^b = \frac{1}{2}\boldsymbol{T}_q(\boldsymbol{q}_a^b)\boldsymbol{\omega}_{ba}^a, \tag{B.8}$$

where

$$\boldsymbol{T}_q(\boldsymbol{q}) = \begin{pmatrix} -\boldsymbol{r} \\ s\boldsymbol{I}_3 + \boldsymbol{S}(\boldsymbol{r}) \end{pmatrix} = \begin{pmatrix} -r_1 & -r_2 & -r_3 \\ s & -r_3 & r_2 \\ r_3 & s & -r_1 \\ -r_2 & r_1 & s \end{pmatrix}, \tag{B.9}$$

similar to Fossen (2011, Ch. 2.2.2), while the second takes the form of

$$\dot{\boldsymbol{q}}_a^b = \boldsymbol{q}_a^b \otimes \begin{pmatrix} 0 \\ \boldsymbol{\omega}_{ba}^a \end{pmatrix}, \tag{B.10}$$

and the third

$$\dot{\boldsymbol{q}}_a^b = \boldsymbol{q}_a^b \otimes \bar{\boldsymbol{\omega}}_{ba}^a, \tag{B.11}$$

resembling the second, where $\bar{\boldsymbol{\omega}}_{ba}^a = (0; \boldsymbol{\omega}_{ba}^a)$. In addition, by defining

$$\boldsymbol{\Xi}_q(\boldsymbol{q}) := \begin{pmatrix} -\boldsymbol{r}^\top \\ s\boldsymbol{I}_3 - \boldsymbol{S}(\boldsymbol{r}) \end{pmatrix}, \tag{B.12}$$

the quaternion differential equation for $\boldsymbol{q}_a^b$, based on the angular velocities $\boldsymbol{\omega}_{ca}^a$ and $\boldsymbol{\omega}_{cb}^b$ may be given as

$$\dot{\boldsymbol{q}}_a^b = \frac{1}{2}\boldsymbol{T}_q(\boldsymbol{q}_a^b)\boldsymbol{\omega}_{ca}^a - \frac{1}{2}\boldsymbol{\Xi}_q(\boldsymbol{q}_a^b)\boldsymbol{\omega}_{cb}^b, \tag{B.13}$$

$$= \frac{1}{2}\boldsymbol{q}_a^b \otimes \begin{pmatrix} 0 \\ \boldsymbol{\omega}_{ca}^a \end{pmatrix} - \frac{1}{2}\begin{pmatrix} 0 \\ \boldsymbol{\omega}_{cb}^b \end{pmatrix} \otimes \boldsymbol{q}_a^b. \tag{B.14}$$

B.3 Navigation Related Notations

In this dissertation coordinate frames are denoted with $\{\cdot\}$. All vectors representing some part of the navigating vehicle's motion is generally presented using the notation

$$\boldsymbol{z}_{bc}^a \in \mathbb{R}^3, \tag{B.15}$$

where $\boldsymbol{z}$ represents either position, velocity or specific force of frame $\{c\}$, relative $\{b\}$, decomposed in $\{a\}$. An overview of variables used to describe PVA and their evolution over time is found in Table B.1 in compliance with the nomenclature.

Table B.1: Navigation related notations.

Type	**Notation**
Position vector	$\boldsymbol{p}^{\star}_{\star\star} \in \mathbb{R}^3$
Linear velocity vector	$\boldsymbol{v}^{\star}_{\star\star} \in \mathbb{R}^3$
Specific force vector	$\boldsymbol{f}^{\star}_{\star\star} \in \mathbb{R}^3$
Angular velocity vector	$\boldsymbol{\omega}^{\star}_{\star\star} \in \mathbb{R}^3$
Gravity vector	$\boldsymbol{g}^{\star}_{b} \in \mathbb{R}^3$
Rotation matrix	$\boldsymbol{R}^{\star}_{\star} \in SO(3)$
Unit quaternion	$\boldsymbol{q}^{\star}_{\star} \in \boldsymbol{Q}$
Latitude	$\mu \in [-\pi/2, \pi/2]$
Longitude	$\lambda \in (-\pi, \pi]$
Height	$h \in \mathbb{R}^1$

C Modeling, Simulations and Discretization

C.1 Modeling of GNSS Colored Noise

The modeling of colored, or transient, GNSS noise or errors, decomposed in the NED frame, $\boldsymbol{z} = (z_n; z_e; z_d)$, can for simulation purposes be modeled as a three-dimensional, first-order, discrete-time Gauss-Markov process

$$\boldsymbol{z}[k+1] = \boldsymbol{\Phi}_{\text{GNSS}}\, \boldsymbol{z}[k] + \boldsymbol{G}\boldsymbol{w}[k], \tag{C.1}$$

where $\boldsymbol{\Phi}_{\text{GNSS}} = \boldsymbol{I}_3 \cdot \exp\left(-\frac{1}{T} \cdot T_s\right)$, while $\boldsymbol{w}[k]$ being the driving unity white noise of the Gauss Markov process, and where $\boldsymbol{G} = \text{blockdiag}(\sigma_n, \sigma_e, \sigma_d)$ contains the respective standard deviations, $\sigma_\star$, of the driving noise, obtained from Rankin (1994), where k denotes the time index. Furthermore, T is the correlation time constant and T_s is the sampling time of the modeled GNSS receiver. The resulting position measurements provided by the receiver in $\{n\}$ can then be given as:

$$\boldsymbol{p}^n_{\text{GNSS}}[k] = \boldsymbol{p}^n_{nb}[k] + \boldsymbol{z}[k] + \boldsymbol{\epsilon}[k]. \tag{C.2}$$

where $\boldsymbol{\epsilon}[k]$ is residual Gaussian white noise.

C.2 Simulation Case Study: Time-invariant versus Time-varying Gains

To study the effects of the gain synthesis suggested for the feedback-interconnected observer above, inertial sensors and position measurements with white Gaussian noise are simulated, and both fixed and time-varying gain schemes are applied to the observers. This is a simplification, made for illustrative purposes, since in general both position and inertial sensors provide measurements containing noise with colored spectral content. The results are transformed to NED coordinates. Conversion from ECEF to NED coordinates is performed by first acquiring the estimated latitude $\hat{\mu}$ and longitude $\hat{\lambda}$ from the position estimate $\hat{\boldsymbol{p}}^e_{eb}$ for instance in closed form with Vermeille (2004). This information is then used to rotate the ECEF estimates to NED with the quaternion $\hat{\boldsymbol{q}}^e_n = \hat{\boldsymbol{q}}_\mu \otimes \hat{\boldsymbol{q}}_\lambda$, where

$$\hat{\boldsymbol{q}}_\mu = \begin{pmatrix} \cos((\hat{\mu} + \pi/2)/2) & 0 & \sin((\hat{\mu} + \pi/2)/2) & 0 \end{pmatrix}^\mathsf{T} \tag{C.3}$$

and

$$\hat{\boldsymbol{q}}_\lambda = \begin{pmatrix} \cos(\hat{\lambda}/2) & 0 & 0 & -\sin(\hat{\lambda}/2) \end{pmatrix}^\mathsf{T}. \tag{C.4}$$

The respective transient performance is shown in Figures C.1–C.3 implemented with IMU noise characteristics $\boldsymbol{\varepsilon}_\omega \sim (0, 0.0025^2)$ and $\boldsymbol{\varepsilon}_f \sim (0, 0.05^2)$ using position as the only aiding TMO measurement. The GNSS noise characteristics where

realized using $\boldsymbol{\varepsilon}_p = (\varepsilon_{p_n}; \varepsilon_{p_e}; \varepsilon_{p_d})$ with $\varepsilon_{p_n} \sim (0, 1.1^2)$, $\varepsilon_{p_e} \sim (0, 1.1^2)$, and $\varepsilon_{p_d} \sim (0, (1.5 \cdot 1.1)^2)$, where n, e and d denotes north, east and down, respectively, such that the GNSS is less accurate in the vertical component after converting to NED.

The fixed-gain synthesis is done with $\theta = 1$ and the algebraic Riccati equation,

$$\boldsymbol{A}^*\boldsymbol{P}^* + \boldsymbol{P}^*(\boldsymbol{A}^*)^\intercal + \boldsymbol{B}^*\boldsymbol{Q}^*(\boldsymbol{B}^*)^\intercal - \boldsymbol{P}^*(\boldsymbol{C}^*)^\intercal\boldsymbol{R}^{-1}\boldsymbol{C}^*\boldsymbol{P}^* = \boldsymbol{0}. \tag{C.5}$$

For both observers, the TMOs were synthesized using $\boldsymbol{S}_f = 0.05^2 \cdot \boldsymbol{I}_3$, $\boldsymbol{S}_{\hat{o}f} = 0.5 \cdot 0.05^2 \cdot \boldsymbol{I}_3$ and $\boldsymbol{S}_p = \text{blockdiag}(1.1 \cdot I_2, 1.65^2)$, after converting from ECEF to NED coordinates, with initial NED position and attitude error of $\tilde{\boldsymbol{p}}^n_{nb}(0) = (10, -7, 4)^\intercal$ m and $\tilde{\phi}(0) = 10$, $\tilde{\theta}(0) = 7$, $\tilde{\psi}(0) = -10$ degrees, respectively. The attitude gains where chosen as $k_1 = k_2 = 0.5$, $k_I = 0.01$. In the time-varying filter implementation the initial covariance $\boldsymbol{P}^*(0)$, of (3.23), was chosen as $\boldsymbol{P}^*(0) = \text{blockdiag}(10^2 \cdot \boldsymbol{I}_3, \boldsymbol{I}_3, \boldsymbol{I}_3)$. A third case was also run with higher attitude gains $k_1 = k_2 = 20$ during the first 100 seconds, together with the time-varying TMO solution. The transient performance obtained is based on simulated sensors at rest.

The transient performance of the position, velocity and attitude errors is improved using the time-varying Kalman filter to synthesize the TMO as seen in Figures C.1–C.3. As indicated, in Figure C.3 by improving the TMO's estimates, improvements in the attitude convergence properties are also obtained. The fastest attitude covariance properties are witnessed with both a time-varying TMO and higher prescribed initial attitude gains as seen in Figure C.3. What also can be seen from Figures C.1–C.2, is that the convergence properties of the position and velocity estimates are not improved by time-varying attitude gains with the TMO tuning chosen here. It can also been seen in Figures C.1–C.3 that the estimates have not fully converged at 100 seconds. This is due to the gyro bias estimates have not yet fully converged to the true gyro biases.

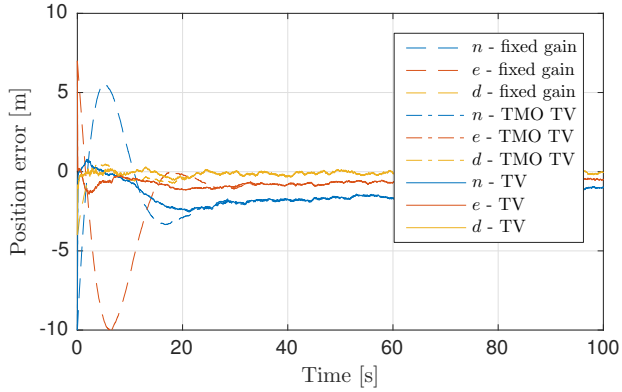

Figure C.1: Position estimation error. North, east and down axes are denoted n, e and d, respectively. The position errors obtained with the steady-state Kalman gain are presented with dash lines. The position errors obtained with the translational motion observer (TMO) applying a time-varying Kalman gain are shown using dash-dot lines. The error in position obtained when both the TMO and the attitude observer applied time-varying gains is shown using solid lines. The results indicate that using a TMO with time-varying gains, with or without an attitude observer prescribed with high initial gains, accelerates the convergence of the position estimates to the true position.

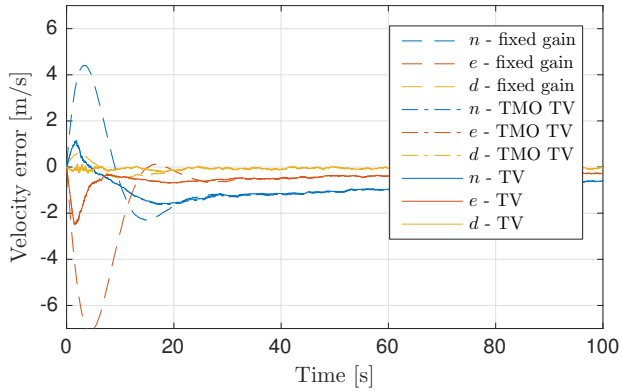

Figure C.2: Velocity estimation error. North, east and down axes are denoted n, e and d, respectively. The velocity errors obtained with the steady-state Kalman gain are presented with dash lines. The velocity errors obtained with the translational motion observer (TMO) applying a time-varying Kalman gain are shown using dash-dot lines. The error in velocity obtained when both the TMO and the attitude observer applied time-varying gains is shown using solid lines. The results indicate that using a TMO with time-varying gains, with or without an attitude observer prescribed with high initial gains, accelerates the convergence of the velocity estimates to the true velocity compared to the fixed-gain solution.

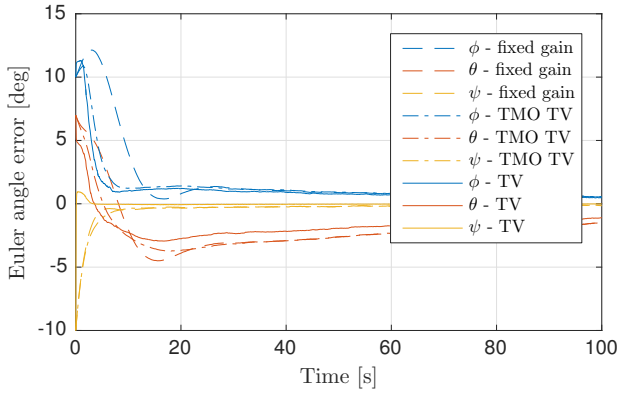

Figure C.3: Attitude estimation error. The attitude error is presented applying Euler angles as attitude representation. The attitude errors obtained in feedback interconnection with the translational motion observer (TMO) using a steady-state Kalman gain are presented with dash lines. The attitude errors obtained in connection with the TMO applying a time-varying Kalman gain are shown using dash-dot lines. The attitude error obtained when both the TMO and the attitude observer applied time-varying gains is shown using solid lines. The results indicate that using a TMO with time-varying gains in feedback interconnection with an attitude observer prescribed with high initial gains accelerates the convergence of the attitude estimates to the true attitude.

C.3 Vessel Simulations

All the simulated sensor measurements, related to marine vessels, in the thesis were generated using the Marine Systems Simulator's (Fossen and Perez, 2010) *DP_ForceRAO.mdl*. All vessel wave-induced motions were generated by exposing the vessel to wave forces and moments generated, due to first-order wave loads, with the JONSWAP wave spectra. In addition, irrotational currents (Fossen, 2011, Ch. 8.3) with fixed speed were also introduced.

C.3.1 Simulations of Section 4.3.6

The significant wave height and peak frequency were chosen as, H_s = 7 m and ω_0 = 0.8 rad/s, respectively. The IMU and the respective observers where simulated at 100 Hz. Gaussian white noise was added to IMU measurements. The chosen heading and position measurements were simulated at 10 Hz and 1 Hz, respectively. Hence, the GNSS correction of the TMOs was carried out at 1 Hz using the corrector-predictor implementation of Fossen (2011, Ch. 11.3.4.). The compass error was simulated as a Gauss-Markov process. The same model was chosen to generate the GNSS errors. See Appendix C.1 for details.

Table C.1: Parameters of dGNSS and gyrocompass error model.

Parameter	dGNSS (hor. comp.)	Compass
Time Constant	$T = 240$ [s]	$T = 60$ [s]
Std. $e(k)$	1.10 [m]	0.14 [°]
Std $w(k)$	0.1 [m]	0.025 [°]
Covariance $w(k), e(k)$	0.01 [m]	-
Std. $e(k)$ (low precision)	2.17 [m]	-
Std $w(k)$ (low precision)	0.2 [m]	-
Covariance $w(k), e(k)$ (low precision)	0.04 [m]	-

C.3.2 Simulations of Section 5.2.4 and Section 6.2.5

The significant wave height and peak frequency were chosen to $H_s = 7$ m and $\omega_0 = 0.8$ rad/s, respectively. In *DP_ForceRAO.mdl* $\omega_e \equiv \omega_0$ since the simulator is based on zero vessel speed. The IMU and the respective observers where simulated at 100 Hz. The chosen heading and position reference were three gyrocompasses and three dGNSS, simulated at 10 Hz and 1 Hz, respectively.

All the sensors were simulated with noise. The dGNSS and gyrocompass noise were simulated with the first-order Gauss-Markov process of (6.1), where Table C.1 present the parameters related to the transient noise for the respective sensor packages. When the compasses were not sampled, the injection term of Σ_1 was implemented as

$$\hat{\boldsymbol{\sigma}}^b_{ib} = k_2(t)\boldsymbol{f}^b_{\text{IMU}} \times \boldsymbol{R}^\intercal(\hat{\boldsymbol{q}}^n_b)\hat{\boldsymbol{f}}^n_{ib}. \tag{C.6}$$

Because of the slow dynamics of DP vessels, this will not affect the performance of Σ_1 even though the stability analysis of Section 4.3.5 and Section 4.4.5, (Bryne et al. (2014) and Bryne et al. (n.d.)) and the reference therein requires two vector measurements. The quaternion unity constraint was enforced with $\hat{\boldsymbol{q}}^n_b = \hat{\boldsymbol{q}}^n_b / \|\hat{\boldsymbol{q}}^n_b\|$ after every quaternion update. Σ_2 was implemented with the discrete-time corrector-predictor scheme presented in Fossen (2011, Ch. 11.3.4) such that the dGNSS measurement update of Σ_2 was carried out every 100th IMU sample. The gyro biases were chosen as $\boldsymbol{b}^b_{\text{gyro}} = (0.17; -0.18; 0.14)$ deg/s.

Tuning and gain structure

The gains of Σ_1 was tuned with $g_a = (k_1(t),\, k_2(t),\, k_I(t))^\intercal$, and

$$\dot{g}_a = -\frac{1}{T}g_a + \frac{1}{T}k_a, \begin{cases} k_a = (20,\, 20,\, 1)^\intercal & \text{if } t \leq 100 \\ k_a = (0.55,\, 0.55,\, 0.01)^\intercal & \text{else.} \end{cases}$$

with $T = 25$ s to speed up the initial convergence of the $\hat{\boldsymbol{q}}^n_b$ and $\hat{\boldsymbol{b}}^b_{\text{gyro}}$. This is similar to Bryne et al. (2014) such that unnecessary amplification of sensor noise

Table C.2: PosRef and gyro compass validity thresholds

Thresholds	PosRef (north and east comp.)	Compass
Outlier	8 [m]	4 [°]
Bias/drift	2 [m]	1.2 [°]

is avoided when the attitude estimates have converged. The fixed gains of Σ_2, on compact form,

$$\boldsymbol{K}^0 = \begin{pmatrix} K^0_{p_I p_I} & \mathbf{0}_{1\times 2} & K^0_{p_z p_I} & \mathbf{0}_{1\times 2} & K^0_{v_z p_I} & \mathbf{0}_{1\times 2} & K^0_{\xi_z p_I} \\ \mathbf{0}_{2\times 1} & \boldsymbol{K}^{0\intercal}_{pp} & \mathbf{0}_{2\times 1} & \boldsymbol{K}^{0\intercal}_{vp} & \mathbf{0}_{2\times 1} & \boldsymbol{K}^{0\intercal}_{\xi p} & \mathbf{0}_{2\times 1} \end{pmatrix}^\intercal,$$

were calculated as $\boldsymbol{K}^0 = \boldsymbol{P}\boldsymbol{C}^{*\intercal}$ where $\boldsymbol{P}$ is the solution of (4.39), where $\boldsymbol{A}^*$ and $\boldsymbol{C}^*$ is found in (4.20), Section 4.3.4 . The numerical values of $\boldsymbol{Q}$ and τ were chosen as:

$$\boldsymbol{Q} = 1 \cdot 10^{-3} \cdot \text{blockdiag}\{2.5 \cdot 10^{-3}, \boldsymbol{I}_2, 2.5 \cdot 10^{-3}, \boldsymbol{I}_2, 2.5 \cdot 10^{-3}, \boldsymbol{I}_2, 2.5 \cdot 10^{-3}\}$$

and $\tau = 1/2$ which resulted in $K^0_{p_I p_I} = 0.5222$, $K^0_{pp_I} = 0.1363$, $K^0_{vp_I} = 0.0208$, $K_{\xi p_I} = 0.0016$, $\boldsymbol{K}^0_{pp} = 0.6387 \cdot \boldsymbol{I}_2$, $\boldsymbol{K}^0_{vp} = 0.2035 \cdot \boldsymbol{I}_2$ and $\boldsymbol{K}^0_{\xi p} = 0.0316 \cdot \boldsymbol{I}_2$. Furthermore, the time-varying gain component, $\varphi(t)$, of Σ_2 was implemented as

$$\begin{aligned} \dot{\varphi} &= -\frac{1}{T}\varphi + \frac{1}{T}k_{tv}, \\ k_{tv} &= \begin{cases} 0.5 & \text{(low)} \quad \text{if } \text{GNSS}_{\text{rms}} > l_{\text{high}} \\ 0.75 & \text{(med)} \quad \text{if } \text{GNSS}_{\text{rms}} > l_{\text{low}} \text{ and } \text{GNSS}_{\text{rms}} < l_{\text{high}} \\ 1 & \text{(high)} \quad \text{if } \text{GNSS}_{\text{rms}} < l_{\text{low}} \text{ or time} < 100 \end{cases} \end{aligned} \tag{C.7}$$

where $\text{GNSS}_{\text{rms}} = (R_{w,\text{xx}}(k) + R_{w,\text{yy}}(k))^{0.5}$ is obtained from the weighting algorithm of (6.19), such that $\varphi(t)$ remains smooth even though the gain is modified over time. Furthermore, $l_{\text{low}} = 0.9$ and $l_{\text{high}} = 1.7$ where chosen as the gain thresholds, together with $T = 5$, such that $\varphi(t)$ will be adaptive with respect to PosRef quality. Moreover, $\vartheta = 1$ was chosen.

For the triple redundant PosRef fault detection, the different $\bar{\boldsymbol{Q}}_j(k)$, for PosRef j, were pre-calculated for each axis of the dGNSS and the compass measurements. These were based on the parameters of Table C.1 including different $\bar{\boldsymbol{Q}}_j(k)$ for low and high dGNSS variance. Regarding the gyrocompass, $\bar{\boldsymbol{Q}}(k) = \boldsymbol{Q}(k)$ was chosen since the cross correlation between the process noise and the measurement noise was deemed negligible based on the parameters of Table C.1. The fault-detection thresholds were chosen as presented in Table C.2.

Time-varying multiplicative gain $\varphi(t)$

Here, some illustrations of the results obtained related to the time-varying gains with the chosen tuning, sensor noise, and simulated dGNSS and heading sensor faults above, are presented.

The time evolution of the time-varying attitude gains, introduced to reduce the convergence time, can be seen in Figure C.4. In Figure C.5 one can observe the

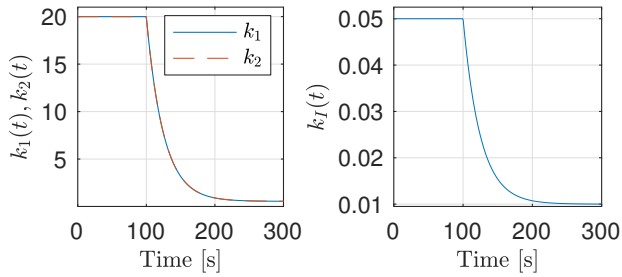

Figure C.4: Time-varying attitude gains.

effect of choosing $\varphi(t)$ according to (C.7) w.r.t. to the chosen tuning, noise levels and the simulated faults presented in Section 6.2.5.

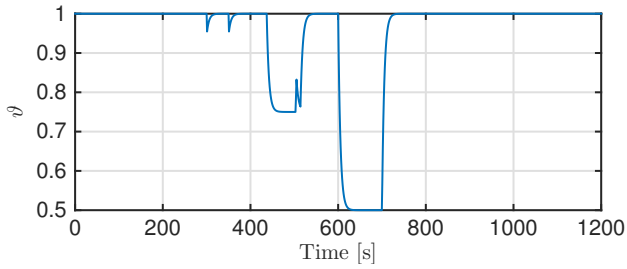

Figure C.5: The time-varying gain component, $\varphi(t)$, in Σ_2.

INS-based wave filtering: Loss of GNSS

Figure C.6 show results related to GNSS loss. Figure C.6a displays the drift of the LF position estimates relative the ship's actual position. In Figure C.6b one can see that the heading estimate is unaffected by the loss of position. This is due to three factors. First, the heading estimate is mainly based on the compass measurements, secondly, the $\boldsymbol{\xi}_{ib}^n$ term in $\hat{\boldsymbol{f}}_{ib}^n$, from Σ_2, will in general be small after $\Sigma_1 - \Sigma_2$ have converged. This makes the attitude observer robust to loss of position references for shorter time periods. This statement is supported by Figure C.6c. The third factor is that the gyro bias is still estimated with high accuracy, as seen in Figure C.6d. Compared to a vessel-model-based strategy, INS-based wave filters have the advantage that the kinetic sway-yaw coupling in the vessel model is avoided altogether such that faulty position estimates not necessarily will induce an error in the heading estimates.

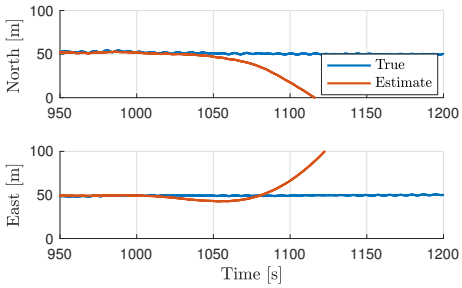

(a) Drifting LF position estimates (red). Vessel position (blue).

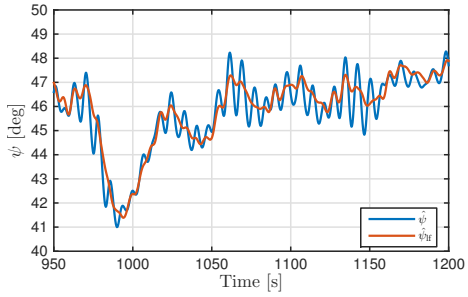

(b) Heading estimates (blue) and LF heading estimates (red).

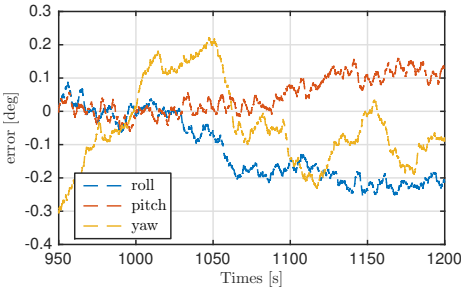

(c) Attitude estimation error.

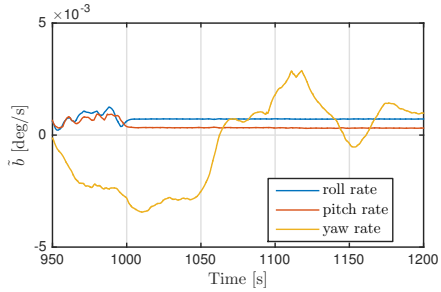

(d) Gyro bias estimation error.

Figure C.6: Effects of loss of position reference at 1000 seconds. Figure C.6a shows the drifting LF position estimates, while Figure C.6c show the attitude estimation performance, in large extent, is still maintained. Figure C.6d shows the gyro bias estimation error remains small. The LF heading estimates are seen in Figure C.6b relative the estimated heading from Σ_1.

An alternative to continue to utilize $\hat{f}_{ib}^n$ when the given source of position reference information is lost would be to switch to an attitude observer based on g_b^n instead cf. Section 5.1.

C.4 Discretization and Measurements Samples

For the discrete-time implementation, the discretization interval T_s and a discrete time index k are utilized such that the continuous time variable t is related to T_s and k with $t = kT_s$ (for a constant T_s).

At a given index k all valid measurements at time $t = kT_s$ are contained in the measurements set $\mathcal{I}_k$ of measurements. If the i^{th} measurement is available and valid, this is indicated by $i \in \mathcal{I}_k$. The opposite case is denoted as $i \notin \mathcal{I}_k$.

Complementary Filtering

D

This appendix is mainly based upon Bryne et al. (2017a).

Complementary filtering is a filtering approach used to estimate unknowns based on measurements corrupted with noise and/or disturbances with known spectral content/characteristics. Typically a reformulation of the original problem is necessary such that filtering techniques (not necessarily an estimator/observer) like the Wiener filter (optimal w.r.t. mean-square error) can be applied without distorting the desired output of the filter.

D.1 Main Concept – Outline

Say one has two measurements of the signal $s(t)$

$$y_1 = s(t) + n_1, \tag{D.1}$$

$$y_2 = s(t) + n_2, \tag{D.2}$$

where both measurements are corrupted with noise/errors n_1 and n_2, respectively, with known spectral densities. With some abuse of notation an estimate of $s(t)$ can be written

$$\hat{s} = G_1(s)y_1 + G_2(s)y_2 \tag{D.3}$$

for two filters represented by $G_1(s)$ ans $G_2(s)$ corresponding to the setup of Figure D.1. So how to design the filters to optimally reconstruct the signal $s(t)$? In

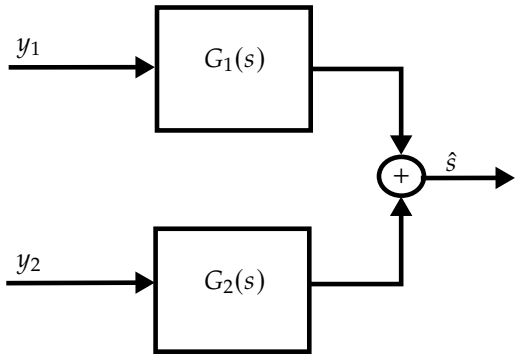

Figure D.1: Original filter problem.

the frequency domain we get

$$\hat{S}(s) = (G_1(s) + G_2(s))\, S(s) + G_1(s)N_1(s) + G_2(s)N_2(s). \tag{D.4}$$

Then to avoid altering $s(t)$, $G_1(s) + G_2(s) = 1$ is a natural choice in the frequency domain. A possible solution is then to choose $G_2(s) = 1 - G_1(s)$, resulting in

$$G_1(s) + G_2(s) = G_1(s) + 1 - G_1(s) = 1.$$

Furthermore, now (D.4) can be modified

$$\begin{aligned}\hat{S}(s) &= (G_1(s) + (1 - G_1(s)))\, S(s) + G_1(s)N_1(s) + (1 - G_1(s))N_2(s) \\ &= S(s) + G_1(s)N_1(s) + (1 - G_1(s))N_2(s) \\ &= S(s) + G_1(s)\left(N_1(s) - N_2(s)\right) + N_2(s)\end{aligned} \tag{D.5}$$

Conceptually this problem is solved according to Brown and Hwang (2012):

1. Choose a filter form that corresponds to the known spectral characteristics of the sensor noise in question.
2. Tune the filter to minimize the mean-squared error as determined from (D.5).

From (D.5) one can draw the block diagram of Figure D.2, obtaining the possibility

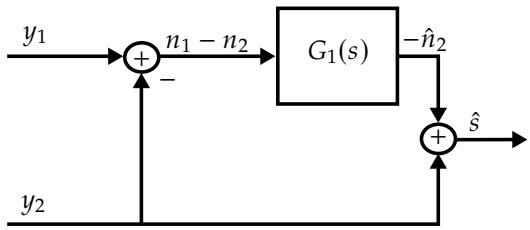

Figure D.2: Modified filter problem: The complementary filter.

to design a filter, used to estimate n_2. The estimate $\hat{s}$ is then obtained by subtracting $\hat{n}_2$ from y_2 such that

$$\hat{s}(t) = y_2 - \hat{n}_2 = s(t) + n_2 - \hat{n}_2 \tag{D.6}$$

based on the known spectral content of $n_1 - n_2$. This can e.g. be done using a Wiener filter (Farrell, 2008, Ch. 7.3.1). We did not know the spectral content of $s(t)$ (obviously since we wanted to estimate it), therefore the Wiener filter could not be applied to the original problem of (D.3) shown in Figure D.1.

The complementary filter is especially useful if the two measurements have complementary spectral characteristic. An obvious example when n_2 primarily have spectral content within the low-frequency range and n_1 primarily has spectral content within the high-frequency range, then G_1 would be chosen as a lowpass filter in some form.

D.2 Complementary Filter for Aided INS based on the Kalman Filter and Filtering on SO(3)

Inertial sensors and aiding sensors, such as GNSS, have these complementary properties (c.f. Table 1.1) and therefore well suited for commentary filtering. In

this context GNSS is used to capture the low frequency vehicle motion, while the inertial sensors are used to capture any high frequency vehicle dynamics. For both attitude and heading reference systems (AHRSs) and complete INSs, complementary filtering is commonly utilized (Farrell, 2008, Ch. 4.10), Mahony et al. (2008); Grip et al. (2015). The general structure of complementary filtering for INSs is illustrated in Figure D.3, while the simplified structure for attitude

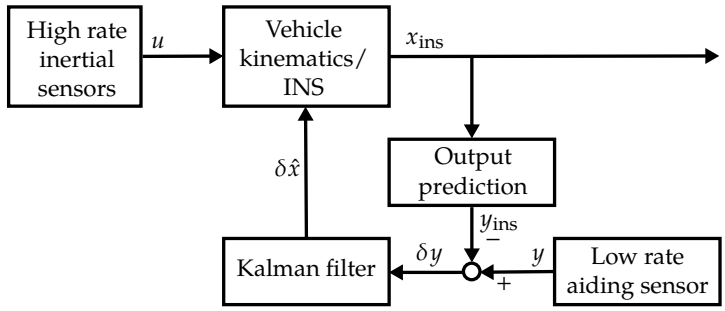

Figure D.3: General complementary filtering for aided INSs using the Kalman filter. The structure is also known as error-state or indirect Kalman filtering. The Kalman filter estimates the error between the INS and low rate aiding sensor. For low frequencies, the aiding sensor is the dominating information sensor in generating the INS output. For high frequencies the high-frequency input from the inertial sensor is the dominating information source in producing the INS output.

estimation, also known as filtering on $SO(3)$, is presented in Figure D.4.

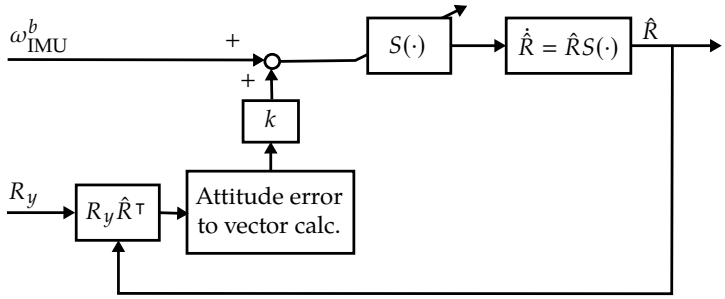

Figure D.4: Complementary filtering on $SO(3)$: Simplified concept. Some reconstructed attitude measurement $\boldsymbol{R}_y \approx \boldsymbol{R}$ is valid for low frequencies. For frequencies lower than the cutoff frequency k, $\boldsymbol{R}_y$ is the dominating information used to calculate $\hat{\boldsymbol{R}}$. For high-frequencies, $\boldsymbol{\omega}^b_{\text{IMU}}$ is the primary sensor used to estimate $\boldsymbol{R}$. By using complementary filtering on $SO(3)$, the effect of the low-frequency gyro bias on the attitude estimate is attenuated.

Inertial Sensors and Sensor Data

E

E.1 Deployment of Inertial Sensors and Collection of Sensor Data

The NLO-based sensor fusion algorithms developed throughout the course of this work were evaluated using data obtained by installing

- 4x ADIS16485 IMUs from Analog Devices, and
- STIM300 IMU from Sensonor

on a ship operating in the Norwegian Sea. The IMUs' specifications are presented in Table E.1. Data from the inertial sensors was collected in the Fall of 2015 using a data acquisition system in parallel with collecting the measurements from onboard sensors such a dGNSSs, gyrocompasses, and VRUs. The ship in question is an offshore vessel with a Rolls–Royce Marine Icon DP system. The vessel type is illustrated in Figure E.1.

The STIM300 and the three of the ADIS16485 IMUs were mounted on a vibration-damped plate, inside a cabinet, while the last ADIS IMU was mounted directly in the cabinet as seen in Figure E.2a. All the sensor data were stored on a server, shown in Figure E.2b, onboard the ship. The cabinet with the IMUs and the data acquisition system was mounted close to the ship's VRUs as seen in Figure E.2c Furthermore, the attitude and heave estimates obtained with the installed MEMS IMUs were compared to output of the onboard industry standard VRUs, with the manufacturer's specifications presented in Table E.2.

Table E.1: IMU specifications from the manufacturer.

	ADIS16485	**STIM300**
In-run Gyro Rate Bias Stability	6.25 $\frac{\text{deg}}{\text{h}}$	0.5 $\frac{\text{deg}}{\text{h}}$
Angular Random Walk	0.3 $\frac{\text{deg}}{\sqrt{\text{h}}}$	0.15 $\frac{\text{deg}}{\sqrt{\text{h}}}$
In-run Accelerometer Bias Stability	0.032 mg	0.05 mg
Velocity Random Walk	0.023 $\frac{\text{m/s}}{\text{h}}$	0.06 $\frac{\text{m/s}}{\text{h}}$

Table E.2: VRU Specifications from the manufacturer.

	Static Roll & Pitch	**Dynamic**[a] **Roll & Pitch**	**Heave**[b]
RMS error	0.02°	0.02°	5 cm or 5 %

[a] For a sinusoidal amplitude of ±5°.
[b] Whichever is higher.

Figure E.1: Illustrations of the offshore vessel. Courtesy Rolls–Royce Marine.

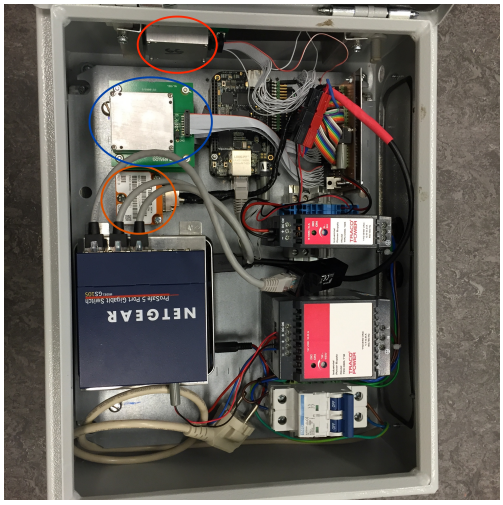

(a) Sensor cabinet with five IMUs. The location of the cabinet-mounted ADIS16485 is indicated with red. The vibration-damped ADIS16485s and STIM300 IMUs are indicated with blue and orange, respectively.

(b) Server installed on board the vessel.

(c) Locations of sensors. Sensor cabinet (bottom right) located close to the onboard VRUs (top left).

Figure E.2: Sensor deployment on board the offshore vessel.

E.2 Additional Results on Full-scale Testing and Validation using Nonlinear Observers

This section contains additional results on full-scale validation of NLOs based on the MEMS IMUs of Appendix E.1, and presents additional material to that provided in Section 5.1.

E.2.1 Full-scale testing: DR capabilities in DP applying MEMS IMUs

Testing the potential of the underlying fault-tolerance properties of integrated INS solutions can be done by evaluating the dead reckoning (DR) capabilities of the IMU-and-estimator combinations. In particular, the DR capabilities are closely linked to the possibility to detect certain PosRef faults such as slow drift. In this section, the evaluation of the DR properties in light of fault detection using the one of the vibration-damped ADIS16485s and the STIM300 is presented. The DR performance evaluation is carried out with data collected in a DP operation whose GNSS track is shown in Figure 4.20a of Section 4.4.8.

First, the heading DR performance obtained when using the available IMUs is discussed, and illustrated with an example. Then, the position DR performance during the particular DP operation is evaluated, applying both IMUs and NLO A, of Section 5.1.2, with Σ_3. The resulting DR related statistics are based on a collection of estimation runs where PosRef corrections were disabled.

DR capabilities: Heading

The heading angle DR capabilities using the IMUs available were found to be in compliance with the IMUs' angular rate specifications, presented in Table E.1. A total of 60 one-hour-long heading DR evolutions of the absolute yaw angle error

$$|\tilde{\psi}| = |\psi_c - \hat{\psi}|, \tag{E.1}$$

compared to the ship's gyrocompass measurements for both sensors, are shown in Figure E.3. The DR was carried out with NLO B, by disabling the observer injection from the gyrocompass by setting $k_2 = 0$, and the observer initialization time was 15 minutes. In addition, the average DR error, of the 60 runs, is highlighted in Figure E.3. Examples of typical angular rate bias estimates are shown in Figure 5.3 on page 115, exhibiting that the STIM300's biases are more in-run stable than those of the ADIS16485.

DR capabilities: Position

Evaluation of the DR capabilities in position is more elaborate than for heading since the theoretical growth of errors are a combination of higher order terms, (Groves, 2013, Ch. 5.7), as opposed to linear growth for heading. In order to

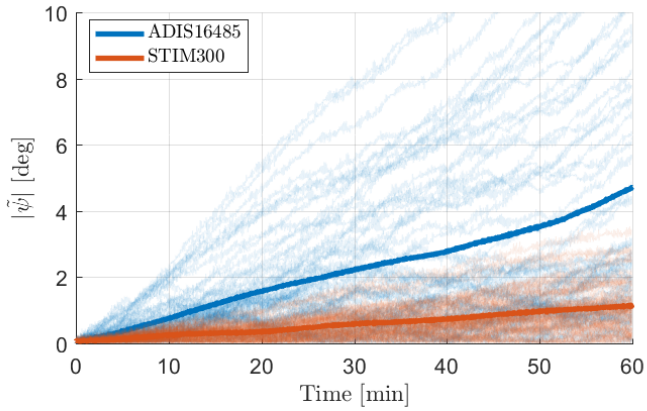

Figure E.3: DR performance in yaw obtained using the ADIS16485 and STIM300 IMUs. Highlighted evolution indicates the average DR error.

obtain statistically significant results related to the position drift while performing DR, each combination of the IMUs and the NLOs was evaluated 60 times (using different data sets) by comparing the DR errors accumulated when disabling GNSS feedback at selected intervals. The DR evaluation is done by taking the norm of the difference between the horizontal components of $\boldsymbol{p}^t_{\text{GNSS}}$ and $\hat{\boldsymbol{p}}^t_{\text{GNSS}}$, defined $\tilde{\boldsymbol{p}}^t_{\text{GNSS}} := \boldsymbol{p}^t_{\text{GNSS}} - \hat{\boldsymbol{p}}^t_{\text{GNSS}}$ where,

$$\hat{\boldsymbol{p}}^t_{\text{GNSS}} = \hat{\boldsymbol{p}}^t_{tb} + \boldsymbol{R}(\hat{\boldsymbol{q}}^t_b)\boldsymbol{r}^b_b, \tag{E.2}$$

and where $\boldsymbol{r}^b_b$ is the lever arm from the IMU to the GNSS antenna position such that

$$\begin{aligned} \|\tilde{\boldsymbol{p}}^t_{\text{GNSS}}\|_2 &= \|\boldsymbol{p}^t_{tb} + \boldsymbol{R}^t_b\boldsymbol{r}^b_b - \hat{\boldsymbol{p}}^t_{tb} - \boldsymbol{R}(\hat{\boldsymbol{q}}^t_b)\boldsymbol{r}^b_b\|_2, \\ &= \|\tilde{\boldsymbol{p}}_{tb} + \left(\boldsymbol{R}^t_b - \boldsymbol{R}(\hat{\boldsymbol{q}}^t_b)\right)\boldsymbol{r}^b_b\|_2. \end{aligned} \tag{E.3}$$

For position DR, only NLO A is to be considered. This is because of NLO B's dependency on PosRef injection in order to improve the attitude estimates. In a dead reckoning situation, one would have to cut the feedback interconnection and use the same reference vector $(-\boldsymbol{g}^t_b/\|\boldsymbol{g}^t_b\|_2)$ as for NLO A, effectively making the NLOs the same. Figure E.4 displays an example of a DR run with the ADIS16485 IMU. The position estimate starts drifting immediately after feedback is cut at $t = 15$ min. Figure E.5 shows the aggregated drift errors over 10 minutes, after PosRef injection is disabled, applying NLO A and Σ_3 for both the ADIS16485 and the STIM300 IMU. The statistical results based on the 60 DR runs are presented in Table E.3. Results related to the DR performance obtained without the residual bias estimation in Σ_3 are presented in Figure E.6 and Table E.4.

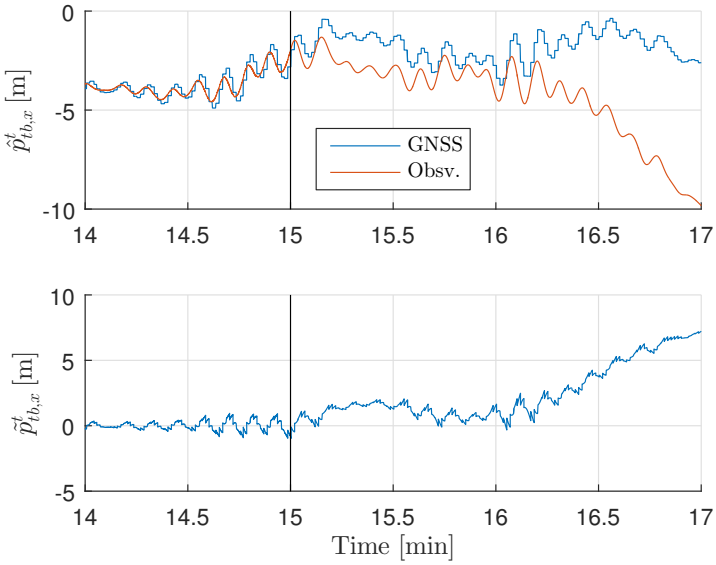

Figure E.4: Example of a DR run with prior bias compensation, where feedback from GNSS is cut after 15 minutes, indicated by vertical the line.

Table E.3: Position DR error statistics with accelerometer bias estimation.

	ADIS16485	**STIM300**
Mean error [m] 1 min	4.7580	4.3560
Mean error [m] 5 min	38.588	44.631
Mean error [m] 10 min	112.07	139.51
Min error [m] after 10 min	4.1972	26.919
Max error [m] after 10 min	244.97	350.30
RMS error [m] after 10 min	125.25	159.93

Discussions

Heading DR

It is evident, with regards to Figure 5.3, that the gyro bias estimates obtained using the STIM300 is smoother and more in-run stable than those found using the chosen ADIS16485 unit, resulting in the performance difference seen in Figure E.3. This is in compliance with the sensor specifications presented in Table E.1. The asymptotic angular rate bias estimation performances seen in Figure 5.3, is representative of what was obtained from run to run.

Position DR

As seen from Table E.3 and Figure E.5, one of the main conclusions from the four

Table E.4: Position DR error statistics without accelerometer bias estimation.

	ADIS16485	**STIM300**
Mean error [m] 1 min	5.1481	4.8861
Mean error [m] 5 min	58.514	64.187
Mean error [m] 10 min	226.00	241.73
Min error [m] after 10 min	73.421	141.35
Max error [m] after 10 min	389.95	422.03
RMS error [m] after 10 min	233.20	250.34

times 60 DR runs performed over the data collected during DP is that using the ADIS16485 results in better DR performance than using the STIM300. Interestingly enough, this is opposite of the conclusion from Rogne et al. (2016a)[1] where the authors used a fixed-gain Σ_3 with no heave estimation incorporated. However, from looking at the results one can see that estimating the accelerometer biases as in (5.12) clearly works. The difference between the IMUs could be explained by the accelerometer in-run bias stability presented in Table E.1 and the results from Section 5.1.5 where the ADIS16485 provides the best heave estimates, which is highly dependent on accelerometer quality. Also, the dead reckoning was done with aiding from the gyrocompass. Had the IMUs been left on their own completely, the STIM300 would have a major advantage because of the superior angular rate sensor and consequently better heading DR capabilities, as presented above.

The results indicate a large spread of DR errors over 10 minutes, and this might be due to noise, mechanical disturbance such as vibration, or insufficient tuning of the observers. Time synchronization of signals is also an issue, as the GNSS and gyrocompasse signals were acquired from a system separate from the IMUs' signal acquisition, with an unknown, albeit small, delay.

Considering the results obtained here, using either of the two MEMS-based IMUs available, gave worse results than those presented in Paturel (2004). In the latter works, an INS with a FOG gyro was applied. In the results presented in Paturel (2004), a position accuracy during GNSS outage stayed within GNSS accuracy for a period exceeding two and a half minutes. The mean position drift after 50 seconds of GNSS outage was less than half a meter. These results are considerably better than the approximately four to five meters error obtained after one minutes of DR for both MEMS IMUs. However, in Paturel (2004) only 10 runs are presented, making a definite statistical comparison difficult due to the few DR trajectories presented. The FOG-based INS product in question is currently advertised to have a 20 meter error with a 50 per cent circular error probability after five minutes of unaided navigation, whereas we obtain approximately 40

[1] Not included in the thesis.

meters averaged error in the same time frame.

As depicted in Figure E.5, a MEMS-based INS may provide relatively stable position estimates (around four meters error) for half a minute, without PosRef injection. From a fault-tolerance perspective, such as Rogne et al. (2016b)[2] the results obtained here indicate what kind of PosRef errors one might detect based on MEMS IMUs. For instance a PosRef drift of 10 centimeters per second results in a PosRef error of 3 meters after half a minute, which might be possible to detect with the results obtained, considering the average DR error is two meters with either of the two IMUs. Moreover, in the situation of PosRef failure during DP, if four meters is an acceptable error margin, 30 seconds is available to the DP operator to decide whether the operation should be aborted or not. This might be sufficient time for PosRef recovery e.g. if tracking is established with one more satellite, resulting in a complete GNSS solution.

The DR performance is not only dependent on the sensor biases, but also on the velocity-random walk and the sensed vibrations on the ship. Integrating these over time, results in a large error even when averaging them out using high-rate integration (1000 Hz). Regarding tuning, more focus towards increased DR performance should be considered such that better results possibility could be accomplished. Here, the tuning is geared towards attaining the smallest errors in attitude and heave, relative to the onboard VRU, as opposed to in Rogne et al. (2016a) were no such regard was given. Also, time-synchronization errors between our IMUs and the onboard GNSS system may result in small errors in velocity and specific force at the time of disabling GNSS injection, resulting in a steeper error slope than otherwise obtained if the position and inertial measurements were synchronized. As for the attitude and heave estimation, it is also difficult to conclude with certainty that the results found using the STIM300 are representative since we used an engineering sample. In, Rogne et al. (n.d.a), the DR results related to position, using the ADIS16485 unit, was improved some compared to the results presented here, by using a triple-redundant ADIS16485s.

E.2.2 Full-scale testing: Vibrations and high-rate MEMS-based INS

Vibrations

During the experiments, three ADIS16485 IMUs were situated on a vibration-isolated plate, supported by four Vibrachoc 7002 dampers, and one was mounted without vibration dampers directly in the cabinet, as shown in Figure E.2a. Below, one of the damped ADIS16485 will be referred to as the ADIS1, while the undamped IMU will be referred to as ADIS2. Figure E.7 shows the difference of the raw measurement in the time domain between these two IMUs, during operation. As one can see, a lot of external noise has been attenuated by the vibration

[2]Not included in the thesis.

Table E.5: Attitude error statistics for vibration isolation in DP.

	Isolated	**Non-Isolated**
Roll mean error [deg]	-0.0017	-0.0028
Pitch mean error [deg]	0.0040	-0.0076
Roll RMS error [deg]	0.0490	0.0685
Pitch RMS error [deg]	0.0968	0.1017
Roll CAEE [deg]	1002.3	1437.0
Pitch CAEE [deg]	1980.1	2071.8

isolation, especially for the accelerometers. For the gyro on the other hand, there is still a lot of noise present. This is reflected also by the frequency domain plot in Figure E.8, showing the estimated power spectral destiny (PSD), where one can see that there are a lot of unwanted frequencies for the ADIS1 in the range of 10-100 Hz. Figure E.8 presents the estimated PSD obtained from the DP operation, depicted in Figure 4.20a, of Section 4.4.8, and the results contained in Figure E.9 stem from steaming, conduced by the ship at ten knots. Whereas there is nothing much above 100 Hz for the ADIS1, there are many high frequency components on the ADIS2. Common for both IMUs, to the far left just above zero Hz one can find the ship motion, and the main engine rotations starts showing up at around 12 Hz, particularly evident for ADIS1. The increased response below 100 Hz for ADIS1 could stem from resonance motion induced by the vibration isolated plate. Regardless, looking at the attitude estimate statistics coming from using each of the IMUs in Table E.5, there is not that much of a difference, owing to the high integration rate of 1000 Hz, thus averaging out the noise components.

With regards to vibration damping, similar or perhaps even better noise reduction results might be obtained from applying for instance a Butterworth lowpass filter to the raw measurements, with a cutoff frequency that is easier to control than for mechanical damping. This would also insulate the sensors from the kind of resonance frequencies induced below 100 Hz. Of course, applying a lowpass filter to a signal is not without disadvantages, as phase delay is introduced.

A simple result that comes from observing Figures E.8–E.9, is that different modes of operation could, in theory, be identified on the basis of the frequency signatures. In addition, the higher frequency components might contain interesting information from a machinery diagnosis point of view. Whether one wants to keep all the frequency components depends consequently on one's application beyond traditional navigation use, but with filters implemented in software more flexibility is achieved in this regard.

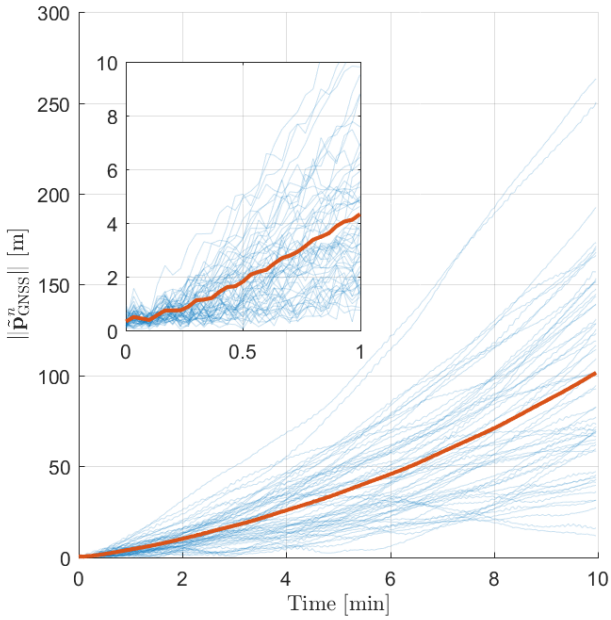

(a) DR errors obtained with ADIS16485

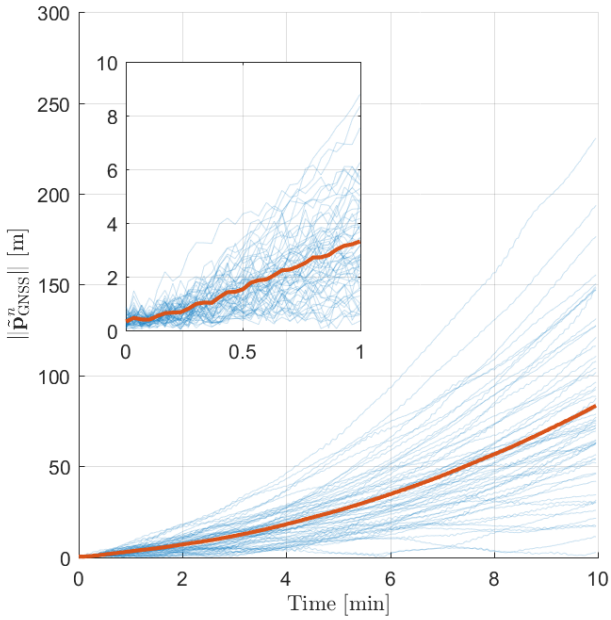

(b) DR errors obtained with STIM300

Figure E.5: Aggregated DR error over 60 runs using NLO A. Red indicates the mean DR error.

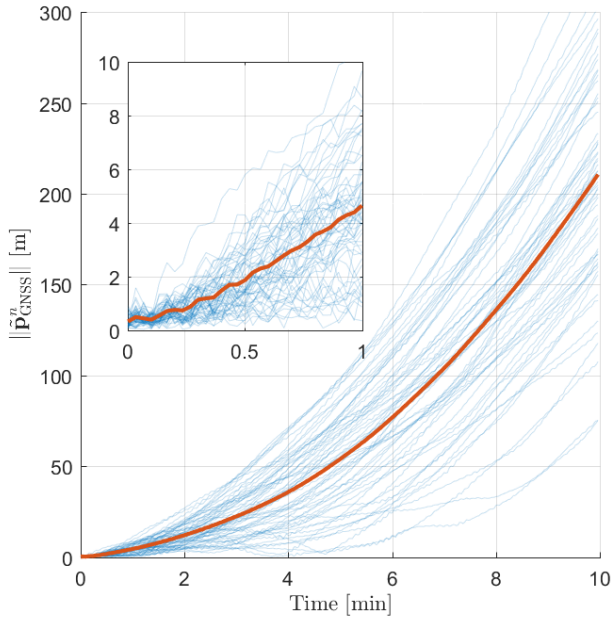

(a) DR errors obtained with ADIS16485

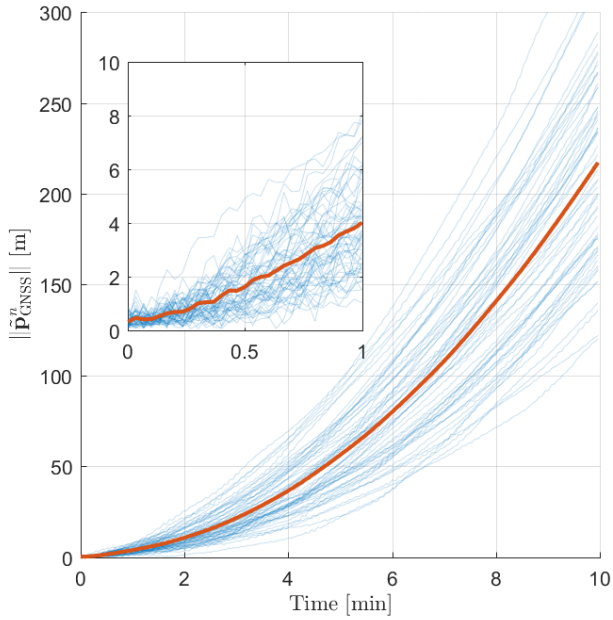

(b) DR errors obtained with STIM300

Figure E.6: Aggregated DR error over 60 runs using NLO A, and no bias estimation in Σ_3. Red indicates the mean DR error.

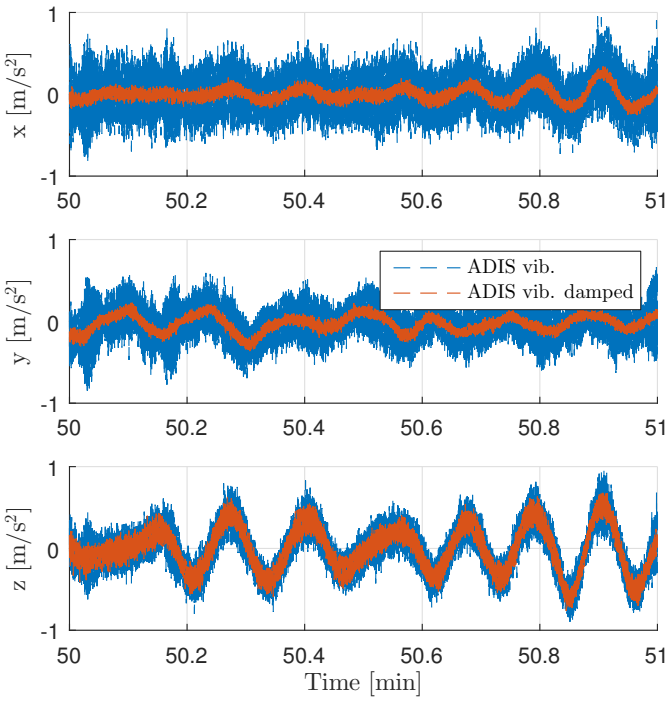

(a) Accelerometer raw measurements.

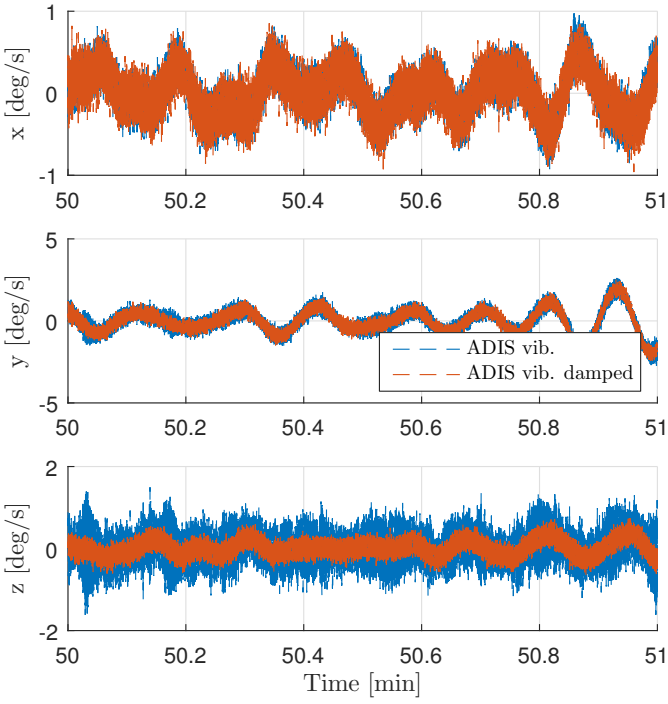

(b) Gyro raw measurements.

Figure E.7: ADIS IMU measurements, vibration isolated (red) and not (blue) in DP.

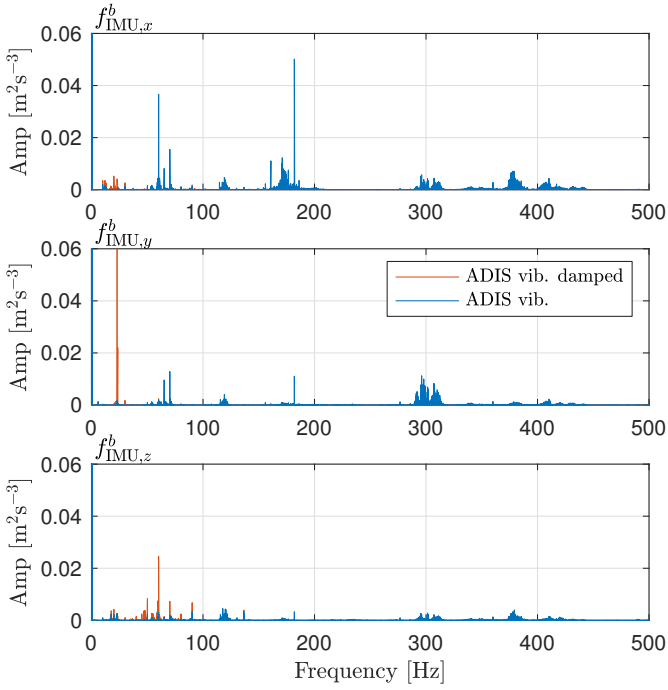

(a) Accelerometer.

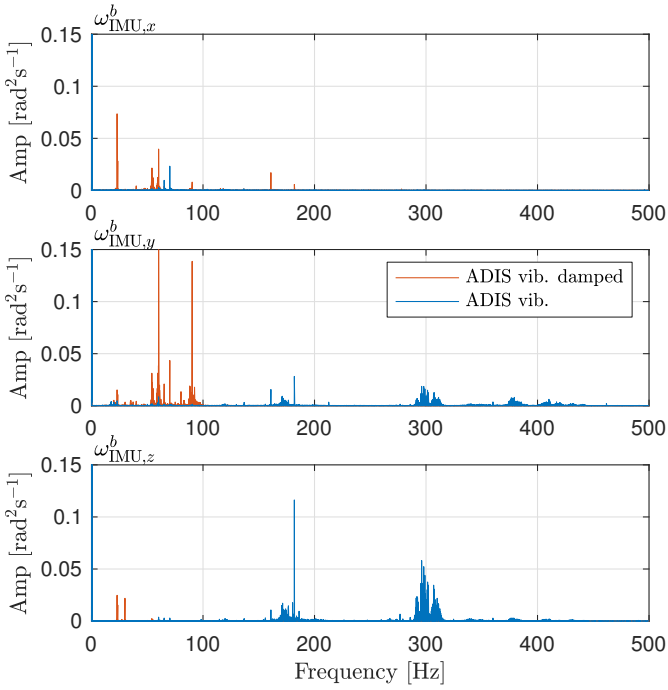

(b) Gyro.

Figure E.8: Power spectral density estimate of IMU measurements, vibration isolated (red) and not (blue) in DP.

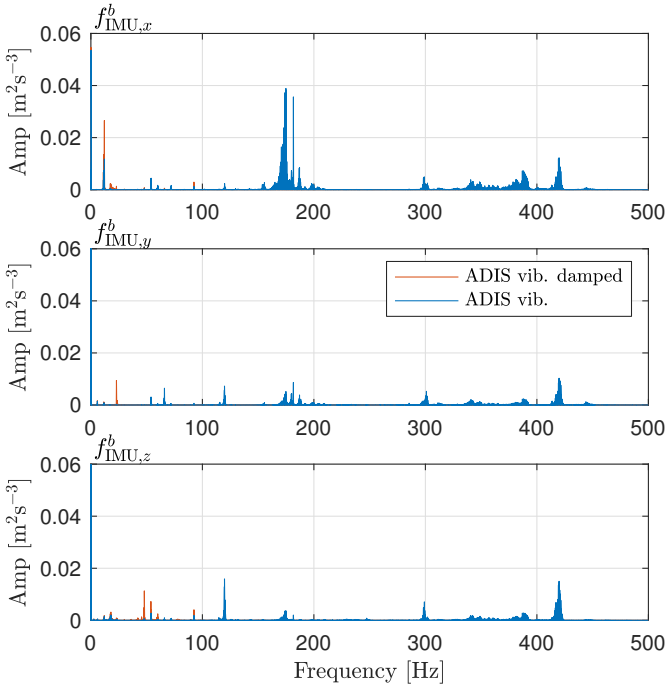

(a) Accelerometer.

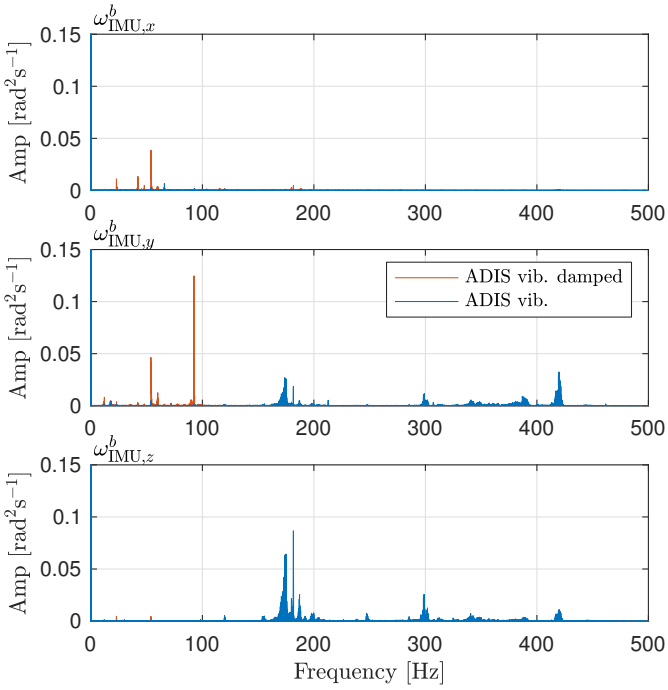

(b) Gyro.

Figure E.9: Power spectral density estimate of IMU measurements, vibration isolated (red) and not (blue) during steaming.

Algorithms

F

F.1 Discrete-time Implementation of the Attitude Observer

The algorithm on the following page presents an outline of the implementation of the attitude observer in discrete time.

Algorithm 4 Discrete-time attitude observer in direct form.

Require: Initializing the observer,

1: $\hat{\boldsymbol{q}}_b^e[0] = \boldsymbol{q}_0(\phi[0], \theta[0], \psi[0])$, $\hat{\boldsymbol{b}}_{\text{gyro}}^b = 0_{3\times 1}$, where q_0 is the mapping from the initial Euler angles $\phi[0]$, $\theta[0]$, $\psi[0]$.
2: Enforcing $\|\hat{\boldsymbol{q}}_b^e[0]\|_2 = 1$, using $\hat{\boldsymbol{q}}_b^e[0] = \hat{\boldsymbol{q}}_b^e[0]/\|\hat{\boldsymbol{q}}_b^e[0]\|_2$.
3: Extracting $s[0]$ and $\boldsymbol{r}[0]$ from $\hat{\boldsymbol{q}}_b^e[0]$ and calculating the initial rotation matrix

$$\boldsymbol{R}(\hat{\boldsymbol{q}}_b^e[0]) = \boldsymbol{I}_3 + 2s[0]\boldsymbol{S}(\boldsymbol{r}[0]) + 2\boldsymbol{S}^2(\boldsymbol{r}[0]) \tag{F.1}$$

Iteration: k

4: Get $\hat{\boldsymbol{f}}_{ib}^e[k]$ from the TMO,
5: Get $\boldsymbol{f}_{\text{IMU}}^b[k]$, $\boldsymbol{\omega}_{\text{IMU}}^b[k]$ from the IMU and performing vector calculations,

$$\underline{\boldsymbol{f}}^b = \boldsymbol{f}_{\text{IMU}}^b[k]/\|\boldsymbol{f}_{\text{IMU}}^b[k]\|_2, \qquad \underline{\boldsymbol{v}_1}^b[k] = \underline{\boldsymbol{f}}^b, \tag{F.2}$$

$$\underline{\boldsymbol{f}}^e = \text{sat}_{M_f}(\hat{\boldsymbol{f}}_{ib}^e[k])/\|\text{sat}_{M_f}(\hat{\boldsymbol{f}}_{ib}^e[k])\|_2, \qquad \underline{\boldsymbol{v}_1}^e[k] = \underline{\boldsymbol{f}}^e, \tag{F.3}$$

$$\hat{\boldsymbol{\sigma}}_1[k] = \frac{\delta t_{\text{acc}}}{T_s} k_1[k] \underline{\boldsymbol{v}_1}^b[k] \times \boldsymbol{R}^\intercal(\hat{\boldsymbol{q}}_b^e[k-1]) \underline{\boldsymbol{v}_1}^e[k], \tag{F.4}$$

6: **if** new magnetometer measurement is available **then**
7: Get $\boldsymbol{m}_{\text{mag}}^b[k]$ from the magnetometer and performing vector calculations,

$$\underline{\boldsymbol{m}}^b = \boldsymbol{m}_{\text{mag}}^b[k]/\|\boldsymbol{m}_{\text{mag}}^b[k]\|_2, \qquad \underline{\boldsymbol{v}_2}^b[k] = \underline{\boldsymbol{f}}^b \times \underline{\boldsymbol{m}}^b \tag{F.5}$$

$$\underline{\boldsymbol{m}}_{eb}^e = \boldsymbol{m}_{eb}^e/\|\boldsymbol{m}_{eb}^e\|_2, \qquad \underline{\boldsymbol{v}_2}^e[k] = \underline{\boldsymbol{f}}^e \times \underline{\boldsymbol{m}}^e \tag{F.6}$$

$$\hat{\boldsymbol{\sigma}}_2[k] = \frac{\delta t_{\text{mag}}}{T_s} k_2[k] \underline{\boldsymbol{v}_2}^b[k] \times \boldsymbol{R}^\intercal(\hat{\boldsymbol{q}}_b^e[k-1]) \underline{\boldsymbol{v}_2}^e[k], \tag{F.7}$$

8: **else**
9: $\hat{\boldsymbol{\sigma}}_2[k] = \boldsymbol{0}_{3\times 1}$.
10: **end if**
11: Calculating the aggregated injection term, $\hat{\boldsymbol{\sigma}}[k] = \hat{\boldsymbol{\sigma}}_1[k] + \hat{\boldsymbol{\sigma}}_2[k]$.
12: Calculating intermediate variables,

$$\hat{\boldsymbol{\omega}}[k] = \boldsymbol{\omega}_{\text{IMU}}^b[k] - \hat{\boldsymbol{b}}_{\text{gyro}}^b[k-1] + \hat{\boldsymbol{\sigma}}[k], \tag{F.8}$$

$$\boldsymbol{\Omega}(\hat{\boldsymbol{\omega}}[k]) = \begin{pmatrix} 0 & -\hat{\boldsymbol{\omega}}^\intercal[k] \\ \hat{\boldsymbol{\omega}}[k] & -\boldsymbol{S}(\hat{\boldsymbol{\omega}}[k]) \end{pmatrix}, \quad \bar{\boldsymbol{\Omega}}(\boldsymbol{\omega}_{ie}^e) = \begin{pmatrix} 0 & -(\boldsymbol{\omega}_{ie}^e)^\intercal \\ \boldsymbol{\omega}_{ie}^e & \boldsymbol{S}(\boldsymbol{\omega}_{ie}^e) \end{pmatrix}, \tag{F.9}$$

$$\mathbf{e}^{\left(\frac{T_s}{2}\boldsymbol{\Omega}(\hat{\boldsymbol{\omega}}[k])\right)} = \cos\left(\frac{T_s}{2}\|\hat{\boldsymbol{\omega}}[k]\|_2\right) I_4 + \frac{T_s}{2}\text{sinc}\left(\frac{T_s}{2}\|\hat{\boldsymbol{\omega}}[k]\|_2\right)\boldsymbol{\Omega}(\hat{\boldsymbol{\omega}}[k]), \tag{F.10}$$

$$\mathbf{e}^{\left(-\frac{T_s}{2}\bar{\boldsymbol{\Omega}}(\boldsymbol{\omega}_{ie}^e)\right)} = \left(\cos\left(\frac{T_s}{2}\|\boldsymbol{\omega}_{ie}^e\|_2\right) I_4 + \frac{T_s}{2}\text{sinc}\left(\frac{T_s}{2}\|\boldsymbol{\omega}_{ie}^e\|_2\right)\bar{\boldsymbol{\Omega}}(\boldsymbol{\omega}_{ie}^e)\right)^{-1}. \tag{F.11}$$

13: Updating attitude estimate,

$$\hat{\boldsymbol{q}}_b^e[k] = \mathbf{e}^{\left(\frac{T_s}{2}\boldsymbol{\Omega}(\hat{\boldsymbol{\omega}}[k])\right)}\mathbf{e}^{\left(-\frac{T_s}{2}\bar{\boldsymbol{\Omega}}\left(\boldsymbol{\omega}_{ie}^e\right)\right)}\hat{\boldsymbol{q}}_b^e[k-1]. \tag{F.12}$$

14: Carry out gyro bias projection and update gyro bias estimate,

$$\hat{\boldsymbol{b}}_{\text{gyro}}^b[k] = \hat{\boldsymbol{b}}_{\text{gyro}}^b[k-1] - T_s k_I[k]\hat{\boldsymbol{\sigma}}[k]. \tag{F.13}$$

15: Enforcing the unit quaternion constraint, $\hat{\boldsymbol{q}}_b^e[k] = \hat{\boldsymbol{q}}_b^e[k]/\|\hat{\boldsymbol{q}}_b^e[k]\|_2$,
16: Extracting $s_q[k]$ and $\boldsymbol{r}_q[k]$ from $\hat{\boldsymbol{q}}_b^e[k]$ and calculating the rotation matrix

$$\boldsymbol{R}(\hat{\boldsymbol{q}}_b^e[k]) = \boldsymbol{I}_3 + 2s_q[k]\boldsymbol{S}(\boldsymbol{r}_q[k]) + 2\boldsymbol{S}^2(\boldsymbol{r}_q[k]), \tag{F.14}$$

and providing $\boldsymbol{R}(\hat{\boldsymbol{q}}_b^e[k])$ to the TMO.
17: $k \leftarrow k+1$.

F.2 Quaternion Averaging with Matrix Weights

For averaging quaternions with matrix weights, we need to solve the optimization problem (Markley, 2007),

$$\begin{aligned}\bar{\boldsymbol{q}}_b^\star &:= \underset{\boldsymbol{q}_b^\star \in \mathcal{S}^3}{\arg\min} \sum_{j=1}^{m} \tilde{\boldsymbol{r}}_j^\mathsf{T} \boldsymbol{R}_j^{-1} \tilde{\boldsymbol{r}}_j \\ &= \underset{\boldsymbol{q}_b^\star \in \mathcal{S}^3}{\arg\min} \sum_{j=1}^{m} (\boldsymbol{q}_b^\star)^\mathsf{T} \boldsymbol{\Xi}_q(\hat{\boldsymbol{q}}_{b,j}^\star) \boldsymbol{R}_j^{-1} \boldsymbol{\Xi}_q^\mathsf{T}(\hat{\boldsymbol{q}}_{b,j}^\star) \boldsymbol{q}_b^\star, \end{aligned} \tag{F.15}$$

equivalent to (6.44). Algorithm 5 presents a similar algorithm to Algorithm 3 for the more general problem applying matrix weights $\boldsymbol{R}_j = \boldsymbol{R}_j^\mathsf{T} > 0$, where $\boldsymbol{R}_j$ may be chosen to represent the small attitude error covariance matrix, resembling a weighted least squares approach. If done so, the solution, $\bar{\boldsymbol{q}}_b^\star$, of (F.15) is a maximum likelihood estimate of $\boldsymbol{q}_b^\star$.

Algorithm 5 Quaternion Weighting with Matrix Weight

Input: Quaternion estimates $\hat{\boldsymbol{q}}_j$, weight matrices $\boldsymbol{R}_j$

1: **for** $j = 1$ **To** m **do**
2: $\quad \boldsymbol{\Xi}_q(\hat{\boldsymbol{q}}_{b,j}^\star)$ using (B.12)
3: **end for**
4: $\boldsymbol{R}_{\text{sum}}^{-1} = \sum_{j=1}^{m} \boldsymbol{R}_j^{-1}$
5: $\mathcal{M} = -\sum_{j=1}^{m} \boldsymbol{\Xi}_q(\hat{\boldsymbol{q}}_{b,j}^\star) \boldsymbol{R}_j^{-1} \boldsymbol{\Xi}_q^\mathsf{T}(\hat{\boldsymbol{q}}_{b,j}^\star)$
6: $\boldsymbol{K}_q = 4\mathcal{M} + \text{trace}\left(\boldsymbol{R}_{\text{sum}}^{-1}\right) \boldsymbol{I}_4$
7: $[\boldsymbol{E}, \boldsymbol{D}_{\text{eig}}] = \text{eig}(\boldsymbol{K}_q)$
8: $[\lambda_{\max}, j_{\max}] = \max(\text{diag}(\boldsymbol{D}_{\text{eig}}))$
9: $\bar{\boldsymbol{q}}_b^\star = \boldsymbol{E}(:, j_{\max})$

Ensure: $\|\bar{\boldsymbol{q}}_b^\star\|_2 = 1$
Output: $\bar{\boldsymbol{q}}_b^\star$

References

Anderson, B. (1971). Stability properties of Kalman-Bucy filters. *Journal of the Franklin Institute*, 1(2): 137–144.

Armenise, M. N., Ciminelli, C., Dell'Olio, F., and Passaro, V. M. N. (2010). *Advances in Gyroscope Technologies*. Springer-Verlag, Berlin Heidelberg.

Auestad, O. F., Gravdahl, J. T., and Fossen, T. I. (2013). Heave motion estimation on a craft using a strapdown inertial measurement unit. In *Proc of the 9th IFAC Conference on Control Applications in Marine Systems*, pp. 298—303, Osaka, Japan. doi: 10.3182/20130918-4-JP-3022.00033.

Balchen, J., Jenssen, N. A., and Sælid, S. (1976). Dynamic positioning using Kalman filtering and optimal control theory. In *In the IFAC/IFIP Symposium On Automation in Offshore Oil Field Operation*, pp. 183—186, Bergen, Norway.

Batista, P. (2015). GES long baseline navigation with unknown sound velocity and discrete-time range measurements. *IEEE Transactions On Control System Technology*, 23(1): 219–230. doi: 10.1109/TCST.2014.2321973.

Batista, P., Silvestre, C., and Oliveira, P. (2009). Necessary and sufficient conditions for the observability of linear motion quantities in strapdown navigation systems. In *Proc. American Control Conference*, pp. 1177–1182, St. Louis, MO. doi: 10.1109/ACC.2009.5159953.

Batista, P., Silvestre, C., and Oliveira, P. (2012a). A GES attitude observer with single vector observations. *Automatica*, 48(2): 388–39. doi: 10.1016/j.automatica.2011.07.005.

Batista, P., Silvestre, C., and Oliveira, P. (2012b). Globally exponentially stable cascade observers for attitude estimation. *Control Engineering Practice*, 20(2): 148–155. doi: 10.1016/j.conengprac.2011.10.005.

Batista, P., Silvestre, C., and Oliveira, P. (2012c). Sensor-based globally asymptotically stable filters for attitude estimation: Analysis, design, and performance evaluation. *IEEE Transactions on Automatic Control*, 57(8): 2095–2100. doi: 10.1109/TAC.2012.2187142.

Bayat, M., Crasta, N., Aguiar, A., and Pascoal, A. M. (2016). Range-based underwater vehicle localization in the presence of unknown ocean currents: Theory and experiments. *IEEE Transactions On Control System Technology*, 24(1): 122–139.

Beard, R. W. and McLain, T. W. (2012). *Small Unmanned Aircraft: Theory and Practice*. Princeton University Press.

Belleter, D. J., Galeazzi, R., and Fossen, T. I. (2015). Experimental verification of a globally exponentially stable nonlinear wave encounter frequency estimator. *Ocean Engineering, Elsevier*, 97(15): 48–56. doi: 10.1016/j.oceaneng.2014.12.030.

Bhat, S. and Bernstein, D. (2000). A topological obstruction to continuous global stabilization of rotational motion and the unwinding phenomenon. *Systems & Control Letters*, 39(1): 63–70. doi: 10.1016/S0167-6911(99)00090-0.

Black, H. D. (1964). A passive system for determining the attitude of a satellite. *AIAA Journal*, 2(7): 1350–1351. doi: 10.2514/3.2555.

Britting, K. R. (1971). *Inertial Navigation Systems Analysis*. John Wiley & Sons Ltd.

Brodtkorb, A. H., Sørensen, A. J., and Teel, A. (2014). Increasing the operation window for dynamic positioned vessels using the concept of hybrid control. In *Proc. of the ASME 2014 33rd International Conference on Ocean, Offshore and Arctic Engineering, OMAE2014*, San Francisco, California, USA.

Brown, R. G. and Hwang, P. Y. C. (2012). *Introduction to Random Signals and Applied Kalman Filtering*. John Wiley & Sons, Inc., Hoboken, New Jersey, fourth edition.

Bryne, T. H., Fossen, T. I., and Johansen, T. A. (2014). Nonlinear observer with time-varying gains for inertial navigation aided by satellite reference systems in dynamic positioning. In *Proc. of the IEEE Mediterranean Conference on Control and Automation*, pp. 1353–1360, Palermo, Italy. doi: 10.1109/MED.2014.6961564.

Bryne, T. H., Fossen, T. I., and Johansen, T. A. (2015a). Design of inertial navigation systems for marine craft with adaptive wave filtering aided by triple-redundant sensor packages. *International Journal of Adaptive Control and Signal Processing*, pp. 1–23. doi: 10.1002/acs.2645.

Bryne, T. H., Fossen, T. I., and Johansen, T. A. (2015b). A virtual vertical reference concept for GNSS/INS applications at the sea surface. In *Proc. of the 10th IFAC Conference on Manoeuvring and Control of Marine Craft (MCMC)*, pp. 127–133, Copenhagen, Denmark. Received the best regular paper award at IFAC MCMC'15. doi: j.ifacol.2015.10.269.

Bryne, T. H., Hansen, J. M., Rogne, R. H., Sokolova, N., Fossen, T. I., and Johansen, T. A. (2017a). Nonlinear observers for integrated INS/GNSS navigation – Implementation aspects. *IEEE Control Systems Magazine*. To Appear.

Bryne, T. H., Rogne, R. H., Fossen, T. I., and Johansen, T. A. (2016). Attitude and heave estimation for ships using MEMS-based inertial measurements. In *Proc. of the 10th IFAC Conference on Control Applications in Marine Systems (CAMS)*, pp. 568–575, Trondheim. doi: 10.1016/j.ifacol.2016.10.496.

Bryne, T. H., Rogne, R. H., Fossen, T. I., and Johansen, T. A. (2017b). Inertial sensors for risk-based redundancy in dynamic positioning. In *Proc. of the ASME 2017 36th International Conference on Ocean, Offshore and Arctic Engineering, OMAE2017*, Trondheim, Norway. To Appear.

Bryne, T. H., Rogne, R. H., Fossen, T. I., and Johansen, T. A. (n.d.). A virtual vertical reference concept for integrated inertial navigation at the sea surface. *Control Engineering Practice*. Submitted for publication.

Chen, H., Moan, T., and Verhoeven, H. (2009). Effect of dGPS failures on dynamic positioning of mobile drilling units in the North Sea. *Accident Analysis and Prevention*, 41(6): 1164–1171.

Chou, J. C. (1992). Quaternion kinematic and dynamic differential equations. *IEEE Transactions on robotics and automation*, 8(1): 53–64.

Daly, K. C., Gai, E., and Harrison, J. V. (1979). Generalized likelihood test for FDI in redundant sensor configurations. *Journal of Guidance, Control, and Dynamics*, 2(1): 9–17. doi: 10.2514/3.55825.

DNV GL (2011). Newbuildings special equipment and systems – additional class: Dynamic positioning systems. In *Rules for classification of ships*, Part 6 Chapter 7. DNV GL. Updated January 2012.

Farrell, J. A. (2008). *Aided Navigation: GPS with High Rate Sensors*. McGraw-Hill.

Fossen, T. I. (2011). *Handbook of Marine Craft Hydrodynamics and Motion Control*. John Wiley & Sons, Ltd.

Fossen, T. I. and Perez, T. (2009). Kalman filtering for positioning and heading control of ships and offshore rigs. *IEEE Control Systems Magazine*, 29(6): 32–46. doi: 10.1109/MCS.2009.934408.

Fossen, T. I. and Perez, T. (2010). Marine Systems Simulator (MSS). Viewed 01.08.2014, www.marinecontrol.org.

Fossen, T. I. and Strand, J. P. (1999). Passive nonlinear observer design for ships using lyapunov methods: full-scale experiments with a supply vessel. *Automatica*, 35(1): 3 – 16. doi: 10.1016/S0005-1098(98)00121-6.

Gade, K. (2004). Navlab, a generic simulation and post-processing tool for navigation. *European Journal of Navigation*, 2(4): 51–59.
URL: *http://www.navlab.net/Publications/*

Gelb, A., Kasper, J. F., Nash, R. A., Price, C. F., and Sutherland, A. A., editors (1974). *Applied Optimal Estimation*. M.I.T. Press, Cambridge, MA.

Godhavn, J.-M. (1998). Adaptive tuning of heave filter in motion sensor. In *OCEANS '98 Conf. Proc.*, volume 1, pp. 174–178, Nice, France.

Godhavn, J.-M. (2000). High quality heave measurements based on GPS RTK and accelerometer technology. In *OCEANS 2000 MTS/IEEE Conference and Exhibition*, volume 1, pp. 309–314, Providence, RI.

Grewal, M., Andrews, A. P., and Bartone, C. G. (2013). *Global navigation satellite systems, inertial navigation, and integration*. John Wiley & Sons, Inc., Hoboken, New Jersey, 3rd edition.

Grip, H. F., Fossen, T. I., Johansen, T. A., and Saberi, A. (2012a). Attitude estimation using biased gyro and vector measurements with time-varying reference vectors. *IEEE Transactions on Automatic Control*, 57(5): 1332—1338. doi: 10.1109/TAC.2011.2173415.

Grip, H. F., Fossen, T. I., Johansen, T. A., and Saberi, A. (2013). Nonlinear observer for GNSS-aided inertial navigation with quaternion-based attitude estimation. In *Proc. of the American Contr. Conf.*, pp. 272–279, Washington, DC. doi: 10.1109/ACC.2013.6579849.

Grip, H. F., Fossen, T. I., Johansen, T. A., and Saberi, A. (2015). Globally exponentially stable attitude and gyro bias estimation with application to GNSS/INS integration. *Automatica*, 51: 158—166. doi: 10.1016/j.automatica.2014.10.076.

Grip, H. F., Fossen, T. I., Johansen, T. A., and Saberi, A. (2016). Nonlinear observer for attitude, position, and velocity: Theory and experiments. In Fourati, H. and Belkhia, D. C., editors, *Multisensor Attitude Estimation*, chapter 17, pp. 291–313. CRC Press (Taylor & Francis Group).

Grip, H. F. and Saberi, A. (2010). Structural decomposition of linear multivariable systems using symbolic computations. *International Journal of Control*, 83(7): 1414–1426. doi: 10.1080/00207171003758760.

Grip, H. F., Saberi, A., and Johansen, T. A. (2012b). Observers for interconnected nonlinear and linear systems. *Automatica*, 48(7): 1339–1346. doi: 10.1016/j.automatica.2012.04.008.

Groves, P. D. (2013). *Principles of GNSS, Inertial, and Multisensor Integrated Navigation Systems*. Artech House, 2nd edition.

Guerrier, S., Waegli, A., Skaloud, J., and Victoria-Feser, M.-P. (2012). Fault detection and isolation in multiple mems-imus configurations. *IEEE Transactions on Aerospace and Electronic Systems*, 48(3): 2015–2031. doi: 10.1109/TAES.2012.6237576.

Gustafsson, F. (2000). *Adaptive filtering and change detection*. John Wiley & Sons, Ltd.

Gustafsson, F. (2012). *Statistical Sensor Fusion*. Studentlitteratur, 2nd edition.

Hamel, T. and Mahony, R. (2006). Attitude estimation on $SO(3)$ based on direct inertial measurements. In *Proc. IEEE Int. Conf. on Robotics and Automation*, pp. 2170–2175, Orlando, FL, United States.

Hansen, J. M., Fossen, T. I., and Johansen, T. A. (2015). Nonlinear observer for INS aided by time-delayed GNSS measuements: Implementation and UAV experiments. In *Proc. International Conference Unmanned Aircraft Systems (ICUAS)*, pp. 157–166, Denver, Colorado. doi: 10.1109/ICUAS.2015.7152287.

Hansen, J. M., Johansen, T. A., and Fossen, T. I. (2016). Tightly coupled integrated inertial and real-time-kinematic positioning approach using nonlinear observer. In *Proc. of the American Contr. Conf.*, pp. 5511–5518, Boston, Ma. doi: 10.1109/ACC.2016.7526534.

Hassani, V., Pascoal, A. M., and Sørensen, A. J. (2013a). A novel methodology for adaptive wave filtering of marine vessels: Theory and experiments. In *Proc. IEEE Conference on Decision and Control*, pp. 6162–6167, Florence, Italy.

Hassani, V., Sørensen, A. J., and Pascoal, A. M. (2013b). Adaptive wave filtering for dynamic positioning of marine vessels using maximum likelihood identification: Theory and experiments. In *Proc. of the 9th IFAC Conference on Control Applications in Marine Systems (CAMS)*, pp. 203–208, Osaka, Japan.

Hassani, V., Sørensen, A. J., Pascoal, A. M., and Aguiar, A. (2012). Multiple model adaptive wave filtering for dynamic positioning of marine vessels. In *Proc. of the American Contr. Conf.*, pp. 6222–6228, Fairmont Queen Elizabeth, Montréal, Canada.

Horn, R. A. and Johnson, C. R. (2013). *Matrix Analysis*. Cambridge University Press, New York, 2nd edition.

Hua, M.-D. (2010). Attitude estimation for accelerated vehicles using GPS/INS measurements. *Control Engineering Practice*, 18(7): 723–732. doi: 10.1016/j.conengprac.2010.01.016.

Hua, M.-D., Ducard, G., Hamel, T., Mahony, R., and Rudin, K. (2014). Implementation of a nonlinear attitude estimator for aerial robotic vehicles. *IEEE Transactions On Control System Technology*, 22(1): 201–212. doi: 10.1109/TCST.2013.2251635.

Hua, M.-D., Martin, P., and Hamel, T. (2016). Stability analysis of velocity-aided attitude observers for accelerated vehicles. *Automatica*, 63: 11–15. doi: 10.1016/j.automatica.2015.10.014.

Ingram, M. J., Tyce, R. C., and Allen, R. G. (1996). Dynamic testing of state of the art vertical reference units. In *Proc. Oceans 96 MTS/IEEE*, pp. 1533–1538.

Johansen, T. A. and Fossen, T. I. (2015). Nonlinear observer for inertial navigation aided by pseudo-range and range-rate measurements. In *Proc. of the European Contr. Conf.*, pp. 1673–1680, Linz, Austria. doi: 10.1109/ECC.2015.7330778.

Johansen, T. A. and Fossen, T. I. (2016). Nonlinear observer for tightly coupled integration of pseudorange and inertial measurements. *IEEE Transactions On Control System Technology*, 24(6): 2199–2206. doi: 10.1109/TCST.2016.2524564.

Johansen, T. A., Fossen, T. I., and Goodwin, G. C. (2016). Three-stage filter for position estimation using pseudo-range measurements. *IEEE Transactions on Aerospace and Electronic Systems*.

Johansen, T. A., Hansen, J. M., and Fossen, T. I. (2017). Nonlinear observer for tightly integrated inertial navigation aided by pseudo-range measurements. *ASME Journal of Dynamic Systems, Measurement and Control*, 139(1): 011007–011007–10. doi: 10.1115/1.4034496.

Kalman, R. and Bucy, R. (1961). New results in linear filtering and prediction theory. *American Society of Mechanical Engineers – Transactions – Journal of Basic Engineering Series D*, 83(1): 95–108.

Khalil, H. K. (2002). *Nonlinear Systems*. Prentice Hall, third edition.

Khosravian, A., Trumpf, J., Mahony, R., and Hamel, T. (2014). Velocity aided attitude estimation on SO(3) with sensor delay. In *Proc. IEEE Conf. Decision and Control*, pp. 114–120, Los Angeles, CA. doi: 10.1109/CDC.2014.7039368.

Khosravian, A., Trumpf, J., Mahony, R., and Hamel, T. (2015). Recursive attitude estimation in the presence of multi-rate and multi-delay vector measurements. In *Proc. American Control Conference*, pp. 3199–3205, Chicago, IL. doi: 10.1109/ACC.2015.7171825.

Krstić, M., Kanellakopoulos, I., and Kokotović, P. V. (1995). *Nonlinear and Adaptive Control Design*. Wiley, New York.

Küchler, S., Eberharter, J. K., Langer, K., Schneider, K., and Sawodny, O. (2011a). Heave motion estimation of a vessel using acceleration measurements. In *Proc. of the 18th IFAC World Congress*, pp. 14742–14747, MIlan, Italy.

Küchler, S., Pregizer, C., Eberharter, J. K., Schneider, K., and Sawodny, O. (2011b). Real-time estimation of a ship's attitude. In *Proc. of the American Contr. Conf.*, pp. 2411–2416, San Francisco, CA.

Lauvdal, T. and Fossen, T. I. (1998). Robust adaptive ship autopilot with wave filter and integral action. *Special Issue on Marine Systems Control, International Journal of Adaptive Control and Signal Processing*, 12(8): 605–622.

Lindegaard, K. P. and Fossen, T. I. (2001). A model based wave filter for surface vessels using position, velocity and partial acceleration feedback. In *Proc of the 40th IEEE Conference on Decision and Control*, pp. 946–951.

Loria, A. and Panteley, E. (2005). Cascaded nonlinear time-varying systems: Analysis and design. In Lamnabhi-Lagarrigue, F., Loria, A., and Panteley, E., editors, *Adv. Top. in Cntrl. Sys. Theory*, volume 311 of *LNCIS*, chapter 2, pp. 23–64. Springer-Verlag. doi: 10.1007/11334774_2.

Mahony, R., Hamel, T., and Pflimlin, J. M. (2008). Nonlinear complementary filters on the special orthogonal group. *IEEE Transactions on Automatic Control*, 53(5): 1203–2018. doi: 10.1109/TAC.2008.923738.

Mahony, R., Hamel, T., Trumpf, J., and Lageman, C. (2009). Nonlinear attitude observers on so(3) for complementary and compatible measurements: A theoretical study. In *IEEE Conf. Decision Control*, pp. 6407—6412.

Markley, F. L. (2003). Attitude error representation for kalman filtering. *Journal of Guidance, Control and Dynamics*, 26(2): 311–317.

Markley, F. L. (2007). Averaging quaternions. *Journal of Guidance, Control and Dynamics*, 30(4): 1193–1196.

Markley, F. L. and Mortari, D. (2000). Quaternion attitude estimation using vector observations. *Journal of the Astronautical Sciences*, 48(2—3): 359—380.

Martin, P. and Salaün, E. (2010). Design and implementation of a low-cost observer-based attitude and heading reference system. *Control Engineering Practice*, 18(7): 712—722. doi: 10.1016/j.conengprac.2010.01.012.

Maybeck, P. (1979). Stochastic models, estimation, and control, volume 1. In *Mathematics in Science and Engineering*, volume 141. Academic Press.

Medvedev, A. (1995). Fault detection and isolation by a continuous parity space method. *Automatica*, 31(7): 1039–1044. doi: 10.1016/0005-1098(95)00008-K.

Misra, P. and Enge, P. (2011). *Global Positioning System: Signals, Measurements, and Performance*. Ganga-Jamuna Press, 2nd rev. edition.

Mohleji, S. C. and Wang, G. (2010). Modeling ADS-B position and velocity errors for airborne merging and spacing in interval management application. https://www.mitre.org/sites/default/files/pdf/10_3026.pdf, The MITRE Corporation, 7515 Colshire Drive, McLean VA 22102.

Nguyen, T. D., Sørensen, A. J., and Quek, S. T. (2007). Design of hybrid controller for dynamic positioning from calm to extreme sea conditions. *Automatica*, 43(5): 768–785.

Nijmeijer, H. and der Schaft, A. V. (1990). *Nonlinear dynamical control systems*. Springer-Verlag. doi: 10.1007/978-1-4757-2101-0.

Paturel, Y. (2004). PHINS, an all-in-one sensor for DP applications. In *Proc. of the Dynamic Positioning Conference*, Houston, TX.

Perez, T. (2005). *Ship Motion Control: Course Keeping and Roll Stabilisation Using Rudder and Fins*. Advances in Industrial Control. Springer-Verlag London Ltd.

Rankin, J. (1994). GPS and differential GPS: An error model for sensor simulation. In *IEEE Position Location and Navigation Symposium*, pp. 260–266, Las Vegas, NV.

Richter, M., Schneider, K., Walser, D., and Sawodny, O. (2014). Real-time heave motion estimation using adaptive filtering techniques. In *Proc. of the 19th IFAC World Congress*, pp. 10119–10125, Cape Town, South Africa.

Roberts, A. and Tayebi, A. (2011). On the attitude estimation of accelerating rigid-bodies using GPS and IMU measurements. In *Proc. Conf. Dec. Cont. and European Cont. Conf.*, pp. 8088–8093, Orlando, FL.

Rogne, R. H., Bryne, T. H., Fossen, T. I., and Johansen, T. A. (2016a). MEMS-based inertial navigation on dynamically positioned ships: Dead reckoning. In *Proc. of the 10th IFAC Conference on Control Applications in Marine Systems (CAMS)*, pp. 139—146, Trondheim. doi: 10.1016/j.ifacol.2016.10.334.

Rogne, R. H., Bryne, T. H., Fossen, T. I., and Johansen, T. A. (n.d.a). Redundant MEMS-based inertial navigation using nonlinear observers. *ASME Journal of Dynamic Systems, Measurement and Control*. Submitted for publication.

Rogne, R. H., Bryne, T. H., Fossen, T. I., and Johansen, T. A. (n.d.b). Strapdown inertial navigation on ships using MEMS sensors and nonlinear observers. *IEEE Transactions On Control System Technology*. Submitted for publication.

Rogne, R. H., Bryne, T. H., Johansen, T. A., and Fossen, T. I. (2016b). Fault detection in lever-arm-compensated position reference systems based on nonlinear attitude observers and inertial measurements in dynamic positioning. In *Proc. of the American Contr. Conf.*, pp. 985–992, Boston, Ma. doi: 10.1109/ACC.2016.7525043.

Rogne, R. H., Johansen, T. A., and Fossen, T. I. (2014). Observer and IMU-based detection of faults in position reference systems and gyrocompasses with dual redundancy in dynamic positioning. In *Proc of the IEEE Conference on Control Applications (CCA)*, pp. 83–88, Antibes, France.

Rogne, R. H., Johansen, T. A., and Fossen, T. I. (2015). On attitude observers and inertial navigation for reference system fault detection and isolation in dynamic positioning. In *Proc. European Control Conference (ECC)*, pp. 3665–3672, Linz, Austria.

RTKLIB (2013) (Last updated: 29.04.2013). Version 2.4.2. Available online at http://www.rtklib.com.

Sælid, S., Jenssen, N. A., and Balchen, J. G. (1983). Design and analysis of a dynamic positioning system based on the Kalman filtering and optimal control. *IEEE Transactions on Automatic Control*, 28(3): 331–339.

Salcudean, S. (1991). A globally convergent angular velocity observer for rigid body motion. *IEEE Trans. Automat. Contr.*, 36(12): 1493 – 1497.

Shuster, M. D. (1983). A survey of attitude representations. *Journal of the Astronautical Sciences*, 41(4): 439–5147.

Shuster, M. D. and Oh, S. D. (1981). Three-axis attitude determination from vector observations. *Journal of Guidance Control and Dynamics*, 4(1).

Simon, D. (2009). *Optimal state estimation: Kalman, H_∞, and nonlinear approaches*. John Wiley & Sons.

SNAME (1950). Nomenclature for treating the motion of a submerged body through a fluid. In *Technical and Research Bulletin No. 1—5*, pp. 1–15, New York. The Society of Naval Architects and Marine Engineers.

Strand, J. P. and Fossen, T. I. (1999). Nonlinear passive observer design for ships with adaptive wave filtering. In Nijmeijer, H. and Fossen, T. I., editors, *New Directions in Nonlinear Observer Design*, volume 244 of *LNCIS*, pp. 113–134. Springer-Verlag.

Sturza, M. A. (1988). Navigation system integrity monitoring using redundant measurements. *Navigation*, 35(4): 483–501. doi: 10.1002/j.2161-4296.1988.tb00975.x.

Sukkarieh, S., Gibbens, P., Grocholsky, B., Willis, K., and Durrant-Whyte, H. F. (2000). A low-cost, redundant inertial measurement unit for unmanned air vehicles. *The International Journal of Robotics Research*, 19(11): 1089–1103.

Thienel, J. and Sanner, R. (2003). A coupled nonlinear spacecraft attitude controller and observer with an unknown constant gyro bias and gyro noise. *IEEE Trans. Automat. Contr.*, 48(11): 2011–2014. doi: 10.1109/TAC.2003.819289.

Titterton, D. H. and Weston, J. L. (2004). *Strapdown inertial navigation technology*. Institution of Electrical Engineers and American Institute of Aeronautics and Astronautics, 2nd edition.

Torsetnes, G., Jouffroy, J., and Fossen, T. I. (2004). Nonlinear dynamic positioning of ships with gain-scheduled wave filtering. In *Proc. IEEE Conference on Decision and Control*, pp. 5340–5347, Paradise Island, Bahamas.

van Loan, C. F. (1978). Computing integrals involving the matrix exponential. *IEEE Trans. Automatic Control*, AC–23(3): 395–404. doi: 10.1109/TAC.1978.1101743.

Veksler, A., Johansen, T. A., and Skjetne, R. (2012). Transient power control in dynamic positioning - governor feedforward and dynamic thrust allocation. In *Proc. the 9th IFAC Conference on Manoeuvring and Control of Marine Craft (MCMC)*, pp. 158–163, Arenzano, Italy.

Vermeille, H. (2004). Computing geodetic coordinates from geocentric coordinates. *Journal of Geodesy*, 78: 94—95.

Vik, B. and Fossen, T. (2001). A nonlinear observer for GPS and INS integration. In *Proc. IEEE Conf. Dec. Cont*, volume 3, pp. 2956–61, Orlando, FL. doi: 10.1109/.2001.980726.

Vik, B. and Fossen, T. I. (1997). Semiglobal exponential output feedback control of ships. *IEEE Transactions On Control System Technology*, 5(3): 360–370.

Vik, B. and Marçal, J. (2003). Experimental testing of vertical reference units. In *Proc. of the 6th IFAC Conference on Manoeuvring and Control of Marine Craft (MCMC)*, pp. 233–238, Girona, Spain.

Waegli, A., Guerrier, S., and Skaloud, J. (2008). Redundant MEMS-IMU integrated with GPS for performance assessment in sports. In *2008 IEEE/ION Position, Location and Navigation Symposium*, pp. 1260–1268. IEEE. doi: 10.1109/PLANS.2008.4570079.

Wahba, G. (1965). A least squares estimate of spacecraft attitude. *SIAM Review*, 7(3): 409—409.

Welch, P. D. (1967). The use of fast fourier transform for the estimation of power spectra: A method based on time averaging over short, modified periodograms. *IEEE Transactions on Audio and Electroacoustics*, 15(2): 70–73. doi: 10.1109/TAU.1967.1161901.

Willsky, A. and Jones, H. (1976). A generalized likelihood ratio approach to the detection and estimation of jumps in linear systems. *IEEE Transactions on Automatic control*, 21(1): 108–112. doi: 10.1109/TAC.1976.1101146.

Zhao, B. and Skjetne, R. (2014). A unified framework for fault detection and diagnosis using particle filter. *Modeling, Identification and Control*, 35(4): 303—315.

Zlotnik, D. E. and Forbes, J. R. (2016). Nonlinear estimator design on the special orthogonal group using vector measurements directly. *IEEE Transactions on Automatic Control*, PP(99). doi: 10.1109/TAC.2016.2547222.